UNIVERSITY OF SOUTHAMPTON

Faculty of Engineering and Physical Sciences
School of Engineering

Towards a Stable, Flexible and Efficient Computational Fluid Dynamics Toolkit for Re-entry Vehicle Design Optimisation - Development, Characterisation and Initial Findings

by

Thomas Jack Greenslade

ORCiD: 0000-0002-9205-8714

A thesis for the degree of
Doctor of Philosophy

August 2023

Supervisor: Dr Minkwan Kim
Co-supervisor: Dr Charlie Ryan

University of Southampton

Abstract

Faculty of Engineering and Physical Sciences
School of Engineering

Doctor of Philosophy

Towards a Stable, Flexible and Efficient Computational Fluid Dynamics Toolkit for Re-entry Vehicle Design Optimisation - Development, Characterisation and Initial Findings

by Thomas Jack Greenslade

The simulation of hypersonic plasma flow is of critical importance to the design, optimisation and construction of re-entry spacecraft. Tools for conducting such simulations must be capable of modelling various kinds of thermochemical non-equilibrium, as well as a high degree of shock resolution and high accuracy post-shock flow characteristics. The development and characterisation of a new toolkit designed for such problems is presented herein; OP2A. The OP2A toolkit is capable of dealing with the complex phenomena arising in re-entry flows and the high accuracy shock resolution required to accurately and precisely simulate post-shock flows. Additionally, OP2A is designed to facilitate the optimisation of space vehicle design through fluid simulation. It does so by prioritising rapid mesh generation and the seamless modification of physical simulation elements and models, to allow for rapid testing of various simulation configurations. In order to achieve this, emphasis has been placed upon the efficiency, flexibility and stability of OP2A, and certain numerical aspects have been chosen to facilitate rapid grid generation. OP2A can resolve simulated quantities to second order accuracy in both space and time. In addition, OP2A is able to simulate the chemistry of various gas compositions, allowing for the simulation of multiple atmospheres. This work documents the theoretical and numerical implementations within OP2A, and details the more notable computational aspects designed to facilitate spacecraft optimisation simulations. OP2A's thermochemical modelling capabilities have been thoroughly evaluated and the results are presented herein. OP2A has also been used to simulate several results of interest to re-entry simulation, detailing the effects of thermochemical non-equilibrium upon plasma flows about a spacecraft. These results are presented and discussed in terms of their significance to re-entry problems and within the context of the surrounding literature. The direction of the future development of OP2A is also discussed, including details of both numerical and computational expansions.

Contents

List of Figures

List of Tables

Listings

Declaration of Authorship

I declare that this thesis and the work presented in it is my own and has been generated by me as the result of my own original research.

I confirm that:

1. This work was done wholly or mainly while in candidature for a research degree at this University;
2. Where any part of this thesis has previously been submitted for a degree or any other qualification at this University or any other institution, this has been clearly stated;
3. Where I have consulted the published work of others, this is always clearly attributed;
4. Where I have quoted from the work of others, the source is always given. With the exception of such quotations, this thesis is entirely my own work;
5. I have acknowledged all main sources of help;
6. Where the thesis is based on work done by myself jointly with others, I have made clear exactly what was done by others and what I have contributed myself;
7. None of this work has been published before submission

Signed:..... Date:.....

Acknowledgements

I would like to thank my supervisors, Dr Minkwan Kim and Dr Charlie Ryan for their continuous and patient advice and guidance throughout this work. I'd like to thank the Iridis team at the University of Southampton for providing their assistance with the Iridis compute cluster for this work. I'd also like to thank the members of my research group; Nathan, Henrike, James and Xin for their feedback and banter. I'd also like to thank my family, and my friends; Ben, Martin, Astrid and Ed for keeping me sane(ish).

Dedicated to my mother and grandmother, for supporting my education even in the toughest of times.

Definitions and Abbreviations

a	Speed of sound (m s^{-1})
c_p	Specific heat at constant pressure (J K^{-1} mol^{-1})
c_v	Specific heat at constant volume (J K^{-1} kg^{-1})
D	Diffusion coefficient (ms^{-1})
E	Total energy (J m^{-3})
e	Specific energy (J kg^{-1} m^{-3})
g	Degeneracy
H	Total enthlapy (J m^{-3})
h	Specific enthlapy (J kg^{-1})
I	Ionisation energy (J m^{-3})
J	Species diffusion rate (kg m^{-1} s^{-1}
Kn	Knudsen number
k_B	Boltzmann constant (1.380×10^{-23} J K^{-1})
K_e	Equilibrium constant
$k_{f/b}$	Chemical reaction rates (kg s^{-1})
L	Characteristic length scale (m)
Le	Lewis number
M	Mach number
M_s	Molecular mass of species s (kg mol^{-1})
m	Mass (kg)
N	Number
N_A	Avogadro's number (6.022×10^{23})
n	Number density (m^{-3})
p	Pressure (Pa)
Q	Charge (C)
q	Heat flux (W m^{-1})
R_s	Specific gas constant (J K^{-1} kg^{-1})
R_u	Universal gas constant (8.314 J $K^{-1}mol^{-1}$)
T	Temperature (K)
T_P	Park temperature (K)
$\vec{u}$	Advective velocity (m s^{-1})
$\vec{v}$	Diffusive velocity (m s^{-1})

w	Source/Sink terms
Y_s	Molar fraction of species s
$\alpha_{thermal}$	Thermal diffusivity ($m^2\ s^{-1}$)
γ_S	Molar concentration of species s (mol kg^{-1})
$\delta_{i,j}$	Kronecker delta
ε_0	Free space permittivity ($8.85418782 \times 10^{-12}\ A^2\ s^4\ m^{-3}\ kg^{-1}$)
λ	Mean free path (m)
λ_D	Debye length (cm)
κ	Thermal conductivity (W $m^{-1}\ K^{-1}$)
μ	Viscosity (Pa s)
ρ	Mass density (kg m^{-3})
σ	Collision cross section (m^2)
τ	Viscous stress
θ	Characteristic temperature (K)
ω_p	Plasma frequency (rad s^{-1})

Subscripts

p	Participants in a chemical reaction
r	Chemical reactions
s	Chemical species

Energies and Temperatures

e	Free electron
el	Bound electronic
r	Rotational
t	Translational
v	Vibrational

Acronyms

AMR	Adaptive Mesh Refinement
CFD	Computational fluid dynamics
DLR	German Aerospace Center (Deutsches Zentrum fur Luft- und Raumfahrt)
DPLR	Data-Parallel Line Relaxation
DSMC	Direct Simulation Monte-Carlo
EAST	Electric Arc Shock Tube
ESA	European Space Agency
HALO3D	High-Altitude Low-Orbit 3D
HTF	Hypersonic Tunnel Facility

IRS	Institut für Raumfahrtsysteme
ISS	International Space Agency
JAXA	Japan Aerospace Exploration Agency
LAURA	Langley Aerothermodynamic Upwind Relaxation Algorithm
LeMANS	Le Michigan Aerothermodynamic Navier Stokes Solver
OOP	Object Oriented Programming
MEESST	Magnetohydrodynamic Enhanced Entry System for Space Transportation
MHD	Magnetohydrodynamic
NASA	National Aeronautics and Space Administration
SSD	Shock Stand-off Distance
TPS	Thermal protection system
VKI	von Karman Institute for Fluid Dynamics.

1

Introduction

"I don't know what you could say about a day in which you have seen four beautiful sunsets."

– John Glenn

1.1 Motivation

1.1.1 Opportunities of Crewed Spaceflight

Crewed spaceflight is at once an inspirational and practical endeavour; with the capacity to ignite the imagination as well as provide opportunities for scientific research and novel manufacturing techniques.

The international space station has provided the foremost platform for such research and development. This has included attempts to detect dark matter outside the confines of Earth's atmosphere, as documented by Aguilar et al. (2013). Biomedical researchers have also utilised the results of several space stations to investigate the effects of low gravity on the human body, and to study the behaviour of organisms which can exist in space; as publicised by Buckey (2006) and Kawaguchi et al. (2020) respectively.

Various manufacturers have invested in off-Earth manufacturing techniques. The Japan Aerospace Exploration Agency (JAXA) have utilised the microgravity environment aboard the ISS to develop protein crystals possessing superior regularity compared to their terrestrially produced alternatives, as presented by Takahashi et al. (2013). Several commercial companies are currently pursuing the production of high bandwidth ZBLAN fibreoptic cables aboard the ISS in order to reduce imperfections within the cabling. Reduction of such imperfections has been projected to yield bandwidth increases of up to an order of magnitude according to Starodubov et al. (2014). Looking

forward, another vitally important application of off-Earth manufacturing may be the growth of human transplantable organs in space. Organs grown on Earth risk collapsing before completion due to gravitational effects. Growing in a microgravity environment removes this risk, and has been recently tested by NASA's BioFabrication Facility which operated aboard the ISS between 2019 and 2020 before being returned to Earth, as Prater et al. (2019) describes in detail.

Besides this, crewed spaceflight offers the potential for even more interesting avenues in the future, from space tourism in the short term, to extraterrestrial resource gathering in the long term, suggested by Mueller (2019) among others. In order for this potential to be realised, it is necessary that spaceflight transitions from a perilous pioneers pursuit to a mature and reliable practice.

In order to facilitate this it is necessary for spaceflight to become safer and more reliable than it is today. Spaceflight must become as routine as air travel if it is to reach its full potential. As such, the safety and reliability of all aspects of spaceflight must be improved, beginning at the design stage of spacecraft development.

1.1.2 Perils of Spaceflight

Within a typical high altitude spaceflight, the most significant challenges occur within the re-entry phase. The challenges of re-entry are manifold, and include withstanding the stresses and strains of high speed entry as well as dealing with communications blackout and mitigating incoming heat fluxes. The latter challenge occurs due to the layer of high temperature (10^5 K) non-equilibrium plasma which forms between the re-entry shock and the vehicle. It is the challenges these non-equilibrium re-entry flows pose to space vehicle design which are the main concern of this thesis.

All re-entry challenges are caused by the upper hypersonic (Mach 10+) velocities that re-entry vehicles achieve. These velocities range up to the fastest re-entry speed to date of 12.9 kms^{-1} ($\sim$ Mach 35) achieved by the Stardust re-entry capsule in 2006 as reported by Desai et al. (2008). Speeds reached are more typically between 7 and 11 kms^{-1} as indicated by Table 1.1.

TABLE 1.1: Synopsis of common re-entry velocities.

Mission	**Maximum speed (kms^{-1})**
Apollo 13	7.5
Apollo 11	10.7
Apollo 10	11.1
Space Shuttle	7.8
Stardust	12.9

These velocities not only produce the expected mechanical strains associated with any high speed movement in atmosphere, but also complicate other aspects of flight. Trajectory deviations in particular become far more problematic simply due to the large changes in landing location for only a small angular deviation lasting little time. However, there is further complication; when the vehicle achieves these speeds they generate strong shock waves. These shock waves cause significant heating of the air between the shock and the vehicle. During the re-entry process, temperatures behind the shock can reach over 10000 K at the stagnation point.

These temperatures cause the atmosphere behind the shock to ionise into a high temperature re-entry plasma. With flows at thousands of Kelvin impinging upon the vehicle, it is obvious that there need to be efforts to mitigate these heat loads, in order to avoid damaging the vehicle forebody. The most common heat flux mitigation method is that of the ablative heat shield, which evaporates over the course of re-entry, carrying heat with it and thus protecting the vital parts of the vehicle. The key drawback to ablative heat shields is their mass, they can account for a large percentage of the total vehicle mass, as described by Table 1.2.

TABLE 1.2: Synopsis of typical heat shield mass percentages, sources: Pezzella (2013).

Capsule	**Total Mass (kg)**	**Heat Shield Mass (kg)**	**%**
Galileo	337	152	45.1
Hayabusa	16.3	10.3	63.2
Stardust	45.8	10.1	22
Genesis	210	37.8	18

Another problem associated with the plasma layer surrounding re-entry vehicles is that of radio blackout. Radio blackout is a period of re-entry, during which communications with ground stations is impossible. This occurs as a side effect of the aforementioned intense heating occurring behind the shock. Upon heating to such degrees, the gas behind the shock begins to ionise, becoming a plasma consisting of positive ions and free electrons. Once a layer of this plasma has formed about the vehicle, electromagnetic signals are impeded by the free electrons based upon the signal's frequency as compared to the plasma frequency,

$$\omega_p = \sqrt{\frac{n_e Q_e^2}{\varepsilon_0 m_e}}, \tag{1.1}$$

where n_e is the electron number density, Q_e electron charge, m_e electron mass, and ε_0 the permittivity of free space. Any signals with frequencies below the plasma frequency will be impeded or outright blocked. Such signals include many of those used for high speed communications and telemetry with spacecraft. The blackout periods experienced by a selection of re-entry capsules are presented in Table 1.3.

TABLE 1.3: Synopsis of common radio blackout periods.

Capsule	Radio Blackout Period (s)
Apollo 13	> 360
Mars Pathfinder	30
Space Shuttle	720
Mars Pathfinder	30

Any loss of communications could prove disastrous as astronauts on board have reduced knowledge of their exact position and trajectory during this time, and ground crews remain unable to communicate with them. During this time, if there were to be an error in the inbound trajectory, the vehicle would have veered hundreds of kilometers off course due to the extremely high velocity of the craft.

Efforts are currently underway to design and test alternative thermal protection systems (TPS) as well as methods of mitigating radio blackout. In 2020 the European Space Agency (ESA) initiated a project to research possibility of utilising on-board magnetic fields to redirect plasma flows, and therefore heat fluxes. The Magnetohydrodynamic Enhanced Entry System for Space Transportation (MEESST) project, first presented by Bögel et al. (2021), is exploring the use of on-board superconducting magnets to alter the local magnetic field about the vehicle for greater heat flux control. If successfully developed, magnetic heat load control would mitigate the need for such large amounts of ablative heat shielding. Additionally, such tools would also allow plasma to be redirected so as to create a window for radio signal transmission as has been suggested by Kim et al. (2008).

As these are some of the most challenging aspects of high altitude spaceflight, any improvements in these capabilities would provide a boon for the forward development of spaceflight. This means utilising both numerical and experimental tools to improve re-entry capsule design so as to avoid these problems where possible, and mitigate their extremes where not.

The design procedure for re-entry capsules is informed directly and indirectly by research into re-entry conditions. With direct research focusing on the specific interactions of vehicles with re-entry flows, whilst indirect research studies the more general properties of these flows. Such research cannot be limited to studies of the behaviour of equilibrium flows, as the speeds and temperatures involved ensure that thermochemical non-equilibrium flows are common, and their effects significant. These non-equilibria are significant as the behaviour of the flows about the vehicle is sensitive to the exact nature of this non-equilibrium, with non-equilibria altering features such as temperature and density profiles. This in turn means that the mechanisms behind radio blackout and heat load deposition are also sensitive to the multiple temperatures which occur in non-equilibrium plasma flows, as well as the chemical composition of

the plasma and how it changes over the course of the flight. Hence, a better understanding of these non-equilibrium effects, both thermal and chemical, is crucial to optimising the design of spacecraft in order to improve the safety and reliability of spaceflight.

1.2 Investigations of Re-entry Plasma Flows

In order to accurately model re-entry flows, there are a myriad of physical difficulties to overcome, including varying flow regimes, thermochemical non-equilibria and electromagnetic effects. Firstly, the vehicle will descend through varying atmospheric pressure moving from rarefied into continuum flows as described by the Knudsen number,

$$Kn = \frac{\lambda}{L}, \tag{1.2}$$

where λ is the mean free path of the gas and L is the characteristic length of the vehicle. The Knudsen number determines the nature of flow as described by Equation 1.3.

$$Kn = \begin{cases} < 0.01 \implies & \text{Continuum flow,} \\ 0.01 - 0.1 \implies & \text{Slip flow,} \\ 0.1 - 1.0 \implies & \text{Transitional flow,} \\ > 1.0 \implies & \text{Free molecular flow.} \end{cases} \tag{1.3}$$

As vehicles enter the atmosphere, they descend in altitude with the Knudsen number decreasing in parallel. Each of these flow regimes features markedly different behaviour and each needs to be understood, as well as these understandings bridged together to provide a complete description of re-entry. Furthermore, there are additional complexities arising from turbulent boundary layer interactions, including boundary layer transition, and instabilities occurring through the interaction of turbulent and laminar flows.

The particular focus of this work are the thermal and chemical non-equilibria and the significant effects that they have on the key aerothermodynamic quantities within the continuum flow regime. These quantities include the deposited heat loads, plasma frequency and shock stand-off distance.

1.2.1 Thermochemical Non-Equilibrium Flows

In an atmospheric plasma, there exist 5 distinct internal energy modes; translational E_t, rotational E_r, vibrational E_v, bound electronic E_{el}, free electron E_e and another reservoir of energy contained within the formation enthlapy of chemical species E_{h0}. Within

the plasma, all atoms posses translational and bound electronic energy; molecules further possess rotational and vibrational; whilst electrons possess free electron energy (simply their translational energy). Most chemical species possess some formational energy, though others have a formational energy of zero. The distinction between translational energy for atoms/molecules, and free electron energy for electrons, exists due to the mass difference between electrons and atoms, otherwise the two energy modes are identical in mechanics. This mass difference leads to the motion of these particles leading and lagging one another as originally described by the Born-Oppenheimer approximation, initially presented by Born and Oppenheimer (1927).

Under thermal equilibrium conditions, one temperature can describe the temperature of the system; under a non-equilibrium condition, multiple temperatures are required. Additionally rotational and vibrational temperatures can be assumed to be uniform between different molecule types, or can be described individually if large differences are expected. Failure to properly observe the differences in temperature between modes can lead to significant discrepancies between theory and reality, such as those noted by Tam and Li (1989), additionally, discrepancies can be further reduced through the application of more detailed models, such as those implemented by Furudate et al. (2000). Because of the differences between models, it is highly valuable when investigating non-equilibrium effects to be able to rapidly compare models as the individual system requires.

Thermal non-equilibrium develops due to the way in which energy is deposited into the fluid behind the shock. Said energy is deposited non-uniformly, predominantly into the translational mode due to the closeness of translational energy levels. This energy is then transferred between modes until equilibrium is reached. The time frame for equilibrium to occur has been found by Boyd and Josyula (2011) to be of the order of $10^{-5} - 10^{-6}$ s, meaning that in most circumstances a state of thermal equilibrium can be assumed. However, with velocities of the order of 10^4 ms^{-1} and characteristic lengths of the order 10^{-2} m the plasma will have been swept downstream of the vehicle by the time equilibrium has been achieved; hence the plasma directly about the vehicle's forebody exists in a continual state of thermal non-equilibrium.

A similar situation occurs for chemical non-equilibrium, with the chemical equilibrium relaxation times of the order of 10^{-5} s and above (for Earth's atmosphere). This means that the plasma will have been swept downstream of the vehicle by the time any chemical equilibrium is established. An added complication for establishing chemical equilibrium, is that chemical reactions can depend upon different temperatures which are in turn dependent upon the degree of thermal non-equilibrium present. This indicates that chemical equilibrium cannot be established until thermal equilibrium has stabilised.

Thermal non-equilibrium causes additional complexity in processes with temperature dependencies, especially relevant when attempting to predict heat loads impinging upon a vehicle and the subsequent ablation. Whilst chemical non-equilibrium creates similar complexities depending upon the atmosphere involved, for example differing chemical compositions can cause differing electron densities, affecting the plasma frequency and in turn radio blackout. Changes in chemical composition also affect the temperature(s) of the flow, creating feedback between thermal and chemical non-equilibrium. Both thermal and chemical non-equilibrium contribute to changes in the features of the shock itself, for example shock stand-off distance. Understanding and predicting the effects of these non-equilibria is crucial when undertaking and optimising the design of spacecraft in order to better overcome re-entry difficulties. This understanding can be furthered by both experimental and numerical means; the advantages, drawbacks and synergies of these techniques will now be examined.

1.2.2 Experimental Explorations of Non-Equilibrium Flows

Experimental recreation of non-equilibrium flows allows for space capsule components to be directly tested, contributing directly to the optimisation of space vehicles. There exist multiple experimental facilities suitable for conducting hypersonic flow experiments. Such facilities can be divided into distinct categories; conventional wind tunnels, shock-heated wind tunnels, shock tubes, arc-heated test facilities, and ballistic, free-flight ranges. However, each of these facilities can only recreate a simulacrum of re-entry flow with only certain flow parameters matched. An example of this is NASA's "Hypersonic Tunnel Facility" (HTF) which can create hypersonic flows with suitable enthlapy levels. However the HTF can create such flows only up Mach 7, far short of the needed velocities shown in Table 1.1. In addition, NASA operates the "Electric Arc Shock Tube" (EAST) facility, which is capable of generating flows for the investigation of; nitrogen relaxation behaviour, radiative heating of the Galileo probe, and the electrical conductivity of shock heated air, among the many uses catalogued by Grinstead et al. (2010). The last of these, the electrical conductivity of shock heated air, is a key parameter for the understanding of magnetohydrodynamic effects in post-shock plasma.

All of these facilities are however limited by the size of objects which can be tested within them, often this size limit is quite small. For example, the SCIROCCO plasma wind tunnel in Italy has a diameter limit of 600 mm for test objects, whilst its sibling the GHIBLI tunnel has a size limit of 80 mm.

An additional limitation is that all types of facilities are only capable of operating continuously for a small fraction of the average re-entry time. The HTF can recreate Mach 7 flow for up to 180 seconds under its optimal conditions set. This compares poorly against re-entry times which can run up to several minutes, with Apollo 13's radio

blackout period lasting 6 minutes as noted in Table 1.3. Lastly there are problems with creating flows with ionisation levels that accurately mimic real re-entry flow. This remains an ongoing area of concern as noted by Park (2013), with electron density levels often differing significantly from predictions as presented by Yamada (2022) among others.

In spite of these limitations, experimental facilities are still capable of producing data which is both pertinent and exciting. An example of this being the experimental simulations of entry into the Neptunian atmosphere, which was performed in the PWK4 tunnel at IRS at the University of Stuttgart by Loehle et al. (2022).

However these limitations do mean that in order to perform comprehensive testing of a re-entry vehicle component, it must be tested in multiple facilities. This compounds another difficulty - the cost of these facilities. Typical yearly operating costs often reach of millions of US$. There are a number of causes of these costs, one of which is the extremely high power requirements during operations. This requirement necessitates coordinating power requirements with local power suppliers; facilities often have their own power substations to prevent negative effects to local power grids. The high costs of these facilities means that they are limited in number. This coupled with the fact that they can only operate for a limited portion of the day means that there is great competition for experimental slots.

Due to these factors, it is clearly important to optimise the use of the available experimental slots for testing components with the best chances of positive results. Hence, numerical simulation is used to ascertain the most viable candidates prior to conducting any experimental testing. In turn, these optimised experimental results generate data which can be used to improve the accuracy of numerical modelling in a positive feedback loop. For example, the L3K arc heated wind tunnel at DLR Cologne is regularly used to generate thermal response data relevant to thermal protection systems as shown by Mungiguerra et al. (2022) and Kim et al. (2011) among many others. Similar studies are regularly undertaken at VKI's Plasmatron facility, including those of Helber et al. (2012) and Lequang et al. (2009). The data produced by these facilities, as well as many others, feeds directly into the improvement of numerical simulation techniques.

1.2.3 Numerical Simulation of Hypersonic Flows

The numerical simulation of hypersonic non-equilibrium plasma flows involves the combination of specific CFD techniques with methods for the resolution of the aforementioned thermochemical non-equilibrium.

The required CFD techniques must be able to resolve the sharp shocks associated with hypersonic flows, and must have appropriate stability at high flow speeds. Due to the additional complexity introduced by non-equilibrium, more computations are required

when compared to non-hypersonic CFD, hence an even greater importance is placed upon computational efficiency. Lastly, when considering simulations for the optimisation of spacecraft, flexibility of methods and rapid grid generation are key concerns.

The resolution of thermochemical non-equilibria requires several additions to standard fluid dynamics models, in order to account for the changes to temperature and chemical species concentrations. Thermal non-equilibrium requires the determination of multiple temperatures and energies in order to evaluate the different energy modes and the transfer of energy between them. Additionally, thermodynamic functions for the calculation of temperatures and pressure must be adjusted to account for the different energy modes and any exchanges between them. The number and nature of energies, and the exact thermodynamic functions vary depending upon the thermal model under consideration. Chemical non-equilibrium requires the addition of individual species density terms and calculations to account for the creation and destruction of various chemical species. These chemical models can vary in complexity and functionality based on the accuracy level required and the atmospheric composition. Additionally, the chemical model chosen must be capable of utilising specific controlling temperatures as determined by the thermal non-equilibrium model; in this manner chemical modelling is dependent upon thermal modelling. The resolution of flows in chemical non-equilibrium places additional constraints upon the choice of CFD methods, as the timescales for chemical reactions and standard CFD flows differ widely resulting in a stiff set of equations. This stiffness places restrictions upon the choices of numerical methods which can converge flows within reasonable simulation times.

In addition to non-equilibrium modelling, electromagnetic modelling would be needed in order to simulate the effects of applied electromagnetic fields upon the plasma flows about the vehicle. Such modelling is necessary to test the methods such as magnetohydrodynamic (MHD) flow control. Additionally, radiative and ablative modelling techniques are required to gain accurate knowledge of radiative and ablative heat loads.

These components combined can be used to simulate the performance of capsules and their components in order to optimise their design prior to any experimental testing being required. Such simulations have been undertaken by a number of different parties. A brief review of the history and progress of these simulations is now presented.

1.3 Review of Non-Equilibrium Modelling

Attempts to numerically model the non-equilibrium effects of high temperature re-entry gases have been carried out for a number of purposes. These include modelling heat loads impinging upon vehicle surfaces and accurate prediction of radiative heat transfer rates during re-entry aerobraking. The limits of predictive modelling were made apparent in the 1980s when observational data from Fire and Apollo missions

was reviewed. Radiative heat fluxes were found to be lower than lab based experiments as presented by Park (1985b). Thermal non-equilibrium effects are also thought to have been behind discrepancies between expected and actual angles of attack for Apollo and Space Shuttle missions as noted by Park (2013). These discrepancies had the potential to be catastrophic, as they pushed their respective re-entry trajectories to the limits of safe operation. Such discrepancies cannot be resolved without the application of thermochemical non-equilibrium methods, which come in many varieties.

1.3.1 Non-Equilibrium Theoretical Models

Investigations into the effect of thermal non-equilibrium upon re-entry flows occurred throughout the 1960s and 70s with groups at Imperial College London (Stollery et al. (1964)), the University of Massachusetts (Bowen and Park (1971)) and NASA Ames (Allen et al. (1962)). In 1963 Millikan and White (1963) at General electric published the first method describing the mechanics of relaxation between the translational and vibrational energy modes. This method was a specific application of earlier work by Landau and Teller (1936), and provided the basis for energy exchange between two energy modes.

Two Temperature Models

Major progress occurred in 1985 when Chul Park, then with NASA Ames, proposed a two temperature model for fluids in thermochemical non-equilibrium in the publication of Park (1985a). This model built on the work of Millikan & White formalising thermal relaxation relationships, and proposed a correction factor to one of their formulae in order to better represent relaxation rates at temperatures above $10,000$ K. This work also proposed a split between a translational-rotational temperature, T_{tr}, and a vibrational-electronic-electron temperature, T_{vee}, and was the first to divide chemical reactions according to their temperature dependence. This model was then expanded with the addition of an intermediate temperature, between the two existing temperature values by Park (1988). This temperature, henceforth referred to as the Park temperature was defined as

$$T_P = T_{tr}^{a_P} T_{vee}^{b_P}, \tag{1.4}$$

where a and b are tunable parameters. Park initially suggested values of 0.5 for both a_P & b_P, with later adopters such as Casseau et al. (2016b) proposing values of $a_P = 0.7$ and $b_P = 0.3$. This Park temperature was utilised within this two-temperature model as the controlling temperature for most Earth atmosphere reactions. Park's first application of this model, to weakly ionised N_2 reduced the size of several discrepancies between theory and the existing experimental data. This experimental data came predominantly from a series of shock tube studies conducted at the Avco Everett Research

Laboratory. Whilst improvements were reported in several temperature predictions, as well as spectra predictions, discrepancies remained. In particular, the vibrational temperature estimations were deemed to be not in agreement with experiments, necessitating further model improvements.

In spite of these limitations, Park's two temperature model represented a significant step forward. It was the first comprehensive multi temperature thermochemical model to link thermal and chemical non-equilibrium and model their effects upon one another. From this point in the late 1980s, thermochemical modelling progress accelerated. Several models similar in form to Park's were proposed and sought to improve upon the predicted capabilities Park's model offered.

A later model applied to non-equilibrium flows actually derived from an earlier source; Marrone and Treanor (1963) utilised detailed modelling of vibrational energy levels to describe chemical dissociation reactions. This was then utilised in conjunction with multi-temperature modelling to produce what is commonly referred to as the Treanor model (as can be seen in Degrez et al. (2009)). Treanor's model is limited in the assumption that chemical reactions do not inherently change the shape of the vibrational energy distribution.

In 1995, Knab et al. (1995). extended the Treanor model to cover reaction types other than dissociations. Knab's model maintains the assumption that chemical reactions do not affect the vibrational energy distribution, in common with the Treanor model. Additionally, both models feature tunable parameters, which must be calibrated to the flow under consideration.

At around the same time, Macheret et al. (1994) were adding greater depth to the modelling of dissociation reactions. They introduce a split in dissociation regime based upon the molecule's vibrational energy level; high energy dissociation rates are governed by the vibrational temperature, whilst low energy dissociations are controlled by translational temperature.

The Treanor and Knab models have been used to simulate re-entry flows in various configurations as in the work of Allouche et al. (2014) and Gerlinger et al. (1997). The Macheret model has similarly been used to simulate re-entry flows, including by Wan et al. (2004) who investigated the possibility of generating energy using MHD methods during re-entry.

In spite of these advancements, many thermochemical models used in re-entry investigations bear a close resemblance to Park's original model. Indeed, Park's model is still used extensively today as in investigations of the OREX, FIRE-II and Hayabusa capsules, as evinced by Gupta et al. (1997), Scalabrin and Boyd (2007) and Suzuki et al.

(2014). This is likely due to both its simplicity and computational efficiency. Alternative methods based upon more fundamental physics quickly run into limitations of computational resources.

New Park-type models are continually being developed with variations being made to each. An example of such a variation is the treatment of unique vibrational temperatures for different molecular species, together with vibrational-vibrational relaxation coupling. This approach was initially developed using a semi-classical formulation by Rapp and Englander-Golden (1964). This treatment was of interest due to the strong link between vibrational temperatures and dissociation rates and has been utilised in hypersonic flow research such as that of Lee et al. (2020).

Recent development of a novel thermochemical model was presented by Macdonald (2019) at the University of Illinois. They have implemented methods to combine energy modes into groupings based upon chemical species, and compute a reduced order approximation to state-to-state chemistry. This approach constitutes a major departure from Park-type models, replacing empirical data based models with *ab initio* modelling. However, outside this approach, most models remain close to Park's original model. The main departure most novel models make is the exact nature of the temperature split used.

Three Temperature Models

All aforementioned models still utilised a two temperature split of the same kind as Park's. However this two temperature split still resulted in discrepancies between numerical and observed data, particularly at high pressures as Park himself noted Park (2013) among others such as Chae et al. (2020).

Hence, there were concurrent efforts to investigate alternative temperature splits. Holman and Boyd (2009) proposed a model featuring a split between a translational mode, a rotational mode and a vibrational-electronic-electron mode. This work built upon an earlier version utilising a two temperature split between translational and rotational modes. Various improvements over two temperature models are noted for particulate methods such as Direct Simulation Monte-Carlo (DSMC), including those noted by Deschenes et al. (2011), Schwartzentruber and Boyd (2015) and Deschenes and Boyd (2011). The behaviour of rotational temperatures has received impetus from the work of Panesi et al. (2013), who demonstrated that relaxations between the translational and rotational modes are comparable to those of translational-vibrational relaxations at temperatures of the order of 10^5 K. Whilst such temperatures are not typically associated with re-entry flows, the relationship between these relaxation times warrants further study in order to ascertain the temperature at which translational-rotational relaxation times become significant.

Another three temperature split was proposed by Kim et al. (2012), involving splitting the temperatures between translational-rotational, vibrational and electronic-electron modes. This use of a separate temperature for electrons allows for precise investigation of radio blackout, which is dependent upon electron density and temperature values. This three temperature model has been found by Clarey and Greendyke (2018) to yield improved fidelity for a range of hypersonic re-entry flow conditions. In another example, Clarey (2018) utilised this temperature split together with a translational-rotational, vibrational-electronic & electron split to investigate non-equilibrium effects on slender bodies. The three temperature models were again found to produce higher fidelity results than the two temperature equivalent.

Four Temperature Models

A recent class of models to be considered are those which treat all or nearly all energy modes separately. The most common four temperature model treats all modes individually. This model has been utilised in re-entry simulations by Ozawa et al. (2011) together with quantum kinetic models for excitation processes; this combination leads to a substantial change in predicted ionisation rates.

The choice of exact temperature split is influenced by the computational efficiency required to complete simulations in a timely manner. Another factor which greatly affects the convergence times of non-equilibrium simulations is how to deal with the chemistry stiffness problem.

Chemical Non-Equilibrium Modelling Constraints

Whilst the implementation of thermal non-equilibrium modelling required minimal constraints upon the overall CFD methods used, the same was not found to be true of chemical non-equilibrium. The principal difficulty with chemical non-equilibrium was found to be the timescales associated with chemical and CFD processes, which differ wildly. This means that the resulting equation set describing the system is extremely stiff. This stiffness manifests as the chemical evolution requiring much smaller time steps than the general CFD procedure when integrating using explicit methods. A method of estimating the time steps required for accurate resolution of chemical kinetics was performed by Chiang and Hoffmann (1989).

Solutions to chemistry stiffness can be grouped into three categories; fully implicit, semi-implicit hybrid and under-relaxation. Under-relaxation methods are one of the simplest methods to implement. Palmer presented an early under-relaxation approach

in Palmer (1988). Such approaches involve treating the evolution of species mass fractions, rather than their individual densities. The evolution of such fractions is determined at the larger CFD time step, and a damping performed in order to mitigate extremes of flux associated with the chemical modelling. This approach, whilst straightforward, comes with a major drawbacks. Namely control of the damping factor, which must be determined in advance and is simulation dependent; a value of 0.0004 is presented in Palmer (1988) whilst a value of 0.01 is used in Palmer (1990). No extrapolation is presented for the determination of this value, hence limiting the generalisability of the method. It is likely for this reason that such methods have not seen widespread adoption, with a comparison to arcjet flow by Babikian et al. (1995) being one of few examples.

Fully implicit methods possess the greatest consistency, simply treating both the CFD and chemistry integrations implicitly. Explicit methods calculate new system states from previously known states, whilst implicit methods calculate new states from new and known states. A typical stencil for explicit and implicit methods is shown in Figure 1.1, with the new state (red) being calculated according to simple implicit and explicit methods.

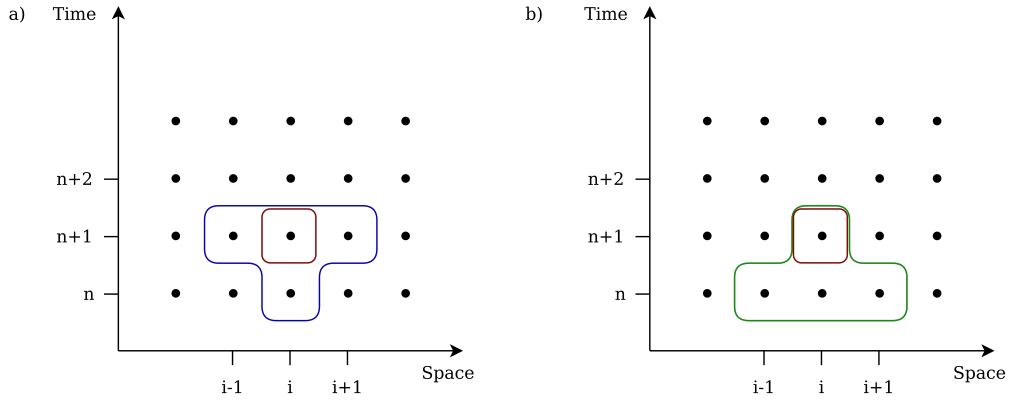

FIGURE 1.1: Stencil demonstrating differences in integration techniques between implicit (a) and explicit (b) methods.

Fully implicit methods also benefit from the advantages afforded to implicit methods, mainly the ability to integrate at CFL numbers exceeding 1. Such methods are also referred to as fully coupled or strongly coupled methods. The first example of the use of implicit methods for solving these stiff equation sets is that of Curtiss and Hirschfelder (1952).

Semi implicit hybrid methods utilise both explicit methods for the CFD integrations and implicit methods for the chemistry integrations. Such methods are also referred to as loosely/weakly coupled methods. These methods also begin with the work presented by authors including Smoot et al. (1976) and Otey and Dwyer (1979), which was later extended into multiple dimensions by Bussing and Murman (1988). As was

pointed out by Langer (2012), the point implicit method, whilst technically fully implicit, can be recognised as a preconditioned semi-implicit method; hence some nomenclature should be considered mutable.

State of the Art Techniques

A novel solution to this stiffness problem was presented very recently by Zanardi et al. (2022). involving the use of Machine Learning (ML) algorithms to learn the solutions of the stiff set of kinetics equations. This method has been reported to achieve speedups of up to two orders of magnitude, but will require further work in order to expand and demonstrate its applicability.

Another novel approach to non-equilibrium chemistry in CFD which has been pursued in recent years is the state-to-state vibrational kinetics model, which has been extensively explored by Pepe et al. (2013). This method deviates significantly from more established multi-temperature models by calculating chemical reaction rates from vibrational energy distributions, rather than the more typical use of empirical data. This approach brings with it several advantages. Firstly, the use of actual vibrational energy distributions removes the requirement of assuming Boltzmann like distributions; thus allowing for more accurate modelling when real world applications stray from Boltzmann like energy distributions. Secondly, less reliance upon existing empirical data allows for the simulation of gas mixtures for which little data may currently exist. These advantages are considerable, and have caused significant interest in this approach, as evidenced by the work of Tuttafesta et al. (2013), Kewley (1975) and de Gavelle de Roany et al. (1993) to name but a few. The state-to-state method comes with one large drawback however, the high computational workload it imparts in exchange for its accuracy. Because of this, the state-to-state method was not employed to obtain the results presented herein, but it did influence the work in ways which will be described later.

Once non-equilibrium models are combined with numerical methods capable of overcoming chemical stiffness constraints, non-equilibrium flows can be reliably simulated, as has been demonstrated by several CFD suites.

1.3.2 Non-Equilibrium Software Tools

There exist many non-equilibrium flow simulation tools are often developed by academic groups and local space agencies. Some of these pieces of software are proprietary, some open-source. This work will be focused on the widely available open-source software, however a brief overview of proprietary CFD tools will be presented before the open-source suites are covered.

There are several major hypersonic capable CFD suites developed by NASA. NASA Ames' OVERFLOW, a fully implicit Navier-Stokes solver to which chemical modelling capabilities were added by Olsen et al. (2004). OVERFLOW has recently seen use by Halstrom et al. (2022) in analysing proposed propulsion systems for Mars entry vehicles. NASA Ames also developed the Data-Parallel Line Relaxation (DPLR) suite, a 2D axisymmetric and 3D toolkit which has been recently utilised to perform simulations of the Hayabusa2 and Stardust capsules during re-entry, including by Scott and Inman (2022) and Trumble et al. (2010a). NASA Langley meanwhile relies upon the Langley Aerothermodynamic Upwind Relaxation Algorithm (LAURA). The capabilities of these suites (together with US3D developed in conjunction with the university of Minnesota) are well documented by Hash et al. (2007b) using simulations of the Orion capsule. The US3D suite has also been regularly employed alongside the other NASA suites in order to provide comparisons between structured and unstructured meshes, as in the work of Candler et al. (2015a). These mesh differences cause differences not only in the simulation's numerical methods, but also in the methods which must be employed to generate a simulation mesh in the first place. Unstructured meshes, such as those employed by US3D take significantly more time to generate, which greatly complicates efforts to use numerical methods to optimise spacecraft design. These meshing differences will be explored in detail as they pertain to the work undertaken in the course of this thesis in Chapter 3.

A use of machine learning methods applied to hypersonic relevant flows is the recent work undertaken by NASA Langley as presented by Demir et al. (2022) using their VULCAN-CFD code. Outside of NASA, another prominent north American suite is the (Le) Michigan Aerothermodynamic Navier-Stokes Solver (LeMANS) developed at the University of Michigan. This suite is regularly employed in non-equilibrium flow simulation, a recent example of this being the work of Kim and Jo (2021). A relative newcomer to these suite is one developed by McGill University in collaboration with ANSYS, the High-Altitude Low-Orbit 3D (HALO3D) Casseau et al. (2022). HALO3D is capable of simulating re-entry across the rarefied-continuum boundary and simulates thermochemical non-equilibrium in both regimes.

Within Europe, there are also several non-equilibrium flow suites including the unstructured CFD suite TAU developed by the German Aerospace Center (DLR). TAU has been used in the simulation of re-entry vehicles in the transitional regime between rarefied and continuum flow, as in the work of Hannemann et al. (2018). A suite focusing on the magnetohydrodynamics of non-equilibrium flows is SAMSA from the University of Stuttgart. SAMSA is capable of simulating the magnetohydrodynamics required to assess radio blackout mitigation schemes as evidenced in Müller et al. (2019). Additionally, the MISTRAL suite combines both CFD and DSMC methods within a single suite, and has been used for the simulation of space debris by Annaloro et al. (2020) and hypersonic weapons by Scott et al. (2004).

In addition to the aforementioned proprietary suites, there exist a number of open-source suites. These suites benefit from interoperability, being readily usable by multiple different groups; this facilitates quicker testing and reproduction of acquired results. Because of this, open-source suites constitute the main focus of this thesis. One such suite is another European suite, the Von Karman Institute's COOLFluiD, which is capable of performing simulations to assess the feasibility of radio blackout mitigation methods, as presented by Giangaspero et al. (2021) with simulations of the Schiaparelli capsule.

Recent notable additions to these CFD suites include the expansion of the open-source toolkit OpenFOAM into non-equilibrium flows. This expansion was performed by Casseau et al. (2015) at the University of Strathclyde and has allowed OpenFOAM to be used to simulated 5 species air chemistry with a two temperature model; this capability has been utilised by Casseau et al. (2016b). Also developed at the University of Strathclyde is SU2-NEMO; developed in collaboration with Stanford University, the University of Arizona and the Von Karman Institute. SU2-NEMO is a non-equilibrium expansion to Stanford's SU2 multiphysics CFD suite, and is capable of simulating multiple atmospheres in various configurations. This has included ground based facilities, as demonstrated by Needels et al. (2022) and various aerodynamic bodies as presented by Maier et al. (2021).

Another recent addition, Eilmer3, has been developed at the University of Queensland. Eilmer3 has been used to perform two-temperature simulations of several wind tunnel studies as well as the Hayabusa capsule as presented by Fahy et al. (2021). Lastly, WARPCFD is an open source code from the University of Arizona which also has the capability to simulate combusting gas mixtures, as has been demonstrated by Rodríguez Fuentes and Parent (2023) and Fuentes and Parent (2022).

A key feature of all of these open-source suites is that they all utilise unstructured meshes, which provide benefits when conducting simulations for the indirect study of re-entry flows. For undertaking direct studies of re-entry flows and their effects upon space capsules, rapid mesh generation is hugely desirable. This can be achieved through the use of block-structured meshes, which combine some of the flexibility of unstructured meshes with the rapid generation of structured meshes. All of the object-oriented suites also utilise a pure MPI parallelisation strategy appropriate for distributed memory systems However additional efficiency can be obtained through the use of hybrid systems featuring a fusion of MPI and OpenMP parallelisation.

These potential improvements have provided the impetus for the work presented herein, to create a software suite prioritising the simulation of flows which can be used to directly optimise space capsule design. This software utilises block-structured Cartesian grids, for faster grid generation when capsule design modifications are to be tested. Block-structured Cartesian grids also allow for the ready implementation of automatic

mesh adaptation techniques, allowing for more efficient use of computational resources. It also requires a readily modifiable and extensible framework, to facilitate the switching of mathematical models as required by the capsule modifications. Lastly, such software needs high stability, to maintain consistency when models and geometries are switched; and high efficiency facilitated by hybrid parallelisation to be able to conduct high precision simulations in a reasonable timeframe. These requirements led to the overall research objectives of the presented work.

1.4 Research Objectives

The aim of this research has been to answer the question; is it possible to produce a numerical toolkit better tailored to capsule optimisation simulations. Such a toolkit would be able to assist with the design and construction of space capsules, in order to allow them to better withstand the rigours of atmospheric entry. What would be the advantages and limitations of such a toolkit and which simulation methods would be optimal.

Herein, work has been undertaken to answer these questions by producing such a toolkit; which can support the design and optimisation of such capsules by allowing for modifications to be made to simulated craft geometry with minimal additional simulation time needed. To this end, emphasis has been placed upon ensuring several key software qualities are prioritised. In order to be able to rapidly switch between craft shapes and configurations, numerical methods must allow for the rapid generation of new simulation meshes. As differing craft configurations may require differing levels of precision in certain models, the simulation framework must allow for the seamless switching of mathematical models. In order to ensure that such switching does not adversely affect simulation outcomes, high stability is required. Lastly, in order to ensure that non-equilibrium effects can be modelled at high precision, a high level of efficiency is required, achieved by hybridising MPI and OpenMP parallelisation strategies.

This work has produced the OP2A toolkit. Emphasis has been placed upon creating a toolkit which has the ability to perform several feats. Firstly, to mix and match components through a high flexible and extensible modular framework as described in detail in Chapter 4. This allows for thermochemical models to be utilised interchangeably with little time taken. Secondly, to facilitate rapid grid generation as required by changes to space capsule geometry, described further in Chapter 3. And lastly, perform the required computations with the stability and efficiency necessary. C++ was the chosen language due to its high efficiency and object oriented nature, which enabled the creation of the aforementioned modular framework.

This work aims further to determine the optimal methods to achieve a CFD toolkit for supporting the design of space capsules; hewing to the priorities described herein. This

work will also demonstrate the capabilities and limitations of the OP2A toolkit that was developed in pursuit of these aims.

1.5 Outline of this Thesis

The remainder of this thesis is laid out as shown in Figure 1.2.

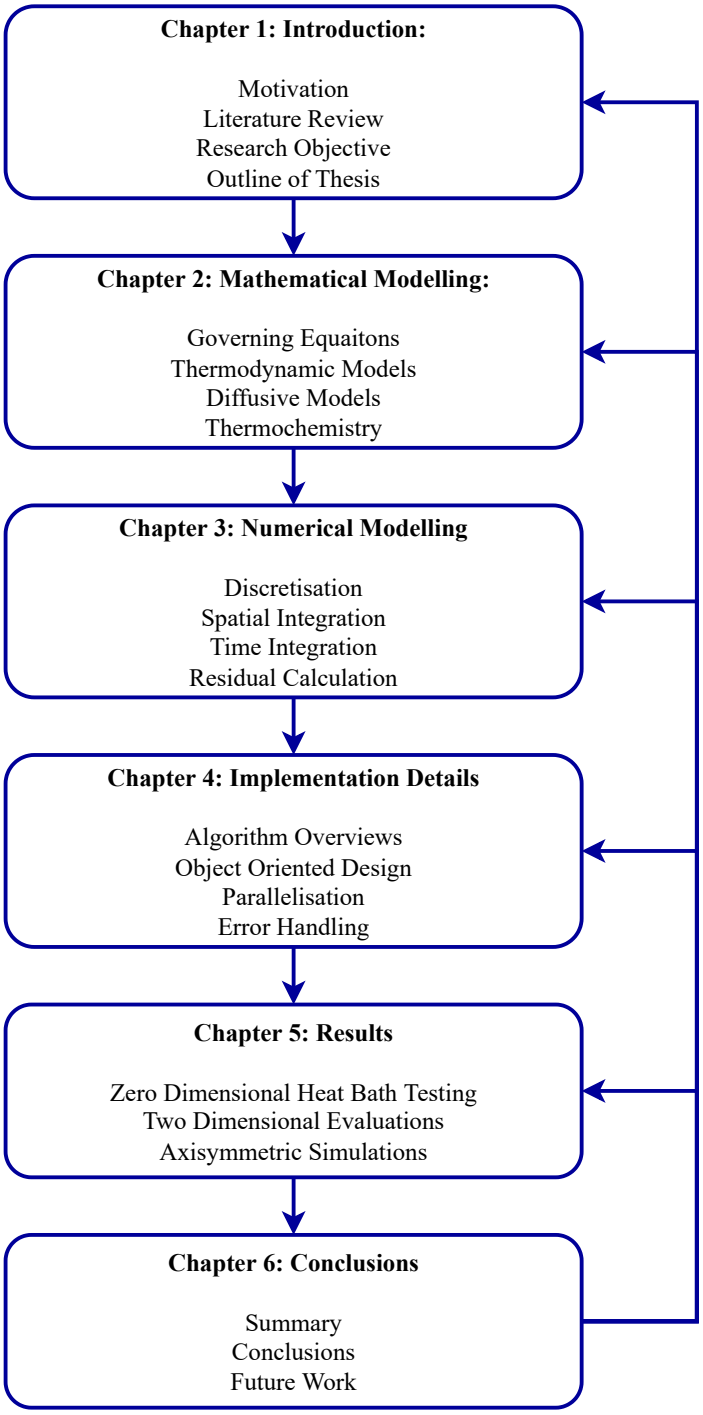

FIGURE 1.2: Overview of the structure of this thesis.

Chapter 2 details the mathematical models which were chosen to be implemented in the created multiphysics CFD toolkit OP2A. Chapter 3 follows this with details of the numerical methods with which this theory is implemented, including grid generation and processing considerations. Emphasis is placed upon the ways in which grid choices benefit a software toolkit aimed at capsule optimisation simulations. An overview of how OP2A operates computationally is presented in Chapter 4, including details of parallelisation, object oriented structure and other details including error handling routines. Details are presented as to how these computational features contribute to the flexibility, extensibility and efficiency required of OP2A. The results of initial simulations are presented in Chapter 5, beginning with a zero dimensional analysis designed to assess the performance of the thermochemical models in modelling non-equilibria. Following this several common CFD test cases and are used to determine the capabilities and limitations of OP2A, including simulations of capsules undergoing re-entry. The results of all of these investigations are discussed in detail within this chapter. The final chapter, Chapter 6 summarises OP2A's current status, and the results of investigations which it has been used to undertake. This is followed by the overall conclusions drawn from this work regarding OP2A's performance and the work's initial research objectives. Lastly, suggestions for future work with OP2A are presented and discussed.

1.5.1 Publications & Presentations

Papers Published

OP2A: A Multiphysics Fluid Simulation Framework; Proceedings of Scitech 2021; Published by AIAA; 2021.

Conference Presentations Performed

OP2A: A Multiphysics Fluid Simulation Framework; UK Fluids Conference; Southampton, UK; 2021.

OP2A: A New Hypersonic CFD Suite; Scitech 2021; Nashville, Tennessee; 2021.

2

Mathematical Modelling

"All models are wrong, but some models are useful."

– George P. E. Box

Within this chapter, the mathematical underpinnings of OP2A are presented. This begins from a statement of the conserved CFD quantities, and proceeds by describing the steps required to advance these quantities in time and space. This chapter includes details of the thermodynamic formulae necessary for determinations of temperatures and pressure as well as specific heats and internal energies. This is followed by a description of the methods implemented to determine various viscous quantities including diffusion rates and viscous tensors. This chapter concludes with theoretical models applicable to flows in chemical and thermal non-equilibrium including details of the relaxation models implemented. Wherever relevant, the reasoning behind chosen models is presented, as well as an idea of their limitations.

2.1 Governing Equations

For a fundamental description of a fluid there exist three core conserved variables; mass, momentum and energy. The core of OP2A's CFD simulation is the evolution of these conserved quantities both temporal and spatial. This evolution is described by the Navier-Stokes equations, the most fundamental of the theory incorporated into OP2A.

Considering a fluid consisting of several chemically reacting species s, the conservation of mass for each species is described by Equation 2.1.

$$\frac{\partial \rho_s}{\partial t} + \nabla.(\rho_s \vec{u}) = -\nabla.(\rho_s \vec{v}_s) + w_s, \tag{2.1}$$

where ρ_s represents the density of each chemical species, $\vec{u}$ represents an advection velocity, $\vec{v}_s$ are species' diffusive velocities and w_s is the source term for each species. This source term can theoretically include both atmospheric and ablative components. The terms in Equation 2.1 describe, from left to right; the total temporal change in species density, advection by the overall fluid velocity, diffusion by a unique species diffusive velocity, and all species source and sinks, respectively. Equation 2.1 can be summed over all species, in which case it reduces to the conservation equation for total density ρ, the traditional continuity equation, seen in Equation 2.2.

$$\frac{\partial \rho}{\partial t} + \nabla.(\rho \vec{u}) = -\nabla.(\rho \vec{v}) \tag{2.2}$$

The conservation of linear momentum $\rho \vec{u}$ is similarly described by Equation 2.3.

$$\frac{\partial (\rho \vec{u})}{\partial t} + \nabla.(\rho \vec{u} \times \vec{u} + pI) = \nabla.\vec{\tau} \tag{2.3}$$

Within Equation 2.3; p represents pressure, I the identity matrix and $\vec{\tau}$ the viscous stress tensor. The terms within 2.3 represent; the overall change in momentum, advective and pressure diffusive changes and change due to shear forces, from left to right respectively. As mentioned in Chapter 1, fluids in thermal non-equilibrium, require multiple equations to describe the conservation of energy within the fluid. The nature and combination of these equations differ depending upon the nature of the non-equilibrium; which energy modes are in equilibrium with which others. These energy equations share a commonality in the need for a conservation equation for total energy per unit volume E:

$$\frac{\partial E}{\partial t} + \nabla.\left((E + p)\,\vec{u}\right) = \nabla.\left(\vec{\tau}\vec{u}\right) - \nabla.\left(q\right) - \nabla.\sum_s \left(\rho_s h_s \vec{v}_s.\right) \tag{2.4}$$

Within Equation 2.4, q describes the total heat flux and h_s the enthlapy of formation of a given species, s. Total heat flux q is computed by summing any individual components. The terms within this equation describe the change in total energy, change due to advection, change due to shear forces, convective heat flux and formation enthlapy changes, from left to right respectively. The formational enthlapy changes are required to compute the changes to the fluid's energy from endothermic and exothermic chemical reactions as well as any radiative terms. The state of energy within the fluid is not yet fully described for an fluid in thermal non-equilibrium. A description of the states of various sub-energies is required.

Within the work currently presented, one initial multi-temperature model has been chosen to represent the thermal non-equilibrium involved in hypersonic plasma flows: the Park two temperature model as described in Chapter 1 and which can be found

in Park (1990). This model assumes that the translational and rotational modes are in equilibrium; and that the vibrational, electronic and electron modes are in equilibrium. Hence resulting in a two temperature system. The utility of this model comes from the fact that the relaxation times between the translational and rotational, and between the vibrational and electronic/electron are often far smaller than those for other relaxations. In addition, this model forms a useful starting point from which other models can be built, as will be noted in Chapter 4. As previously mentioned, the Park two temperature model is also extensively used, leading to a good quantity of comparison data for verification purposes. Henceforth, the two Park model modes will be referred to as translational and vibrational for brevity. With this thermal model in place, the total energy of the system E is defined as,

$$E = \sum_{s \neq e} \rho_s c_{v,tr,s} T_{tr} + \frac{1}{2}\rho \vec{u}^2 + \sum_{s \neq e} \rho_s h_s + E_{vee} \tag{2.5}$$

where h_s is the enthlapy of formation of a given species and $c_{v,tr,s}$ is the specific heat at constant volume for the translational mode. This choice of non-equilibrium model requires the addition of one more conservation equation, for the conservation of vibrational energy E_{vee}. This conservation equation differs slightly in form from its total energy equivalent, and is given by Equation 2.6.

$$\frac{\partial E_{vee}}{\partial t} + \nabla.\left(E_{vee}\vec{u}\right) = -\nabla.\vec{q}_{vee} - \nabla.\sum_{s}\left(\rho_s e_{vee,s}\vec{v}_s\right) + w_v \tag{2.6}$$

In 2.6, q_v is the heat flux for the vibrational energy mode, $e_{v,s}$ is the internal vibrational energy per unit mass for species s, and s_v is the vibrational energy source terms. The terms of this equation describe the total vibrational energy change, advective changes, convective changes, diffusive changes and other sources, from left to right respectively. This source term describes any change in vibration energy caused by; electron pressure gradients, chemical reactions, relaxation between translational and vibrational modes, electron-heavy collisions and electron impact ionisations. Such a source term may also include contributions due to radiation, however these are not considered in the work presented. Evaluation of this source term is a key priority of the simulation of thermal non-equilibrium flows, and will be detailed in a following section. Before proceeding with additional details, it is possible to reformulate the existing equation set in vector form as

$$\frac{\partial Q}{\partial t} + \left(F_{inv} - F_{vis}\right) + \left(G_{inv} - G_{vis}\right) + \left(H_{inv} - H_{vis}\right) = S. \tag{2.7}$$

The components of Equation 2.7 include the vector of conserved quantities, Q:

$$Q = \begin{pmatrix} \rho_1 \\ \vdots \\ \rho_{Ns} \\ \rho u \\ \rho v \\ \rho w \\ E \\ E_{vee} \end{pmatrix}. \tag{2.8}$$

Whilst the source term S is described by

$$S = \begin{pmatrix} w_1 \\ \vdots \\ w_{Ns} \\ 0 \\ 0 \\ 0 \\ 0 \\ w_v \end{pmatrix}. \tag{2.9}$$

Fluxes, both inviscid and viscous are described by Equations 2.10 and 2.11 respectively:

$$F_{inv} = \begin{pmatrix} \rho_1 u \\ \vdots \\ \rho_{Ns} u \\ \rho u^2 + p \\ \rho v u \\ \rho w u \\ (E+p)u \\ E_{vee} u \end{pmatrix}, G_{inv} = \begin{pmatrix} \rho_1 v \\ \vdots \\ \rho_{Ns} v \\ \rho u v \\ \rho v^2 + p \\ \rho w v \\ (E+p)v \\ E_{vee} v \end{pmatrix}, H_{inv} = \begin{pmatrix} \rho_1 w \\ \vdots \\ \rho_{Ns} w \\ \rho u w \\ \rho v w \\ \rho w^2 + p \\ (E+p)w \\ E_{vee} w \end{pmatrix}. \tag{2.10}$$

$$
F_{vis} = \begin{pmatrix} J_{x,1} \\ \vdots \\ J_{x,Ns} \\ \tau_{xx} \\ \tau_{xy} \\ \tau_{xz} \\ -(q_{x,t} + q_{x,v}) + u\tau_{xx} + v\tau_{xy} + w\tau_{xz} - \sum_s (J_{x,s} h_s) \\ -q_{x,v} - \sum_s (J_{x,s} e_{v,s}) \end{pmatrix},
$$

$$
G_{vis} = \begin{pmatrix} J_{y,1} \\ \vdots \\ J_{y,Ns} \\ \tau_{yx} \\ \tau_{yy} \\ \tau_{yz} \\ -(q_{y,t} + q_{y,v} + u\tau_{yx} + v\tau_{yy} + w\tau_{yz} - \sum_s (J_{y,s} h_s) \\ -q_{y,v} - \sum_s (J_{y,s} e_{v,s}) \end{pmatrix}, \tag{2.11}
$$

$$
H_{vis} = \begin{pmatrix} J_{z,1} \\ \vdots \\ J_{z,Ns} \\ \tau_{zx} \\ \tau_{zy} \\ \tau_{zz} \\ -(q_{z,t} + q_{z,v}) + u\tau_{zx} + v\tau_{zy} + w\tau_{zz} - \sum_s (J_{z,s} h_s) \\ -q_{z,v} - \sum_s (J_{z,s} e_{v,s}) \end{pmatrix}.
$$

These equations form a closed set when combined with equations of state, the first of which is formed by combining the ideal gas law with Dalton's law of partial pressures:

$$
p = \sum_{s \neq e} \frac{\rho_s R_u T_{tr}}{M_s} + \frac{\rho_e R_u T_{vee}}{M_e}, \tag{2.12}
$$

where R_u is the universal gas constant, M_s molecular weight of species s, and T_{tr} and T_{vee} the translational and vibrational temperatures respectively.

These extended Navier-Stokes equations (Equations 2.1 - 2.6) together with an equation of state (2.12) begin to describe the conservation of mass, momentum and energy for a single fluid.

However, in order to accurately simulate charged species, multiple velocities may be

required as charged species may be accelerated by electromagnetic fields, whilst neutrals remain unaffected. In order to achieve this, multiple fluids can be simulated, with each being described by its own set of Navier-Stokes equations.

In order to solve this set of equations, it is necessary to compute the various terms presented above as well as include further equations of state to close the system. These caloric equations of state will now be presented, as well as methods of calculating various terms necessary for the solution of the extended Navier-Stokes system.

2.2 Thermodynamic Quantities

The evaluation of many of the terms within the Navier-Stokes equation set requires the knowledge of several thermodynamic properties of the fluid. Specifically, these are the internal energies of various modes, and their rates of change together with various specific heats at constant volume.

To begin with, the relationship between the specific heats of different energy modes is defined;

$$c_{v,s} = \begin{cases} c_{v,t,s} + c_{v,r,s} + c_{v,v,s} + c_{v,el,s} & \text{for molecules,} \\ c_{v,t,s} + c_{v,el,s} & \text{for atoms,} \\ c_{v,e,s} = c_{v,t,e} & \text{for electrons,} \end{cases} \tag{2.13}$$

where the electron specific heat is simply the translational specific heat applied to free electrons.

Evaluating total specific heat for $c_{v,s}$ clearly requires knowledge of each modal specific heat. For example Equation 2.5 requires the translational-rotational specific heat $c_{v,tr,s} = c_{v,t,s} + c_{v,r,s}$. Each particle possesses 3 degrees of translational freedom, each of which contributes $\frac{R_s}{2}$ to the specific heat, where R_s is the specific gas constant. Hence the translational specific heat is described for all species by

$$c_{v,t,s} = \frac{3R_u}{2M_s} = \frac{3}{2}R_s, \tag{2.14}$$

where $R_s = \frac{R_u}{M_s}$ is the specific gas constant for species s. The rotational mode possesses an additional two degrees of freedom, hence rotational specific heat is described by

$$c_{v,r,s} = \begin{cases} R_s & \text{for molecules,} \\ 0 & \text{for atoms and electrons.} \end{cases} \tag{2.15}$$

Note that the rotational degrees of freedom are determined by the number of atoms within the molecule and their orientation. The above treatment assumes two degrees

of freedom, each providing $\frac{R_s}{M_s}$. Hence the treatment provided in Equation 2.15 is only valid for diatomic molecules and linear polyatomic molecules such as CO_2.

Classical models have been used for the translational and rotational specific heats as these modes are fully excited at low temperatures. However this is not true of the vibrational, and electronic modes. The vibrational specific heat is determined by assuming a simple harmonic oscillator model for any polyatomic molecule. This model has been found by Keck and Carrier (1965) to remain accurate for low energy modes whilst higher energy modes are inaccurate, but carry little enough energy as to cause negligible overall inaccuracy in $c_{v,v}$ as stated by Lee (1984).

$$c_{v,v,s} = \begin{cases} \dfrac{R_u \left(\frac{\theta_{v,s}}{T_{vee}}\right)^2 e^{\frac{\theta_{v,s}}{T_{vee}}}}{M_s \left(e^{\frac{\theta_{v,s}}{T_{vee}}} - 1\right)^2} & \text{for molecules,} \\ 0 & \text{for atoms and electrons.} \end{cases} \tag{2.16}$$

$$e_{v,s} = \begin{cases} \dfrac{R_u \theta_{v,s}}{M_s \left(e^{\frac{\theta_{v,s}}{T_{vee}}} - 1\right)} & \text{for molecules,} \\ 0 & \text{for atoms and electrons.} \end{cases} \tag{2.17}$$

This assumption remains valid only for the lower vibrational energy states, hence, the validity of this assumption is limited to cases where higher energy levels contain a negligible fraction of the total vibrational energy as noted by Lee (1984). The electronic specific heat is defined as

$$c_{v,el,s} = \begin{cases} \dfrac{\partial e_{el,s}}{\partial T_{el}} & \text{for molecules and atoms,} \\ 0 & \text{for electrons,} \end{cases} \tag{2.18}$$

where $e_{el,s}$ is the electronic energy per unit mass for species s defined as

$$e_{el,s} = \begin{cases} \dfrac{R_u \sum_{i=1}^{\infty} g_{i,s} \theta_{el,i,s} e^{-\frac{\theta_{el,i,s}}{T_{el}}}}{M_s \sum_{i=0}^{\infty} g_{i,s} e^{-\frac{\theta_{el,i,s}}{T_{el}}}} & \text{for molecules and atoms,} \\ 0 & \text{for electrons,} \end{cases} \tag{2.19}$$

where $g_{i,s}$ is the degeneracy of energy level i and $\theta_{el,i,s}$ is the characteristic electronic temperature of energy level i. The differential required for calculation of the electronic

specific heat is calculated using the quotient rule to be

$$\frac{\partial e_{el,s}}{\partial T_{el}} = \frac{R_u}{M_s}\left(\frac{\sum_{i=1}^{\infty} g_{i,s}\left(\frac{\theta_{el,i,s}}{T_{el}}\right)^2 e^{-\frac{\theta_{el,i,s}}{T_{el}}}}{\sum_{i=0}^{\infty} g_{i,s} e^{-\frac{\theta_{el,i,s}}{T_{el}}}} - \frac{\sum_{i=1}^{\infty}\left(g_{i,s}\theta_{el,i,s} e^{-\frac{\theta_{el,i,s}}{T_{el}}}\right)\sum_{i=0}^{\infty}\left(g_{i,s}\left(-\frac{\theta_{el,i,s}}{T_{el}^2}\right)e^{-\frac{\theta_{el,i,s}}{T_{el}}}\right)}{\left(\sum_{i=0}^{\infty} g_{i,s} e^{-\frac{\theta_{el,i,s}}{T_{el}}}\right)^2}\right). \quad (2.20)$$

Modelling of electronic specific heat shares the limitations of the vibrational specific heat, with the requirement that higher energy levels contain a low proportion of total electronic energy in line with the work of Lee (1984).

Lastly, the electron specific heat is physically identical to translational specific heat, hence it is intuitively given by

$$c_{v,e,s} = \begin{cases} 0 & \text{for molecules and atoms,} \\ c_{v,t,e} & \text{for electrons.} \end{cases} \quad (2.21)$$

With these quantities described, the total energy of the vibrational mode can be described as

$$E_{vee} = E_v + E_{el} + E_e. \quad (2.22)$$

With the viscous and diffusive terms in the Navier-Stokes set can now be expanded, beginning with the terms associated with viscous forces.

2.3 Viscous Terms

The key viscous quantities which require evaluation are the viscous stress tensor $\vec{\tau}$, the heat flux q and the species diffusion rates J_s. In keeping with the choice of thermal non-equilibrium model, the heat flux can be split into separate components $q = q_t + q_v$ where q_t and q_v are the translational-rotational and vibrational-electronic-electron heat fluxes respectively. Hence, two heat fluxes will be required to solve the equation set.

2.3.1 Viscous Stress Tensor

The viscous stress tensor is a tensor with dimensionality $N_d \times N_d$, where N_d is the number of spatial dimensions under consideration.

$$\vec{\tau} = \begin{pmatrix} \tau_{1,1} & \cdots & \tau_{1,N_d} \\ \vdots & \ddots & \vdots \\ \tau_{N_d,1} & \cdots & \tau_{N_d,N_d} \end{pmatrix} \tag{2.23}$$

Noting briefly that the viscous stress tensor is symmetrical, hence $\tau_{0,1} = \tau_{1,0}$, this implies that several of these sub-terms still need to be evaluated.

These terms are evaluated under the assumption of a Newtonian fluid using Stokes' hypothesis:

$$\tau_{i,j} = \mu \left(\frac{\partial u_i}{\partial x_j} + \frac{\partial u_j}{\partial x_i} \right) - \frac{2}{3} \mu \nabla \vec{u} \delta_{i,j}, \tag{2.24}$$

where μ is the fluid viscosity, and $\delta_{i,j}$ is the Kronecker delta:

$$\delta_{i,j} = \begin{cases} 1 & \text{if } i \text{ equals } j \\ 0 & \text{otherwise.} \end{cases} \tag{2.25}$$

Hence, evaluation of the viscous stress tensor requires evaluation of the fluid's dynamic viscosity μ which in turn requires a formulation of the fluid's transport properties. The two distinct formulations included in OP2A are described in section 2.4.

2.3.2 Heat Fluxes

The heat fluxes can be modelled by Fourier's law

$$\vec{q} = -\kappa \nabla T, \tag{2.26}$$

where κ is the thermal conductivity of the fluid. Each discrete energy mode present in the fluid requires its own separate heat flux $\vec{q}$ and thermal conductivity κ, leading to

$$\vec{q}_{tr} = -\kappa_{tr} \nabla T_{tr}, \qquad \vec{q}_{vee} = -\kappa_{vee} \nabla T_{vee} \tag{2.27}$$

Similarly to the specific heats, heat fluxes and thermal conductivities within equilibrated modes are cumulative, for example

$$\vec{q}_{tr} = \vec{q}_t + \vec{q}_r = -\left(\kappa_t + \kappa_r\right) \nabla T_{tr}. \tag{2.28}$$

Hence evaluation of heat fluxes requires evaluation of the thermal conductivities, which are presented in section 2.4.

2.3.3 Diffusion Rates

Diffusive components of the Navier-Stokes set each contain a mass diffusion term $\rho_s \vec{v}_s$. This mass diffusion can have a number of causes, including gradients in species concentration, pressure and temperature. For computational reasons, evaluation of all of these contributions is impractical, hence only the most significant will be evaluated, that being species concentration gradient. Such a simplification is not uncommon for hypersonic CFD simulations and can be seen in the work of Scalabrin (2007) among others.

$$\rho_s \vec{v}_s = -\rho D_s \nabla \left(\frac{\rho_s}{\rho} \right), \tag{2.29}$$

where D_s is the diffusion coefficient for species s. Equation 2.29 is combined with the modified version of Fick's law to ensure that the sum of all heavy species diffusions is equal to zero, as seen in Sutton and Gnoffo (1998). Electrons are excluded from this assumption due to their extremely low mass when compared with other species.

$$\sum_{s \neq e} \rho_{s \neq e} \vec{v}_{s \neq e} = -\rho D_{s \neq e} \nabla \left(\frac{\rho_{s \neq e}}{\rho} \right) = 0. \tag{2.30}$$

Use of this law ensures that conservation of mass is respected. Once again, evaluation of the species diffusion coefficient requires evaluation of various transport properties of the fluid. The diffusion of electrons is evaluated by assuming ambipolar diffusion throughout the fluid, hence

$$\rho_{s=e} \vec{v}_{s=e} = M_e \sum_{s \neq e} \frac{\rho_s \vec{v}_s Q_s}{M_s}, \tag{2.31}$$

where Q_s is the charge of species s.

2.4 Transport Properties

Evaluation of transport quantities can be performed in a number of ways, each a different level of approximation. The transport methods included in OP2A are the Gupta-Yos model (Gupta model hereafter), and a method which combines Wilke's semi-empirical mixing rule with Blottner curve fits and the Eucken relation henceforth referred to as the Wilke model.

The Wilke model is the more straightforward, and the easiest to generalise, however it is unsuited to temperatures above around 7000 K, as it underestimates viscosity significantly as noted by Palmer and Wright (2003). The Gupta method is valid for temperatures up to around 9000 K, after which it begins to overestimate mixture viscosity as Palmer and Wright (2003) notes. However, the Gupta model requires accurate knowledge of collision integrals for all chemical species. Hence, whilst the Gupta model is usually preferable, when collision integral data is unavailable, the simpler Wilke model must instead be used. All presented results should be assumed to employ the Gupta model unless otherwise stated.

2.4.1 Wilke Model

The Wilke model evaluates the fluid viscosity μ, thermal conductivities κ and diffusion coefficients D using the semi-empirical mixing rule of Wilke (1950) as its starting point. This model describes the viscosity μ and thermal conductivity κ as

$$\mu = \sum_s \frac{n_s \mu_s}{n \phi_s} \qquad \kappa = \sum_s \frac{n_s \kappa_s}{n \phi_s}, \tag{2.32}$$

where n_s is the number density of species s, n is the total number density of the fluid and the term ϕ_s contains components based upon species masses and viscosities relative to one another. ϕ_s is described by

$$\phi_s = \sum_t \frac{n_t}{n} \frac{\left(1 + \sqrt{\frac{\mu_s}{\mu_t}} \left(\frac{M_t}{M_s}\right)^{\frac{1}{4}}\right)^2}{\sqrt{8\left(1 + \frac{M_s}{M_t}\right)}}. \tag{2.33}$$

The species individual viscosities μ_s are evaluated using curve fits originally presented by Blottner et al. (1971).

$$\mu_s = 0.1 e^{(A_s \ln(T_{tr}) + B_s) + C_s}, \tag{2.34}$$

where A_s, B_s and C_s are unique constants for each species. Values of A_s, B_s and C_s are presented in appendix A for the species utilised in this work.

Species thermal conductivities κ_s are evaluated using the Eucken factor $\frac{\kappa}{\mu c_v}$, modified for polyatomic gases, first presented by Reid et al. (1987),

$$\kappa_{tr,s} = \frac{5}{2} \mu_s c_{v,t,s} + \mu_s c_{v,r,s}, \qquad \kappa_{vee,s} = \mu_s c_{v,v,s} + \mu_s c_{v,el,s} + \frac{5}{2} \mu_s c_{v,e,s}. \tag{2.35}$$

Finally, the species diffusion coefficients are streamlined by replacing each individual coefficient D_s with a single value for the fluid D. This is undertaken under the assumption of a constant Lewis number Le for the fluid, defined as

$$Le = \frac{\alpha_{thermal}}{D}, \tag{2.36}$$

where $\alpha_{thermal}$ is the thermal diffusivity of the fluid. α is given by

$$\alpha_{thermal} = \frac{\kappa_{tr}}{\rho c_{p,tr}}, \tag{2.37}$$

where $c_{p,tr}$ is the specific heat per unit mass at constant pressure for the translational and rotational modes for the entire fluid. Hence, through rearrangement

$$D = \frac{Le\kappa_{tr}}{\rho c_{p,tr}}. \tag{2.38}$$

For the remainder of this document, the Lewis number is at a constant value of 1.4 unless otherwise stated.

The above assumption is valid only in cases where the Lewis number is constant, which limits applicability to velocities below 1×10^4 m s^{-1}. This approach is not tenable for all hypersonic cases, hence OP2A utilises the Gupta model in place of the Wilke model for velocities above this limit.

2.4.2 Gupta Model

The Gupta method evaluates fluid viscosity, thermal conductivities and diffusion coefficients using the mixing rule presented by Gupta et al. (1990). This rule is an approximation of the first-order Chapman-Enskog formulae valid for neutral or weakly ionised gases, such as the weakly ionised plasma relevant to re-entry simulations. The exact ionisation limits are that the electron pressure should remain below the threshold described by Equation 2.39. This limit allows the Gupta formulation to be utilised for common aerospace applications as noted by Gupta et al. (1990).

$$p_e < 0.0975 \left(\frac{T_{vee}}{10^3} \right)^4 \tag{2.39}$$

This limitation arises from the use of Coulomb potentials in the calculation of the shielding properties of charged species.

The original formulation by Gupta et al. (1990) describes fluids in both thermal equilibrium and non-equilibrium; the extension from single to multi-temperature system is straightforward. The only consideration which needs to be made which temperature

controls a given equation; these fall into two categories, situations where the heavy particle temperature (T_{tr}) controls the collision, and situations where the electron temperature (T_{vee}) controls the collision. The following multi-temperature Gupta formulation utilises the electron temperature in the case of collisions involving electrons, and the heavy particle temperature otherwise. This is justified simply by the higher velocity of electrons relative to heavy particles.

Beginning from the formulation of fluid viscosity,

$$\mu = \sum_{s \neq e} \frac{M_s \gamma_s}{N_A \left(\sum_{t \neq e} \gamma_t \Delta_{st}^{(2)} + \gamma_e \Delta_{se}^{(2)} \right)} + \frac{M_e \gamma_e}{N_A \sum_t \gamma_t \Delta_{et}^{(2)}}, \tag{2.40}$$

where N_A is the Avogadro number Δ values are collisional terms to be evaluated and γ_s is the molar concentration of species s, defined as

$$\gamma_s = \frac{\rho_s}{\rho M_s}. \tag{2.41}$$

As previously noted, within Equation 2.40 the Δ collisional values must be evaluated with the appropriate temperature depending upon the presence of electrons within the collisional pair.

The description of the various thermal conductivities are provided by Gupta et al. (1990) beginning with translational

$$\kappa_t = \frac{15}{4} k_B \sum_{s \neq e} \frac{\gamma_s}{\sum_{t \neq e} \alpha_{st} \gamma_t \Delta_{st}^{(2)} + 3.54 \gamma_e \Delta_{se}^{(2)}}, \tag{2.42}$$

where k_B is the Boltzmann constant and α_{st} is a mass ratio described by

$$\alpha_{st} = 1 + \frac{\left(1 - \frac{M_s}{M_t}\right)\left(0.45 - 2.54 \frac{M_s}{M_t}\right)}{\left(1 + \frac{M_s}{M_t}\right)^2}. \tag{2.43}$$

The rotational thermal conductivity is given by

$$\kappa_r = k_B \sum_{s=mol} \frac{\gamma_s}{\sum_{t \neq e} \gamma_t \Delta_{st}^{(1)} + \gamma_e \Delta_{se}^{(1)}}, \tag{2.44}$$

the vibrational-electronic by

$$\kappa_{vel} = k_B \frac{c_{v,v}}{R_u} \sum_{s=atom,mol} \frac{\gamma_s}{\sum_{t \neq e} \gamma_t \Delta_{st}^{(1)} + \gamma_e \Delta_{se}^{(1)}}, \tag{2.45}$$

and the free electron thermal conductivity by

$$\kappa_e = \frac{15}{4} k_B \frac{\gamma_e}{\sum_s 1.45 \gamma_s \Delta_{es}^{(2)}}. \tag{2.46}$$

As mentioned in the description of the Wilke model, thermal conductivities are cumulative, hence

$$\kappa_{tr} = \kappa_t + \kappa_r, \qquad \kappa_{vee} = \kappa_v + \kappa_{el} + \kappa_e, \tag{2.47}$$

can be used to obtain thermal conductivities relevant to the two temperature model.

The two collisional terms $\Delta^{(1)}$ and $\Delta^{(2)}$ are dependent upon collision integrals as described by

$$\Delta_{st}^{(1)} = \frac{8}{3} \left(\frac{2 M_s M_t}{\pi R_u T \left(M_s + M_t \right)} \right)^{\frac{1}{2}} 10^{-20} \pi \Omega_{st}^{(1,1)}, \tag{2.48}$$

$$\Delta_{st}^{(2)} = \frac{16}{5} \left(\frac{2 M_s M_t}{\pi R_u T \left(M_s + M_t \right)} \right)^{\frac{1}{2}} 10^{-20} \pi \Omega_{st}^{(2,2)}, \tag{2.49}$$

where the temperature T is the electron temperature when the collision involves electrons, and translational in their absence. Collision integrals $\pi \Omega_{st}^{(1,1)}$ and $\pi \Omega_{st}^{(2,2)}$ are calculated using curve fits according to whether the colliding particles include any neutral species. For any collisions with neutral species involved, $\pi \Omega_{st}^{(a,a)}$ is described by

$$\pi \Omega_{st}^{(a,a)} = D T^{\left(A (\ln(T))^2 + B \ln(T) + C \right)}, \tag{2.50}$$

where A, B, C and D are known coefficients for a given species pair s and t. For any collisions which don't involve any neutral species, the collision integrals are defined by

$$\pi \Omega_{st}^{(a,a)} = 5.0 \times 10^{15} \pi \left(\frac{\lambda_D}{T} \right)^2 \ln \left(D_n T^* \left(1 - C_n e^{-c_n T^*} \right) + 1 \right), \tag{2.51}$$

where T^* is a reference temperature described by

$$T^* = \frac{\lambda_D k_B T}{Q_e^2}, \tag{2.52}$$

and λ_D is the Debye length described by

$$\lambda_D = \sqrt{\frac{k_B T}{4 \pi n_e Q_e^2}}. \tag{2.53}$$

Note that the units of Debye length are cm in this formulation. The variables c_a, C_a and D_a are again known values which are unique for each collision species pair. The curve fits describing $\pi \Omega$ for charged species are approximations to Coulomb shielding models. The coefficient values utilised for the Gupta model are provided in appendix A. With these variables evaluated, the species diffusion coefficients can be evaluated.

Unlike the Wilke model, diffusion coefficients for species are determined individually, each being given by

$$D_s = \frac{\left(\sum_t \gamma_t\right)^2 M_s \left(1 - M_s \gamma_s\right)}{\sum_{t \neq s} \frac{\gamma_t}{D_{st}}}, \tag{2.54}$$

where D_{st} represents a collisional coefficient unique to a particular collisional pair. These coefficients are determined using the collisional terms Δ^1_{st}:

$$D_{st} = \frac{k_B T}{p \Delta^{(1)}_{st}}. \tag{2.55}$$

2.5 Chemical Non-Equilibrium Modelling

In order to accurately model chemical non-equilibrium, it is necessary to calculate various reaction rates between all chemical species which are present in non-negligible quantities, as shown in Equation 2.1 by the term w_s. In addition, this information is required to accurately model changes to vibrational energy in thermal non-equilibrium. These chemical reactions are modelled in OP2A using a finite-rate chemistry model. The presented model is applicable to reactive Earth atmosphere mixtures as well as other mixtures, as detailed in section 2.5.2.

2.5.1 Species Sources

The starting principle for the calculation of species source terms in Equation 2.1 is that the total species creation rate is equal to the sum of all chemical reactions c involving said species s.

$$w_s = \sum_c w_{s,c}, \tag{2.56}$$

where each chemical reaction can be described generically as

$$\sum_s \alpha_s \rightleftharpoons \sum_s \beta_s. \tag{2.57}$$

Each of these individual contributions are then evaluated by the finite rate kinetics model

$$w_{s,c} = \left(\beta_{s,c} - \alpha_{s,c}\right) \left(k_{f,c} \prod_p \left(\frac{\rho_p}{M_p}\right)^{\alpha_{p,c}} - k_{b,c} \prod_p \left(\frac{\rho_p}{M_p}\right)^{\beta_{p,c}} \right), \tag{2.58}$$

where α and β are the reaction's stoichiometric coefficients, k_f and k_b are the forward and backward reaction rates respectively and subscript p denotes participants in the reaction c. The stoichiometric coefficients are unique to each species and reaction, and

values for all reactions considered in this work are provided in appendix B and are originally sourced from Park et al. (2001).

Each forward reaction rate is extrapolated from empirical data by way of Arrhenius curve fits of the form

$$k_{f,c} = C_{f,c} T^{\eta_c} e^{\frac{\theta_c}{T}}, \tag{2.59}$$

where the parameters $C_{f,c}$, η_c and θ_c are provided in appendix B. The temperature T used throughout this section is determined by the type of reaction being evaluated:

$$T = \begin{cases} T_{tr} & \text{for exchange, charge exchange and recombination ionisation reactions,} \\ T_{vee} & \text{for electron impact ionisation reactions,} \\ T_P & \text{for dissociation reactions,} \end{cases} \tag{2.60}$$

where the Park temperature T_P is an averaging of the translational and vibrational temperatures, and is given by

$$T_P = T_{tr}^{a_P} T_{vee}^{b_P}, \tag{2.61}$$

where a_P and b_P can have various values. Henceforth, the values used are assumed to be $a_P = 0.5$ and $b_P = 0.5$, in common with Park et al. (2001) unless otherwise stated. The choice of these coefficients has been found to have a small effect upon outcomes such as convective heat fluxes Hash et al. (2007b).

Backward reaction rates are calculated through the equilibrium constant K_e which is the ratio of forward to backward reaction rates for a given reaction.

$$K_{e,c} = \frac{k_{f,c}}{k_{b,c}}. \tag{2.62}$$

The equilibrium constant is itself extrapolated from a five parameter curve fit described by

$$K_e = e^{\left(A_1\left(\frac{T}{10000}\right)+A_2+A_3\ln\left(\frac{10000}{T}\right)+A_4\left(\frac{10000}{T}\right)+A_5\left(\frac{10000}{T}\right)^2\right)}, \tag{2.63}$$

where the parameters $A1$ - $A5$ used in this work can be found in appendix B.

2.5.2 Chemical Mixtures

The described chemical model provides reasonable accuracy for Earth atmosphere mixtures. Within the present work an both 5 and 11 species air mixtures are used, henceforth referred to as the air-5 and air-11 mixtures respectively. The air-5 mixture contains the species N_2, O_2, NO, N, O. The air-11 mixture contains the species N_2, O_2, NO, N, O, N_2^+, O_2^+, NO^+, N^+, , O^+, e.

All reactions between these species fall into one of several categories; dissociation, electron impact dissociation, dissociative recombination, particle exchange, charge exchange and electron impact ionisation. Dissociation and electron impact dissociation reactions are those in which molecules are divided by the impact of heavy particles and electrons respectively. Dissociative recombination reactions are those in which neutral atoms collide and combine into charged molecules together with the emission of an electron. Exchange and charge exchange reactions involve the transfer between particles of and atom or electron respectively. Electron ionisation reactions involve the removal of an electron from a heavy particle by way of collision with another electron.

It is necessary for the type of reaction to be recorded by OP2A when calculating chemical species production rates. This is because the electron impact ionisation rate will be re-used in the calculation of vibrational energy sources as part of thermal non-equilibrium modelling.

The total chemical reactions present for the 5 species air model are presented in Table 2.1. The variable values associated with these reactions are presented in appendix B.

Reaction	**Reaction Type**	**Controlling Temperature**
N_2+N=N+N+N	Dissociation	T_P
N_2+O=N+N+O	Dissociation	T_P
N_2+N_2=N+N+N_2	Dissociation	T_P
N_2+O_2=N+N+O_2	Dissociation	T_P
N_2+NO=N+N+NO	Dissociation	T_P
O_2+N=O+O+N	Dissociation	T_P
O_2+O=O+O+O	Dissociation	T_P
O_2+N_2=O+O+N_2	Dissociation	T_P
O_2+O_2=O+O+O_2	Dissociation	T_P
O_2+NO=O+O+NO	Dissociation	T_P
NO+N=N+O+N	Dissociation	T_P
NO+O=N+O+O	Dissociation	T_P
NO+N_2=N+O+N_2	Dissociation	T_P
NO+O_2=N+O+O_2	Dissociation	T_P
NO+NO=N+O+NO	Dissociation	T_P
N_2+O=NO+N	Exchange	T_{tr}
NO+O=O_2+N	Exchange	T_{tr}

TABLE 2.1: Reactions present within a 5 species air mixture, together with their controlling temperatures.

The total chemical reactions modelled herein for the 11 species air model are those of the 5 species mixture combined with those presented in Table 2.2.

Reaction	Reaction Type	Controlling Temperature
$N_2+N^+=N+N+N^+$	Dissociation	T_P
$N_2+O^+=N+N+O^+$	Dissociation	T_P
$N_2+{N_2}^+=N+N+{N_2}^+$	Dissociation	T_P
$N_2+{O_2}^+=N+N+{O_2}^+$	Dissociation	T_P
$N_2+NO^+=N+N+NO^+$	Dissociation	T_P
$O_2+N^+=O+O+N^+$	Dissociation	T_P
$O_2+O^+=O+O+O^+$	Dissociation	T_P
$O_2+{N_2}^+=O+O+{N_2}^+$	Dissociation	T_P
$O_2+{O_2}^+=O+O+{O_2}^+$	Dissociation	T_P
$O_2+NO^+=O+O+NO^+$	Dissociation	T_P
$NO+N^+=N+O+N^+$	Dissociation	T_P
$NO+O^+=N+O+O^+$	Dissociation	T_P
$NO+{N_2}^+=N+O+{N_2}^+$	Dissociation	T_P
$NO+{O_2}^+=N+O+{O_2}^+$	Dissociation	T_P
$NO+NO^+=N+O+NO^+$	Dissociation	T_P
$N+O=NO^++e$	Dissociative Recombination	T_{tr}
$N+N={N_2}^++e$	Dissociative Recombination	T_{tr}
$O+O={O_2}^++e$	Dissociative Recombination	T_{tr}
$N_2+{O_2}^+={N_2}^++O_2$	Charge Exchange	T_{tr}
$NO^++N=O^++N_2$	Charge Exchange	T_{tr}
$NO^++O=N^++O_2$	Charge Exchange	T_{tr}
$NO^++O_2={O_2}^++NO$	Charge Exchange	T_{tr}
$NO^++N={N_2}^++O$	Charge Exchange	T_{tr}
${O_2}^++N=N^++O_2$	Charge Exchange	T_{tr}
$O^++NO=N^++O_2$	Charge Exchange	T_{tr}
$NO^++O={O_2}^++N$	Charge Exchange	T_{tr}
$O^++N_2={N_2}^++O$	Charge Exchange	T_{tr}
$N_2+e=N+N+e$	Dissociation	T_P
$N+e=N^++e+e$	Electron Impact Ionisation	T_e
$O+e=O^++e+e$	Electron Impact Ionisation	T_e

TABLE 2.2: Reactions present within an 11 species air mixture, together with their controlling temperatures.

The numerical values for these chemical reactions are presented in appendix B. An additional mixture included in OP2A is utilised not as an atmosphere, but rather to simulate lab experiments. This mixture contains Ar, Ar^+ and electrons e, and only one reaction is simulated as described by Table 2.3.

Reaction	Reaction Type	Controlling Temperature
Ar+e=Ar^++e+e	Electron Impact Ionisation	T_e

TABLE 2.3: Reactions present within an argon mixture, together with their controlling temperatures.

2.6 Thermal Non-Equilibrium Modelling

Accurate modelling of thermal non-equilibrium requires evaluating the vibrational energy source term contained in Equation 2.6, which contains a number of separate contributions as described below.

$$w_v = w_{\nabla e,v} + w_{c,v} + w_{h-e,v} + w_{e-ion,v} + w_{t-v,v}. \tag{2.64}$$

Note that Equation 2.64 is limited in that it does not account for radiative or ablative losses, which as previously mentioned can be significant for re-entry simulations. Outside of these limits, Equation 2.64 represents a reasonably comprehensive description of vibrational energy contributions.

Each of the terms on the right hand side requires evaluation in order to accurately compute any changes in vibrational energy. $w_{\nabla e,v}$ represents the change in E_{vee} brought about by the electric field induced by any variations in electron density, it is described mathematically by Scalabrin (2007) as

$$w_{\nabla e,v} = -p_e \nabla . \vec{u}. \tag{2.65}$$

$w_{c,v}$ represents any and all changes to vibrational and electronic energy as a result of chemical reactions and is described by

$$w_{c,v} = \sum_s w_s \left(D_{s,pref} + e_{el,s} \right), \tag{2.66}$$

where w_s is the source term of a given species s, described in the prior section on chemical modelling (section 2.5). Within the present work a preferential model is utilised, which assumes that molecules are created and destroyed at energy levels above the average. Hence the contribution to vibrational energy is some fraction of the known dissociation energy of that molecule D_s;

$$D_{s,pref} = a_{pref} D_s, \tag{2.67}$$

where a_{pref} is henceforth referred to as the preferential factor. A preferential factor of 0.3 was utilised for this work unless otherwise stated. This preferential factor was utilised

in order to facilitate comparisons with existing simulation work, as there is a wealth of literature which utilises a value of 0.3. Alternative values have been put forward by Luo et al. (2018); Singh and Schwartzentruber (2018).

The third term details energy transfer between the translational and electron modes due to elastic collisions between electrons and heavy particles. The mathematical description of this term is

$$w_{h-e,v} = 3R_u\rho_e\left(T_{tr} - T_{vee}\right)\sqrt{\frac{8R_uT_{vee}}{\pi M_e}}\sum_{s\neq e}\frac{\rho_s N_A}{M_s^2}\sigma_{s,e}, \tag{2.68}$$

where electron mass, M_e, is in units of grams per mol and $\sigma_{s,e}$ is the cross section for collisions between electrons and species s, which is in turn described by

$$\sigma_{s,e} = \begin{cases} 10^{-20} & \text{for electron - neutral collisions,} \\ \dfrac{8\pi e^4}{27k_B^2T_e^2}\ln\left(1+\dfrac{9k_B^3T_e^3}{4\pi n_e e^6}\right) & \text{for electron - ion collisions,} \end{cases} \tag{2.69}$$

where n_e is the number density of electrons. The choice of value for $\sigma_{s,e}$ for electron - neutral collisions is another point of divergence within published work. The choice of value must therefore be considered to be an approximation whose impact upon output simulations should be noted where applicable.

The fourth term describes electron energy changes due to electron impact ionisation reactions. This terms is simply calculated as the product of ionisation energy I and the frequency of electron impact ionisations:

$$w_{e-ion,v} = \sum_{s=ion} a_{e-ion}M_sI_sw_{s,e-ion}. \tag{2.70}$$

A correction factor a_{e-ion} is applied to this product in order to more accurately model ionisation energy changes. This factor represents energy contributions from sources other than free electrons, which would be present in real reactions. A value of $a_{e-ion} = 0.3$ was utilised throughout this work unless otherwise stated.

The final term of Equation 2.64 details the transfer of energy between the two energy modes of the Park model. Evaluation of this term requires the use of a relaxation model, as well as a determination of appropriate relaxation times.

2.6.1 Relaxation Model

The original estimations of these relaxation times were determined empirically for various combinations of chemical species by Fogg et al. (1953). The first comprehensive description of vibrational relaxation was put forth by Millikan and White (1963). This

semi-empirical model consists of modelling the translational-vibrational energy exchange rate $w_{t-v,v}$ as a Landau-Teller function Landau and Teller (1936) of the form

$$w_{t-v,v} = \sum_s \rho_s \frac{e^*_{vee,s} - e_{vee,s}}{\tau_s}, \tag{2.71}$$

where $e_{vee,s}$ is the species vibrational energy per unit mass, evaluated using the vibrational temperature. $e^*_{vee,s}$ is then the vibrational energy per unit mass evaluated at the translational temperature. τ_s is a species specific relaxation time, this relaxation time for a given species s is described as

$$\tau_s = \frac{\sum_t Y_t}{\sum_t \frac{Y_t}{\tau_{s,t}}}, \tag{2.72}$$

where Y_t is the molar fraction of the species t and $\tau_{s,t}$ is the inter-species relaxation time between species s and t. Millikan and White (1963) describes this parameter empirically as

$$\tau_{s,t} = \frac{101325}{p} e^{\left(A_{s,t}\left(T^{-\frac{1}{3}} - B_{s,t}\right) - 18.42\right)}, \tag{2.73}$$

where $A_{s,t}$ and $B_{s,t}$ are referred to as the Millikan-White parameters. The factor of 101325 exists in order to convert between Pa and atm. The parameters $A_{s,t}$ and $B_{s,t}$ are respectively described as

$$\begin{aligned} A_{s,t} &= 1.16 \times 10^{-3} \mu_{s,t}^{\frac{1}{2}} \theta_{v,s}^{\frac{4}{3}}, \\ B_{s,t} &= 0.015 \mu_{s,t}^{\frac{1}{4}}, \end{aligned} \tag{2.74}$$

where $\theta_{v,s}$ is the characteristic vibrational temperature of a given species s and $\mu_{s,t}$ is the reduced mass of the species pair, and is described as

$$\mu_{s,t} = \frac{M_s M_t}{M_s + M_t}, \tag{2.75}$$

where M_s is the molecular weight of species s in g/mol.

The above series of equations (Equations 2.71 - 2.75) are hereby referred to as the Millikan-White system. This system is capable of producing accurate results across a large temperature range for conventional applications, with the first major inaccuracy occurring at 1000 K. However further inaccuracies develop as temperature increases according to Millikan and White (1963), with a further inaccuracy being reported at $2500K$ by Colgan and Levitt (1967), and multiple discrepancies between predictions and reality developing by $4000K$ as shown by Streicher et al. (2020). In order to correct for this, Park (1990) proposed a correction term to be introduced into Equation 2.72.

This alters the equation to become

$$\tau_s = \frac{\sum_t Y_t}{\sum_t \frac{Y_t}{\tau_{s,t}}} + \tau_{P,s}, \tag{2.76}$$

where $\tau_{P,s}$ is the Park correction term. This term is described as

$$\tau_{P,s} = \frac{1}{\sigma_s a_s n}, \tag{2.77}$$

where n is the total number density of the fluid. σ_s is a limiting cross section, described as

$$\sigma_s = 10^{-20} \left(\frac{50000}{T} \right)^2. \tag{2.78}$$

And c_s is the average molecular speed of species s, described as

$$c_s = \sqrt{\frac{8 R_u T}{\pi M_s}}, \tag{2.79}$$

where R_u is the universal gas constant. Note that within Equation 2.79 the value of M_s used must be in units of grams per mole, contrary to the rest of this work. This system of equations, with Equation 2.72 replacing 2.76, is henceforth referred to as the Park two temperature model. This model has been extensively explored for spaceflight applications including by Hash et al. (2007a), Park (1993) and Park et al. (1994), other non-equilibrium flows including by Neitzel et al. (2017) and numerical method comparisons such as those presented by Olynick et al. (1994). Thus it is considered to be an appropriate choice for the simulations of interest to this work, as well as having a rich reservoir of comparison literature to draw from for verification purposes.

2.7 Summary

Mathematical models have been outlined which can describe a re-entry plasma in thermochemical non-equilibrium. These models include the Gupta model for the determination of various diffusive terms, accurate at the necessary high temperatures, but requiring collisional data; and the Wilke model to be used where such data is unavailable. Also described are the thermochemical modelling techniques, which utilise a finite rate chemistry model in conjunction with a multi-temperature thermal model. This thermal model splits energy between the translational-rotational mode and the vibrational-electronic-electron mode; hereafter referred to as the translational and vibrational modes for brevity. This setup allows for temperatures to be evaluated independently and for chemical reactions to be controlled by different temperatures according to the exact nature of the reaction. The reactions modelled for different gas

mixtures, together with their controlling temperatures have been shown. These models have each been utilised extensively for hypersonic non-equilibrium CFD simulation; however their combination, together with the numerical methods described in Chapter 3 is heretofore unique. These numerical methods, together with spatial discretisation technique are discussed in the following chapter.

3

Numerical Methods

"A theory has only the alternative of being right or wrong. A model has a third possibility: it may be right, but irrelevant."

– Manfred Eigen

This chapter discusses the methods used to discretise the continuous formulae presented thus far. This includes the integration methods used, and the meshing used to divide the physical simulation domain. The reasoning behind these choices as well as the limitations that they impose will also be presented. A description of the meshing techniques mentioned in Chapter 1 is also presented within this chapter.

OP2A currently achieves discretisation using finite volume methods which split the simulation domain into discrete cells, store simulation quantities at the cell centres and calculate gradients at the faces between cells. The simulation domain is discretised upon structured Cartesian grids, and the simulation evolved using explicit time integration methods.

3.1 Finite Volume Methods

There exist several discretisation techniques for Navier-Stokes systems; finite difference methods (FDM), finite volume methods (FVM) and finite element methods (FEM). Finite difference methods are unsuited to high precision hypersonic fluid simulation as they lack accuracy when encountering complex boundary shapes. Finite element methods provide a practicable solution, however similar to FDM they are not fully conservative. They are also considered the most time and memory consuming to implement as they require a polynomial representation of simulation quantities across all grid points. Finite volume methods are fully conservative and capable of dynamic refinement. They

are also more efficient than FEM due to the assumed uniformity of quantities throughout a given cell, hence they were utilised throughout this work.

Finite volume methods are a relatively mature category of methods, used as far back as 1971 by McDonald (1971). These methods involve the construction of discrete control volumes, within which certain amounts of the conserved CFD quantities exist. Each control volume consists of the polygonal body or cell, surrounded by faces, with grid nodes existing at the intersections of faces. The finite volume formulation calls for simulation quantities to be located at cell centres and evolved in discrete increments or time steps dt. Evolution of these quantities occurs through one of two methods; movement through the faces surrounding the volume, or sources/sinks within the volume. These are henceforth referred to as face centred and cell centred respectively. The calculation of the location of these centres is performed through a simple unweighted averaging of node locations.

Hence the Navier-Stokes equation set described in Chapter 2 is reformulated according to this description. The finite volume formulation of Equation 2.7 is a simple modification to account for the geometric considerations of the area/volume of faces/cells and can be seen in Equation 3.1.

$$\frac{\partial Q}{\partial t} dV + (F_{inv} - F_{vis})\, dA + (G_{inv} - G_{vis})\, dA + (H_{inv} - H_{vis})\, dA = S dV, \tag{3.1}$$

where dV represents cell volume, and dA face area.

3.1.1 Spatial Domain Discretisation

With the discretisation technique determined, it is now necessary to describe how the spatial domain is divided. OP2A utilises a block-structured quadrilateral (hexahedral) Cartesian grid to discretise fluid quantities; with conserved quantities located at cell centres and fluxes located at face centres. As mentioned in Chapter 1, rapid grid generation is an extremely helpful feature for any software which is required to simulate varying geometries. Block-structured Cartesian grids allow for rapid grid generation even for complex geometries. Additionally, it means that the time integration is utilising fluxes located at known locations; allowing for a simpler and more efficient integration algorithm, lacking the need for additional geometric analysis when mesh changes occur. Any node centred values, which are occasionally needed for gradient evaluation, are linearly interpolated from cell centred values as required by OP2A. A sample of such meshing is shown in Figure 3.1 for a capsule surface, with grid directions aligned with the cardinal flow direction. Structured grids are also amenable to automatic refinement and coarsening through automatic mesh refinement (AMR) algorithms. This allows the mesh to be refined in areas where additional resolution is required, and

coarsened where not; thus optimising the use of computational resources. The underlying data structures of OP2A are designed to facilitate AMR, as noted in Chapter 4.

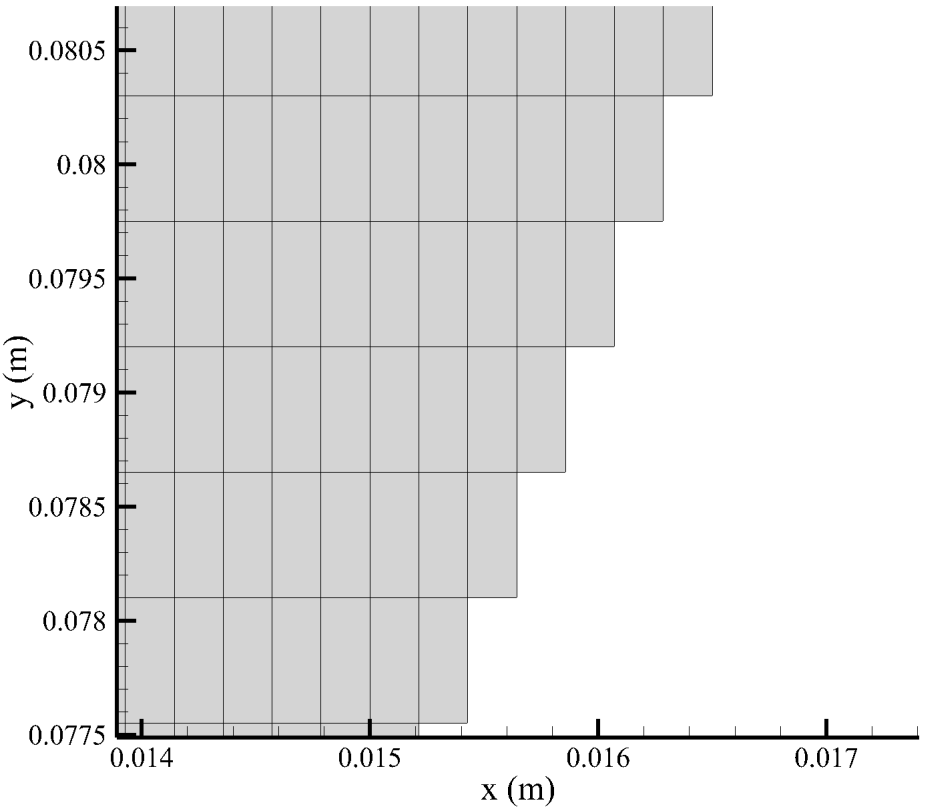

FIGURE 3.1: Sample of OP2A's structured Cartesian grid at a capsule surface.

The choice of structured Cartesian grids brings several advantages and drawbacks. A useful advantage is the ability to align a cardinal grid direction with the principal flow direction; this reduces the relative magnitude of diffusive terms in computation, and speeds up convergence. The biggest advantage concerning capsule optimisation simulations is the lack of complexity involved in generating grids initially. Unstructured and hybrid grids can require more extensive developer attention, and much more time to create.

A prominent difficulty with Cartesian meshing is that it can be difficult to accurately represent curved and other complex surfaces, as well as achieve sufficient resolution around shocks and boundary layers. This difficulty is largely mitigated by AMR, as has been demonstrated by Atkins and Deiterding (2020) and Baskaya et al. (2022) among others.

3.1.2 Explicit Time Integration

As described in section 1.3, the choice of time integration technique has a profound effect upon many aspects of simulation. The framework of OP2A was constructed to support the use of either explicit or implicit techniques. Explicit techniques were chosen for this work due to their simplicity of implementation which allowed for a more extensive verification process within the time frame of this work.

Explicit time integration schemes calculate simulation values at the future time step $n+1$ using only data from the previous time step n. Such methods are limited by the CFL number constraint, stating that the CFL number can never exceed 1 for a stable simulation. This CFL number is defined as

$$CFL = u\frac{dt}{dx} \leq 1, \tag{3.2}$$

this condition ensures that fluid quantities cannot cross more than one cell per time step. In practice, the CFL number must often be limited to below 1 to ensure stability.

3.1.3 Reformulated Governing Equations

With the discretisation and integration techniques determined, the finite volume formulae can be explicitly reformulated as

$$Q_{i,j,k}^{n+1} = Q_{i,j,k}^{n} - \frac{dt}{dV}\left((F_{i+\frac{1}{2}} - F_{i-\frac{1}{2}})^n dA - (G_{j+\frac{1}{2}} - G_{j-\frac{1}{2}})^n dA - (H_{k+\frac{1}{2}} - H_{k-\frac{1}{2}})^n dA\right) + dt\left(S_{i,j,k}^{n}\right), \tag{3.3}$$

where $F = F_{inv} - F_{vis}$ represents total flux contributions both inviscid and viscous. i, j and k are cell centre locations, with faces centred at $i \pm \frac{1}{2}$; n is the time step integer, dt the time step size and dx is the distance between opposing face centres.

The terms within Equation 3.1 begin with Q, which represents the vector of conserved quantities as shown in Equation 3.4.

$$Q = \begin{pmatrix} \rho_1 \\ \vdots \\ \rho_{Ns} \\ \rho u \\ \rho v \\ \rho w \\ E \\ E_v \end{pmatrix}, \tag{3.4}$$

Wherein all quantities are cell centred and Ns is the number of chemical species present.

The F_{inv}, G_{inv} and H_{inv} terms represent advective fluxes across faces in the x, y and z cardinal directions respectively; with F_{vis}, G_{vis} and H_{vis} representing their diffusive (viscous) equivalents. These terms all face centred, and are described by Equations 3.5 and 3.6 respectively.

$$F_{inv} = \begin{pmatrix} \rho_1 u \\ \vdots \\ \rho_{Ns} u \\ \rho u^2 + p \\ \rho v u \\ \rho w u \\ (E+p)u \\ E_v u \end{pmatrix}, G_{inv} = \begin{pmatrix} \rho_1 v \\ \vdots \\ \rho_{Ns} v \\ \rho u v \\ \rho v^2 + p \\ \rho w v \\ (E+p)v \\ E_v v \end{pmatrix}, H_{inv} = \begin{pmatrix} \rho_1 w \\ \vdots \\ \rho_{Ns} w \\ \rho u w \\ \rho v w \\ \rho w^2 + p \\ (E+p)w \\ E_v w \end{pmatrix}. \tag{3.5}$$

$$
F_{vis} = \begin{pmatrix} J_{x,1} \\ \vdots \\ J_{x,Ns} \\ \tau_{xx} \\ \tau_{xy} \\ \tau_{xz} \\ -(q_{x,t} + q_{x,v}) + u\tau_{xx} + v\tau_{xy} + w\tau_{xz} - \sum_s (J_{x,s} h_s) \\ -q_{x,v} - \sum_s (J_{x,s} e_{v,s}) \end{pmatrix},
$$

$$
G_{vis} = \begin{pmatrix} J_{y,1} \\ \vdots \\ J_{y,Ns} \\ \tau_{yx} \\ \tau_{yy} \\ \tau_{yz} \\ -(q_{y,t} + q_{y,v} + u\tau_{yx} + v\tau_{yy} + w\tau_{yz} - \sum_s (J_{y,s} h_s) \\ -q_{y,v} - \sum_s (J_{y,s} e_{v,s}) \end{pmatrix}, \tag{3.6}
$$

$$
H_{vis} = \begin{pmatrix} J_{z,1} \\ \vdots \\ J_{z,Ns} \\ \tau_{zx} \\ \tau_{zy} \\ \tau_{zz} \\ -(q_{z,t} + q_{z,v}) + u\tau_{zx} + v\tau_{zy} + w\tau_{zz} - \sum_s (J_{z,s} h_s) \\ -q_{z,v} - \sum_s (J_{z,s} e_{v,s}) \end{pmatrix}.
$$

Within Equations 3.5 & 3.6 all variables are defined in the same manner as in Chapter 2.

Lastly, the term S represents the combined, cell-centred source terms. These source terms can vary considerably depending upon the exact system under consideration. Herein, we limit ourselves to considering the effects of thermal and chemical non-equilibrium. The effects of considering other sources, including axisymmetric and radiative will be discussed in Chapter 6. These thermal and chemical non-equilibrium source terms are described by Equation 3.7.

$$S = \begin{pmatrix} w_1 \\ \vdots \\ w_{Ns} \\ 0 \\ 0 \\ 0 \\ 0 \\ w_v \end{pmatrix}. \tag{3.7}$$

Each of the terms within Equation 3.7 is evaluated as described in the Chapter 2. It should be noted that no total energy source term is evaluated within OP2A at present. Whilst this is reasonable for the scope of the current work, this will prove to be a limitation for certain kinds of plasma simulation, which may feature direct energy injection into the translational or rotational modes.

With the fluxes and sources thus evaluated, there remains the question of how to integrate these quantities over time and space. It is necessary to define a method to interpolate face centred quantities for flux evaluation, and to determine how quantities change over a time step.

3.2 Spatial Integration Methods

OP2A's base spatial integration method is the Liou-Steffen scheme, or Advection Upstream Splitting Method (AUSM), a flux vector splitting (FVS) method presented by Liou and Steffen (1993). This was one of the earliest FVS methods to achieve the accuracy of flux difference splitting (FDS) whilst maintaining the $O(N_{eq})$ time complexity of FVS methods (N_{eq} being the number of distinct equations in the system). It is a high-order accuracy integration scheme capable of capturing the sharp shocks associated with hypersonic flows and has been used in the simulation of hypersonic flows by Zheleznyakova A.L. (2014).

AUSM also possesses the key advantage of being the progenitor of a range of other schemes. These include the AUSM+ scheme (Liou (1996)), AUSMPW (pressure weighted) scheme (Hong Kim et al. (1998)), and the AUSMPW+ scheme (Kim et al. (2001)) among others such as those presented by Shima and Kitamura (2011) and sheng Chen et al. (2020). Each of these possess distinct advantages and have also been used extensively in hypersonic CFD modelling Shu-sheng et al. (2021). The advantage of using AUSM as the primary spatial integration scheme is that it allows for subsequent schemes to be

built upon it, such as those presented by Liou (2010). This advantage helps to satisfy the requirement for extensibility mentioned in Chapter 1.

3.2.1 Advection Upstream Splitting Method

The AUSM method, as the name suggests, utilises upstream values for a range of simulation quantities. The quantities which are not upstreamed are pressure and Mach number, which are instead calculated using a split of upstream and downstream values. The AUSM procedure begins by splitting the inviscid fluxes into convective and pressure components as follows.

$$F_{inv,i+\frac{1}{2}} = M_{i+\frac{1}{2}} \begin{pmatrix} \rho_1 a \\ \vdots \\ \rho_{N_s} a \\ \rho a u + p \\ \rho a v \\ \rho a w \\ a(E+p) \\ a E_v \end{pmatrix} = M_{i+\frac{1}{2}} \begin{pmatrix} \rho_1 a \\ \vdots \\ \rho_{N_s} a \\ \rho a u \\ \rho a v \\ \rho a w \\ a(E+p) \\ E_v \end{pmatrix} + \begin{pmatrix} 0 \\ \vdots \\ 0 \\ p_{i+\frac{1}{2}} \\ 0 \\ 0 \\ 0 \\ 0 \end{pmatrix} = F^c + F^p \quad (3.8)$$

Within Equation 3.8 F^c and F^p are the convective and pressure flux components respectively. a is the speed of sound within the fluid, defined as

$$a = \frac{\sqrt{\gamma p}}{\rho}, \quad (3.9)$$

where gamma is the heat capacity ratio, defined as

$$\gamma = \frac{c_p}{c_v}, \quad (3.10)$$

where c_p is the specific heat capacity at constant pressure.

Note the separation of a pressure term p and Mach number term M within Equation 3.8. All other simulation quantities besides these p and M terms are determined through upstreaming according to:

$$\xi_{i+\frac{1}{2}} = \begin{cases} \xi_i & \text{if } M_{i+\frac{1}{2}} \geqslant 0, \\ \xi_{i+1} & \text{if } M_{i+\frac{1}{2}} < 0, \end{cases} \quad (3.11)$$

wherein ξ represents any simulation quantity besides the specified p and M. These Mach number and pressure terms are then defined according to specific formulae:

$$\begin{aligned} M_{i+\frac{1}{2}} &= M_i^+ + M_{i+1}^-, \\ p_{i+\frac{1}{2}} &= p_i^+ + p_{i+1}^-, \end{aligned} \tag{3.12}$$

where M_i^+ and M_{i+1}^- represent the left and right contributions respectively. Within Equation 3.12 the left and right contributors are defined for Mach number and pressure respectively as

$$\begin{aligned} M^{\pm} &= \begin{cases} \pm\frac{1}{4}(M \pm 1)^2 & \text{if } |M| \leqslant 1, \\ \frac{1}{2}(M \pm |M|) & \text{if } |M| > 1, \end{cases} \\ p^{\pm} &= \begin{cases} \pm\frac{1}{4}p(M \pm 1)^2(2 \mp M) & \text{if } |M| \leqslant 1, \\ \frac{1}{2}p\frac{(M \pm |M|)}{M} & \text{if } |M| > 1. \end{cases} \end{aligned} \tag{3.13}$$

This formulation is second order accurate in space. The original presentation of the AUSM scheme by Liou and Steffen (1993) contains an alternate definition of the left and right pressure contributions which is first order accurate in space.

$$p^{\pm} = \begin{cases} \frac{p}{2}(1 \pm M) & \text{if } |M| \leqslant 1, \\ \frac{p}{2}\frac{(M \pm |M|)}{M} & \text{if } |M| > 1. \end{cases}$$

This formulation is available within OP2A, but is not utilised within this work and is included here for completeness only.

Whilst the AUSM scheme is capable of resolving sharp shocks, it still possesses vulnerability to quantity overshoots under certain conditions. Hence, a further spatial integration scheme has been implemented which overcomes this problem.

3.2.2 AUSMDV

The AUSM scheme proved susceptible to pressure overshoots behind strong shock waves. In order to rectify this, the AUSMDV scheme was later developed by Wada and Liou (1997). This scheme is implemented in OP2A and utilises slightly different flux vector splitting techniques which split fluxes according to pressure and mass fluxes.

$$F_{inv} = \frac{1}{2}(\rho u)_{i+\frac{1}{2}}(\psi_i + \psi_{i+1}) - \frac{1}{2}D_{DV}(\psi_{i+1} - \psi_i) + \zeta_{i+\frac{1}{2}}, \tag{3.14}$$

where

$$\psi = \begin{pmatrix} 1 \\ \vdots \\ 1 \\ u \\ v \\ w \\ \frac{(E+p)}{\rho} \\ \frac{E_v}{\rho} \end{pmatrix}, \tag{3.15}$$

and

$$\zeta = \begin{pmatrix} 0 \\ \vdots \\ 0 \\ p_{\frac{1}{2}} \\ 0 \\ 0 \\ 0 \\ 0 \end{pmatrix}. \tag{3.16}$$

Calculation of the quantities $p_{i+\frac{1}{2}}$ and $(\rho u)^{\pm}_{i+\frac{1}{2}}$ is achieved by,

$$p_{i+\frac{1}{2}} = p^{+}_{5,\alpha} p_i + p^{-}_{5,\alpha} p_{i+1}, \tag{3.17}$$

$$(\rho u)_{i+\frac{1}{2}} = a_{\frac{1}{2}} \left(\rho_i M^{+}_{\frac{1}{2}} + \rho_{i+1} M^{-}_{\frac{1}{2}} \right), \tag{3.18}$$

where

$$p^{\pm}_{5,\alpha} = \begin{cases} \frac{1}{M} M^{+}_1 & \text{if } |M| \geqslant 1, \\ \frac{1}{4}(M \pm 1)^2 (2 \mp M) \pm \alpha M (M^2 - 1)^2 & \text{otherwise,} \end{cases} \tag{3.19}$$

where α is restricted to between $\frac{-3}{4}$ and $\frac{3}{16}$. Within this work a value of $\frac{3}{16}$ is used unless otherwise stated. Mach number calculation is performed according to

$$M^{\pm}_1 = \frac{1}{2}(M \pm |M|), \tag{3.20}$$

and

$$M^{\pm}_{4,\beta} = \begin{cases} M^{\pm}_1 & \text{if } |M| \geqslant 1, \\ \pm\frac{1}{4}(M \pm 1)^2 \pm \beta (M^2 \pm 1)^2 & \text{otherwise,} \end{cases} \tag{3.21}$$

where β is restricted to between $\frac{1}{16}$ and $\frac{1}{2}$ and a value of $\frac{1}{8}$ is used throughout this work. Intermediate quantities are defined as

$$M^{+}_{\frac{1}{2}} = \left(\omega^{+}_{\frac{1}{2}} M^{+}_{4,\beta} + (1-\omega^{+}_{\frac{1}{2}}) M^{+}_{1}\right), \tag{3.22}$$

and

$$M^{-}_{\frac{1}{2}} = \left(\omega^{-}_{\frac{1}{2}} M^{-}_{4,\beta} + (1-\omega^{-}_{\frac{1}{2}}) M^{-}_{1}\right), \tag{3.23}$$

where

$$\omega^{+}_{\frac{1}{2}} = \frac{2\frac{p_i}{\rho_i}}{(\frac{p_i}{\rho_i} + \frac{p_{i+1}}{\rho_{i+1}})}, \tag{3.24}$$

and

$$\omega^{-}_{\frac{1}{2}} = \frac{2\frac{p_{i+1}}{\rho_{i+1}}}{(\frac{p_i}{\rho_i} + \frac{p_{i+1}}{\rho_{i+1}})}. \tag{3.25}$$

Lastly, the value of D_{DV} is defined as

$$D_{DV} = |(\rho u)_{\frac{1}{2}}|. \tag{3.26}$$

3.2.3 Flux Limiting

The spatial integration methods described in section 3.2 are high resolution methods, meaning they possess a high degree of accuracy when resolving flow features, but can be susceptible to oscillations in fluid variables. In order to be successfully utilised, these fluctuations must be mitigated and the flow made to be total variation diminishing (TVD). In order to achieve this, flux limiting or slope limiting methods are required. Flux limiting schemes modify the calculated fluxes using additional low resolution fluxes in order to ensure that no new maxima or minima occur. Slope limiting schemes work in a similar manner, however they operate upon system values (eg. p, ρ etc.), rather than fluxes. Flux limiting methods were chosen to be implemented within OP2A in common with general hypersonic simulation techniques such as those presented in Candler et al. (2015b).

Such limiting methods modify overall fluxes according to

$$F_{i+\frac{1}{2}} = F^{low}_{i+\frac{1}{2}} + \phi(F^{high}_{i+\frac{1}{2}} - F^{low}_{i+\frac{1}{2}}), \tag{3.27}$$

where F^{low} and F^{high} are the low and high resolution fluxes respectively. The low resolution flux chosen in this instance was a Roe flux (see Roe (1981) for details) with upwinded variables as described by Equation 3.28.

$$F_{i+\frac{1}{2}} = \begin{pmatrix} \rho_1 u \\ \vdots \\ \rho_{Ns} u \\ \rho u^2 + p \\ \rho v u \\ \rho w u \\ (E+p)u \\ E_v u \end{pmatrix}_{\iota}, \text{where } \iota = \begin{cases} i & \text{if } M \geqslant 0, \\ i+1 & \text{if } M < 0. \end{cases} \tag{3.28}$$

The variable ϕ in Equation 3.27 defines the degree of smoothness (lack of oscillations) in the fluid. ϕ varies between zero and one, representing completely oscillatory and completely smooth respectively. Hence the full high resolution flux is used in regions of TVD, and the low resolution flux in highly oscillatory regions. ϕ itself is a function of the smoothness parameter r, which is defined as

$$r = \frac{Q_i - Q_{i-1}}{Q_{i+1} - Q_i}. \tag{3.29}$$

In order to ensure the TVD qualities of a flux limiting scheme, ϕ and r are subject to certain conditions:

1. $0 \leq r \leq 1$,
2. $\phi(1) = 1$,
3. $\phi \to 0$ as $r \to \mp\infty$,
4. $\frac{\phi(r)}{r} = \phi(\frac{1}{r})$,
5. $r \neq \mp\infty$ when $(Q_{i+1} - Q_i) = 0$.

Condition 1. ensures that the calculated flux remains bounded by the low and high resolution flux values. The second and third conditions ensure the correct TVD behavior at smooth and oscillatory locations respectively. Condition 4. mandates symmetrical behaviour, preventing discrepancies from occurring between opposing gradients. The final condition is a computational concern; care needs to be taken to ensure that infinities do not occur in regions with little to no difference between Q_{i+1} and Q_i.

Several schemes for determining ϕ are possible, each applying flux limitation in a slightly different manner. This manner can be illustrated through Sweby diagrams, which determine the TVD regions for a given scheme. Several of these schemes are briefly presented together with their Sweby diagrams. All of the presented schemes are implemented within OP2A; the schemes utilised for any results will be given with the results. All presented limiters are second order TVD.

Superbee

The superbee limiter calculates ϕ according to

$$\phi(r) = \max(0, \min(r, 2), \min(2r, 1)), \tag{3.30}$$

which leads to a limiter which tracks along the upper edge of the second order TVD region, as shown in Figure 3.2 (second order TVD region in grey).

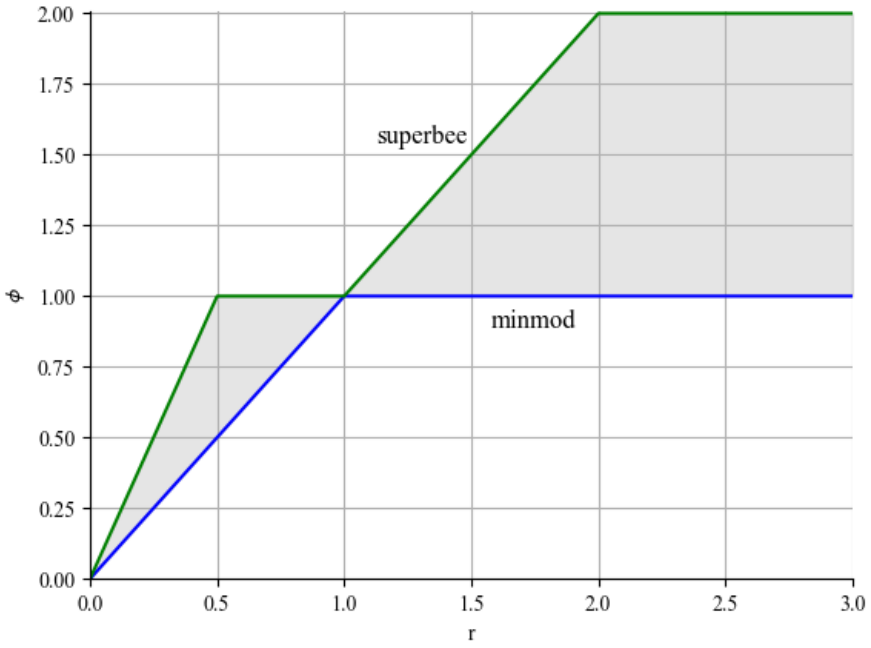

FIGURE 3.2: Sweby diagram illustrating limiter functions mapping to the second order TVD region (in grey).

minmod

The minmod limiter calculates ϕ as

$$\phi(r) = \max(0, \min(r, 1)), \tag{3.31}$$

leading to fluxes which follows the lower edge of the second order TVD region, as shown in Figure 3.2.

As Figure 3.2 shows, these limiter variants provide coverage of a wide range of TVD coverage and possess varying levels of efficiency according to their time complexity.

3.2.4 Boundary Conditions

With the AUSM scheme chosen as the basis for spatial integration, it is necessary to be able to calculate fluxes at the edge of the simulation domain. Such boundaries are controlled by ghost cells existing outside the simulation domain. These ghost cells are updated at the beginning of each iteration such that their contents describe various different boundary conditions (BC). Hence, OP2A implements Dirichlet boundary conditions at domain edges, as shown in Figure 3.3.

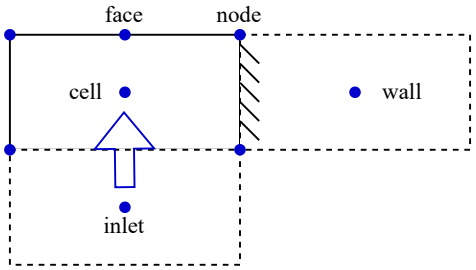

FIGURE 3.3: Example ghost cell generation at domain edges.

The exact contents of ghost cells depend upon the boundary being simulated.

Inlet

Ghost cells adjacent to inlet faces contain fixed inlet quantities which are prescribed at the beginning of the simulation. The primitive variables vector U for the contents of an inlet ghost cell is

$$U_g = \begin{pmatrix} \rho_1 \\ \vdots \\ \rho_{N_s} \\ u \\ v \\ w \\ T \\ T_v \\ p \end{pmatrix}_{inlet}, \tag{3.32}$$

where subscript g refers to the ghost cell. Such inlet ghost cell contents can be constant or varying in time, depending upon the requirements of a given simulation. OP2A currently supports exclusively constant inlets.

Outlet

Outlet ghost cells contain fluid quantities identical to those in their adjacent real cell.

$$U_g = U_{real} \tag{3.33}$$

Their values are updated at the beginning of each iteration.

Freestream

Freestream ghost cells behave in a similar manner to both inlet and outlet ghosts. When the flow direction at the face is into the ghost cell, they behave as outlet ghosts, mirroring the contents of their adjacent real cell:

$$U_g = U_{real}, \qquad \text{if flow is directed into ghost cell} \tag{3.34}$$

When the flow direction is out of the ghost cell, the ghost's contents are fixed to prescribed values in the same manner as inlet ghosts:

$$U_g = \begin{pmatrix} \rho_1 \\ \vdots \\ \rho_{N_s} \\ u \\ v \\ w \\ T \\ T_v \\ p \end{pmatrix}_{fs}, \qquad \text{if flow is directed out of ghost cell.} \tag{3.35}$$

Walls

Physical walls exist in several possible configurations and the exact contents of wall-adjacent ghost cells depends upon the wall type. Walls can be set to slip or no-slip

condition as well as being adiabatic or isothermal. For a slip adiabatic wall perpendicular to the x direction

$$\begin{aligned}
\rho_{1,g} &= \rho_{1,real} \\
&\vdots \\
\rho_{N_s,g} &= \rho_{N_s,real} \\
u_g &= -u_{real} \\
v_g &= v_{real} \\
w_g &= w_{real} \\
T_g &= T_{real} \\
T_{v,g} &= T_{v,real} \\
p_g &= p_{real}
\end{aligned} \tag{3.36}$$

The only change applied to the real cell quantities when copied to the ghost is the reversal of perpendicular velocity (and therefore momentum). This ensures that $u_{normal} = 0$ at the wall face. Whilst a slip adiabatic wall may be suited to inviscid simulation, viscous flow simulation requires the use of no-slip walls. The ghost cell quantities for a no-slip adiabatic wall are

$$\begin{aligned}
\rho_{1,g} &= \rho_{1,real} \\
&\vdots \\
\rho_{N_s,g} &= \rho_{N_s,real} \\
u_g &= -u_{real} \\
v_g &= -v_{real} \\
w_g &= -w_{real} \\
T_g &= T_{real} \\
T_{v,g} &= T_{v,real} \\
p_g &= p_{real}
\end{aligned} \tag{3.37}$$

Within Equation 3.37 all velocities are reversed between real and ghost cells. This ensures that all velocity components at the face equate to zero; fulfilling the no-slip condition. Finally, for cases where thermal conduction across surfaces is significant, such as re-entry flows, isothermal no-slip walls are required

$$\begin{aligned}
\rho_{1,g} &= \rho_{1,real} \\
&\vdots \\
\rho_{N_s,g} &= \rho_{N_s,real} \\
u_g &= -u_{real} \\
v_g &= -v_{real} \\
w_g &= -w_{real} \\
T_g &= 2T_w - T_{real} \\
T_{v,g} &= 2T_{v,w} - T_{v,real} \\
p_g &= p_{real}
\end{aligned} \tag{3.38}$$

where T_w is the wall temperature, which must be prescribed for any given simulation. This formulation is the same as for the adiabatic no-slip case excepting the temperature terms. These are set such that there exists a linear temperature gradient between real and ghost cells, across the wall. The ghost cell temperature is chosen relative to the real cell temperature, such that the temperature at the wall will be equal to the specified T_w.

Catalytic walls are not considered within the scope of this work, but would be accommodated with the addition of a further wall class object containing a species density term of the same form as the temperatures. Construction of such an additional class object is elaborated on in Chapter 4.

Axisymmetry

The 2D axisymmetric boundary is identical to the adiabatic slip wall boundary. However, there are some additional conditions which must be applied in the case of a 2D axisymmetric simulation. Firstly the finite volume formulation shown in Equation 3.1 must be recast as

$$y_c \frac{\partial Q}{\partial t} dV + y_f \left(F_{inv} - F_{vis}\right) dA + y_f \left(G_{inv} - G_{vis}\right) dA = y_c S dV + S_{axi} dV, \tag{3.39}$$

where y_c and y_f are the y positions of the cell and face centres respectively and S_{axi} is the axisymmetric source term. This axisymmetric source term is defined in common with the work of Nompelis (2004) as

$$S_{axi} = \begin{pmatrix} 0 \\ \vdots \\ 0 \\ 0 \\ p - 2\mu\frac{v}{y} + \frac{2}{3}\mu\nabla.\vec{u} \\ 0 \\ 0 \end{pmatrix}. \tag{3.40}$$

3.3 Temporal Integration Methods

OP2A currently features two separate time integration methods, which can be utilised independently of other simulation parameters.

Choice of time integration method is very significant for simulations. The most straightforward explicit time integration scheme is the Forward Euler method.

3.3.1 Forward Euler Method

The Forward Euler method can be considered to be the least computationally expensive method of integrating simulation quantities over a time step. This method consist of a simple linear extrapolation of the current data using fluxes and sources,

$$Q^{n+1} = Q^n + dt(\sum_f F^n + S^n), \tag{3.41}$$

where f represents faces adjacent to the cell, and Q, F and S are evaluated at time step n.

Such a scheme is conditionally stable based upon the CFL condition. Whilst this scheme will perform well for a range of simulation cases. Problems may occur in specific regions due to overshooting values. For example, considering a case where a low temperature fluid is losing temperature through a combination of fluxes and sources. In such a case, the time step may cause an overshoot into negative temperatures even if that time step obeys the CFL condition.

In order to mitigate this, more accurate estimates of fluxes and sources can be established through the use of multi-step methods.

3.3.2 Runge-Kutta 2 Method

The second order Runge-Kutta method (RK2) involves the use of multiple steps in evaluating a single time step. Fluxes and sources are calculated, and then a $\frac{1}{2}$ time step 'phantom' iteration is performed. New fluxes and sources are then calculated at this $n + \frac{1}{2}$ midpoint. The old and new fluxes are then averaged, and these averages are then used to evolve the original time step to $n \rightarrow n + 1$. Mathematically, this can be summarised as

$$\begin{aligned} Q^{n+1} &= Q^n + dt\frac{K_1+K2}{2}, \\ K_1 &= \sum_f F^n + S^n, \\ K_2 &= \sum_f F^{n+\frac{1}{2}} + S^{n+\frac{1}{2}}. \end{aligned} \tag{3.42}$$

Such a scheme requires more memory when implemented in order to store both sets of fluxes. However, in the case of OP2A, this memory will be re-utilised later as part of an error correction system described in Chapter 4.

Considering the case described at the end of section 3.3.1. The new calculated fluxes and sources allow the numerical iteration to better represent the underlying physics. Thus the probability of an overshoot into negative temperature is reduced.

As with the forward Euler method, the RK2 method is conditionally stable based upon the CFL condition.

3.4 Residuals Calculation

Within OP2A, residuals are calculated in the same manner as the CFD suite Fluent's density based solver. The residual of quantity ξ is

$$R(\xi) = \sqrt{\sum \left(\frac{\partial \xi}{\partial t} \right)^2}. \tag{3.43}$$

These residuals are normalised according to

$$R(\bar{\xi}) = \frac{R(\xi)}{R_5(\xi)}, \tag{3.44}$$

where $R_5(\xi)$ is the largest of the first 5 residuals of ξ.

3.5 Summary

A selection of numerical methods for the simulation of non-equilibrium plasma have been described. Finite volume methods were chosen, the forward Euler and RK2 time integration schemes described. Block-structured Cartesian meshes were chosen to facilitate rapid grid generation for the purposes of capsule optimisation simulations. The AUSM and AUSMDV spatial integration schemes were chosen due to their potential for the future extensibility of OP2A. These schemes have also been described in detail, as have various flux limiters methods. Boundary conditions and residual calculation methods have also been described to provide a complete outlook of the numerical methods chosen for OP2A. The following chapter details some of the practical aspects of the implementation of these methods.

4

OP2A Software Architecture and Implementation Aspects

"There are only 2 things wrong with C++: the initial concept and the implementation."

– Bertrand Meyer

As noted in Chapter 1, OP2A is designed to be a tool for conducting simulations for space capsule design optimisation. Hence, it is necessary that OP2A's implementation is capable of allowing various simulation methods to be used interchangeably. This required flexibility should be pared with extensibility; the ability to add new methods with minimal alterations required to the pre-existing source code. In addition, OP2A needs to be capable of performing the required computations efficiently in order to integrate the aforementioned multiphysics components within reasonable simulation time frames. The way in which these three requirements; flexibility, extensibility and efficiency are achieved will be explored within this chapter with specific reference to capsule optimisation simulations. To begin, an outline of the overall OP2A algorithm is presented in order to provide context and a reference point for additional explanations. These additional explanations begin with details of the class objects created and their interactions, followed by parallelisation aspects and concluded with memory management details. The choices made to satisfy the three requirements of efficiency, flexibility and extensibility will be highlighted throughout.

4.1 Algorithm Overview

OP2A is written entirely in object oriented C++. OP2A's overall algorithm contains two main subroutines as described by Figure 4.1. OP2A's operation begins with the initialisation of global variables regarding version information and simulation nomenclature. This is followed by the preprocessing and processing algorithms respectively, these are both large enough to require detailed examination. Finally, the overall algorithm concludes with final simulation outputting and memory cleanup.

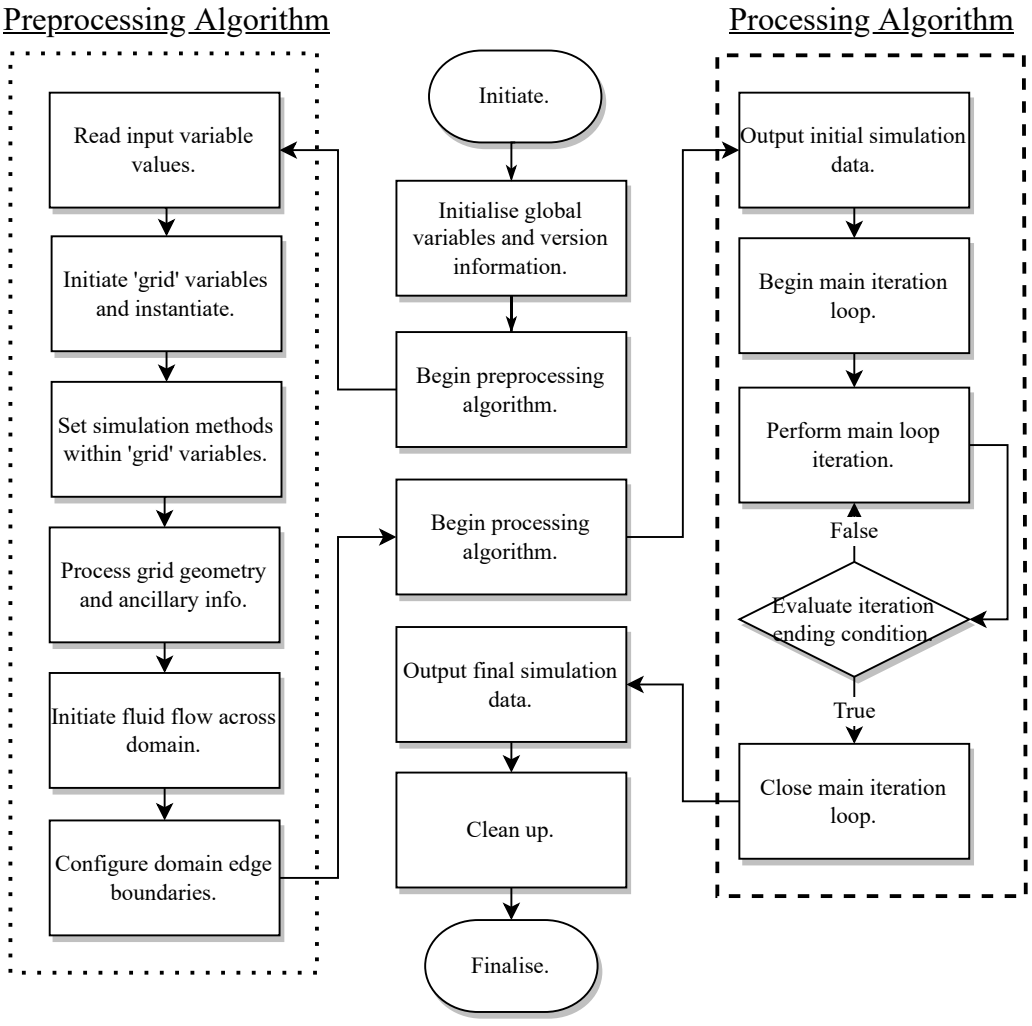

FIGURE 4.1: An overview of the entire OP2A procedure.

Whilst many of these steps are self-explanatory and are not in need of further elaboration, the contents of the preprocessing and processing algorithms are highly significant.

4.1.1 Preprocessing

The preprocessing algorithm consists of a number of distinct stages, as outlined in Figure 4.2. These stages include; input parameter reading, grid and fluid initialisation, methods initialisation, and sanity checking.

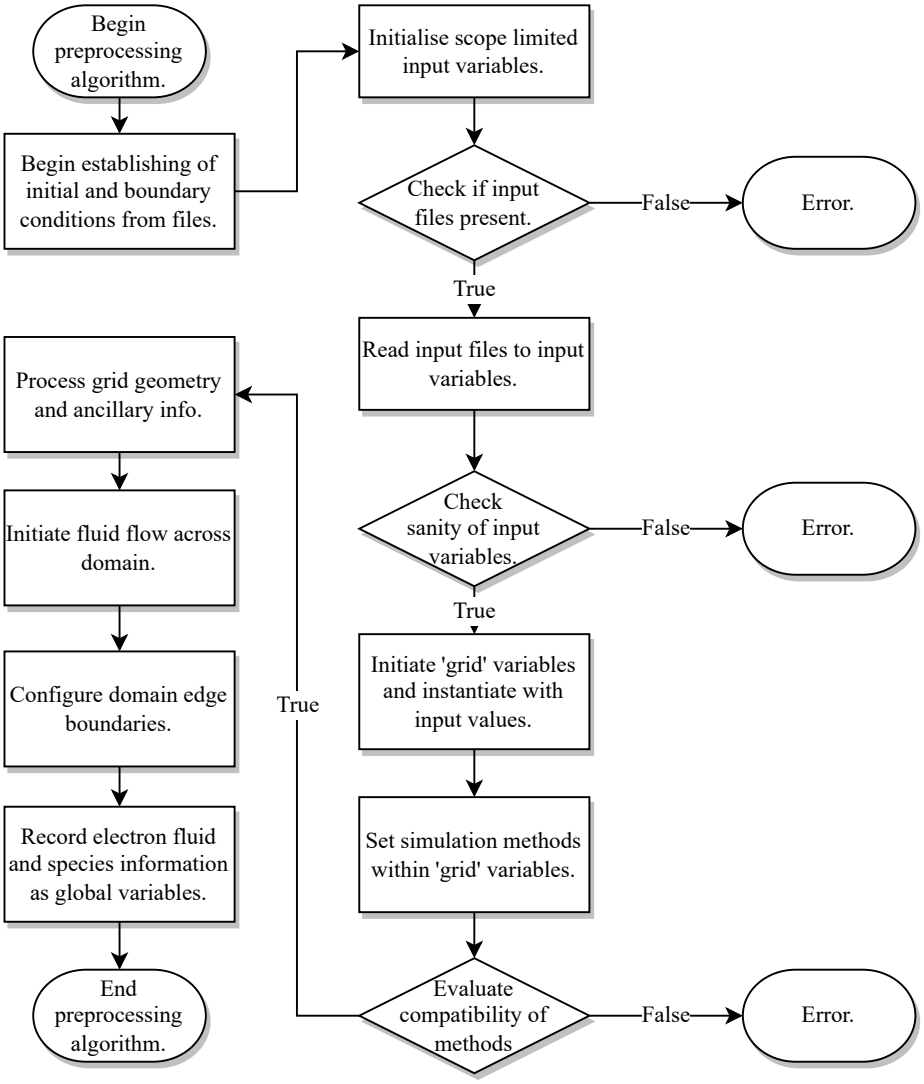

FIGURE 4.2: An overview of the preprocessing algorithm.

Input parameter reading is straightforward, consisting of reading input parameters from plain text files and/or Tecplot formatted files. Subsequent steps are less straightforward, these input parameters are then used for the initialisation of the simulation grid and methods. This is done at runtime using overriding polymorphism to provide the necessary flexibility and extensibility to OP2A.

Overriding Polymorphism for Runtime Parameter and Method Selection

Overriding polymorphism is a practice in object oriented programming (OOP) which allows simulation objects to have their type determined dynamically at runtime. Such practice is commonly used among modern CFD suites. This is implemented by declaring a pointer to a base class at compile time, then assigning this pointer to a derived class object. An example of such an implementation in OP2A is shown in Listing 4.1.

```
// global.hpp
// Variable declaration at compile time.

    class GlobalMethods
    {
        ⋮
        time_integration *TimeIntBase;
        ⋮
    }

// global.cpp
// Variable instantiation at runtime.
    void set_methods()
    {
        switch(int time_integration_method)
        {
            case 0:
                time_integration = new TimeIntEuler();

            case 1:
                time_integration = new TimeIntRK2();
        }
    }
```

LISTING 4.1: Example of overriding polymorphism implementation within OP2A.

The effect of this is that the simulation software does not need to be interrupted, modified or recompiled in order to use different simulation methods. OP2A is fully flexible with regards to all of the methods outlined in Chapters 2 and 3. This allows for simulation models and methods to be switched instantaneously when required by alterations made to capsule geometry, satisfying one of OP2A's key requirements. Whilst the use of OOP is by no means unique to OP2A, this is the first attempt to explicitly exploit this technique to the end of improving capsule optimisation simulations. The variables shown in Listing 4.1 are dynamically allocated, however this is not true for all variables within an OP2A simulation. The memory allocation methods used is dependent upon the nature of the variable.

Memory Management

Within OP2A both static and dynamic memory allocation are utilised according to requirements. Within C++ static memory is scope limited whilst dynamic memory must be explicitly deallocated. As shown in Listing 4.2, input parameter storage utilises static memory allocation whilst grid storage utilises dynamic.

```
// problem_numerical_method.hpp
// Static memory allocation examples.

    class ProblemNumericalMethod
    {
        ⋮
        int max_terations;
        double max_CFL;
        ⋮
    }

// global.hpp
// Dynamic memory allocation examples.
    class GridGlobalInfo
    {
        ⋮
        int *max_iterations = new int(-1);
        double max_CFL = new double(-1.0);
        ⋮
    }

// Passing of values from statically allocated variables to
// their dynamically allocated equivalents.
    void GridGlobalInfo::read()
    {
        *max_iterations = problem_numerical_method.max_iterations;
        *max_CFL = problem_numerical_method.max_CFL;
    }
```

LISTING 4.2: Examples of static and dynamic memory allocation within OP2A.

As Listing 4.2 shows, input parameters are initially read to statically allocated memory. These values are then passed to dynamically allocated equivalents assuming that they are required beyond the preprocessing stage.

Assigning grid variables dynamically allows for the large amount of memory needed for the grid to be stored on the heap, freeing the more efficient stack memory to be utilised by function specific variables and global commonly used variables. This use of dynamic memory allocation also allows for greater contiguity of vectorised data. This in turn means an small increase in processing and iteration speed, especially for vectorised operations. In addition, any caching required will be accelerated by a small amount. These improvements collectively contribute to improving OP2A's computational efficiency, helping to satisfy the efficiency requirement outlined in Chapter 1.

As the problem input variables are statically allocated, their memory is automatically freed upon the completion of the preprocessing algorithm. This memory can then be reutilised for temporary variables in the course of the execution of simulation methods. These methods are executed within the processing subroutine.

4.1.2 Processing

The processing subroutine's algorithm contains all the necessary steps for the execution of the methods described in Chapters 2 & 3. A schematic overview of the processing stage is presented in Figure 4.3.

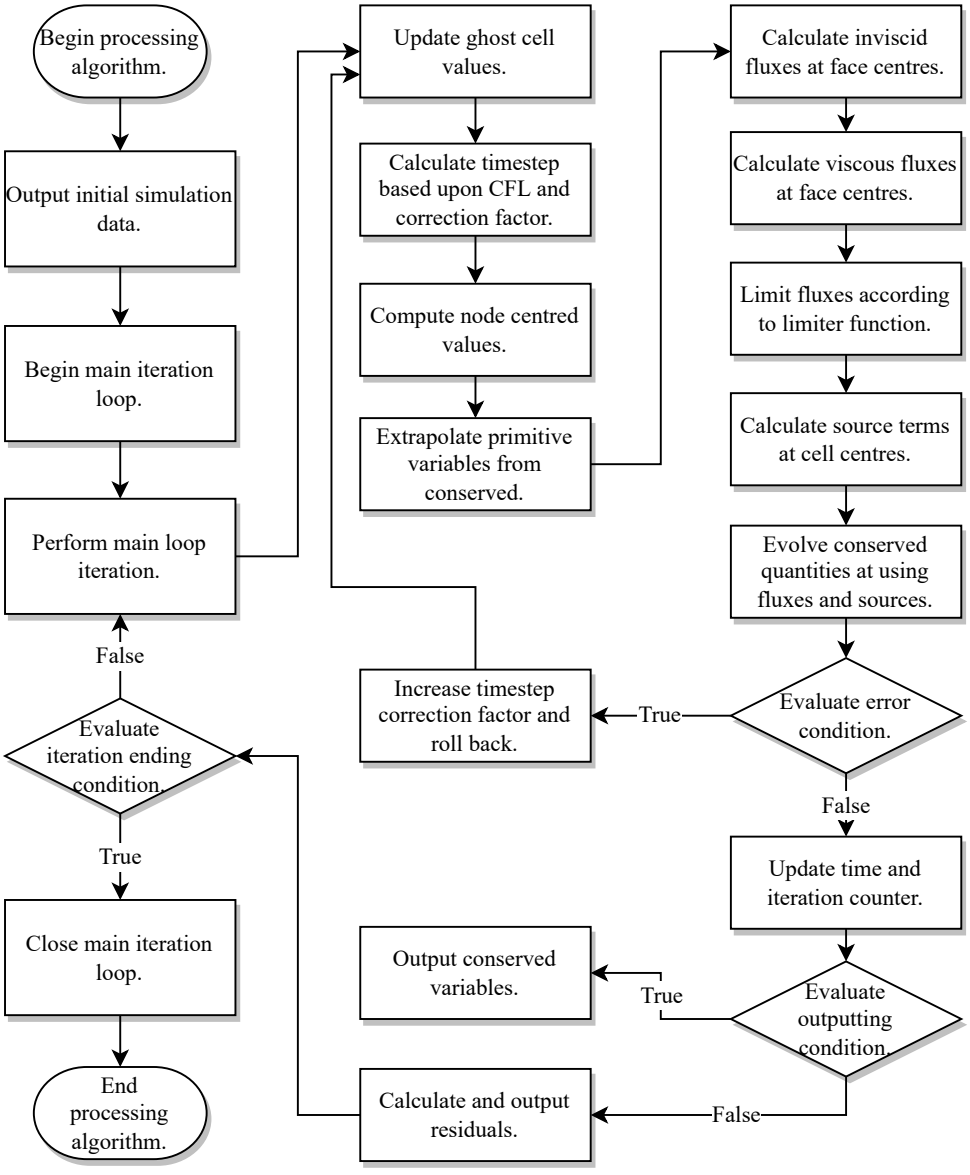

FIGURE 4.3: An overview of the processing algorithm.

As can be seen in Figure 4.3 most steps of the algorithm represents the execution of a particular method heretofore discussed. These methods can by dynamically chosen at runtime using overriding polymorphism as previously outlined. Each of these methods has a class object associated with it, and these objects interact with the main grid storage object throughout execution. Each method is contained within its own C++ class object so as to enhance the flexibility and extensibility of OP2A. Whilst such structuring is not unique to OP2A, its inclusion contributes to the creation of a space capsule optimisation toolkit by providing the required flexibility of simulation methods. Such structuring also provides benefits to the maintainability, and hence extensibility of the codebase.

4.2 Key Object Classes and their Interactions

The key classes within OP2A's processing stage are divided according to whether they contain data pertinent to the entire simulation domain, or only a subset of the domain. These classes are **GridGlobal** and **GridLocal** respectively and are related to the containing **Grid** class by a 1:1 composition relationship as shown in Figure 4.4.

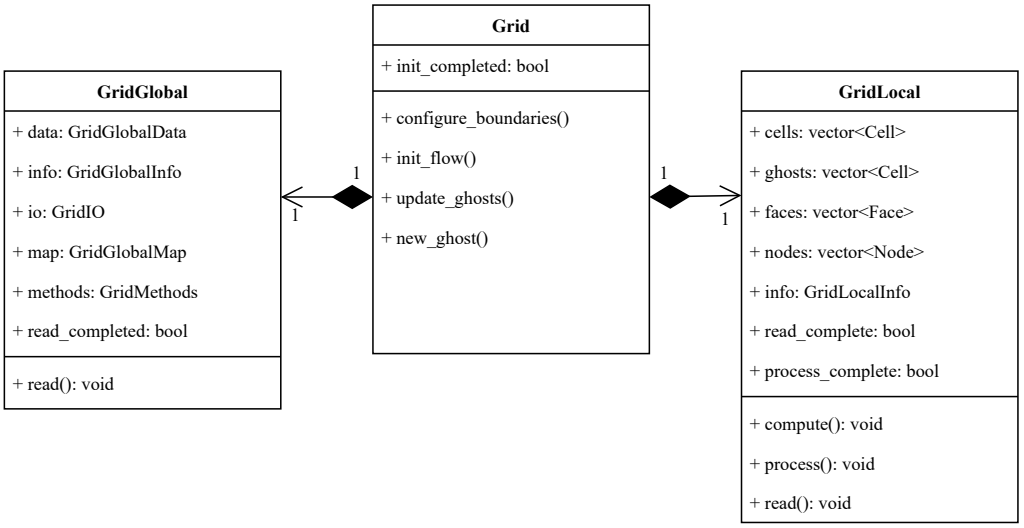

FIGURE 4.4: An overview of the structure and contents of the **Grid** class.

4.2.1 GridLocal

The **GridLocal** class is predominantly a data storage class, it contains all information unique to specific regions of the simulation domain. This includes the simulation quantity values at cells, faces and nodes, as well as local grid information pertinent to distributed memory parallelisation. Most relationships are again 1:1 compositions within the **GridLocal** class as shown in Figure 4.5.

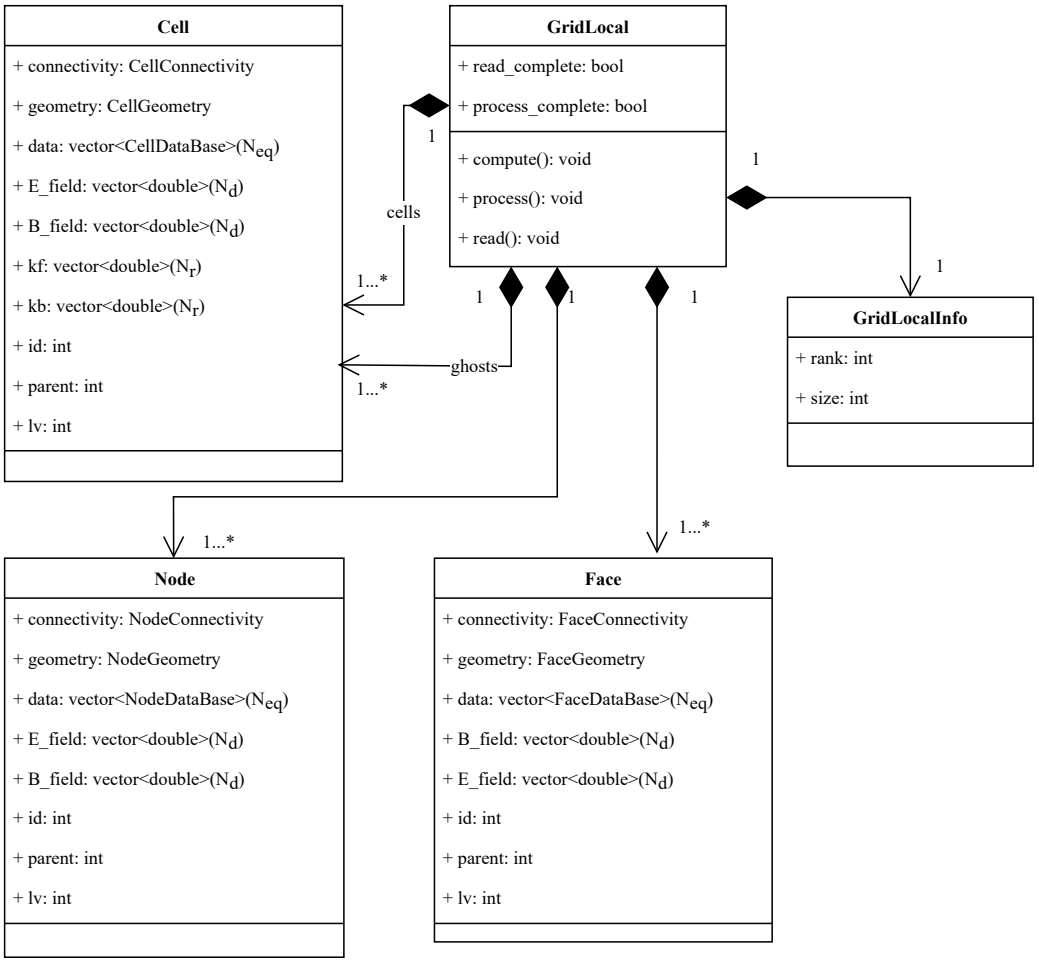

FIGURE 4.5: An overview of the contents and structure of the **GridLocal** class.

As shown in Figure 4.5, the single **GridLocal** object contains many **Face** and **Node** objects, and two sets of **Cell** objects. OP2A treats real and ghost cells identically within the processing algorithm, allowing for less unnecessary duplication of code. Each of the four other objects in Figure 4.5 are worth examining in detail.

GridLocalInfo

The **GridLocalInfo** class contains any grid information unique to a particular computational node. This class is forward looking to the implementation of distributed memory parallelisation and hence includes various data for use in grid distribution algorithms.

The **GridLocalInfo** class within the **GridLocal** class is closely analogous to its counterpart within the **GridGlobal** class.

Cell

The **Cell** class is predominantly a container for simulation quantities at cell centres, as described by Figure 4.6.

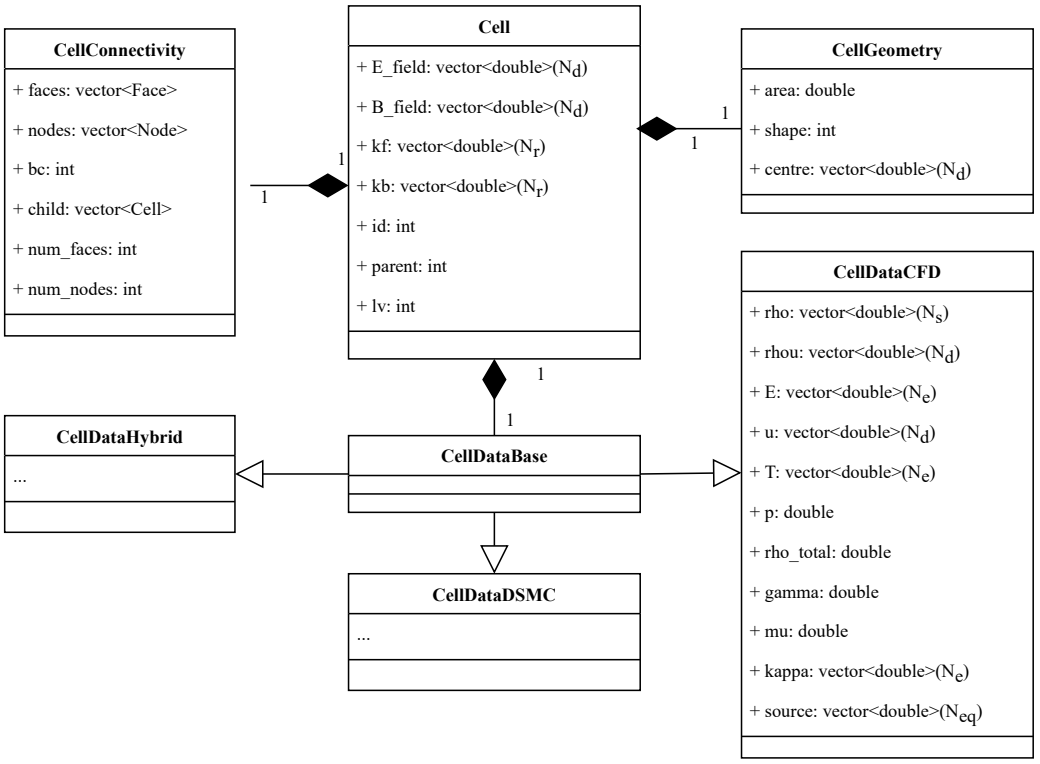

FIGURE 4.6: An overview of the contents and structure of a **Cell** class object.

As indicated by Equation 3.3, **Cell** objects contain not only the conserved and primitive CFD quantities at time t, but also the numerical sources needed to calculate the quantities at time $t + dt$. These data values are stored within C++ vector containers with memory automatically allocated. This allows OP2A to take advantage of compiler memory optimisations upon these values, improving OP2A's computational efficiency.

The ghost cells described in Chapter 3 exist as special instances of the **Cell** class. These objects are cleared of unnecessary data to save memory space. Whilst they are objects of the same class type, they are stored separately from 'real' cells, as shown in Figure 4.5. Functions which accept **Cell** class objects can accept both real and ghost cell instances, reducing code duplication. In addition, newly implemented simulation methods do not require distinction between cell types, enhancing the extensibility of OP2A. **Cell** objects, as well as **Face** and **Node** objects, are capable of containing data for DSMC and hybrid simulations, as well as the default CFD data. This facility is another addition to facilitate future extensibility, however it will not be explored further as the data presented herein is exclusively produced from CFD simulations.

Face

The **Face** class is structured similarly to the **Cell** class, but containing flux and gradient data rather than source data. Its overall structure and contents are otherwise similar to that of the **Cell** class. As with the data contained within **Cell** objects, the flux data is stored with automatic memory allocation.

Node

Similar to both the **Cell** and **Face** classes, the **Node** class is a container for a small amount of simulation data required for the calculation of certain gradients within viscous flux calculations. These contents are then utilised for calculating fluxes face centres parallel to face orientation.

The choice of shape function used to interpolate data at the nodes from cell centred values can be determined independently and is stored as a method object within the **GridGlobal** class.

4.2.2 GridGlobal

The **GridGlobal** class contains all of the information which is constant across the entire simulation domain. This includes chemical and collisional coefficients, global grid information and simulation methods as shown in the class diagram in Figure 4.7.

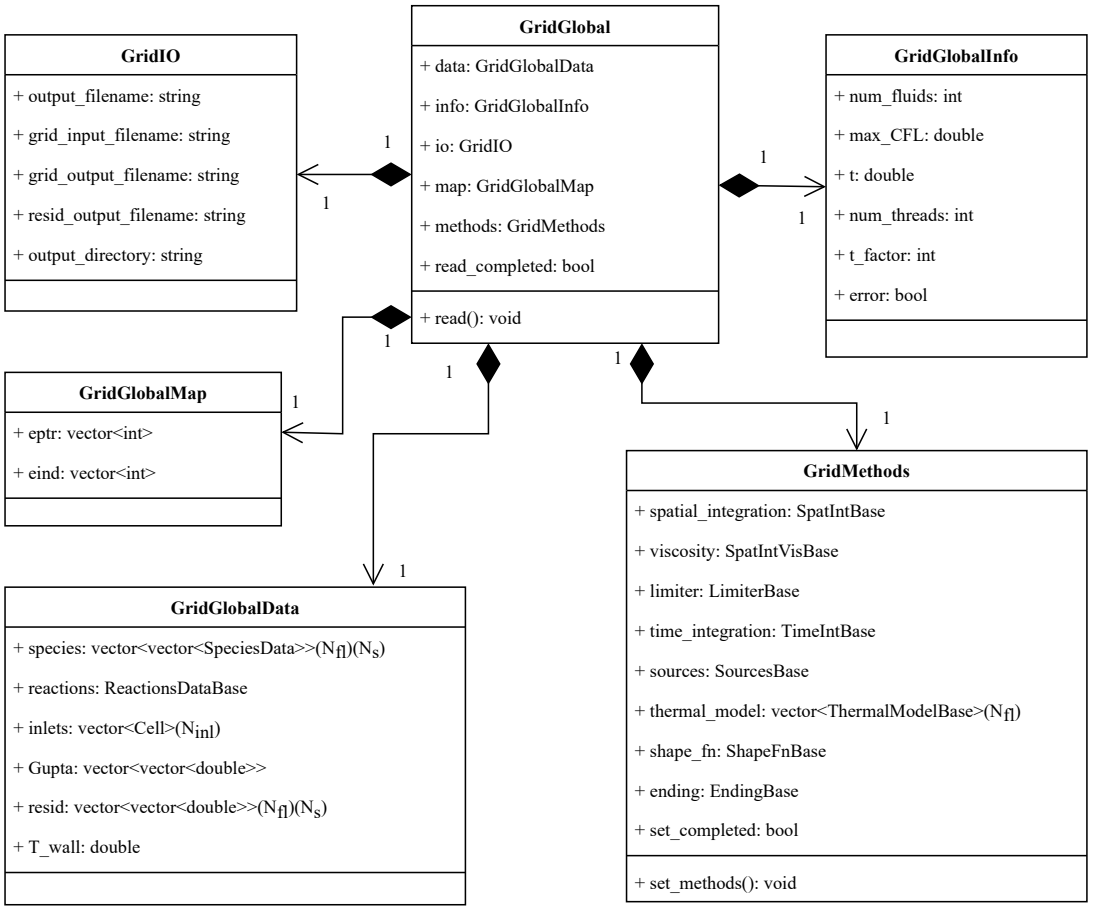

FIGURE 4.7: An overview of the structure and contents of the **GridGlobal** class.

Within **GridGlobal** there are three primary sub-classes; **GridGlobalData** containing chemical and collisional data, **GridGlobalInfo** containing global grid information, and **GridMethods** containing implementations of simulation methods. The contents and features of these three sub-classes shown in Figure 4.7 are worthy of further inspection.

GridGlobalInfo

The **GridGlobalInfo** sub-class contains any global information outside the scope of the physical and chemical information contained within the data sub-class. This includes information governing simulation time steps, parallelisation info and error handling variables. The information contained within this sub-class is purely data, and the class possesses no methods of its own.

GridGlobalData

The **GridGlobalData** sub-class contains chemical coefficients, several sets of curve fitting parameters and any other empirical physical data required for the diffusive and

chemical calculations outlined in Chapter 2. Values of the physical data used in this work are provided in appendices A & B. The data stored within this class is stored in C++ vector containers. These containers have been used throughout OP2A for their maturity and efficiency when accessed via index; accessing global data via index is the most efficient method of data access when utilising structured grids.

The contents of the **GridGlobalData** class is run-time modifiable with the modification of plain text files containing the relevant data. Such modifications extend to the addition of new chemical mixtures, species information, reaction data and collisional data. All of these can be modified and extended without requiring any source code modifications or recompilation of OP2A. This flexibility allows for simulations to have their data updated seamless mid-simulation in line with the requirements set out in Chapter 1.

GridMethods

The most significant sub-class within the **GridGlobal** class is the **GridMethods** class. This class is key in facilitating the flexibility requirement of OP2A; it contains sub-classes pertaining to each of the modular simulation components described within Chapters 2 & 3. These contents and their interactions are described by Figure 4.8.

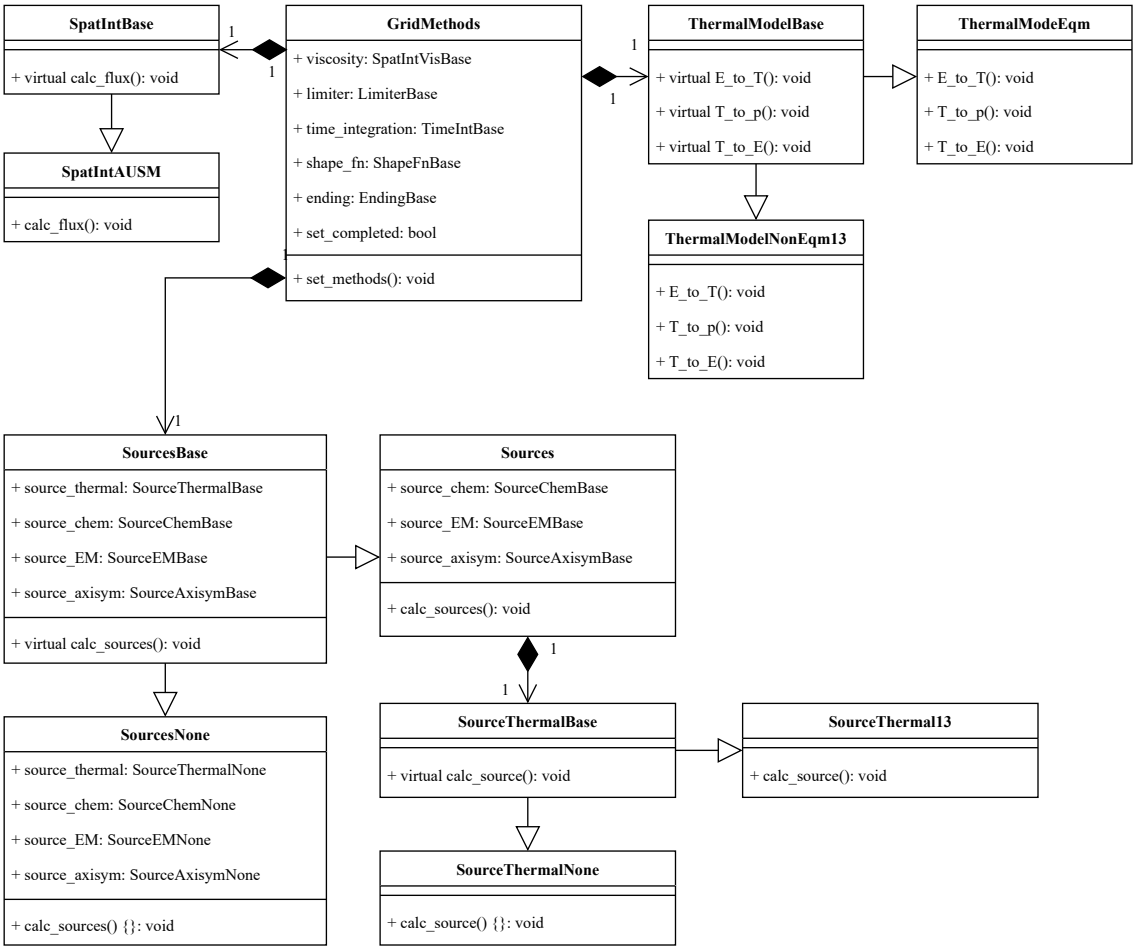

FIGURE 4.8: An overview of the structure and contents of the **GridMethods** class.

Figure 4.8 shows the existence of base and derived classes for each method. As seen in Figure 4.8, some classes possess multiple levels of nested derived class objects. One example of this is the method for evaluating source terms.

The source term base class **SourcesBase** features two derived class objects, chosen depending upon whether any source terms are required. The **Sources** class contains four sub classes, one for each potential source term. These four sub-classes consist of base and derived classes as with the containing source class. This formulation allows various physical sources to be independently configured, again facilitating flexibility. Additionally, new sources can be added straightforwardly by simply utilising the existing source term formats, thereby maximising extensibility. The uniformity of source term methods also extends to other methods' implementations. This allows new thermochemical models to be implemented similarly swiftly.

In line with the **GridGlobalData** class, the methods contained within **GridMethods** can be switched mid-simulation, further meeting the requirements set out in Chapter 1. All of the discussed methods are parallelised over shared memory systems, as are the contents of the processing algorithm.

4.3 Parallelisation Techniques

OP2A is equipped to parallelise the simulation mesh through a hybrid of both shared and distributed memory parallelisation. Shared memory parallelisation has been implemented throughout the entire processing stage using OpenMP. This parallelisation presently splits the grid's spatial domain between processing threads. OpenMP was chosen to be implemented prior to distributed parallelisation with MPI for purely practical reasons. Firstly performance considerations; the simulations required of OP2A were capable of being performed upon singular nodes, for which OpenMP parallelisation was judged to be optimal. Secondly scripting considerations; OpenMP parallelisation can be implemented in a modular fashion, this can then be straightforwardly wrapped within an MPI framework at a later point with little modification of the pre-existing OpenMP script. Contrarily, were MPI to be implemented first, this MPI script would need significant modification upon the addition of OpenMP.

An investigation of the speedup achieved through this parallelisation has been performed by utilising a simple 2D shock tube case, and comparing performance as a result of varying the number of cores used.

Parallelisation Efficiency

The shock tube case presented in Chapter 5 was simulated with a resolution of 1000 cells in the x direction. This simulation was performed with a variety of different numbers of computational cores in order to assess the efficiency of OP2A's shared memory parallelisation scheme.

OP2A currently features OpenMP parallelisation, with the grid domain being split across multiple cores. This parallelisation scheme can at best achieve linear performance increases with an increasing number of cores. The results of this assessment can be seen in Figure 4.9.

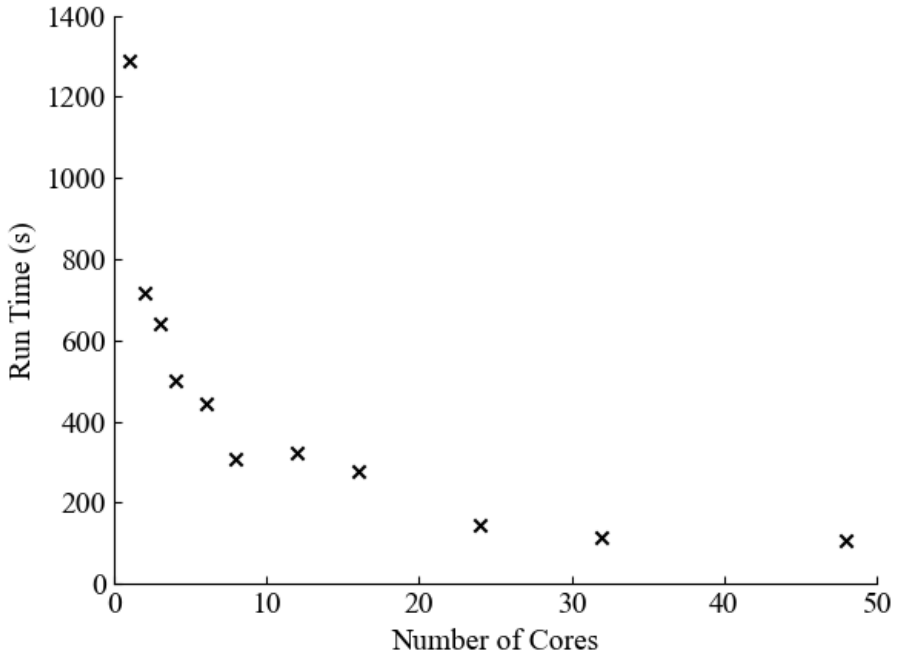

FIGURE 4.9: Decrease of run time with increasing number of compute cores for the shock tube case.

The performance scaling shown in Figure 4.9 is quite close to its optimal capability, with a decrease of close to 50% in run time for a doubling of core number. This can be seen more clearly in a semi-log plot, as shown in Figure 4.10 which shows a near linear decrease outside the extreme values of core number.

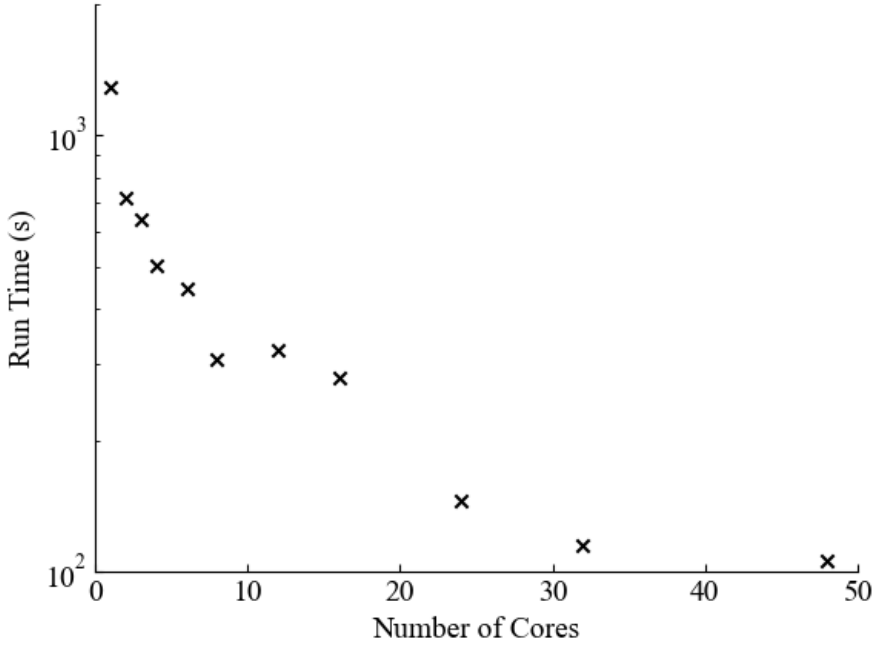

FIGURE 4.10: Decrease of run time with increasing number of compute cores for the shock tube case shown on a semi-log scale.

This indicates that the OpenMP implementation carries little overhead cost, and these costs are certain to be negligible when compared to the overall computational load of a typical capsule re-entry simulation.

4.4 Stability & Error Handling

In order to ensure accuracy of results when simulation components are altered, it is necessary for OP2A to contain systems to monitor for spurious deviations and thus ensure consistency and stability. The error handling system in OP2A features such routines, as well as allowing for a simulation roll-back should catastrophic events occur.

Error Checking, Correction & Recovery System

A problem common to hypersonic CFD simulations is the occurrence of negative temperatures and/or densities. These often occur in wake regions, as well as in the presence of complex geometric features and can be exacerbated by fluid chemistry. In order to avoid a dreaded simulation failure, some method must be used in order to either prevent or mitigate these occurrences.

Within OP2A a system is of time step modification is utilised. When a disallowed negative value occurs, OP2A rolls back to the previous iteration and reduces the size of the time step by a factor of 10. OP2A then performs 30 iterations at this reduced time step before attempting to increase the time step back to its original size. This system can be performed repeatedly and recursively, with a possible maximum reduction factor of up to 10^{10}. All of the numerical parameters associated with this system are fully customisable. Hence, OP2A achieves improved stability through adaptive time step control.

The memory utilisation to allow this iteration reversal to be performed is similar to that utilised by the multi-step time integration methods. OP2A essentially contains two copies of the conserved CFD quantities, one for the current, and one for the prior iteration. This allows the iteration reversal to be performed with no loss of accuracy and minimal additional computation required.

This system is also utilised in overcoming extreme value errors, including infinities and divide by zero errors which can occur due to the inherent limits of machine representations of continuous values.

4.5 Summary

Details have been provided regarding OP2A's computational aspects. OP2A satisfies several of the requirements set out in Chapter 1 through computational means. Overriding polymorphism is used in conjunction with a modular object oriented structure to provide OP2A with its required flexibility. Stability is provided with a system of time step modification to ensure consistency when simulation aspects are altered. OP2A's computational efficiency is facilitated in a number of ways, including through memory management, but predominantly through its parallelisation scheme which is unique among its open-source counterparts. An assessment of this parallelisation scheme's efficiency has been presented, and said efficiency found to be high. These details conclude the overview of OP2A's models, methods and their implementations. With these components, a number of simulations were performed to evaluate OP2A's numerical and mathematical accuracy.

5

Results

"...in real life mistakes are likely to be irrevocable. Computer simulation, however, makes it economically practical to make mistakes on purpose. If you are astute, therefore, you can learn much more than they cost."

– John H. Mcleod

This chapter details the methodology and results of a number of investigations performed using OP2A. Theses investigations demonstrate the capabilities of OP2A with regards to capsule optimisation simulations; including thermochemical modelling in addition to viscous, hypersonic Navier-Stokes simulation. Each investigation is described in detail with the aim of providing reproducibility, before results are presented and discussed. Finally, the capabilities of OP2A are discussed with reference to all of the investigations presented.

5.1 Zero Dimensional Analyses

In order to demonstrate the capacity of OP2A to simulate thermochemical non-equilibrium conditions a series of zero dimensional analyses were performed. These heat bath simulations consist of a single grid cell containing gas in thermal and/or chemical non-equilibrium. These heat baths were simulated using the Euler time integration method, the cell was surrounded by adiabatic walls with no heat transfer.

5.1.1 Thermal Non-Equilibrium Analysis

In order to demonstrate the accuracy of OP2A's thermal non-equilibrium modelling, a two-temperature nitrogen (N_2) heat bath was simulated with a variety of initial temperatures. These heat baths were simulated with frozen chemistry, and no external

temperature sources. The progress of each heat bath is then shown with a plot of showing the progression of temperatures over time.

These thermal heat baths were simulated within a range of temperatures relevant to hypersonic flow simulations. The first simulated heat bath contained N_2 gas with a high translational temperature and low vibrational temperature, mirroring the initial conditions presented by Casseau et al. (2016b) in order to facilitate comparisons with existing works. These initial conditions are summarised in Table 5.1.

TABLE 5.1: Initial conditions for N_2 thermal non-equilibrium heat bath simulation at a high translational temperature with frozen chemistry.

Variable	**Initial Value**
ρ_{N_2} (kgm^{-3})	34.1×10^{-3}
T_t (K)	10,000
T_v (K)	1,000
p (Pa)	101,269

This heat bath was allowed to equilibrate over the course of 10^{-4} s with a time step size of 10^{-11} s. The results of this equilibration are presented overlaid atop the results of Casseau et al. (2016b) in Figure 5.1 and shows equilibration occurring between 10^{-6} and 10^{-5} s.

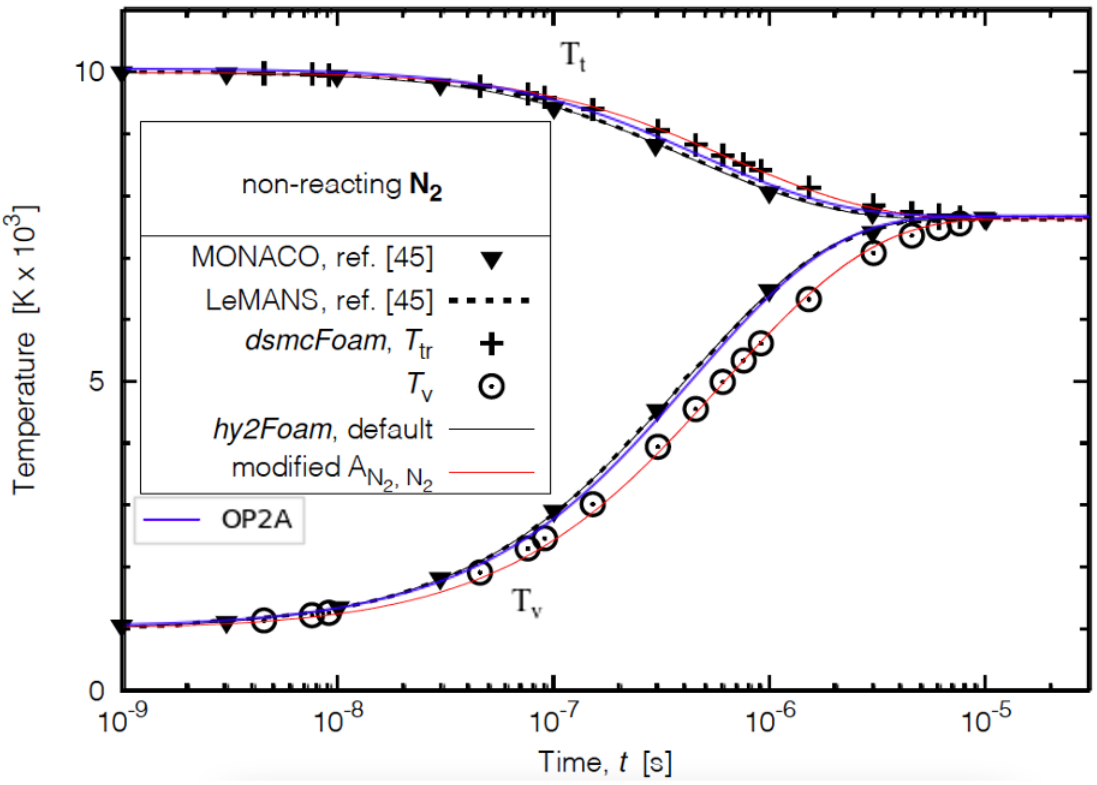

FIGURE 5.1: Evolution of temperatures in a N_2 thermal non-equilibrium heat bath with a high translational temperature with frozen chemistry. Results are shown as presented by Casseau et al. (2016b) including the results produced by hy2foam, as well as those of LeMANS, with OP2A's results overlaid.

5.1 shows strong agreement with results presented by Casseau et al. (2016b), which were performed with both LeMANS and hy2foam as well as the DSMC suite MONACO. These code suites utilise the same thermal model as OP2A, hence the good agreement shown here is both desired and expected.

The overall shape of the equilibration curves matches closely to those presented by Casseau et al. (2016b), both qualitatively and quantitatively; with the resulting equilibrium temperature being close to the translational temperature as expected. The two key quantitative markers to estimate are the equilibration time and temperature. Casseau et al. (2016b) reports an equilibration temperature of 7623 K, whilst OP2A results in an equilibration temperature of 7616 K. This value is well within expected deviation levels based upon the known accuracy of the initial conditions of Casseau et al. (2016b).

The equilibration time t_{eq} of OP2A is around 1×10^{-5} s. This equilibration time is defined as the time taken for the translational and vibrational temperatures to match to within 1 K. This time is not explicitly presented by Casseau et al. (2016b), but can be estimated from the presented plots to be of the order of 1×10^{-5} s. Hence a reasonable 'order of magnitude' alignment is shown for equilibration time when comparing between OP2A and LeMANS and hy2foam.

This thermal heat bath simulation was then repeated with a high vibrational temperature and low translational temperature, with values again chosen for comparison with LeMANS via Casseau et al. (2016b). These new values are shown in Table 5.2 and the results for this high T_v heat bath are presented in Figure 5.2, once again overlaid upon the results of Casseau et al. (2016b).

TABLE 5.2: Initial conditions for N_2 thermal non-equilibrium heat bath simulated at a high vibrational temperature with frozen chemistry.

Variable	Initial Value
ρ_{N_2} (kgm^{-3})	113×10^{-3}
T_t (K)	3,000
T_v (K)	10,000
p (Pa)	101,239

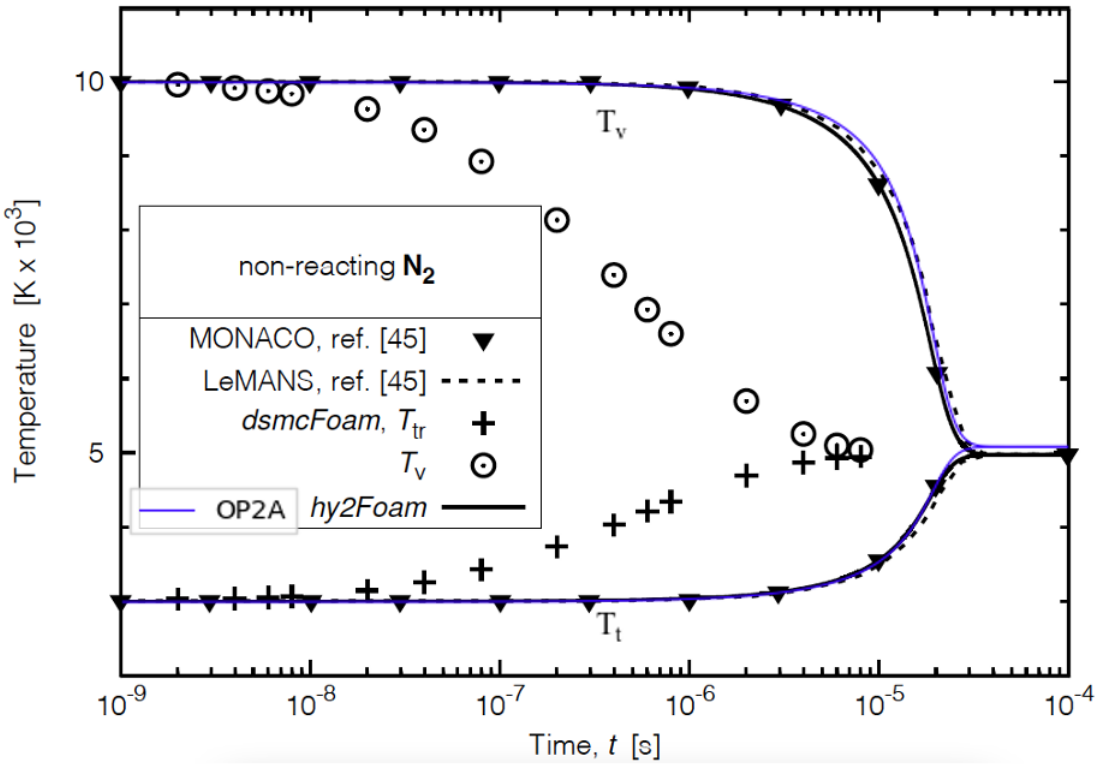

FIGURE 5.2: Evolution of temperatures over time in a N_2 thermal non-equilibrium heat bath with a high vibrational temperature with frozen chemistry. Results are shown as presented by Casseau et al. (2016b) including the results produced by hy2foam, as well as those of LeMANS, with OP2A's results overlaid.

The overall shape of the temperature curves of Figure 5.2 again show good qualitative alignment with the equivalent results presented by Casseau et al. (2016b). The quantitative values also show good agreement. The equilibrium temperature arrived at by OP2A is 5089 K with an equilibrium time of 4.4×10^{-5} s. The corresponding values

found by LeMANS and hy2foam are not explicitly stated, but can be estimated to be; an equilibrium temperature of around 5000 K and an equilibrium time of the order of 1×10^{-5} s. Both of these values can be inferred from presented plots with a reasonable degree of accuracy for the purposes of this comparison. Again, reasonable qualitative and quantitative agreement is found between OP2A and LeMANS and hy2foam for the high T_v thermal heat bath. However, larger differences in final equilibrium temperature are shown in Figure 5.2 than in the previous results (Figure 5.1). These differences are well within expectations given the slight methodological differences; in particular the slightly simplified energy transfer equation used by Casseau et al. (2016b) which excludes some or the terms modelled by OP2A.

These analyses have provided an assessment of thermal modelling accuracy for simple frozen chemistry heat bath cases. This can be expanded by performing analyses with non-frozen chemistry.

5.1.2 Chemical Non-Equilibrium Analysis

To demonstrate the effectiveness of OP2A's chemical modelling, atmospheric heat baths were advanced in time, similar to their thermal counterparts but with non-frozen chemistry. To begin with, a 5 species air mixture was equilibrated in time, and the results compared once again to those presented by Casseau et al. (2016b).

5 Species Air Mixture - Multi-Temperature

The species and chemical reactions present in the 5 species air mixture (henceforth referred to as the air-5 mixture) are as presented in Chapter 2.

The air-5 mixture was simulated in a heat bath at 10,000 K in thermal equilibrium and the mixtures chemical composition monitored over time. The initial conditions are summarised in Table 5.3.

TABLE 5.3: Initial conditions for an air-5 thermal equilibrium heat bath simulated with non-frozen chemistry.

Variable	Initial Value
ρ_{N_2} (kgm^{-3})	1.7×10^{-3}
ρ_{O_2} (kgm^{-3})	0.52×10^{-3}
ρ_{NO} (kgm^{-3})	3.0×10^{-7}
ρ_{N} (kgm^{-3})	1.4×10^{-7}
ρ_{O} (kgm^{-3})	6.8×10^{-6}
T_t (K)	10,000
p (Pa)	6,438

This heat bath was advanced from $t = 0$ x until $t = 1 \times 10^{-3}$ s with time steps of $dt = 1 \times 10^{-11}$ s. The results of this advancing are shown in Figure 5.3, with species number densities presented over time. These number densities are normalised by the initial total number density of the mixture and overlaid upon the results presented by Casseau et al. (2016b).

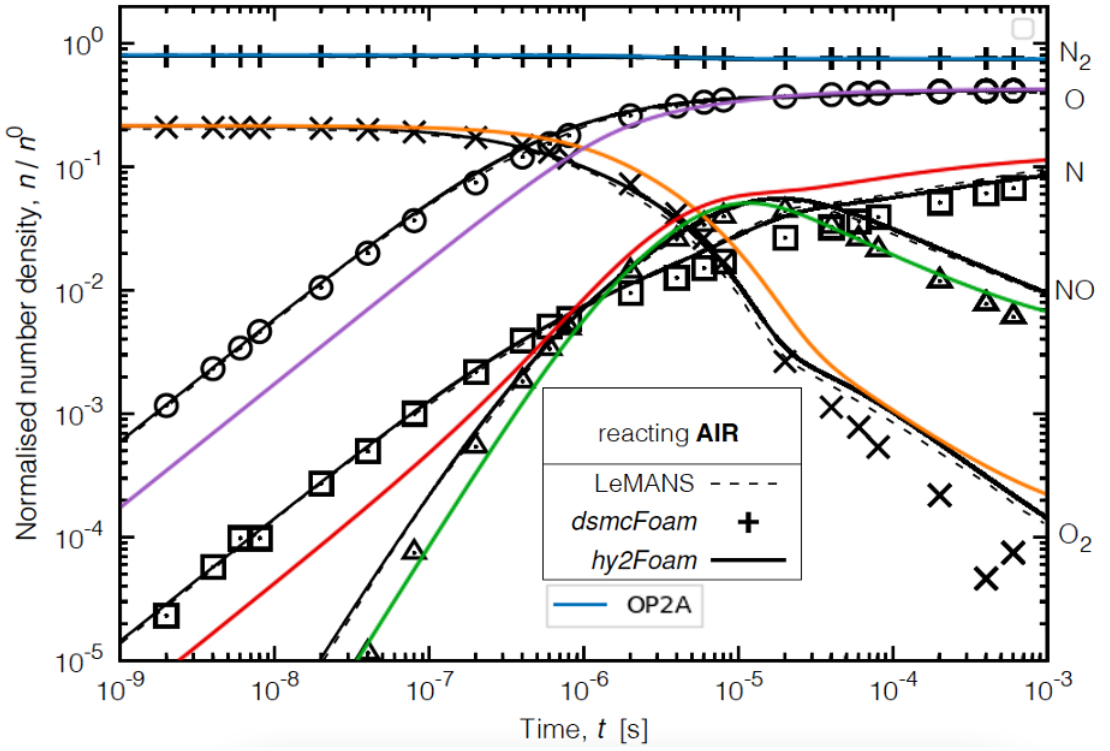

FIGURE 5.3: Evolution of normalised species number densities when relaxed in an air-5 heat bath at thermal equilibrium with $T = 10,000$ K. OP2A's results are overlaid upon those presented by Casseau et al. (2016b).

The OP2A results presented in Figure 5.3 can be compared with those presented by Casseau et al. (2016b), however in this case a caveat is needed. The results presented by Casseau et al. (2016b) utilise a slightly different set of numerical values for the chemical source calculations than those utilised by OP2A, hence an exact quantitative match is not to be expected in all areas. In addition, initial species concentrations may differ due to ambiguities in those used by Casseau et al. (2016b). Instead these results can be qualitatively compared, and assessed in terms of the behaviour of each chemical species; additionally a quantitative comparison of final species concentrations can also be attempted as these should be expected to reach similar levels once sufficient simulation time has elapsed.

Qualitative comparison shows strong correlations in behaviour for each species. A (graphically) small decrease in N_2 density is shown over the course of the simulation, together with a much sharper decrease in O_2 concentration of several orders of magnitude. These results are in common with Casseau et al. (2016b) as well as earlier results

presented by Haas and McDonald (1993) and Scanlon et al. (2015). Similarly, the behaviour of atomic nitrogen and oxygen show strong qualitative agreement, as does that of NO.

The species number density values at $t = 10^{-4}$ show reasonable agreement with those of other works. With the caveat noted previously, direct value comparisons are not tenable for species whose concentrations are rapidly changing at time 10^{-4}. However, the more stable species at $t = 10^{-4}$ s should be directly comparable as final concentrations should not depend strongly upon small differences in initial densities. In this case, N_2 and O densities are plateauing towards the simulation's end. However only atomic oxygen's final density change is visually distinct enough for comparison. OP2A produces a final O normalised number density of 4.1×10^{-1}, a close match to the values of Casseau et al. (2016b); Haas and McDonald (1993); Scanlon et al. (2015). The densities of N, NO and O_2 are still changing rapidly by the end of the simulation time utilised by Casseau et al. (2016b), hence exact quantitative comparison is not possible. These species do remain within the same orders of magnitude, and N & O follow a similar trend. The one exception to this is diatomic oxygen, which appears to have a slightly differing trend at $t = 10^{-3}$ when compared to the LeMANS results. This difference cannot be definitively attributed to a single factor, but is likely the cumulative result of differences in chemical model parameters and initial species concentrations. Another key feature shared by other published heat bath simulations is the 'kink' in the O_2 curve between $t = 10^{-5}$ and $t = 10^{-4}$ s, which is clearly seen in Figure 5.3 when presented on a log-log scale. A minor qualitative distinction is also noticeable, with OP2A's concentration curves appearing to 'lag' LeMANS's curves by a small amount. This behaviour can also be seen to a lesser extent in Figure 5.2 with the vibrational temperature curve. This behaviour may be due to the smaller time steps employed by OP2A. In order to further investigate this, the temperature of this 5 species heat bath can be examined.

A further quantitative comparison can be performed by assessing the behaviour of temperature over the course of the simulation. The primary reactions within this simulation are clearly dissociation reactions, given the decrease in diatomic nitrogen and oxygen, and concurrent increase in their monatomic equivalents. As these dissociations are endothermic, a decrease in temperature over time is to be expected, and this is clearly evidenced in Figure 5.4, along with comparative data from Casseau et al. (2016b).

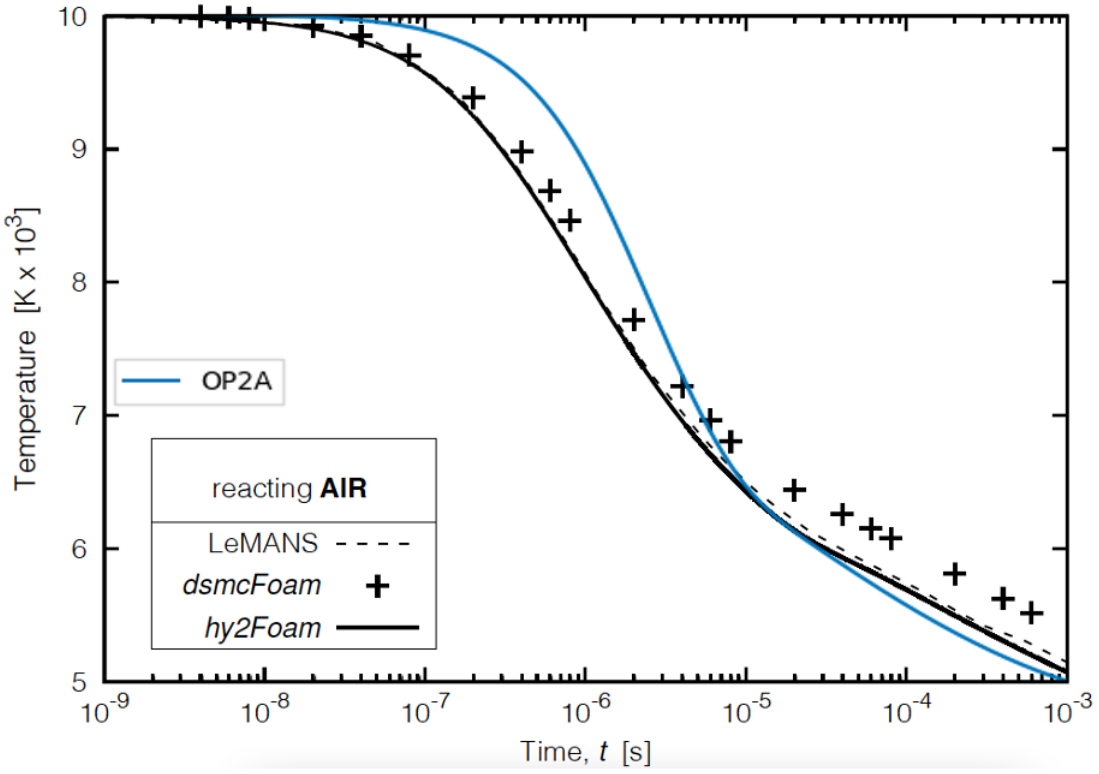

FIGURE 5.4: Evolution of temperature in an air-5 heat bath relaxed in thermal equilibrium at 10,000 K, OP2A results are overlaid upon those presented by Casseau et al. (2016b).

OP2A's results can again be compared to results presented by Casseau et al. (2016b) for a similar 10,000 K heat bath. The overall shape of the relationship reasonable good qualitative agreement, and both feature a final temperature of around 5000 K (4866 K in OP2A's results) by the time 1×10^{-3} s. Perfect alignment in final temperature is not to be expected given the differences in chemical model values used, as well as uncertainty in initial conditions. Additionally, a kink in the temperature curve is present at around 10^{-5} s, which can also be seen in Casseau et al. (2016b). The obvious difference between the results of OP2A and LeMANS is the delayed response of OP2A's temperature curve, mirroring the delays in chemical response visible in Figure 5.3. This difference in response can be attributed to a slower chemical response by OP2A, as the thermal response shows little difference when chemical reactions are excluded. This slower chemical response can potentially be explained by the smaller time step used by OP2A, in addition to the methodological differences already discussed. For further examination of OP2A's chemical modelling, additional heat bath simulations were carried out with differing thermal and chemical properties.

5 Species Air Mixture - Thermal Non-Equilibrium

Both thermal and chemical non-equilibrium models show reasonable agreement with a variety of previously published results. In order to further probe these models, thermal and chemical non-equilibrium were then simulated simultaneously.

The air-5 heat bath as described by Table 5.3 was simulated in thermal non-equilibrium. Firstly, a simulation was performed with both temperatures set to an initial value of 10,000 K. The behaviours of species concentrations and temperatures between $t = 0$ s and $t = 1 \times 10^{-3}$ s are presented in Figures 5.5 & 5.6 respectively. Figure 5.6 shows a small period of slight non-equilibrium occurring between temperatures. From this we should expect only small deviations from thermal equilibrium for the species concentration evolutions and this is clearly evidenced in Figure 5.5.

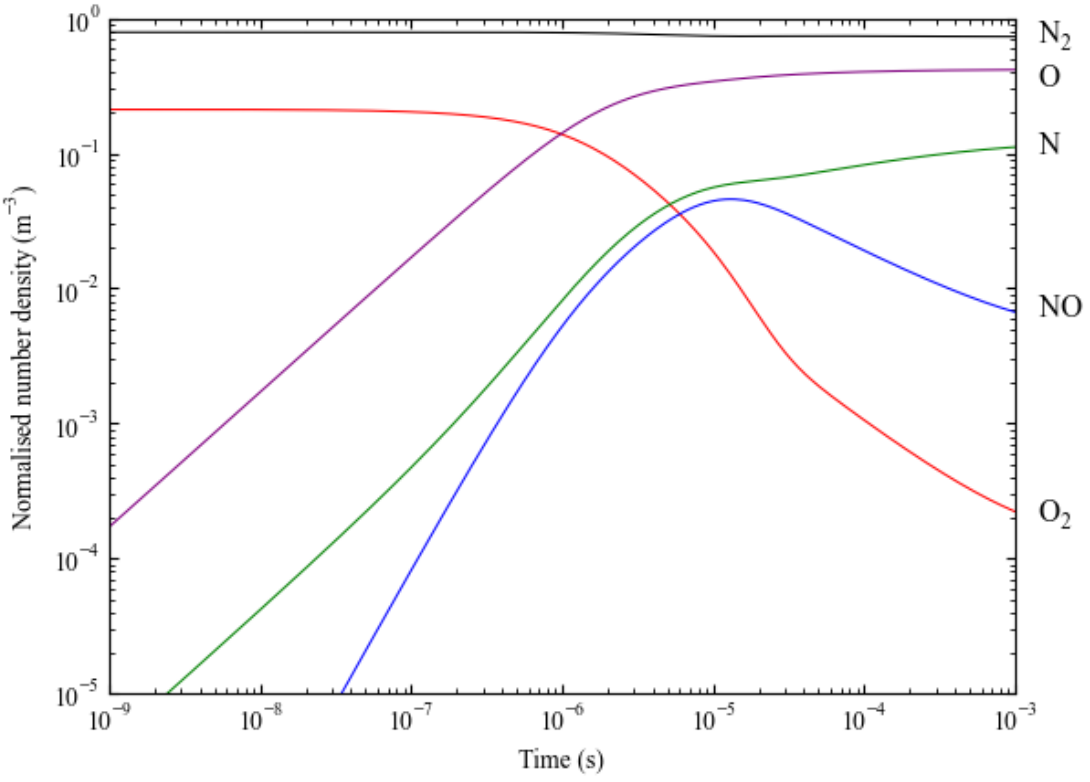

FIGURE 5.5: Evolution of air-5 normalised species number densities when relaxed in a thermal non-equilibrium heat bath at $T_t, T_v = 10,000$ K.

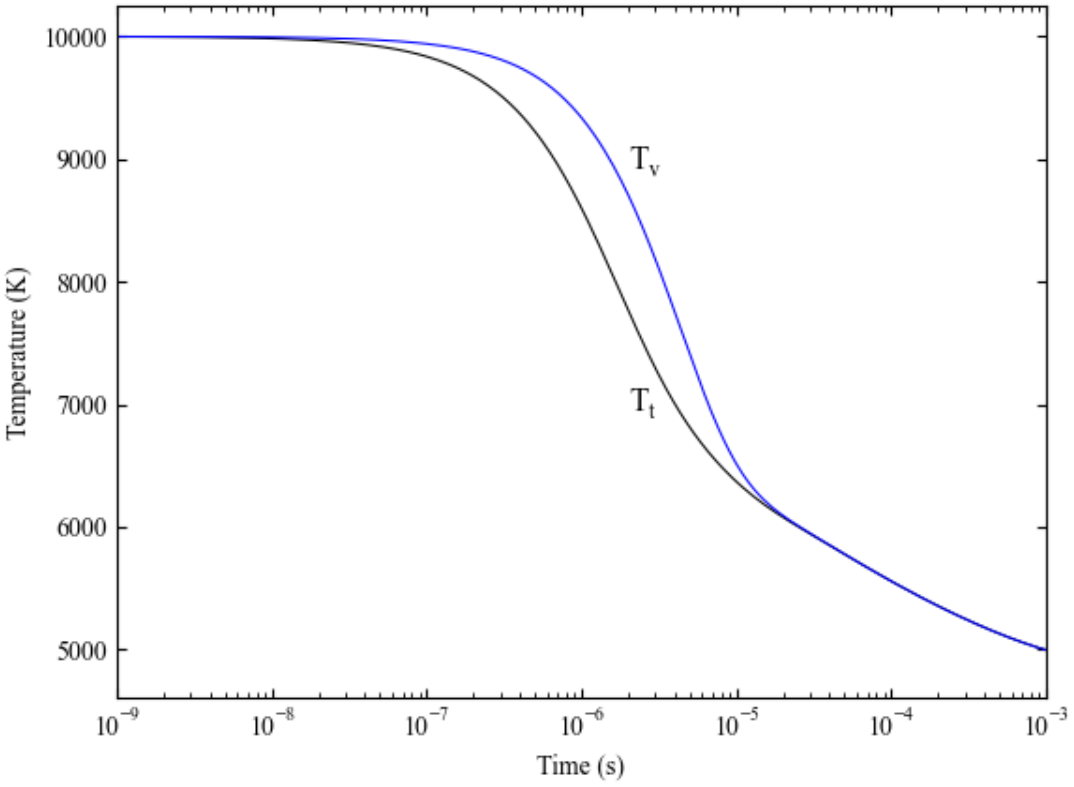

FIGURE 5.6: Evolution of temperatures when an air-5 mixture is relaxed in a thermal non-equilibrium heat bath at $T_t, T_v = 10,000$ K.

From Figure 5.6, it can be seen that the vibrational temperature closely follows the translational temperature throughout the non-equilibrium period. The small size of this non-equilibrium between temperatures results from the fact that most of the temperature decrease is due to dissociation reactions. These endothermic reactions utilise energy from the translational mode, and the removal of diatomic species reduces total vibrational energy. Hence the dominant reaction type reduces both translational and vibrational temperature simultaneously.

In order to further investigate OP2A's thermochemical behaviour, this heat bath was simulated in thermal non-equilibrium with temperatures mirroring those used in section 5.1.1. Firstly, a temperature split of $T_t = 10,000$ K and $T_v = 1,000$ K was used; the behaviour of species concentrations is shown in Figure 5.7.

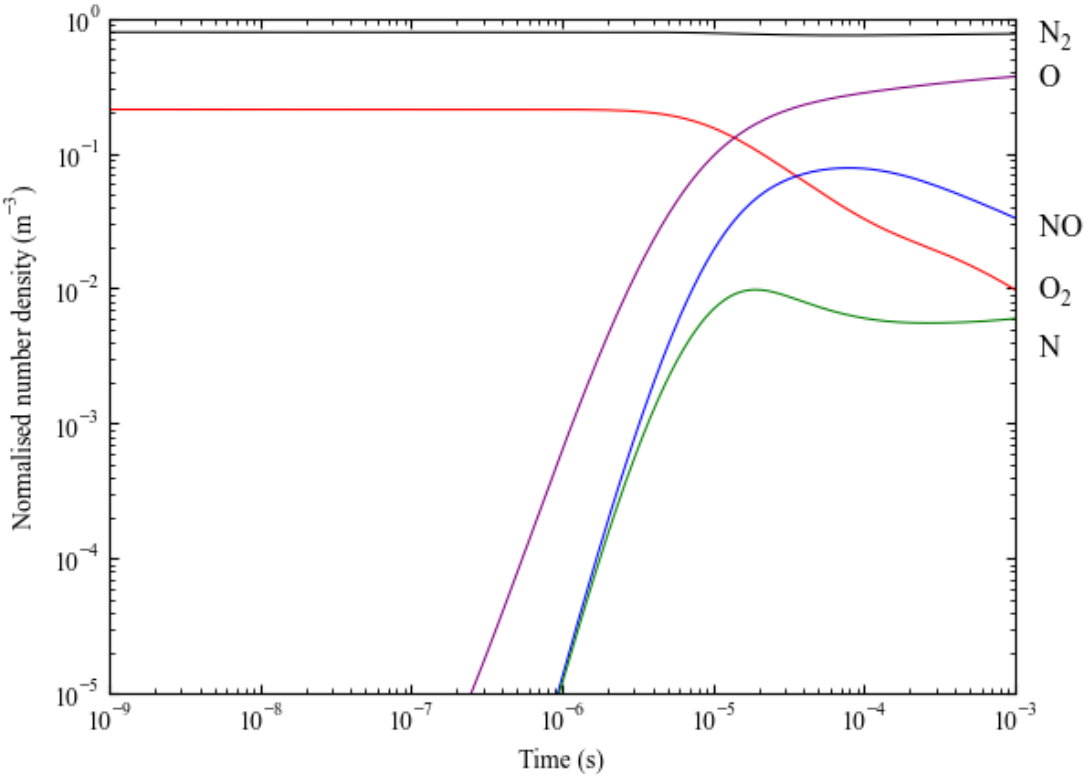

FIGURE 5.7: Evolution of air-5 normalised species number densities when relaxed in a thermal non-equilibrium heat bath at $T_t = 10,000$ K and $T_v = 1,000$ K.

The behaviour of each chemical species is quantitatively distinct from those of the thermal equilibrium case; the principal difference being the later onset of the majority of concentration changes. This is readily explained by the lower Park temperature initially. As the Park temperature, which governs most of the high frequency reactions, scales according to

$$T_P = T_t^{a_P} T_v^{b_P}.$$

Thus it has a maxima when the translational and vibrational temperatures are roughly equal. Meaning that the majority of chemical changes would be expected to follow thermal equilibration. Hence any chemical changes would be expected to be preceded by an increase in vibrational temperature. Analysing the temperature behaviour in Figure 5.8 confirms that this is the case.

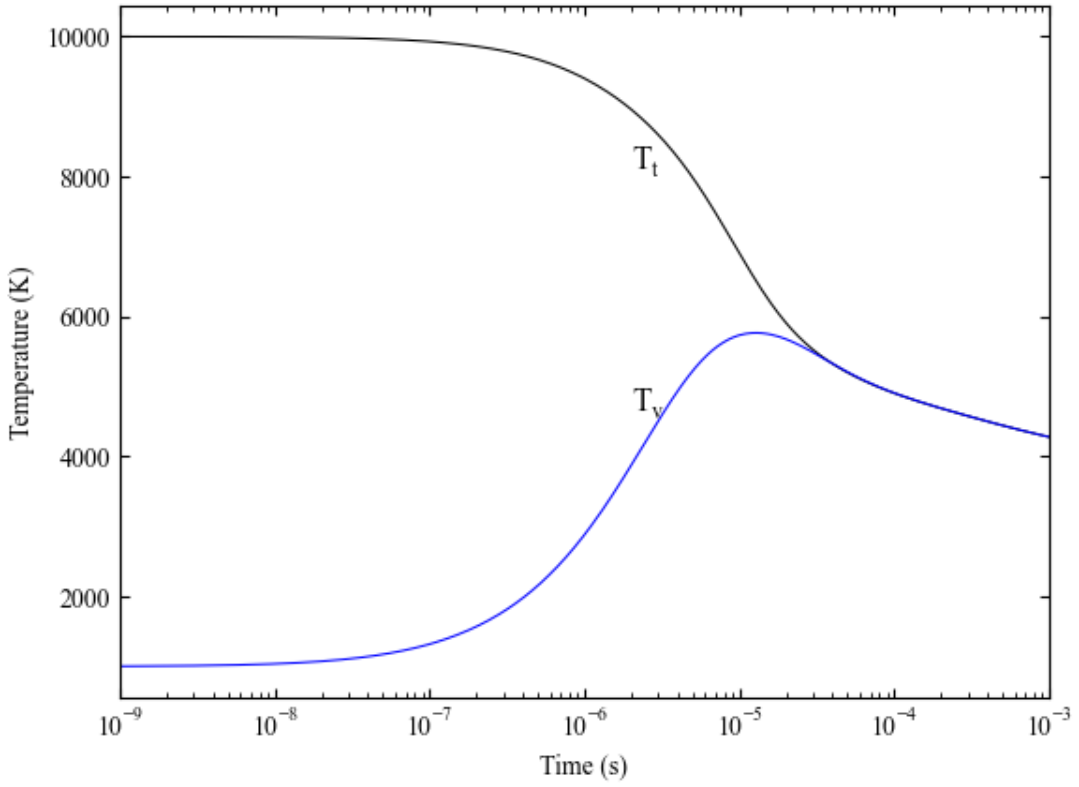

FIGURE 5.8: Evolution of temperatures in an air-5 mixture relaxed in a thermal non-equilibrium heat bath at $T_t = 10,000$ K and $T_v = 1,000$ K.

The other major difference in chemical behaviour is in the relative concentrations of N and NO. The lower concentration of N can be attributed to the low vibrational temperature early in time. This lower concentration is mirrored in the behaviour of O, albeit less evidently. Both of these species are increased through dissociation reactions which are dependent upon the Park temperature which has a maxima when translational and vibrational temperatures are equal. The lessened effects upon O production can be readily attributed to the lower dissociation energy of O_2.

This behaviour can be further explored by utilising a thermal non-equilibrium with an initial high vibrational temperature, such as that simulated in section 5.1.1. The species concentration behaviour of such an investigation is presented in Figure 5.9.

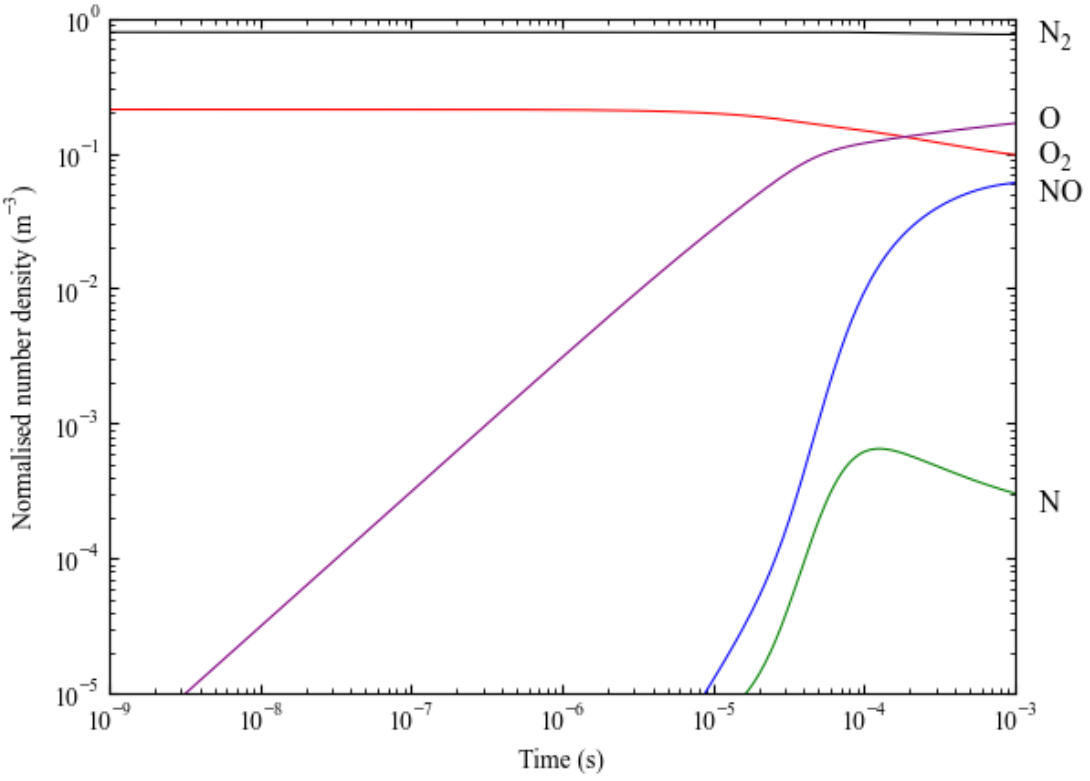

FIGURE 5.9: Evolution of air-5 normalised species number densities when relaxed in a thermal non-equilibrium heat bath at $T_t = 3,000$ K and $T_v = 10,000$ K.

This thermal configuration has a slightly higher Park temperature initially, causing species density changes to begin earlier than in the high T_t case, notably for O_2. However, the high T_v case equilibrates to a lower equilibrium temperature, causing much lower dissociation results overall, especially late in the simulation leading to decreased number fraction changes late in the simulation. This can be seen when comparing densities of O in both cases, O production begins earlier in the high T_v case, but plateaus earlier as well. The reduced production of N can be attributed to the lower translational temperature, which governs the two exchange reaction, both of which produce N. The behaviour of temperatures in the high T_v case can be seen in Figure 5.10.

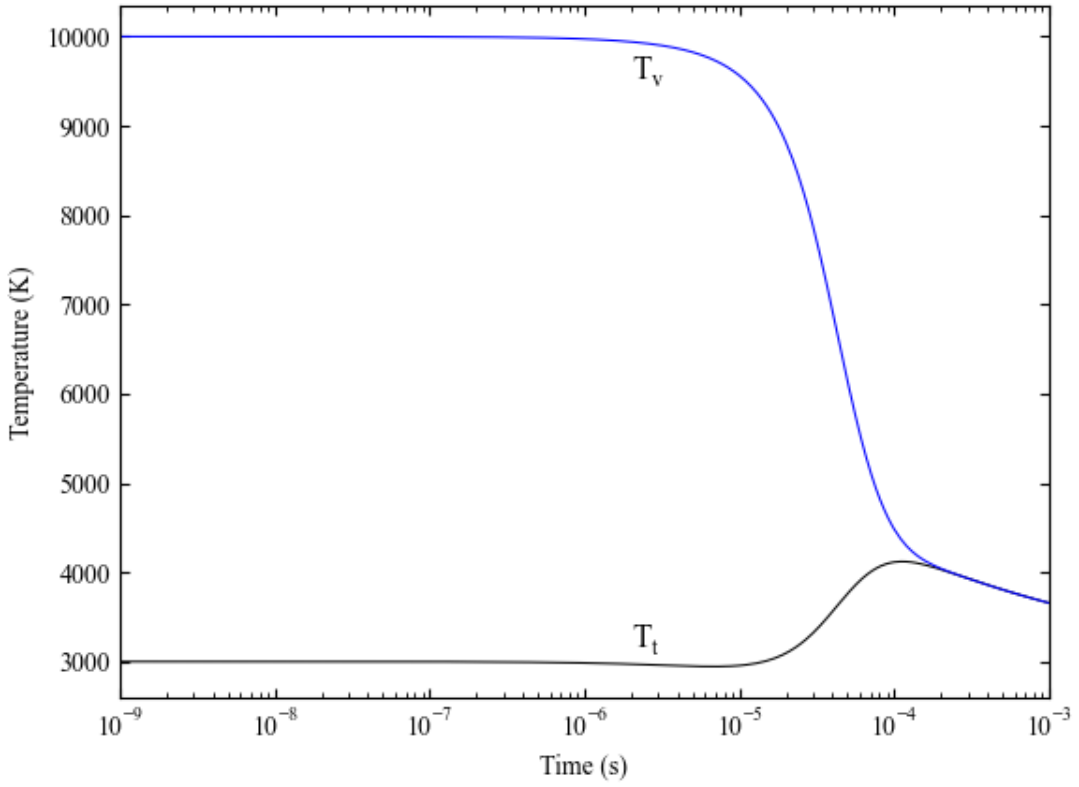

FIGURE 5.10: Evolution of temperatures in an air-5 mixture relaxed in a thermal non-equilibrium heat bath at $T_t = 3,000$ K and $T_v = 10,000$ K.

As in the previous investigations, the temperatures have reached equilibrium by $t = 1 \times 10^{-3}$ s. The temperature profiles shown in Figure 5.10 show the expected timescales. Decreases in both temperatures begin around $t = 10^{-6}$ s, while thermal equilibration is apparent at around $t = 10^{-4}$ s in line with expectations based upon Figure 5.2.

In order to further assess the chemical capabilities of OP2A, chemical heat baths were simulated using an 11 species air mixture. This allows the formation of charged species to be investigated.

11 Species Air Mixture - Thermal Equilibrium

The air-5 mixture heat bath configurations detailed in sections 5.1.2 and 5.1.2 were repeated for an 11 species air mixture, henceforth referred to as the air-11 mixture. This mixture added ionised versions of all air-5 species as well as free electrons. The initial species mass densities used in these heat baths are shown in Table 5.4

TABLE 5.4: Initial conditions for the air-11 chemical heat bath in thermal equilibrium.

Variable	Initial Value
ρ_{N_2} (kg m^{-3})	1.7×10^{-3}
ρ_{O_2} (kg m^{-3})	0.52×10^{-3}
ρ_{NO} (kg m^{-3})	3.0×10^{-7}
ρ_{N} (kg m^{-3})	1.4×10^{-7}
ρ_{O} (kg m^{-3})	6.8×10^{-6}
$\rho_{N_2^+}$ (kg m^{-3})	1.0×10^{-20}
$\rho_{O_2^+}$ (kg m^{-3})	1.0×10^{-20}
ρ_{NO^+} (kg m^{-3})	1.0×10^{-25}
ρ_{N^+} (kg m^{-3})	1.0×10^{-47}
ρ_{O^+} (kg m^{-3})	1.0×10^{-24}
ρ_{e} (kg m^{-3})	5.0×10^{-25}
T_t (K)	10,000
p (Pa)	6,453

The above heat bath configuration was simulated containing 11 species air, featuring charged species. Electron density was chosen so as to ensure quasi-neutrality within the mixture. The full complement of species and reactions simulated is as presented in section 2.5.2, with associated parameter values provided in appendix B. This heat bath was first simulated in thermal equilibrium to ascertain chemical species behaviour without temperature dependence effects. The behaviour of these species' number densities is shown in Figure 5.11. Number densities are again normalised to initial total number density within the heat bath.

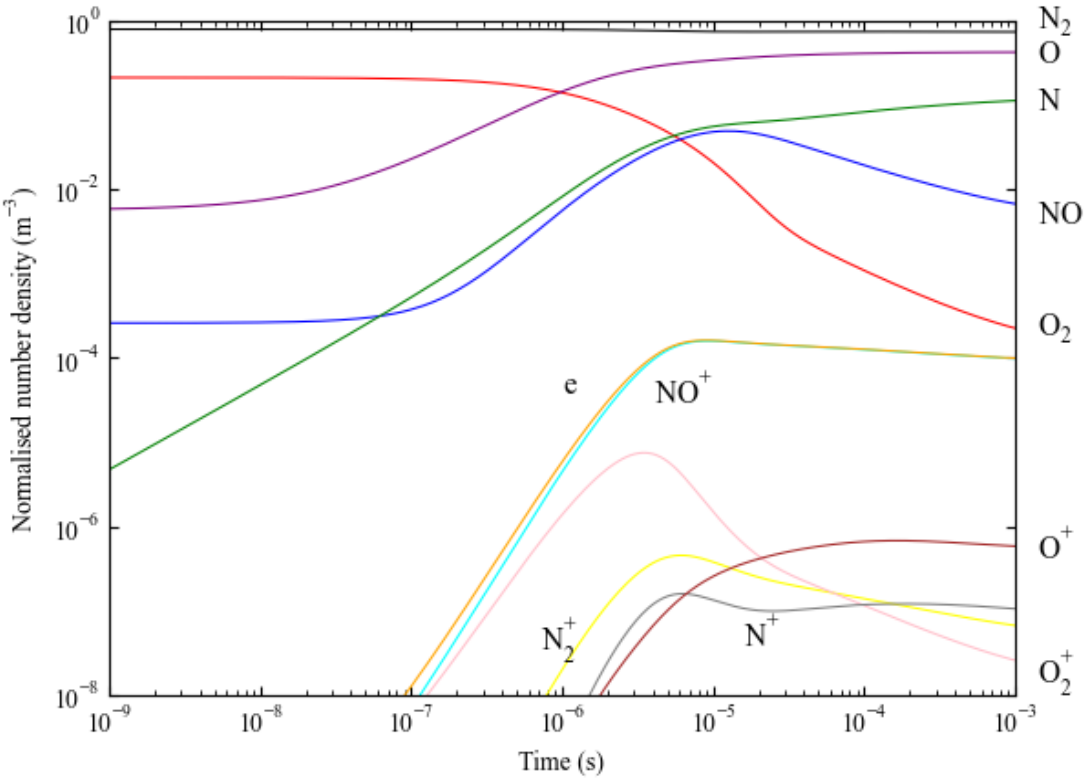

FIGURE 5.11: Evolution of air-11 normalised species number densities when relaxed in a thermal equilibrium heat bath at 10,000 K.

Figure 5.11 shows similar behaviour for the neutral species when compared to its air-11 counterpart, as would be expected given the lower density levels of charged species. Positively charged species show an increase in density fraction initially, followed by a drop-off after $t = 10^{-5}$ s. This behaviour is to be expected if temperature decreases with increasing time as charged species will only exist in significant quantities at temperatures of the order of 10^5 K. An additional feature is the relationship between electron and positive ion number density; it can be seen that electron density tracks close to the total number density of charged species, demonstrating adherence to quasi-neutrality. Observing the temperature behaviour in Figure 5.12 confirms that temperature has dropped significantly by $t = 10^{-5}$ s.

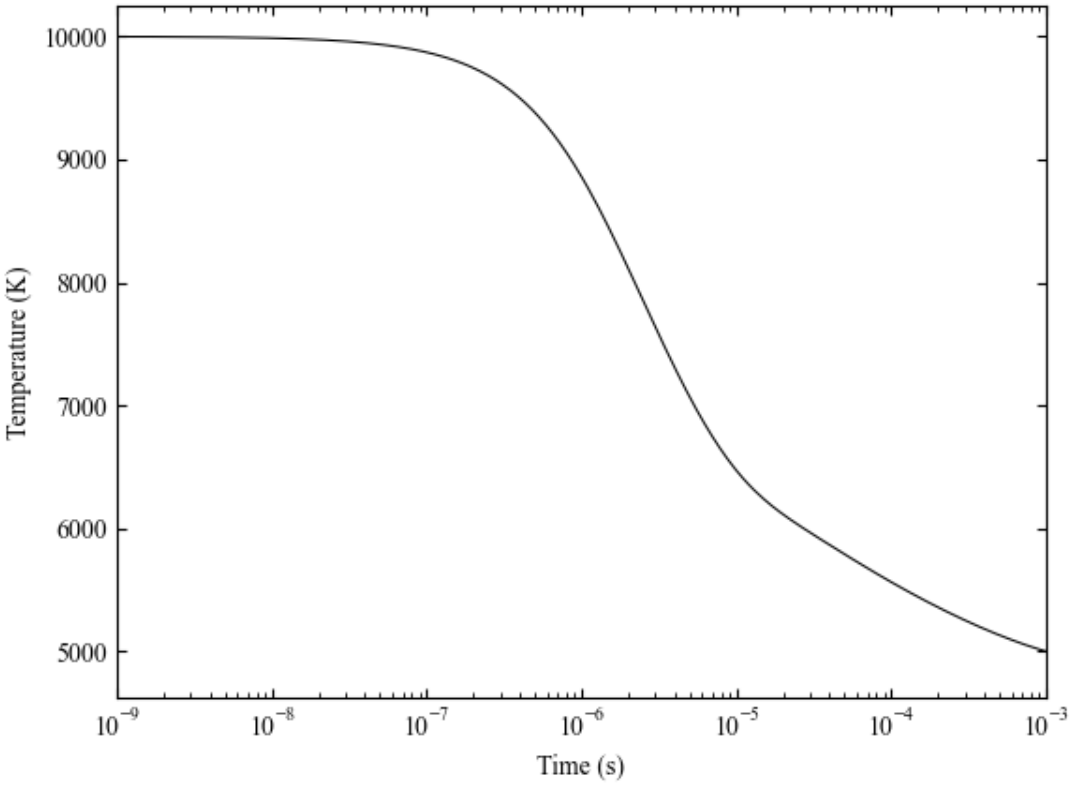

FIGURE 5.12: Evolution of temperature in an air-11 heat bath relaxed in thermal equilibrium at 10,000 K.

The energy changes in this heat bath are dominated by reactions common to the 5 species air model, hence the temperature behaves similarly to its 5 species counterpart in Figure 5.4. The drop in charged species concentration as temperature drops demonstrates expected behaviour for this case.

11 Species Air Model - Thermal Non-Equilibrium

The chemical heat bath containing 11 species air was re-simulated in all of the thermal non-equilibrium configurations utilised in section 5.1.1. For a heat bath with both temperatures initially set to 10,000 K, concentration and temperature results were similar to those of the thermal equilibrium case, as demonstrated in Figures 5.13 & 5.14 respectively.

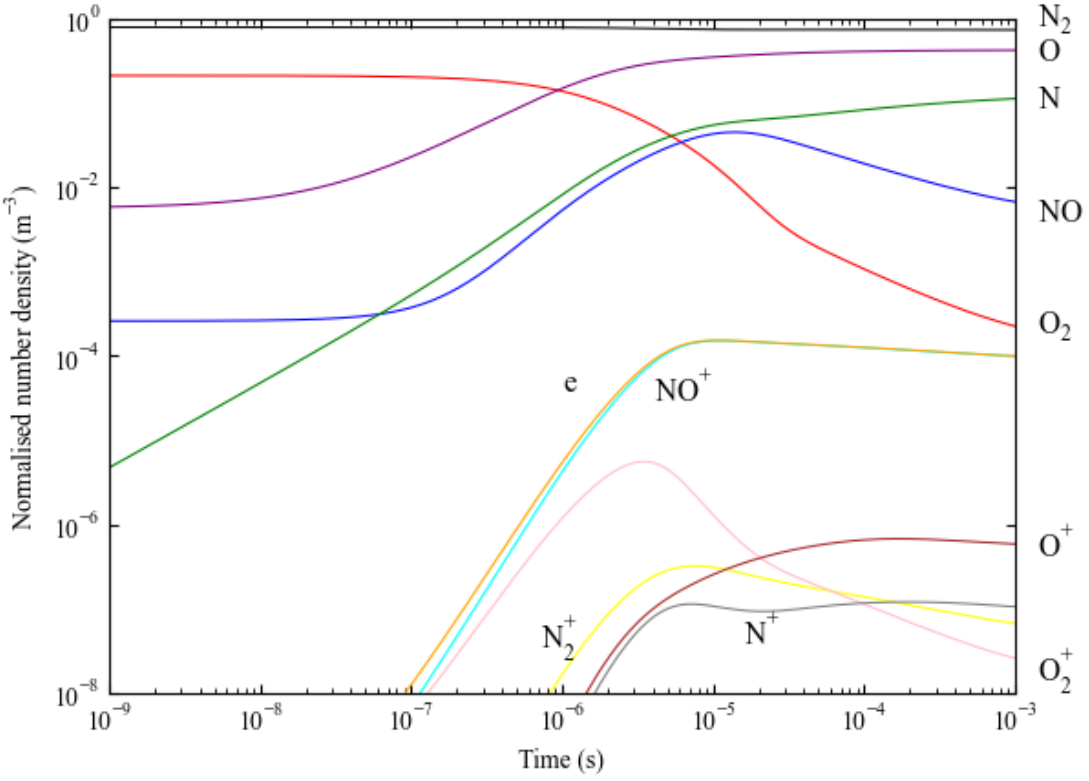

FIGURE 5.13: Evolution of air-11 normalised species number densities when relaxed in a thermal non-equilibrium heat bath at $T_t, T_v = 10,000$ K.

Chemical concentrations shown in Figure 5.13 show only small deviations from their counterparts in thermal equilibrium. This in turn suggests that temperatures should not deviate from thermal equilibrium conditions by a large amount. Figure 5.14 demonstrates this to be true.

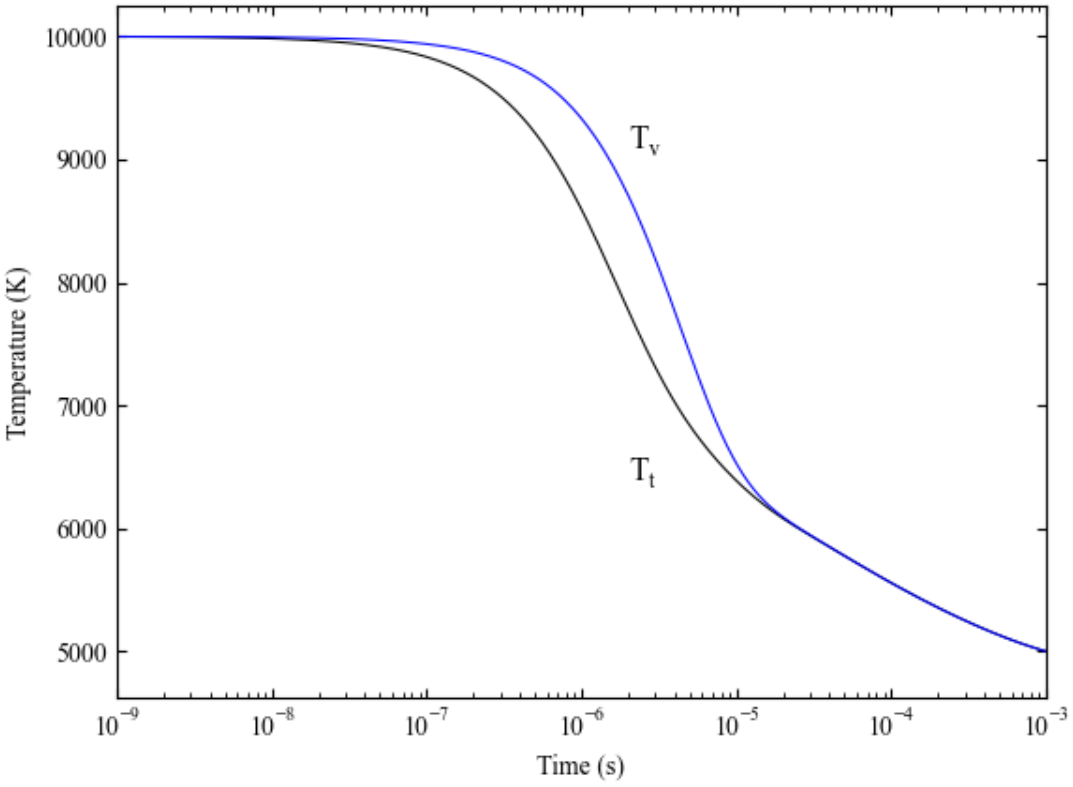

FIGURE 5.14: Evolution of temperatures in an air-11 heat bath relaxed in thermal non-equilibrium at $T_t, T_v = 10,000$ K.

These results show close similarity to their thermal equilibrium counterparts, as with the air-5 case. This demonstrates consistency between the air-5 and air-11 mixtures. Once again, electron density levels show quasi-neutrality to be maintained. This heat bath test was repeated with an increased translational temperature. The behaviour of chemical density fractions with a high initial translational temperature is plotted in Figure 5.15.

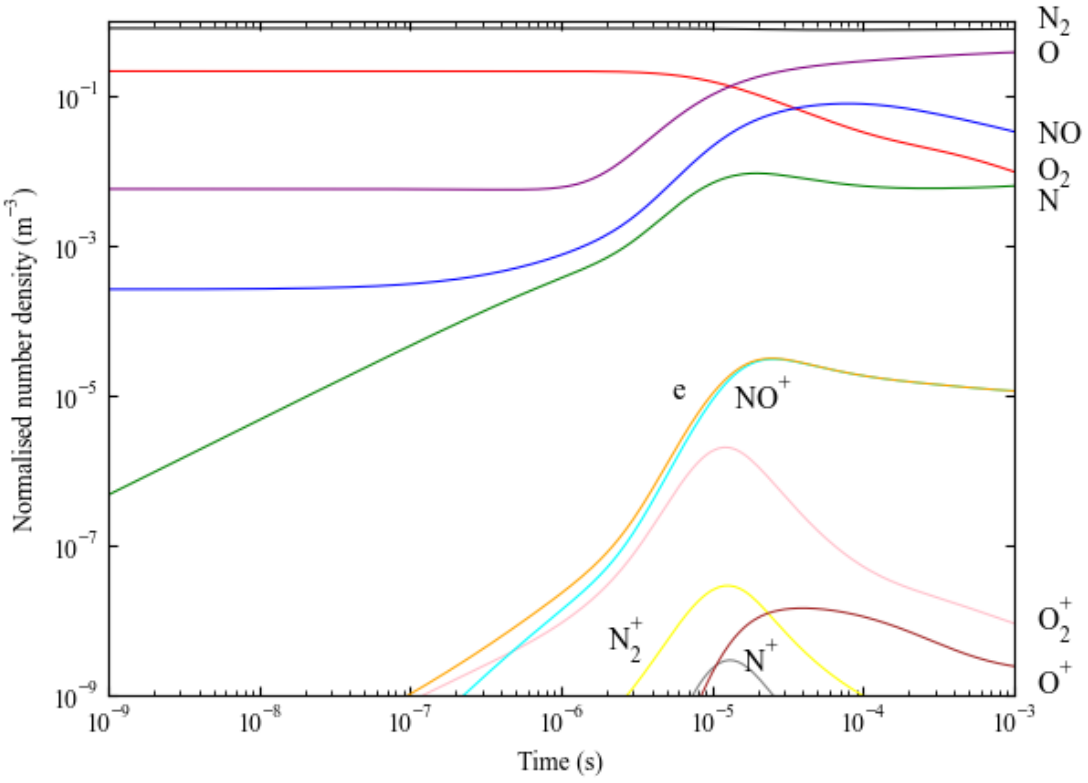

FIGURE 5.15: Evolution of species concentrations in an air-11 heat bath relaxed in thermal non-equilibrium at $T_t = 10,000$ K, $T_v 1,000$ K.

As Figure 5.15 shows, all chemical changes are delayed compared to their thermal equilibrium counterparts. This is in common with the 5 species air model and again caused by the lower initial vibrational temperature leading to a lower Park temperature. Electron production is not significantly delayed in this case compared to the thermal equilibrium case (Figure 5.11), likely due to the fact that initial electron production is controlled by the translational temperature through dissociative recombination reactions.

As the energy effects are still dominated by reactions involving neutral species, temperature behaviour is expected to be similar to its 5 species counterpart. This expected behaviour is clearly evidenced in Figure 5.16.

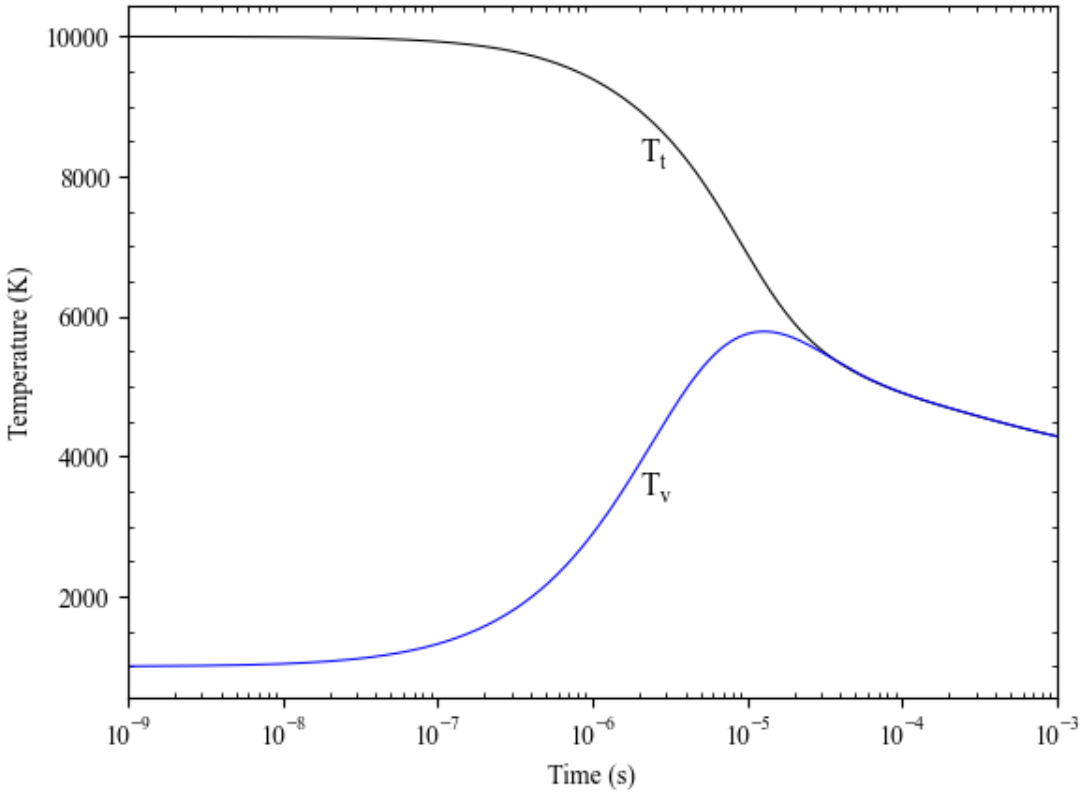

FIGURE 5.16: Evolution of temperatures in an air-5 heat bath relaxed in thermal non-equilibrium at $T_t = 10,000K$ and $T_v = 1,000$ K.

Figure 5.16 shows a very close match with its air-5 counterpart Figure 5.8 as is to be expected given the dominance of neutral species in terms of mass fraction throughout the relaxation.

Lastly, this heat bath test was repeated using a thermochemical non-equilibrium heat bath with a high initial vibrational temperature. The evolution of species concentrations is shown in Figure 5.17.

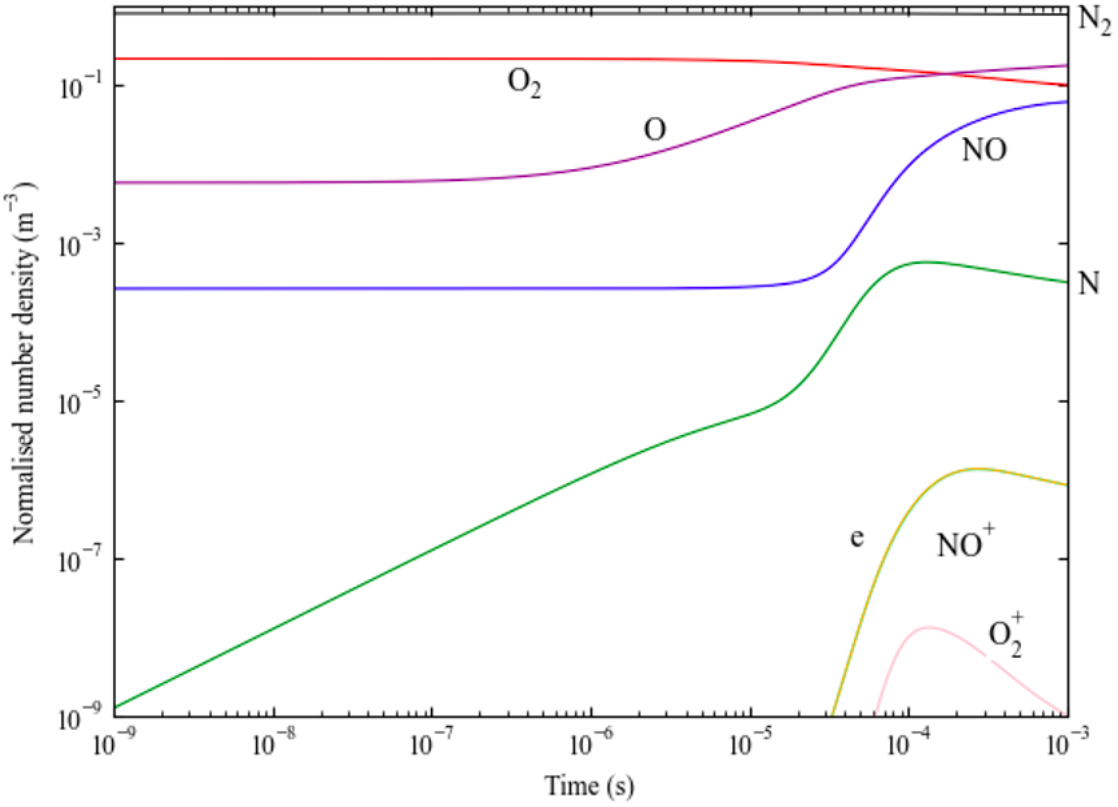

FIGURE 5.17: Evolution of species concentrations in an air-11 heat bath relaxed in thermal non-equilibrium at $T_t = 3,000$ K, $T_v 10,000$ K.

In this case electron production is delayed as expected due to the lower translational temperature reducing the frequency of dissociative recombination reactions. The production of other charged species is similarly impeded, and several positive species aren't produced in significant quantities. This is due to the translational temperature never exceeding 4000 K as shown in Figure 5.18.

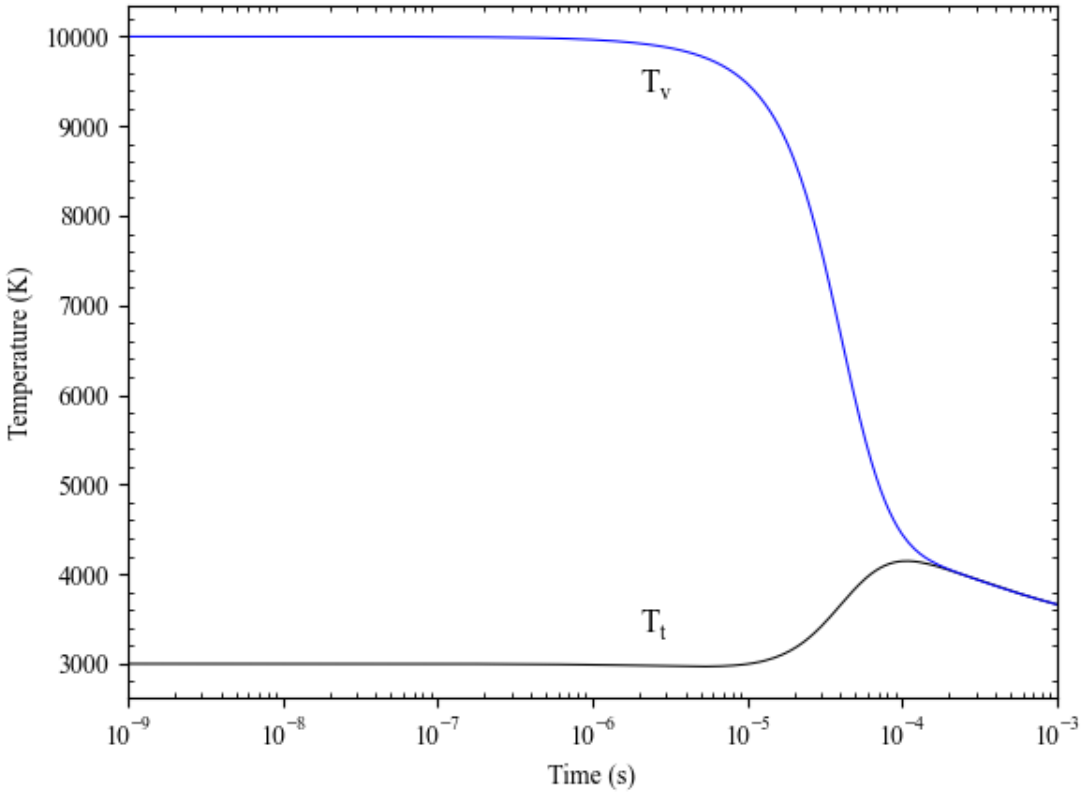

FIGURE 5.18: Evolution of temperatures in an air-5 heat bath relaxed in thermal non-equilibrium at $T_t = 3,000$ K and $T_v = 10,000$ K.

Summary

These thermochemical analyses show strong qualitative and quantitative agreement with a variety of presented works for a five species air mixture; as well as good consistency across other chemical mixtures for which quantitative comparison works were not found. The production of charged species is shown to be linked to temperature differences in the expected manner.

Small lags in simulation response when compared to other data are observed, however these are not considered to be anomalous or deleterious, but likely the result of time step differences. There are no other notable anomalous behaviour shown, nor any problematic values for full simulations of Earth atmospheres. Hence, the zero dimensional simulations were concluded, and more complex multi-dimensional simulations undertaken. These culminated in real capsule simulation, however first accuracy testing of OP2A's spatial and temporal integration routines was undertaken.

5.2 Two Dimensional Analyses

Following verification of the thermochemical components, it was decided to evaluate the accuracy of the spatial and time integration components of OP2A. This case is unsteady, with a predictable analytical solution, making it a prime candidate for use when assessing the performance of OP2A in a number of areas; including grid independence and the parallelisation efficiency test presented in Chapter 4.

5.2.1 2d Shock Tube Simulations and Analytical Comparisons

A two-dimensional shock tube case utilised for evaluating the accuracy of spatial and time integration routines, as well as assessing grid independence and the assessment of parallelisation performance presented in Chapter 4.

The shock tube was first utilised to test the accuracy of integration routines, with the results being compared to the calculated analytical solution for this shock tube case. To this end a shock tube case was simulated using a setup similar to that originally presented by Sod (1978). The shock tube consists of two regions of N_2 gas separated by a discontinuity, released at time $t = 0$ s and allows to evolve over time. The walls are in this case chosen to be adiabatic slip walls in order to have no effect on the gas, in line with one dimensional studies of this case. The initial conditions for the shock tube case are shown in Table 5.5.

TABLE 5.5: Initial values for the simulated shock tube case.

	left	right
ρ (kg m^{-3})	1.0	0.125
u (m s^{-1})	0.0	0.0
p (Pa)	99951.5	9995.2

Whilst the shock tube can be considered a one dimensional case, these results were simulated in two dimensions, as demonstrated by Figure 5.19. This image shows the expected lack of variance in the y direction.

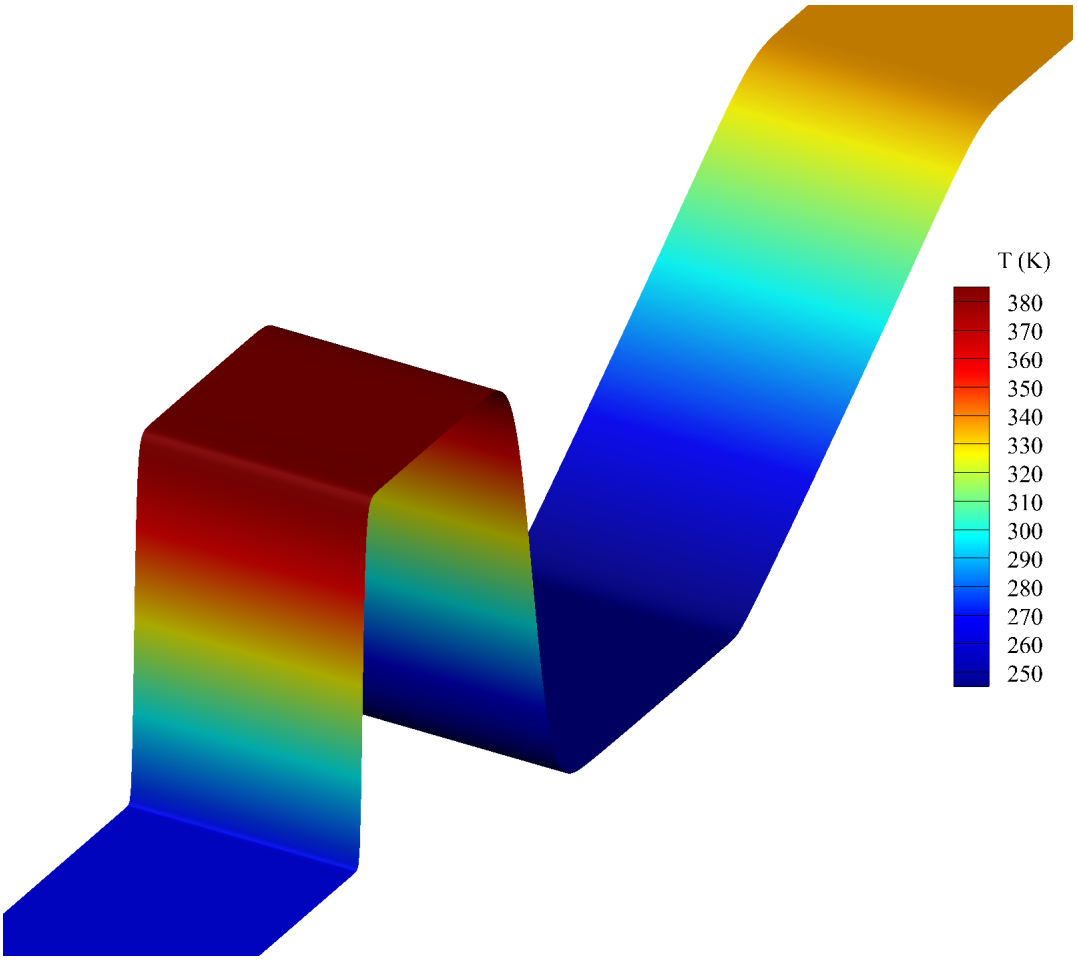

FIGURE 5.19: Two dimensional view of shock tube temperature profile after 0.01 s.

The significant results of this simulation can be most easily seen in one dimensional plots, which are used in order to demonstrate the accuracy of OP2A's solutions. The one dimensional results of the simulation after 0.01 s are shown in Figure 5.20 alongside an analytical calculation of their expected outcomes. These results serve as part of the validation of OP2A.

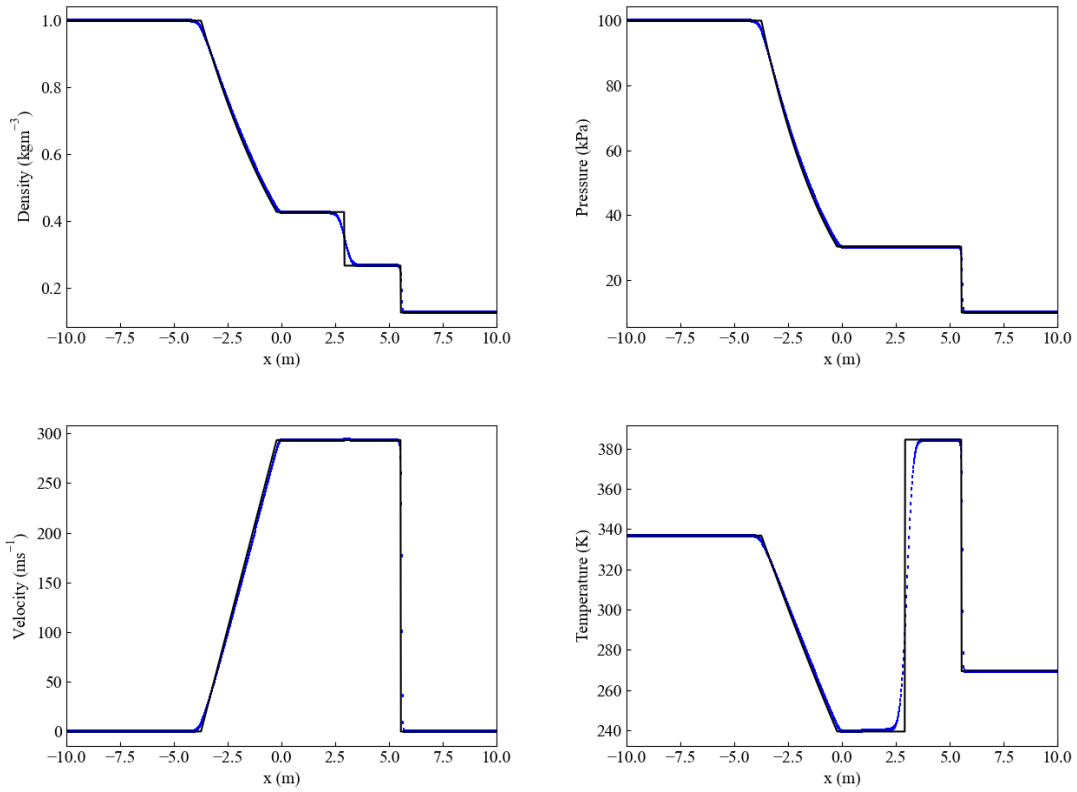

FIGURE 5.20: Shock tube numerical results (blue) after 0.01 s of time evolution with their analytical equivalents (black); a) Mass density, b) Pressure, c) Velocity, d) Temperature.

The results shown in Figure 5.20 were generated using the AUSM spatial integration scheme. The time integration scheme utilised was the forward Euler method.

The presented results show small levels of discrepancy between numerical and analytical results, particularly about discontinuity points due to resolution limitations. These results are well in line with expectations and compare reasonably to shock tubes simulated with the AUSM scheme presented by Hajman et al. (2007). It would be expected that the discrepancies between numerical and analytical solutions will reduce with increasing resolution and that results will otherwise be unaffected. Hence, a brief investigation of grid resolution independence was undertaken.

Grid Independence

Simulation results were obtained for shock tubes with x-direction resolutions of 500, 1000 and 2000 cells across the -10 m to 10 m domain. These results, shown in the temperature plot in Figure 5.21, display the expected behaviour of numerical results approaching analytical results as resolution increases. No anomalous behaviour is noted.

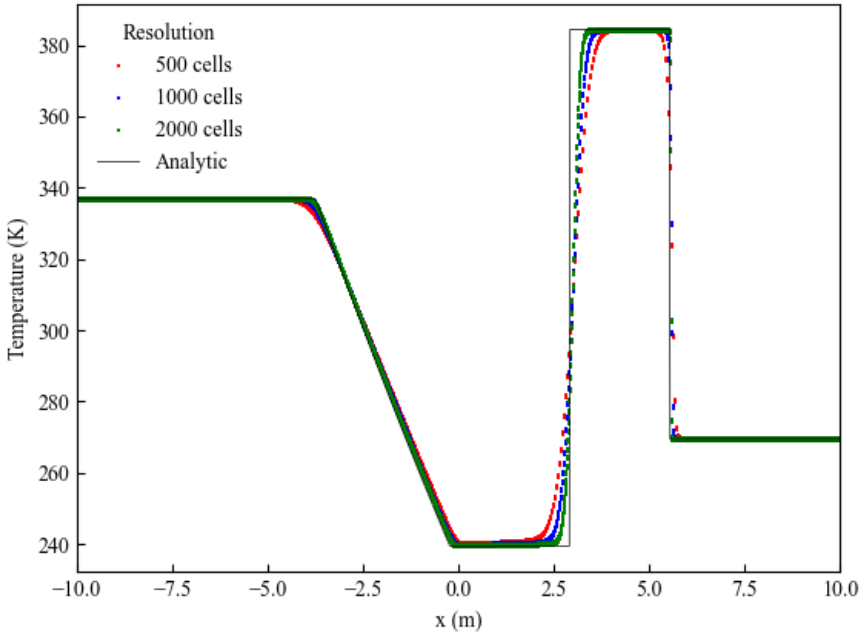

FIGURE 5.21: Shock tube temperature profile at different x direction resolutions.

Summary

Shock tube plots show accurate performance by spatial and time integration routines for this subsonic case. Grid independence has also been demonstrated and parallelisation efficiency has been assessed and found to be satisfactory, as presented in Chapter 4.

With this work completed, the fundamental components of OP2A were considered to be successfully verified. Thus, in order to demonstrate OP2A's utility for capsule optimisation simulations, a series of axisymmetric simulations were performed.

5.3 Two Dimensional Axisymmetric Investigations

Following evaluation of the spatial and time integration routines, a series of two dimensional simulations were performed in an axisymmetric configuration. These began with the hypersonic double-cone flow case; a commonly used validation case for CFD suites which has been utilised by Candler et al. (2002); Holloway et al. (2022); Knight et al. (2012); Expósito and Rana (2019) to name but a few.

5.3.1 Double Cone Investigations

The double-cone case produces a number of complex interacting fluid phenomena, including interactions between shock and expansion waves, a separation region and a detached boundary layer. The shape of the double cone is relevant to several areas of re-entry craft geometry, hence its common usage. This case is also noteworthy for it non-equilibrium behaviour; as its features can be resolved numerically and found to agree well with experiments when in thermochemical equilibrium, but results differ significantly when non-equilibrium is simulated, as described within Park (2013).

The standard double cone setup consists of two differently inclined cones as described by Figure 5.22. The lower boundary of the cones is an axisymmetric boundary.

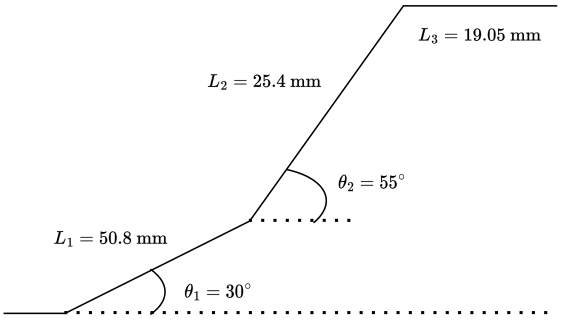

FIGURE 5.22: Geometry of the axisymmetric double cone spatial domain.

This case was simulated using the AUSM spatial integration scheme and the forward Euler time integration scheme. The geometry described in Figure 5.22 was simulated in a N_2 flow with freestream conditions described in Table 5.6.

TABLE 5.6: Freestream flow conditions for the double cone case in thermal equilibrium.

Variable	Freestream Value
ρ_{N2} (kgm^{-3})	5×10^{-4}
u (ms^{-1})	3,000
T_t (K)	250
p (Pa)	37.1

This simulation produces an overall flow shape as shown in the Mach number profile in Figure 5.23. This Mach number flow field's overall shape shows strong qualitative agreement with similar work both numerical and experimental presented by Knight et al. (2012).

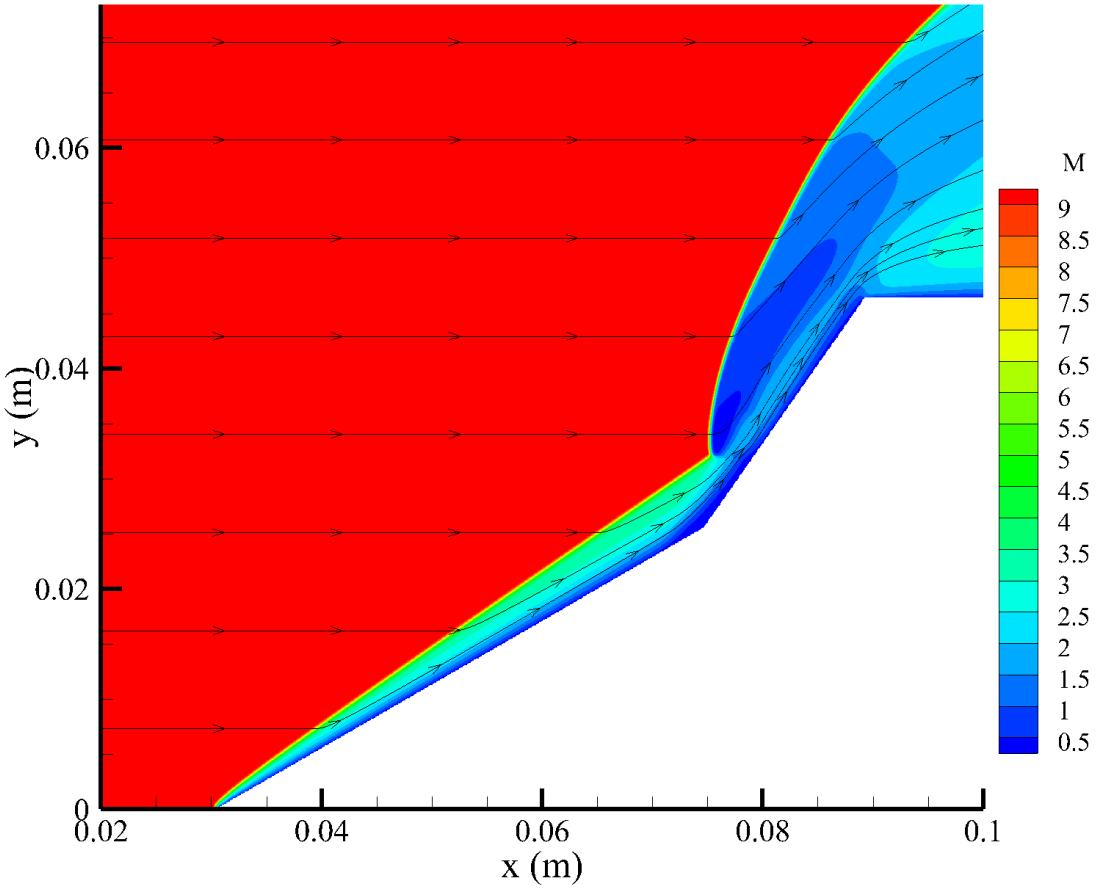

FIGURE 5.23: Overview of Mach number distribution for the axisymmetric double cone case in thermal equilibrium across the entire domain.

The streamlines shown in Figure 5.23 show no unexpected behaviour, with those entering below the triple point ($\sim y = 0.3$ m) being contained within the supersonic region. A closer look at the region around the triple point (Figure 5.24) shows the sonic line separating the subsonic and supersonic regions as evidenced by Knight et al. (2012).

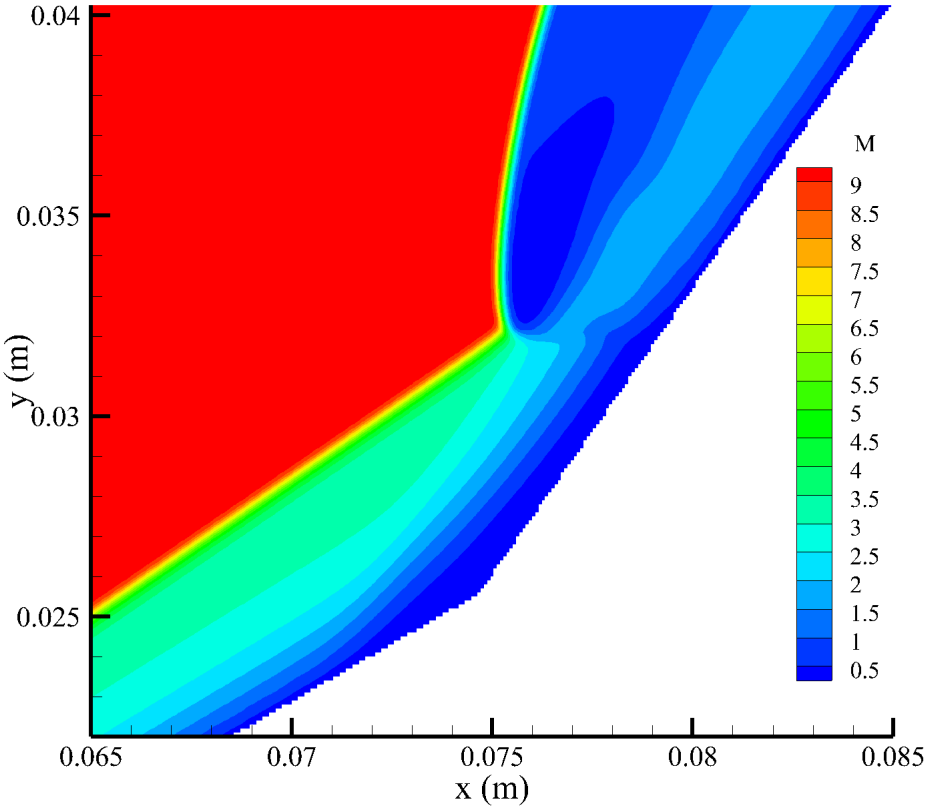

FIGURE 5.24: Overview of Mach number behaviour about the point of shock interaction for the axisymmetric thermal equilibrium double cone case.

Figure 5.24 also shows evidence of a separation region at the intersection of the cones. Observing a plot of the pressure contours (Figure 5.25) shows some limitations with the achieved results.

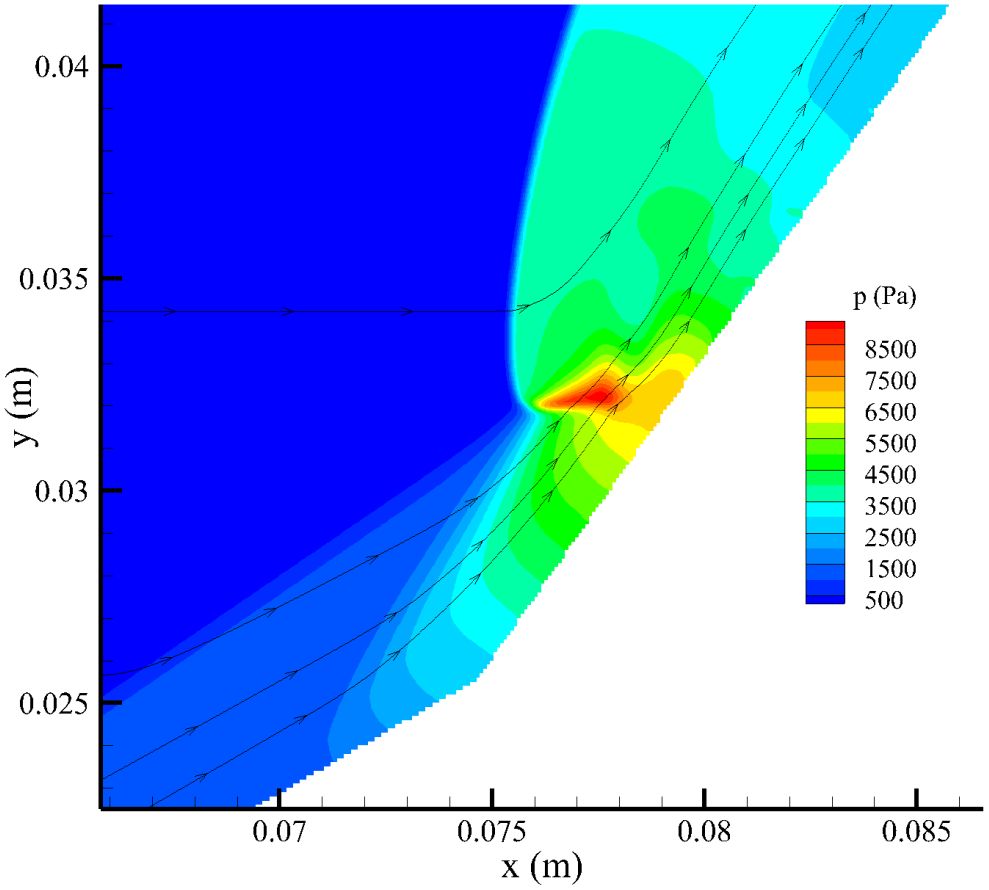

FIGURE 5.25: Overview of pressure behaviour about the point of shock interaction for the thermal equilibrium double cone case.

Figure 5.25 shows clear evidence of a recompression shock occurring downstream of the shock interactions. However, a limitation is clear in the appearance of the two high pressure regions. These regions would be expected to be distinct and clearly separated from one another, Figure 5.25 shows them to be interconnected. The expected disconnected zones are shown in the results of Knight et al. (2012) presented in figure 5.26.

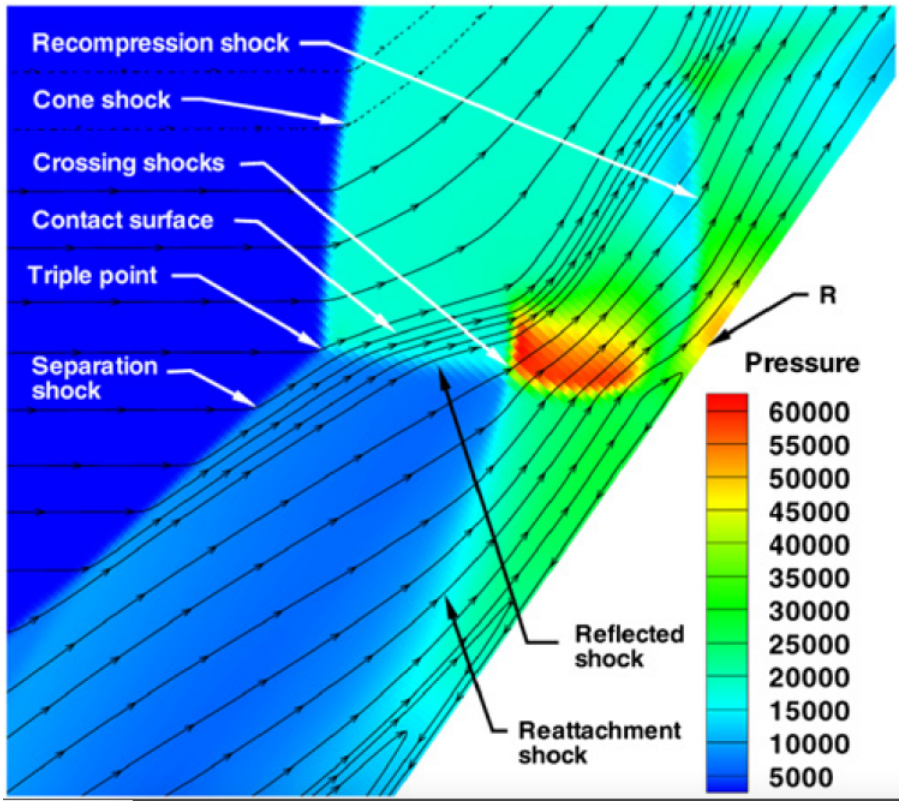

FIGURE 5.26: Results of pressure behaviour about the point of shock interaction for the thermal non-equilibrium double cone case as presented by Knight et al. (2012)

The differences between these results has likely come about as a result of the limited resolution of the simulations achievable within the time frame of this work. As such, improving available resolution constitutes a clear area for future work, such work will be made easier by the parallelisation system described in Chapter 4. The temperature profile for this case is shown in Figure 5.27 and shows good agreement with the work of Candler et al. (2002) presented in Figure 5.28.

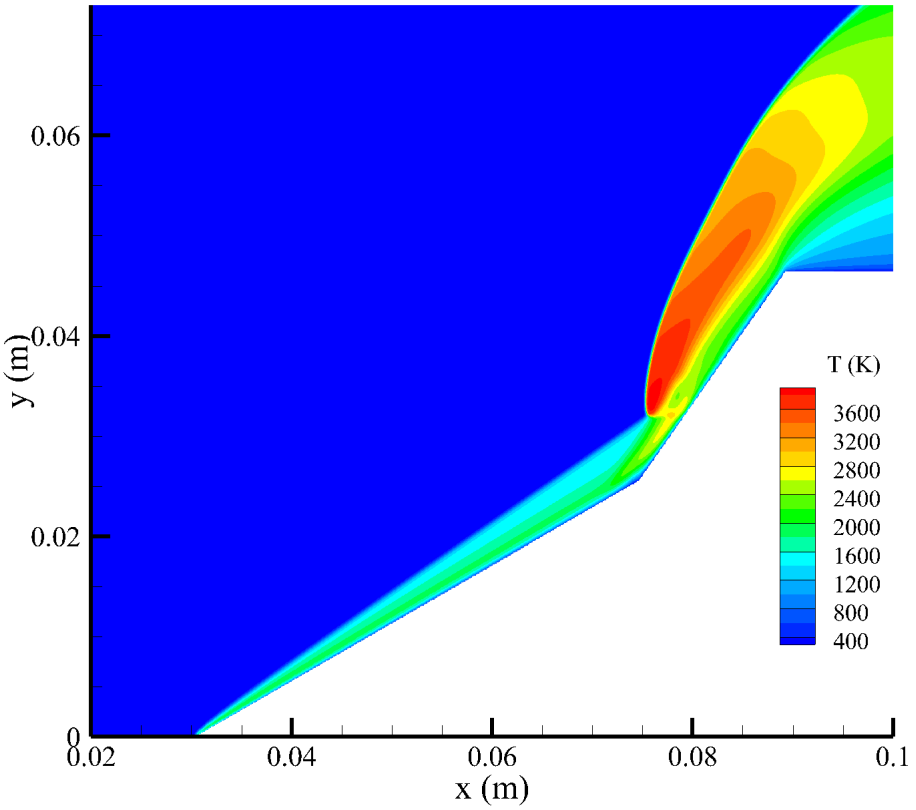

FIGURE 5.27: Overview of temperature behaviour across the whole simulation domain for the thermal equilibrium double cone case. Translational temperature is shown on the left figure, and vibrational on the right.

Figure 5.28 displays the results of a double cone flow with similar geometry, but with quantitatively different flow parameters, thus an exact quantitative match is not to be expected. The work of Candler et al. (2002) also concerns a thermal non-equilibrium case, leading to a lower overall temperature in Figure 5.28. Key reproduced qualitative features include the triple point, sonic line and separation shock as previously mentioned, though positions differ, as is to be expected due to the quantitative flow differences.

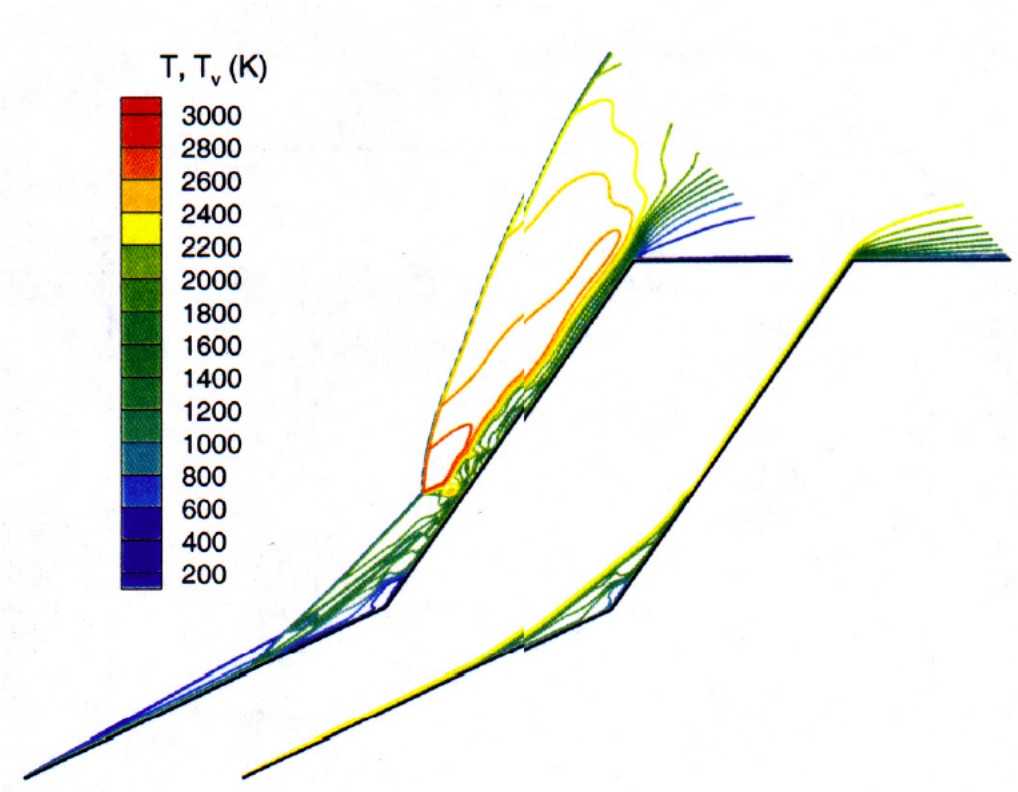

FIGURE 5.28: Temperature contours over the simulation domain of a qualitatively similar double cone case, as presented by Candler et al. (2002).

Key features of Figure 5.27 include the temperature profile include a high temperature subsonic region and a low temperature region at the cone intersection. In addition, density gradient profiles can be extracted from these results for further analysis, and are presented in Figure 5.29.

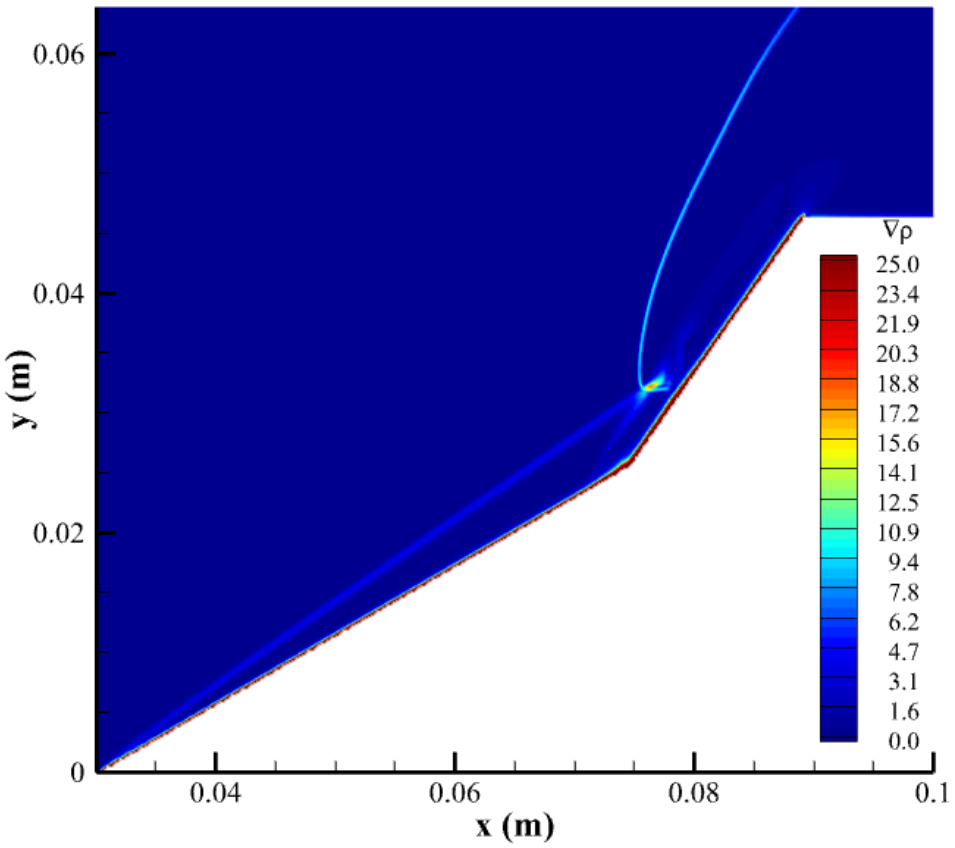

FIGURE 5.29: Density gradient magnitude across the simulation domain for the thermal equilibrium double cone case.

Figure 5.29 can be compared with the results of a similar simulation presented by Expósito and Rana (2019) shown in Figure 5.30. Simulation conditions are not identical between these works, hence exact quantitative alignment is not to be expected. Gradient profiles should however be expected to align well.

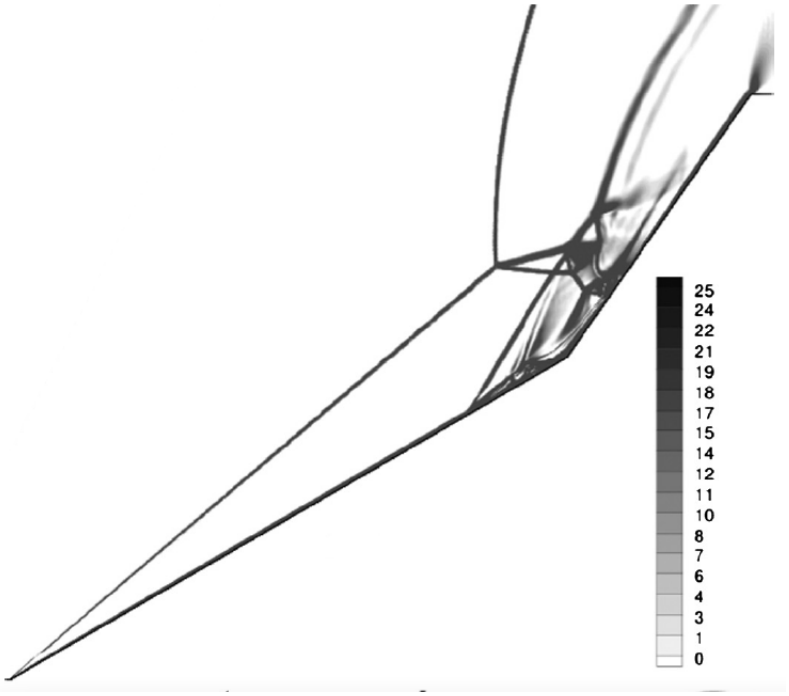

FIGURE 5.30: Density gradient magnitudes for a thermal equilibrium double cone case, as presented by Expósito and Rana (2019).

Figures 5.29 & 5.30 show reasonable qualitative agreement with one another. Individual shock and expansion distinguishing lines are distinct, with similar geometries. As previously, quantitative flow values differ between works, hence exact quantitative alignment is not to be expected. However, these results, whilst not constituting a conclusive quantitative verification, provide reassurance of OP2A's ability to resolve complex flow features.

Summary

Double cone behaviour has been simulated with reasonable accuracy using OP2A. Key flow features including multiple shocks and their interactions have been shown and examined in multiple profiles, together with comparisons to other published works showing good agreement. The limits of achievable resolution have been shown in areas of complex shock interactions, and will need to be considered for future simulation work. Following this, a series of axisymmetric capsule forebody simulations were performed in order to examine their flow features and post shock thermochemistry.

5.3.2 Capsule Simulations

The last set of investigations were a series of capsule simulations were performed in order to investigate the post shock thermochemical behaviour whose significance was

described in Chapter 1. Each of these capsules was simulated at zero angle of attack. It should be noted that these capsule simulations are limited in their lack of modelling of radiative and ablative effects, both of which have been reported by Winter et al. (2019) to affect flow features such as shock standoff distance.

Hayabusa Capsule Forebody Simulation

The Hayabusa re-entry capsule re-entered Earth's atmosphere in June of 2010 carrying samples from the asteroid Itokawa, as part of a JAXA mission. This capsule's forebody was simulated by OP2A in a two dimensional axisymmetric configuration. The forebody shape consists of a hemisphere nose with diameter of 202 mm leading into a conic side body with a cone half angle of 45°. This geometric configuration mirrors that used by ISHII et al. (2008) and is shown in Figure 5.31.

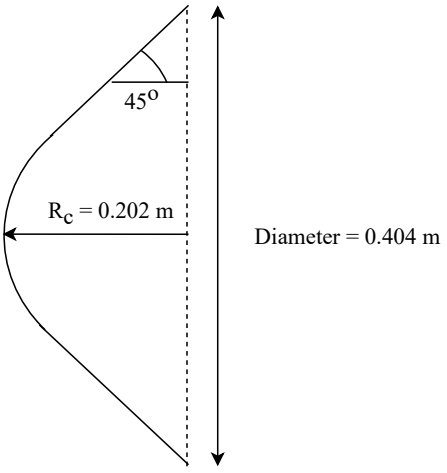

FIGURE 5.31: Geometry of the Hayabusa capsule forebody cross-section, the dotted line marks the edge of the forebody.

This capsule forebody was simulated at zero angle of attack with flow conditions which mirror those found at an altitude of 60 km, as outlined in Table 5.7. An axisymmetric boundary was placed at $y = 0.0$ m which corresponds to the capsule symmetry axis.

TABLE 5.7: Freestream flow conditions for the Hayabusa capsule forebody simulation at altitude 60 km.

Variable	Freestream Value
ρ (kgm^{-3})	3.1×10^{-4}
u (ms^{-1})	11,029
T_t (K)	247.2
T_v (K)	247.2
p (Pa)	37.1

The conditions in Table 5.7 are obtained from the work of Takahashi and Yamada (2018). This capsule was simulated using the AUSM scheme in a 5 species air flow with active chemistry in thermal non-equilibrium, with the aim of studying the stagnation line chemistry profile. The resulting pressure distribution is shown in Figure 5.32.

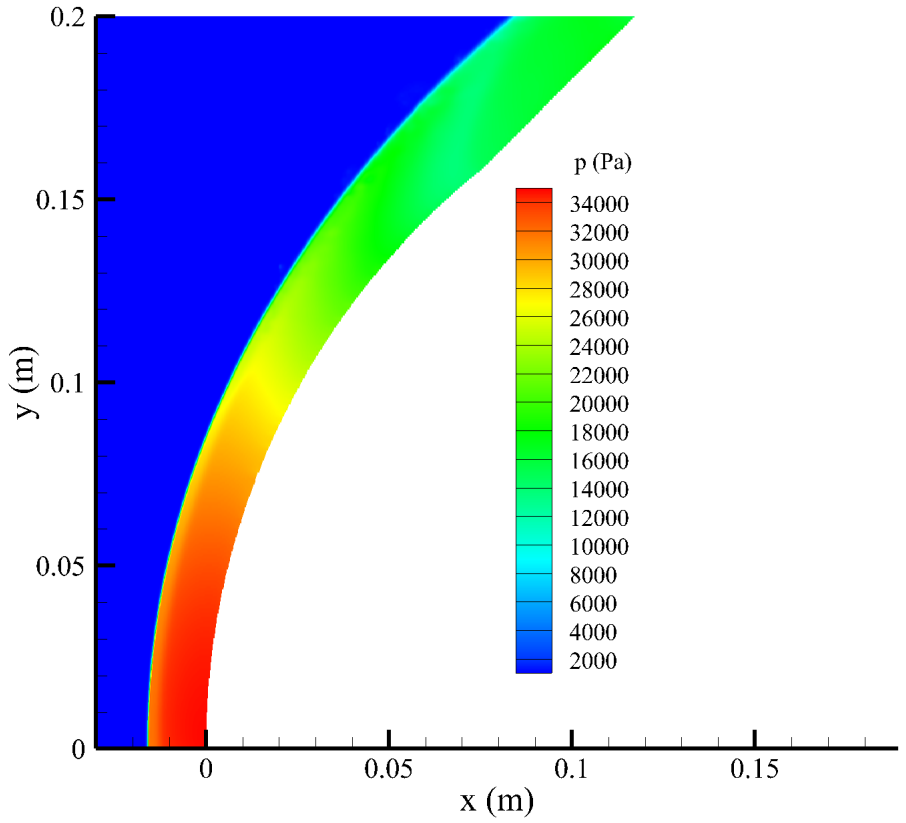

FIGURE 5.32: Pressure distribution across the Hayabusa forebody at 60 km at zero angle of attack.

This pressure distribution shows a sharp shock front consistent with expectations. In order to examine chemical behaviour, we can observe the behaviour of nitrogen species in the vicinity of the stagnation point, shown in Figures 5.33 & 5.33.

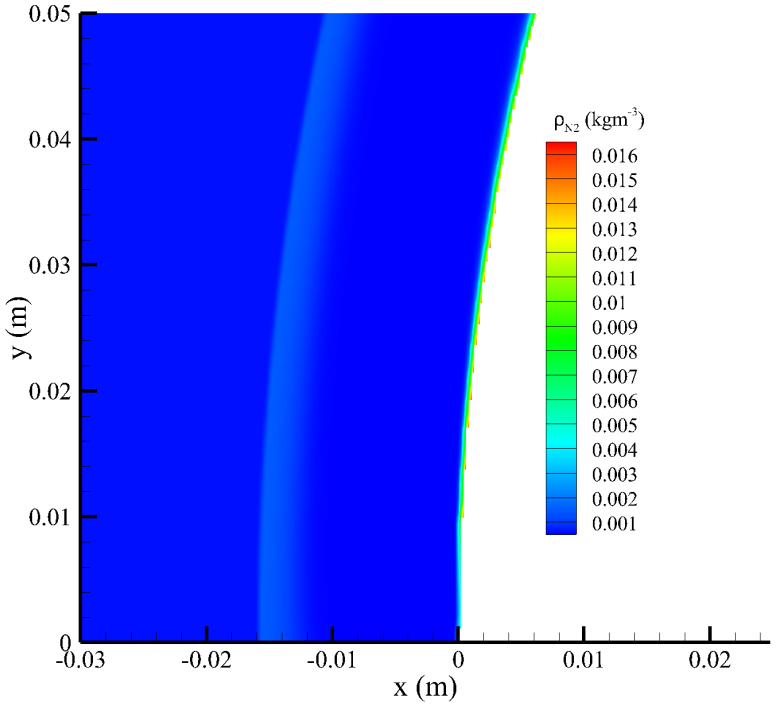

FIGURE 5.33: N_2 mass density distribution in the vicinity of the stagnation point.

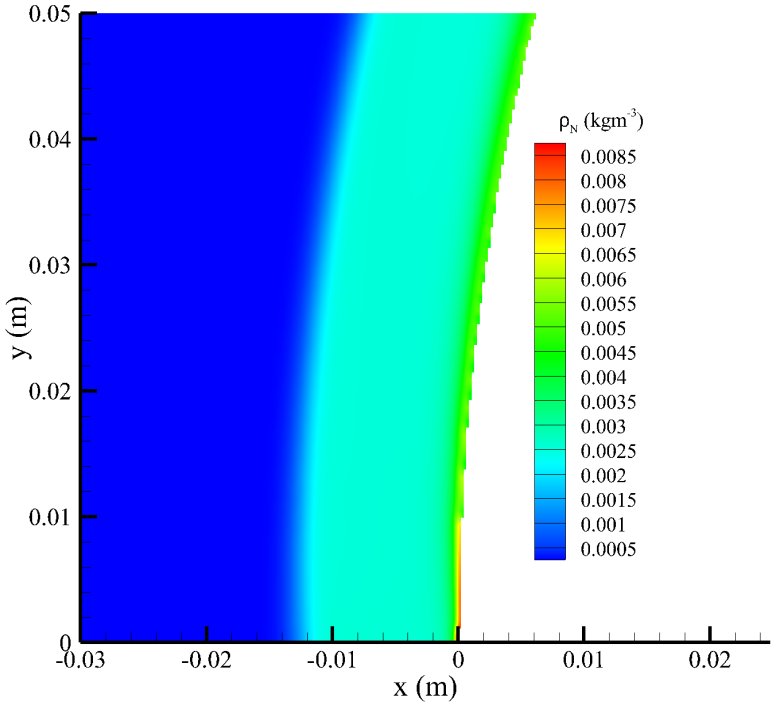

FIGURE 5.34: N mass density distribution in the region of the stagnation point.

Figures 5.33 & 5.34 appear to confirm the expected behaviour of nitrogen dissociation upon entering the high temperature region behind the shock. This behaviour can be examined in greater detail using stagnation line plots of chemical species ratios, as seen in Figure 5.35.

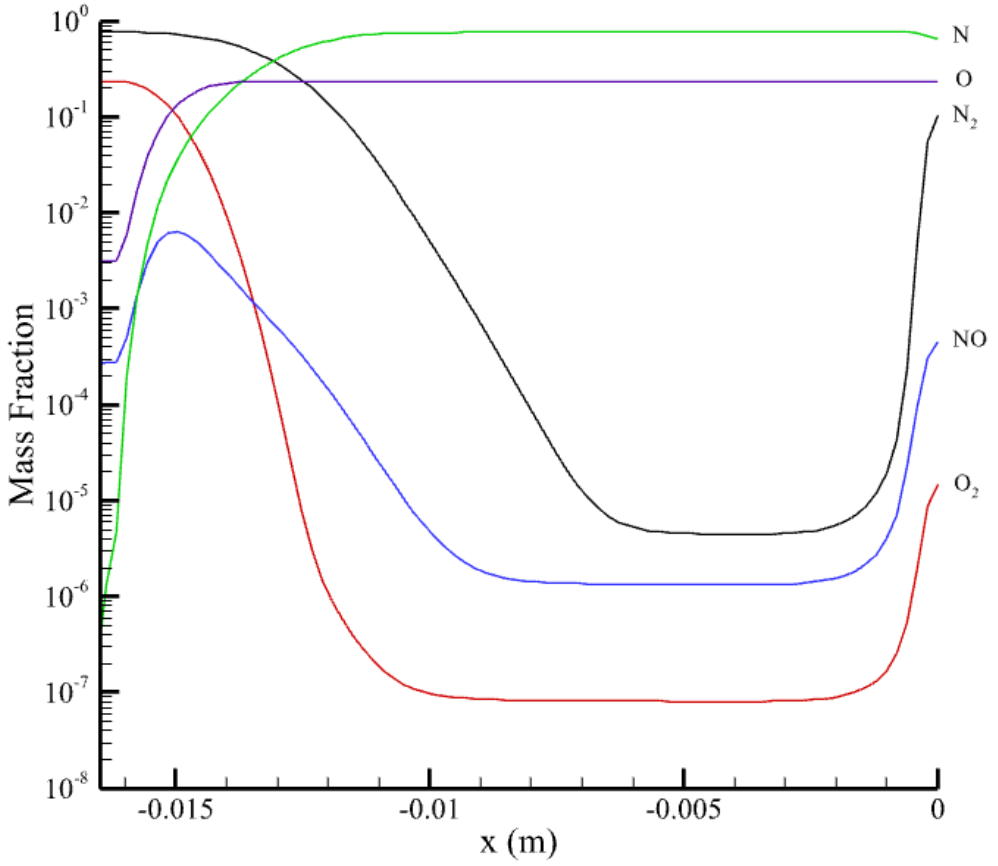

FIGURE 5.35: Chemical species mass density fractions along the stagnation line of the Hayabusa capsule.

The mass density fractions in Figure 5.35 show diatomic species declining sharply in the region of highest temperature, with their monatomic counterparts concurrently increasing, as seen in Figure 5.36.

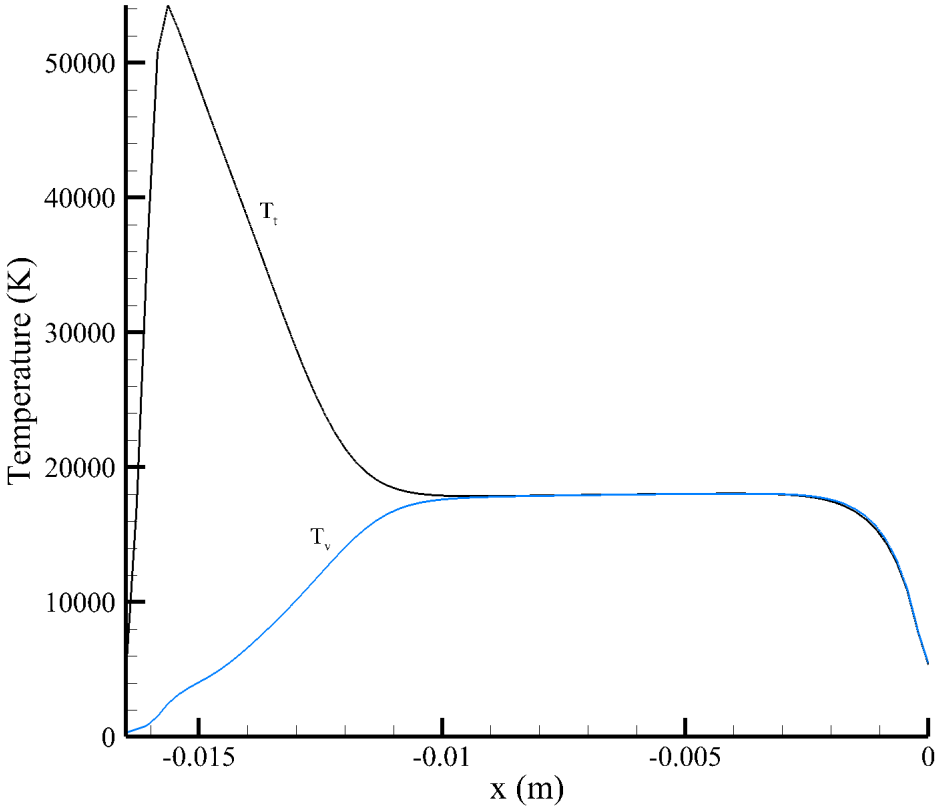

FIGURE 5.36: Temperatures along the stagnation line of the Hayabusa capsule.

Figures 5.35 & 5.36 can be directly compared to other published works which simulate the Hayabusa re-entry, and shows strong qualitative agreement with many others, including those of Takahashi and Yamada (2018) shown in Figure 5.37.

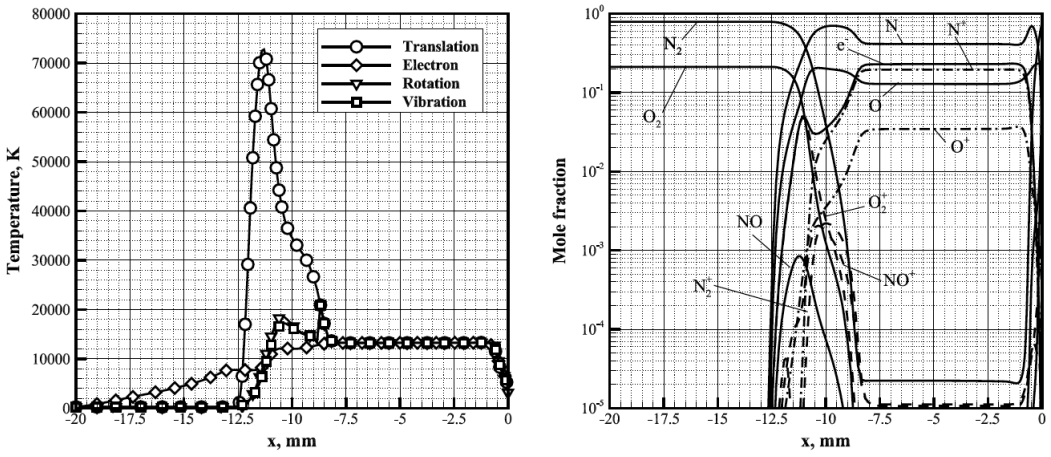

FIGURE 5.37: Temperatures and species mole fractions along the stagnation line of the Hayabusa capsule as presented by Takahashi and Yamada (2018) at an altitude of 57.9 km.

The results produced by OP2A along the stagnation line also show strong qualitative agreement with other Hayabusa capsule simulations including those of Ozawa et al. (2011); Fahy et al. (2021); Suzuki et al. (2014). OP2A's results also show a strong quantitative alignment with the results of Ozawa et al. (2011), which produce a peak and an equilibrium temperature of around 54,000 K and 18,000 K respectively for similar inflow conditions. OP2A's temperature profile results can also be quantitatively compared to those of Kihara et al. (2013), shown in Figure 5.38.

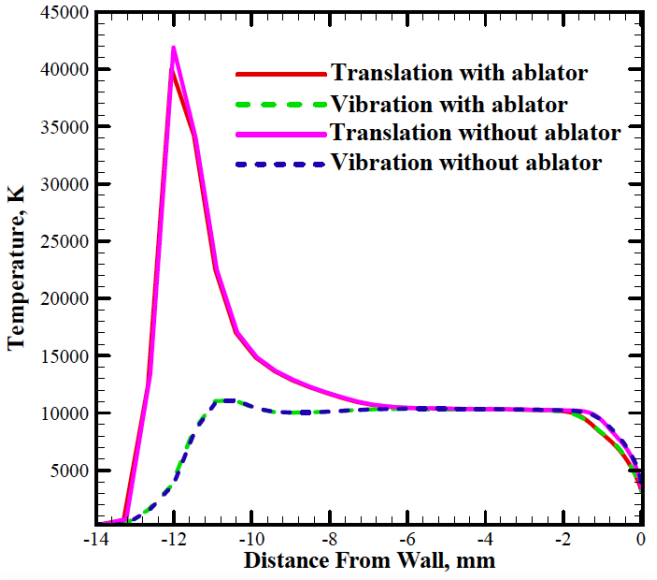

FIGURE 5.38: Temperatures along the stagnation line of the Hayabusa capsule as presented by Kihara et al. (2013) at an altitude of 52.2 km.

The presented results of Kihara et al. (2013) were obtained using an inflow velocity that was over 1,000 ms^{-1} lower than OP2A's; corresponding to a lower altitude than OP2A's results. Due to this there is a difference in the peak and equilibrium temperatures of the order of 10^4 K. Such differences are to be expected for such a magnitude of inflow velocity difference; as can be seen in the peak temperature of Takahashi and Yamada (2018), which is tens of thousands of Kelvin higher, caused by a 2,000 ms^{-1} increase in inflow velocity.

One particular quantitative point which can still be noted, is the high equilibrium temperature produced by OP2A when compared to other published Hayabusa simulations. This behaviour is a limitation of the AUSM spatial integration scheme, which is known to produce overshoots in quantities behind shocks under certain conditions (as noted in Chapter 3). This can also be seen to affect the shock standoff distance in Figure 5.32, which is approximately 3 mm larger than would be expected based on similar work. In spite of this limitation, the results produced by OP2A fall well within the expected quantitative ranges of other published works. Temperature profile shapes remain reasonable, and chemical species profiles show strong qualitative agreement with the results of Fahy et al. (2021) in particular. Additionally, OP2A reproduces flow

shapes and features about the capsule very well, with no qualitative errors being apparent.

Stardust Capsule Forebody Simulation

The Stardust re-entry vehicle returned to Earth in 2006 as part of a NASA comet sample collection mission. This capsule forebody consists of a hemispheric nose with a curvature diameter of 0.2286 m, leading into a cone of half angle 60°. This geometry mirrors that utilised by Liu et al. (2010) and is shown in Figure 5.39.

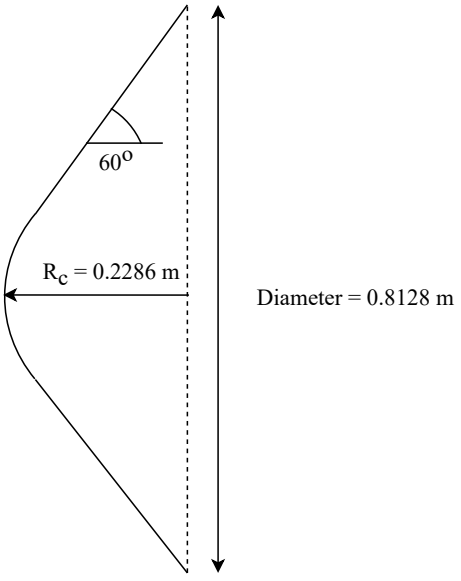

FIGURE 5.39: Geometry of a cross-section of the Stardust capsule forebody, the dotted line marks the edge of the forebody.

An axisymmetric boundary is placed at the capsule symmetry axis, $y = 0.0$ m. This capsule forebody was simulated in flow with freestream conditions approximating 65 km altitude, as presented by Liu et al. (2010) and summarised in Table 5.8.

TABLE 5.8: Freestream flow conditions for the Stardust capsule forebody simulation.

Variable	Freestream Value
ρ (kgm^{-3})	1.4×10^{-4}
u (ms^{-1})	11,414
T_t (K)	230.8
T_v (K)	230.8
p (Pa)	9.4

This capsule was simulated using the AUSM scheme in a 5 species air flow with active chemistry in thermal non-equilibrium, with the aim of studying the stagnation line chemistry profile. The resulting pressure field is shown in Figure 5.40.

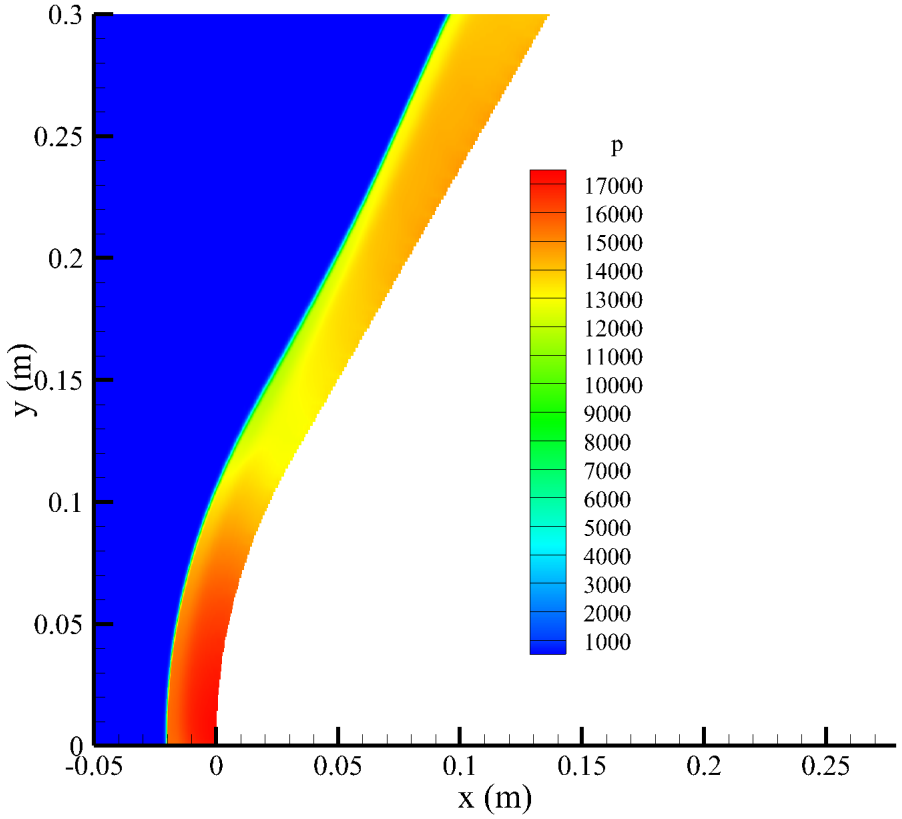

FIGURE 5.40: Pressure distribution across the Stardust forebody.

The pressure distribution shows the desired strong shock, however, in common with the earlier Hayabusa simulations, shock standoff distance is overestimated when compared to similar work such as that of Liu et al. (2010). This can again be attributed to a limitation of the AUSM scheme, together with post-shock temperature overshoots, as evidenced in Figure 5.41.

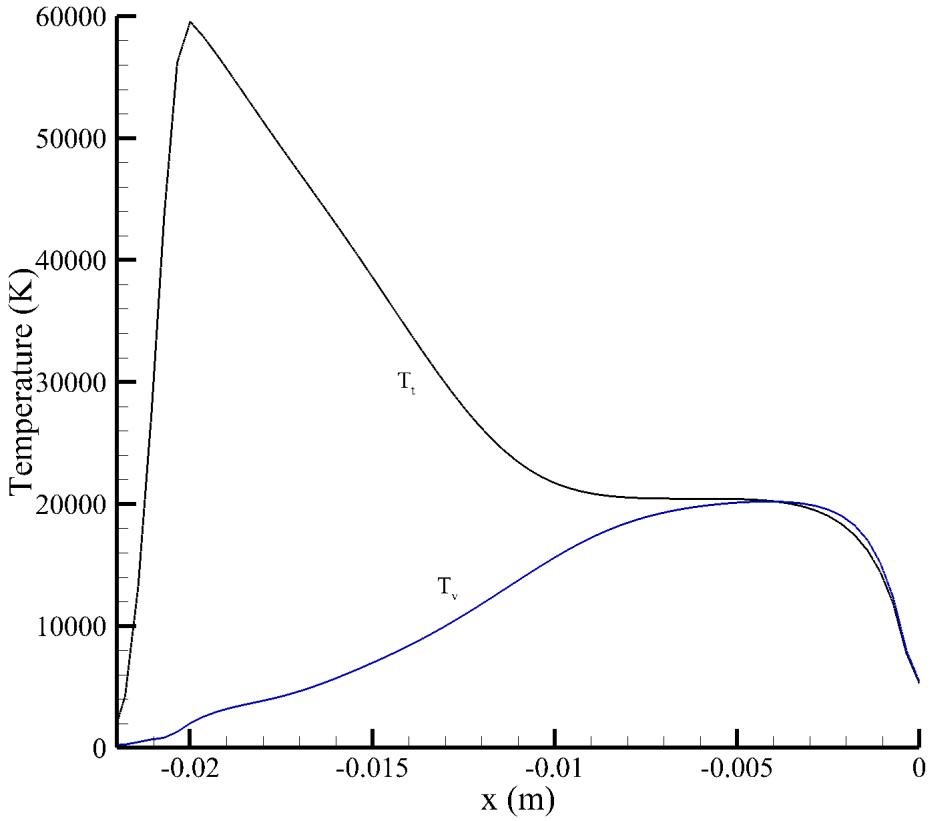

FIGURE 5.41: Temperature profiles along the stagnation line of the Stardust capsule.

In common with the Hayabusa capsule, these overshoots do not appear to drastically modify the temperature profile shapes, which are qualitatively comparable to those of Mankodi et al. (2019), shown in Figure 5.42.

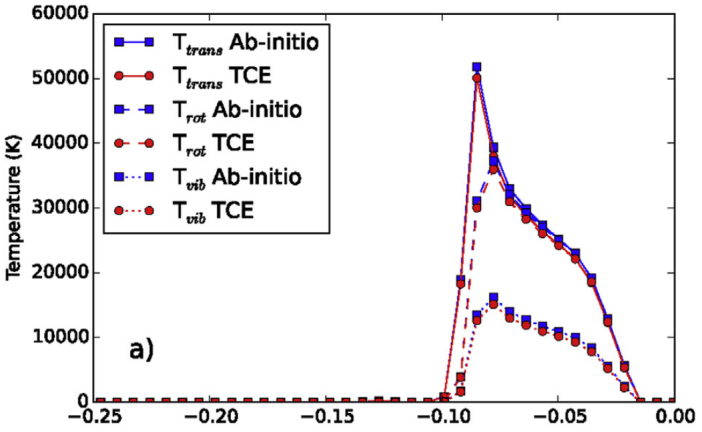

FIGURE 5.42: Temperature profiles along the stagnation line of the Stardust capsule as presented by Mankodi et al. (2019).

Similarly, chemical concentrations along the stagnation line maintain a reasonable profile shape, as seen in Figure 5.43.

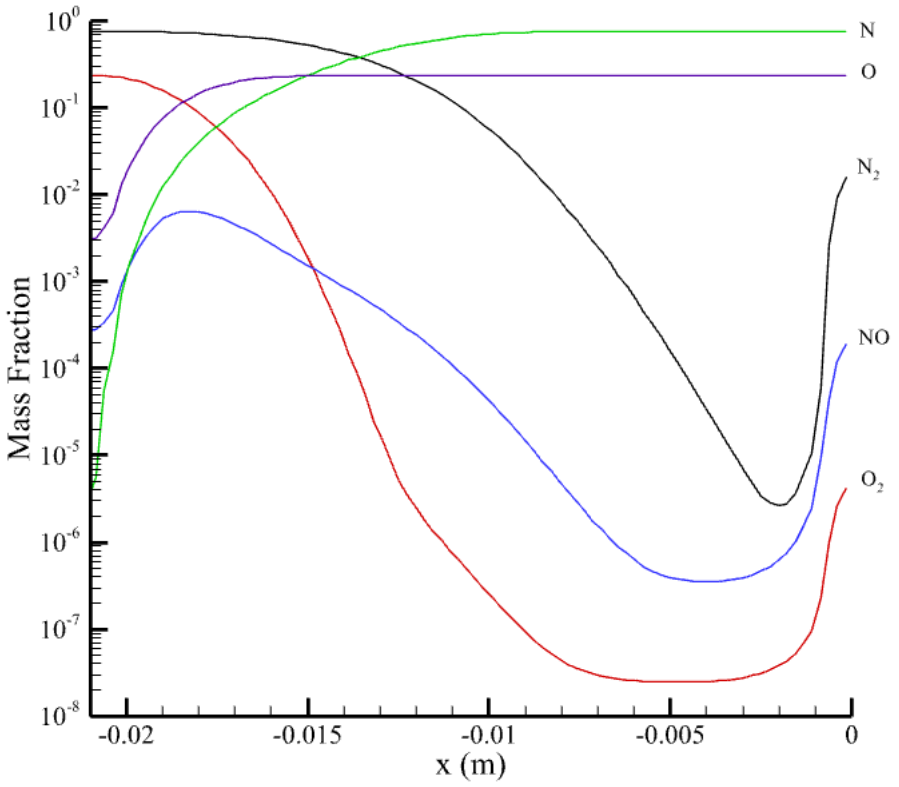

FIGURE 5.43: Chemical species mass density fractions along the stagnation line of the Stardust capsule.

These species concentration profiles show shapes show some qualitative similarity to those presented by Liu et al. (2010) and Mankodi et al. (2019). This chemical behaviour can be seen to exhibit no anomalous changes when moving radially away from the stagnation line, as can be seen in the behaviour of oxygen species' concentrations in Figures 5.44 & 5.45.

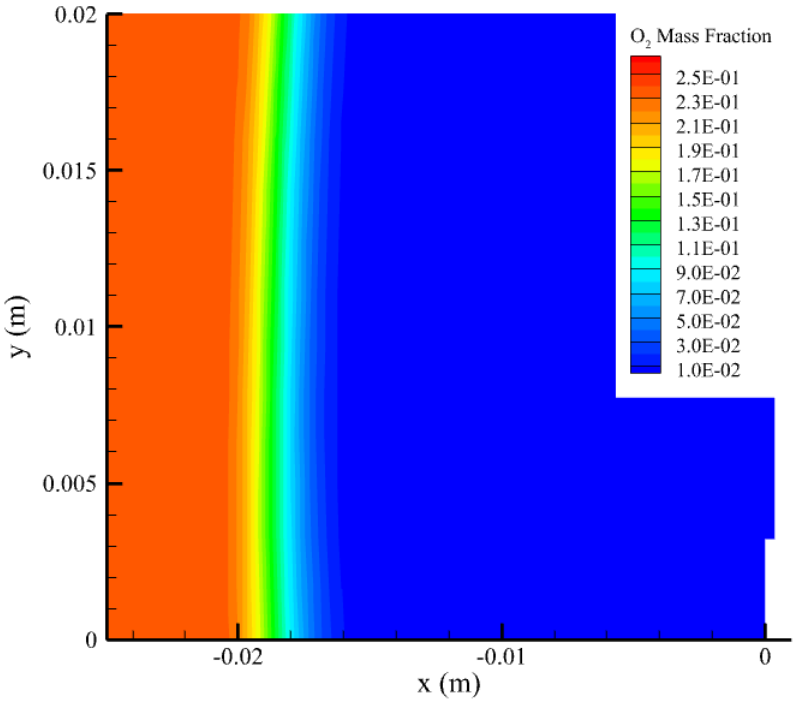

FIGURE 5.44: O_2 mass fraction distribution in the region of the Stardust capsule's stagnation point.

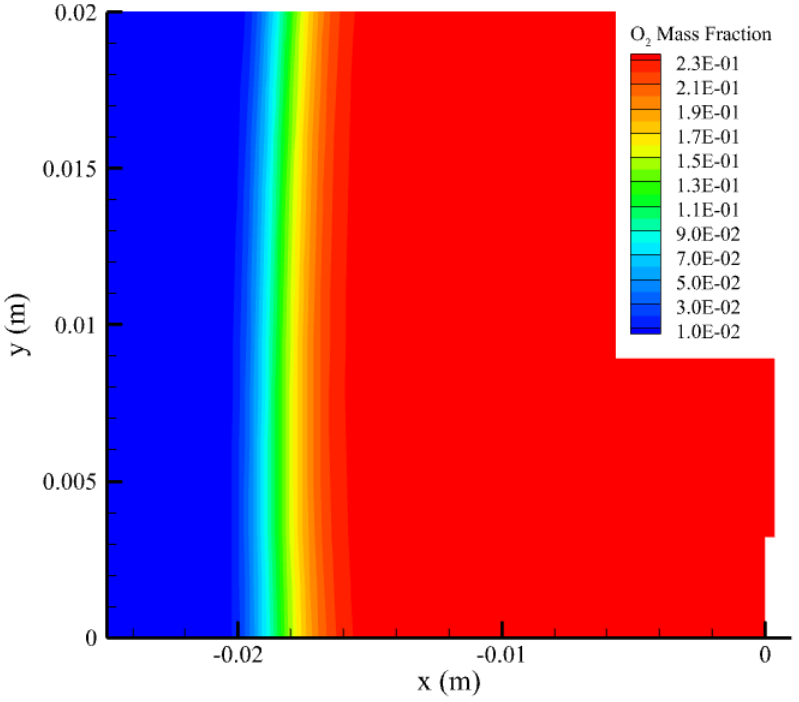

FIGURE 5.45: O mass fraction distribution in the region of the Stardust capsule's stagnation point.

In the case of the Stardust capsule, discrepancies are more prominent when compared to the Hayabusa results. In particular, when OP2A's Stardust results are quantitatively

compared to those of Liu et al. (2010), large differences can be observed. In particular, peak and equilibrium temperatures of around 60,000 K and 22,000 K respectively, are higher than would be expected, and much higher than the values of approximately 26,000 and 12,000 presented by Liu et al. (2010). Indeed, OP2A's results are more in line with those of Mankodi et al. (2019) and Martin et al. (2012), both of which utilise higher inflow velocities. This large quantitative disagreement is likely due to the limitations of the AUSM scheme causing post shock quantity overshoots. This can be rectified through the use of the AUSMDV scheme as outlined in Chapter 3, however this undertaking was not possible within the timeframe of this work. This point is discussed further in Chapter 6

Summary

The simulation of two capsule forebodies, Hayabusa and Stardust, was performed using OP2A with the specific aim of examining thermochemical behaviour along the capsule's stagnation line. Both capsule forebodies have been successfully simulated, but the limitations of the AUSM spatial integration scheme have been made apparent particularly for the Stardust capsule. Limitations upon attainable resolution within the timeframe of this work may also have played a part, as is discussed further in Chapter 6. This Stardust discrepancy also causes the apparent agreement of the Hayabusa simulations to require further examination, as will also be discussed in Chapter 6. In spite of this, good qualitative agreement is shown for temperature and species mass fraction profile shapes across both capsules. In addition, flow fields show strong qualitative agreement with other works and no anomalous features.

6

Conclusions and Future Work

"By no process of sound reasoning can a conclusion drawn from limited data have more than a limited application. "

– Joseph William Mellor

6.1 Summary

This work has been undertaken to investigate the possibilities of producing a numerical toolkit specialising in capsule optimisation simulations. Work has been put into determining the optimal methods for doing so, and investigating advantages and limitations. An effort has been undertaken to create a CFD toolkit specialising in conducting simulations for the optimisation of space capsule design. The motivation behind, development of, and initial results obtained by this toolkit, 'OP2A' have been presented. OP2A is a new multiphysics hypersonic CFD toolkit written in object oriented C++ by the author. OP2A is designed to be optimised for the simulation of hypersonic flows in thermochemical non-equilibrium, such those about re-entry vehicles; with a number of specific features to facilitate simulations pertaining to space vehicle design optimisation.

OP2A is unique among open-source non-equilibrium CFD toolkits, as it discretises using block-structured Cartesian meshes, in order to facilitate rapid mesh generation, as well as efficient processing due to mesh regularity. This rapid mesh generation facilitates the rapid simulation of different capsule geometries with minimal additional time requirements. OP2A utilises the properties of object oriented programming to create an efficient, flexible and extensible toolkit in order to facilitate the testing of thermochemical non-equilibrium models. Overriding polymorphism is used throughout, and

allows the user to select simulation components interchangeably, including thermochemical models and numerical integration methods. This allow simulation methods to be rapidly interchanged, as required by changes to re-entry capsule geometry. This polymorphism also makes OP2A easy to extend to additional models and methods, an extremely useful trait when investigating thermochemical non-equilibrium effects.

OP2A simulates an extended system of Navier-Stokes equations. This includes formulae governing the effects of thermochemical non-equilibria upon the Navier-Stokes system. Such models include multiple tools for calculating viscous quantities; the Wilke model and the Gupta model. As well as the capacity to simulate different chemical mixtures in varying states of thermal non-equilibrium. Multiple temperatures can be specified in order to model the degree of thermal non-equilibrium within a mixture. These chemical mixtures include Earth and Mars atmospheres and Argon mixtures commonly found in laboratory work. Work has been presented using the 5 and 11 species Earth atmosphere mixtures, with full chemistry included featuring 17 and 41 reactions respectively as well as a three species Argon mixture.

OP2A is fully flexible regarding the choice of simulation methods employed and features multiple models for the solution of the extended Navier-Stokes system as well as multiple numerical methods for their evolution. These include the AUSM and AUSMDV spatial integration schemes and two time integration schemes; forward Euler and Runge-Kutta two step. In addition there are multiple flux limiting schemes incorporated. All of these components and models can be used interchangeably allowing for additional flexibility.

OP2A feature a hybrid parallelisation scheme and is parallelised over shared memory systems and utilises overriding polymorphism to allow for run-time simulation changes. The efficacy of this parallelisation has been presented in terms of simulation run-time decrease and found to be close to optimal, with very little evidence of implementation overheads. OP2A is also designed to facilitate hybrid parallelisation with MPI for the undertaking of larger scale simulations. OP2A also features an error handling system allowing it to overcome difficulties associated with thermochemical non-equilibrium adaptively, allowing for optimised time step values throughout an unsteady simulation, outside of the regular CFL considerations. This system provides additional stability to simulations upon altering simulation geometry and/or models.

OP2A has been used to perform various simulations in order to demonstrate the effective implementation of its models. These begin with zero dimensional analyses of the thermochemical models implemented; performed by simulating heat baths and relaxing them over time. These were performed for a variety of temperatures and with a variety of chemical mixtures. Their results were then used to determine the accuracy of

the thermochemical models currently present in OP2A. Simulations of diatomic nitrogen in states of thermal non-equilibrium showed a strong degree of qualitative agreement with results produced by LeMANS as well as the hy2foam results of Casseau et al. (2016b), in addition to strong quantitative agreement.

A series of heat baths were simulated containing a five species air mixture containing; N_2, O_2, NO, N, O. These simulations again show a strong degree of qualitative alignment with the work of Casseau et al. (2016b) as well as Haas and McDonald (1993) and Scanlon et al. (2015). A limited quantitative assessment has also shown good agreement with other published works including Casseau et al. (2016b). These air-5 heat baths were simulated in various states of thermal non-equilibrium and both chemical and temperature behaviour was found to be as expected when compared to the earlier N_2 heat bath tests.

This series of air-5 heat baths was followed by a series of similar simulations utilising an 11 species air mixture; containing all of the air-5 species as well as their charged equivalents and electrons. The behaviour of neutral species' concentrations over time remained largely unchanged from the air-5 testing. This was expected behaviour and occurred simply due to the relatively lower levels of charged species. The behaviour of charged species' concentrations was examined and found to be explicable with reference to the behaviour of temperature(s) over the simulation timeframe. No particular anomalous behaviour was noted in either temperature or species concentration behaviour over the course of these simulations. These zero dimensional tests served to provide information on the accuracy of OP2A's thermochemical modelling components.

Next a series of two dimensional simulations was performed. These utilised a standard shock tube setup, with two regions of static N_2 gas separated by a discontinuity and is useful due to the existence of an analytical solution. This case was simulated in thermochemical equilibrium and used to test OP2A's spatial and time integration routines. The resulting numerical profiles for density, temperature, pressure and velocity were compared to their analytic expectations. These profiles showed minor differences located at discontinuity points, in common with other presented shock tube work such as Hajman et al. (2007). This case was then used to test a number of ancillary qualities of OP2A. Grid independence was tested by simulating the shock tube case at various resolutions. As expected, the numerical results approached their analytical equivalent as resolution increased, and no anomalous results were noted. The shock tube case was also used to test the performance of OP2A's parallelisation scheme. The shock tube case was simulated with varying numbers of computational cores and the total run time recorded. The run time decreased close to linearly with increasing core numbers, demonstrating an efficient parallelisation scheme with little overhead.

Lastly, a series of two dimensional axisymmetric simulations were performed. These began with simulations of a double cone object in a hypersonic flow. This setup was simulated in an axisymmetric configuration and flow distributions were analysed for the presence of key features. These features, including shock waves and their various interactions were clearly identified, and directly compared to other published results including those of Expósito and Rana (2019). Whilst exact quantitative comparison was not possible, qualitative agreement was found to be strong.

The next series of axisymmetric simulations were of re-entry capsule forebodies. These simulations were undertaken with the aim of investigating OP2A's ability to model the flow about re-entry capsules, including their thermochemical behaviour along the capsule's stagnation line. The first capsule to be simulated was the Hayabusa re-entry capsule utilised by JAXA. This capsule's forebody was simulated in an axisymmetric configuration in an air-5 flow in thermochemical non-equilibrium. The AUSM spatial integration method was utilised. The presented results show the existence of the expected sharp bow shock, and temperature profiles show shapes along the stagnation line which are both qualitatively and quantitatively similar to those presented by other similar works. Chemical species concentration levels show similarly accurate shapes. However, the temperature profiles showed some discrepancies in the average equilibrium temperatures behind the shock, as well as shock stand-off distance, likely a limitation of the AUSM scheme.

A similar simulation was performed using the forebody of the Stardust capsule. This simulation showed a similar level of qualitative agreement with other works when evaluating profile shapes, for temperatures and species concentrations, along the stagnation line. However, a larger discrepancy in temperature profile along the stagnation line was noted when compared to the work of Liu et al. (2010). These discrepancies were again attributed to the limitations of the spatial integration scheme used. Both of these capsule simulations have demonstrated the immediate capabilities and limitations of OP2A and the models it employs.

6.2 Conclusions

This work set out with the aim of determining whether a numerical toolkit could be created to better simulate re-entry flow for capsule design optimisation. In addition, this work aimed to ascertain the advantages and limits of such an approach. To this end a new hypersonic CFD toolkit, OP2A, has been developed and presented, together with its initial results. OP2A specialises in performing simulations which can inform the design of space vehicles, and has been designed and built with a number of features

specifically to facilitate this. The effectiveness of OP2A in performing simulations pertinent to the study of re-entry flows and capsule design has been evaluated and several significant simulation results have been obtained.

OP2A is an object-oriented multiphysics CFD toolkit featuring a novel combination of features designed to facilitate simulations for space capsule design testing. OP2A is unique among open-source object-oriented multiphysics CFD suites in prioritising block-structured Cartesian meshes over the more commonly used unstructured mesh. This feature permits much more rapid mesh generation, an extremely useful quality for performing capsule optimisation simulations. OP2A also features the capability of hybrid parallelisation, over both shared and distributed memory systems, with OpenMP and MPI respectively. This provides a more efficient parallelisation scheme than pure MPI implementations, particularly when operating on machines with large number of cores per compute node. Once these features were designed and implemented, work was done to test OP2A and draw conclusions regarding its strengths and limitations.

Any space vehicle re-entry simulation requires the ability to model non-equilibrium flows. Zero dimensional heat bath testing was used to evaluate the efficacy of OP2A's thermal relaxation modelling in order to demonstrate the software's ability to model post shock flows in thermal non-equilibrium. The results show clear and strong agreement with those obtained using LeMANS and hy2foam, presented by Casseau et al. (2016b). This was clear both in terms of qualitative behaviour and using estimated quantitative metrics such as eventual equilibrium temperature. The only noted difference being a very small 'lag' in vibrational temperature equilibration in the high T_v case, readily attributable to the lower time step utilised by OP2A. This constitutes a welcome result for a two temperature model splitting energy between a translational-rotational mode and a vibrational-electronic-electron mode. This result was obtained using various temperature splits, limited by the range of temperatures under which the diffusive and thermal relaxation models are known to be valid. These temperatures cover a reasonable portion of those expected in the hypersonic regime. Overall temperature equilibrated towards the translational temperature, as expected, and no anomalous behaviour was noted. Whilst these temperature ranges are hypersonic relevant, they do not cover the entire range of temperatures used in this work, due to unexpected overshoots, as will be discussed later within this section. Whilst these results are constrained to only one temperature split with two temperatures total, they demonstrate the ability of OP2A to correctly model energy exchange between modes. This means that thermal modelling capabilities are both reasonably accurate and readily expandable, satisfying two key requirements.

Zero dimensional heat bath simulations were also used to assess the accuracy of OP2A's chemical modelling, another vital component to re-entry capsule simulation. Results were obtained using 5 and 11 species air mixtures in various states of thermal non-equilibrium. The 5 species air model, relaxed in thermal equilibrium, produced results

which were directly qualitatively comparable to the work of Casseau et al. (2016b). When compared, the behaviour of species concentrations showed good qualitative agreement with such works. In particular, the rates of the dominant dissociation reactions showed strong agreement. Certain aspects of OP2A's chemical response were found to lag their comparators from LeMANS, which was evident in both chemical and thermal response. However such a degree of divergence is not considered to be unexpected given differences in simulation time step and uncertainties in initial species concentrations applied. Repetition of these heat bath simulations with an exact time step match would be of interest to quantify the relative magnitude of the effects of time step differences and initial concentration uncertainty. Overall, the agreement between OP2A's results and those of other comparable code suites was found to be strong. This testing was then repeated in thermal non-equilibrium. Whilst direct comparison with existing work was not possible, all aspects of concentration behaviour were readily explained by the relative magnitudes of the translational, vibrational and Park temperatures. The behaviour of temperatures over the simulated time period appeared as a straightforward combination of the chemical and thermal relaxation effects shown in prior simulations, as expected.

These air-5 heat bath tests were repeated using an 11 species air mixture. Neutral species' behaviour shows strong similarity with their air-5 counterparts, as should be expected given their higher concentrations at the temperatures considered. Charged species show expected qualitative behaviours based upon the behaviour of temperatures over time. The strong match between electron density and positive ion density shows that quasi-neutrality was achieved throughout to a reasonable degree of accuracy with less than 1% discrepancy. This chemical modelling was however limited in a key regard, OP2A utilises a single controlling temperature for each reaction, for both forward and backward reaction rates. This likely leads to inaccurate predictions of reactions rates for multiple reaction types. In particular, reactions involving electrons as a participant in one direction only (for example dissociative recombination reactions) will be likely governed by electron temperature in one direction and translational temperature in the other. The modelling performed by OP2A did not account for this, and may thus have some discrepancy when compared to other work. However, such reactions are typically low in frequency in the case studied herein, hence these discrepancies should be small. Regardless, an assessment of this effect would constitute a clear avenue for future work.

Whilst the thermochemical testing showed no anomalous behaviour in reaction rates and strong agreement with other work in a number of metrics, it was also limited by overall modelling constraints. The presented results lack any evaluation of radiative effects, and electromagnetic effects are limited to those presented by electron pressure gradients. Both of these limitations will exclude certain types of behaviour which may

be significant in certain thermochemical environments and will be discussed in the following section in greater detail.

The evaluation of the accuracy of time and spatial integration routines began with a two dimensional shock tube case, utilised due to its calculable analytic solution. This was simulated using N_2 in thermochemical equilibrium using the AUSM and forward Euler schemes for spatial and time integration respectively. The numerical results produced by OP2A align well with analytic expectations, with differences at expected levels for the schemes used. This case was then used to demonstrate grid resolution invariance, and evaluate the effectiveness of OP2A's parallelisation scheme. Grid invariance was clearly demonstrated for the shock tube case, further reinforcing the good agreement between numerical and analytical solutions. In future work, grid invariance should ideally be demonstrated for a greater range of cases, particularly more complex cases. Parallelisation was shown to be highly efficient across shared memory systems. This investigation could be expanded in future by investigating the effects of simulation size upon computational efficiency; to ensure that efficiency is not compromised as simulations increase in scale. An avenue for further future verification of OP2A's thermochemical modelling would be through comparison with recently produced quantitative chemistry data, such as that presented by Torres et al. (2022).

In order to demonstrate OP2A's resolution of complex flow fields, a 2d axisymmetric simulation of the double cone case was performed. The results of this simulation were compared to equivalents in the surrounding literature, including Candler et al. (2002) and Expósito and Rana (2019). Whilst these comparisons yielded promising qualitative alignment, they could not be directly compared due to differing inflow conditions. Reappraising this case with identical inflow conditions is a clear opportunity for future work, and would allow a more thorough quantitative assessment. In spite of this, the qualitative comparisons show strong agreement, with no unexplained or anomalous features present.

Simulating cases relevant to capsule design requires OP2A to be able to implement thermochemical non-equilibrium models in more realistic re-entry configurations. In order to investigate such post-shock thermochemical behaviour, various capsule forebodies were simulated in a two dimensional axisymmetric configuration and post shock flows analysed. Grids corresponding to multiple capsules were generated rapidly owing to the simple grid type utilised by OP2A. The behaviour of temperatures and chemical species concentrations along the stagnation line were then presented and examined.

The first chosen capsule was the Hayabusa capsule, simulated in re-entry conditions corresponding to an altitude of 60 km. The gas mixture used was air-5 in thermochemical non-equilibrium. The shape and resolution of the produced boy shock were found to be in good agreement with other published simulations, including those of Kihara

et al. (2013) and Ozawa et al. (2011). Examining temperature and chemical species concentration profiles along the stagnation line showed that they possess strong qualitative agreement with publications of similar simulations. Additionally, reaction behaviours show reasonable behaviour with respect to the behaviour of their controlling temperatures. Quantitative comparisons with existing work were limited by the differences in altitude of conducted simulations. However, quantitative values such as peak and equilibrium temperatures fell within expected quantitative ranges. However a discrepancy in post-shock equilibrium temperature was potentially found; this is found in conjunction with an overestimation of the shock stand-off distance (SSD). These discrepancies are likely a limitation of the AUSM spatial integration scheme used, and lead to temperature and SSD values which align more closely with the DSMC simulations of Ozawa et al. (2011) than most comparable CFD simulation results Takahashi and Yamada (2018); Fahy et al. (2021); Suzuki et al. (2014). The AUSMDV spatial integration scheme is implemented within OP2A, and would be expected to rectify these overshoots Wada and Liou (1997). However, results using this scheme were not obtained within the time frame of this work and hence constitute a promising avenue for future work.

The second capsule simulated was the Stardust capsule, with inflow conditions corresponding to an altitude of approximately 65 km. The overall flow field showed strong qualitative alignment with the simulation results of Trumble et al. (2010b). Again temperature and species concentration profiles along the stagnation line were examined. It remained true that for all profiles reasonable qualitative agreement was shown between OP2A's results and other published works. This included the manner in which Stardust's results differed from Hayabusa's; with a smaller equilibrium region behind the shock in common with Liu et al. (2010). This leads to concurrent smaller plateaus of chemical concentration behind the shock, again in common with Stardust simulations as presented by Liu et al. (2010) among others. However, in the Stardust case, the inflow conditions were chosen to match those of Liu et al. (2010), however, differences in simulation method render exact quantitative alignment of results unfeasible. Specifically, the simulations of Liu et al. (2010) feature not only radiative modelling, but also completely different chemistry including Carbon and Argon species. The temperature profiles of OP2A feature higher peak and equilibrium temperatures than those of Liu et al. (2010). These temperatures are also somewhat above expectations when compared to other Stardust simulations, such as those of Trumble et al. (2010b) and Martin et al. (2012). However, quantitative comparisons with such works are difficult due to differences in inflow conditions used. In addition, published works may vary significantly in output for similar input conditions, as can be seen in the results of Shang and Surzhikov (2011) and Martin et al. (2012), rendering such quantitative comparisons even more difficult. As with the Hayabusa case, these results are attributable to the limitations of the AUSM spatial integration scheme, with Liu et al. (2010) instead utilising the Steger-Warming flux vector splitting scheme.

An additional form of uncertainty is attributable to resolution limitations upon the produced capsule results. In a particular example, the discrepancies in shock stand-off distance may be partially explicable through the capsule geometry uncertainty of order of magnitude of around 0.5 mm. The exact quantitative effects of this upon the produced shock stand-off distance are difficult to estimate ab initio. A grid variance study of the Stardust case would yield information regarding this, and should hence be considered a priority area of future study.

The research aimed to determine whether it is possible to produce a numerical toolkit better tailored to simulations for capsule optimisation. Such a toolkit, OP2A, has been designed, developed and characterised, with verification performed and clear advantages and limitations described. The optimal methods for a capsule optimisation toolkit to use have been put forward and these suggested methods have been implemented within OP2A. OP2A has been used to perform simulations relevant to capsule design in order to test the efficacy of these methods. These completed simulations have demonstrated the efficacy and limitations of the implemented methods, and the creation of a toolkit in line with the objectives set out in Chapter 1 of this document. The creation of OP2A as an open-source software tool will hopefully prove useful for the hypersonic CFD community, both in its current form, and with any of the future refinements which will now be suggested.

6.3 Future Work

Whilst OP2A has been proven to be capable of performing re-entry simulations relevant to space vehicle optimisation, there remain several improvements and expansions which can be made; to expand the range of possible simulations, and to improve the already present capabilities. Such expansions open up possibilities for simulating ever more complex and interesting behaviour, whilst retaining OP2A's rapid simulation capabilities.

The first key area of improvement would be the thorough verification of the AUSMDV spatial integration scheme in order to obtain better evaluations of post-shock temperatures and shock stand-off distances. Beyond this, the most obvious addition to OP2A to allow for more rapid simulation with AUSMDV would be the implementation of implicit time integration methods. Such methods would mitigate a large percentage of the overshoots mentioned in section 4.4 without the need for lower time step increments. OP2A is built so as to allow for different time integration methods to be implemented without requiring modifications to other areas; hence implementing an implicit method will be relatively straightforward. Implicit time integration methods would also be expected to improve the accuracy of derived quantities including those

explored herein. They would also allow for improved direct quantitative comparisons with existing work, many of which utilise implicit time integration schemes.

Implementation of implicit time integration methods would also facilitate the use of further spatial integration schemes. This is due to the fact that more accurate spatial integration methods are more sensitive to time step constraints when explicit time integration schemes are used. For example the AUSMPW+ scheme, which requires additional stencil information for each flux evaluation. This additional stencil information is readily available within OP2A due to the object layout described in Chapter 4.

In order to further improve OP2A's simulation speed and efficiency, a key contribution would be to expand OP2A's parallelisation capabilities in order to efficiently simulate such large domains at reasonable resolutions. This requires the implementation of distributed memory parallelisation using MPI, the framework for which is already present within OP2A, as can be seen in Chapter 4. Any MPI implementation can be readily combined with the existing OpenMP to produce a hybrid system in order to maximise potential parallelisation efficiency Borges et al. (2014). OP2A also has the METIS library (developed by Karypis and Kumar (1998)) integrated for mesh partitioning between compute nodes. This library automatically partitions finite volume/element grids so as to minimise communication workload between compute nodes. Boundaries between compute nodes will require the creation of MPI ghost cells, such ghost cells and associated boundary conditions are already present within OP2A. Unlike the present OpenMP scheme, MPI implementation will also require the construction of routines to pass CFD information between MPI ghost cells. The implementation of MPI parallelisation would also allow OP2A to perform simulations in three dimensions. Comparing 3d simulations to their 2d axisymmetric counterparts would provide additional verification and analyses of the currently implemented models.

The resolution that OP2A can obtain can be further improved through the expansion of adaptive mesh refinement (AMR). AMR refines certain areas of the spatial domain over the course of the simulation according to some criteria (for example high gradient regions). Such refinement can be performed recursively until an acceptable resolution is reached. This allows for high boundary and shock layer resolutions to be achieved without requiring this high resolution to be maintained across the entire domain. The implementation of AMR in OP2A is facilitated by the existence of multiple grid levels within the **Grid** object described in Chapter 4 and the use of block-structured Cartesian meshes as outlined in Chapter 3. These levels allow for a more refined high resolution grid to be stored for certain areas of the spatial domain. These levels are also recursively extensible, meaning that any number of layers can be stored, as required.

A complementary addition would be that of ablative modelling. At the simplest level, this could be implemented as a generic source term for the mass density of ablated species together with an energy source term. The addition of ablated species to the

flow would also necessitate the addition of hydrocarbon species to the currently available air mixtures. This implementation would provide an instantaneous picture of ablative effects. However, such an implementation would neglect the effect of capsule shape changes due to ablation, limiting OP2A's ability to model capsule re-entry continuously. Whilst these shape changes are often neglected (as evinced by Ozawa et al. (2011) and Fahy et al. (2021)), sophisticated simulations account for ablation utilising a mesh which extends within the capsule surface. This method can be implemented straightforwardly owing to the use of block-structured Cartesian meshes, which allow for modifications to the capsule surface geometry to be made easily, with no remeshing required and with no special treatment required by the solvers. The implementation of full ablative modelling will also be made easier with the addition of AMR which will allow additional grid layers to be introduced as required to facilitate high resolution modifications to capsule surface geometry.

Other potential expansions to OP2A would be to expand the types of the physics it can simulate. As described in Chapter 4, OP2A treats each of its cell-centred source terms individually and independently. This makes them readily expandable, allowing for the swift implementation of new cell-centred physical contributions. Such physics could include both radiative and electromagnetic modelling.

Radiative modelling is often incorporated into re-entry simulations in order to perform comparisons with observational data. For example, Takahashi and Yamada (2018) utilises a radiative transport model with an assumed Boltzmann distribution of electronic energy state population. Electronic temperature is used to control a black body type emission model in order to estimate the radiative heat flux impinging upon the Hayabusa capsule. Such an implementation in OP2A would allow for temperatures to be modelled with a higher degree of accuracy, as well as facilitating a better estimate of capsule heat loads and more quantitative comparisons. Implementing such models within OP2A would be relatively straightforward due to the independent modelling of source terms described in Chapter 4.

In a similar vein, electromagnetic (EM) modelling can be implemented through cell centered momentum and energy source terms. The addition of EM modelling effects would allow for modelling of the radio blackout mitigation methods outlined in Chapter 1. In addition, MHD models allow for the simulation of novel applications, such as re-entry power generation suggested by Wan et al. (2004) and MHD heat shielding as proposed by Matsuda et al. (2008). An MHD capable CFD toolkit will be able to contribute to recent efforts to examine MHD effects in the boundary layer, such as the work of Parent et al. (2022).

Another more involved addition would be that of turbulence modelling, which would likely be required to improve the accuracy of results at lower altitudes. Implementation of turbulence modelling would also allow more direct comparisons with existing

experimental results. In particular, experimental studies of the double cone case such as that of Candler et al. (2002), and MHD effects upon cylinders in hypersonic flow such as the work of Bityurin et al. (2004).

Lastly, a more distant aim for OP2A would be to expand the range of altitudes which can be realistically simulated. This would require some degree of hybridisation between OP2A's CFD techniques and DSMC techniques for higher altitudes. OP2A is already prepared for this with the inclusion of varied data holding objects as described in Chapter 4. Such a coupling between CFD and DSMC has been achieved by contemporary work by researchers at the University of Strathclyde. These techniques have been used for the simulation of bodies in Earth atmosphere hypersonic flows as presented by Casseau et al. (2016a) and Espinoza et al. (2016).

Any exploration of the future development to a code suite such as OP2A will necessarily be partial. There are a myriad of ways in which this software could be expanded; as well as undoubtedly many areas for optimisation and improvement of existing code. It is the author's sincere hope that the OP2A toolkit will see both use and improvement from others within the field.

Appendix A

Tables of Diffusive Data Coefficients

These tables list parameter value data used in the calculation of diffusive terms with the Gupta collisional model outlined in chapter 2.

TABLE A.1: Variable values used in calculating Gupta model collision (1,1) integrals $\pi\Omega_{(1,1)}$.

Species 1	Species 2	A	B	C	D
N2	N2	-6.0614558E-03	1.2689102E-01	-1.0616948E+00	8.0955466E+02
N2	O2	-3.7959091E-03	9.5708295E-02	-1.0070611E+00	8.9392313E+02
O2	O2	-8.0682650E-04	1.6602480E-02	-3.1472774E-01	1.4116458E+02
N2	N	-1.0796249E-02	2.2656509E-01	-1.7910602E+00	4.0455218E+03
O2	N	-1.1453028E-03	1.2654140E-02	-2.2435218E-01	7.7201588E+01
N	N	-9.6083779E-03	2.0938971E-01	-1.7386904E+00	3.3587983E+03
N2	O	-2.7244269E-03	6.9587171E-02	-7.9538667E-01	4.0673730E+02
O2	O	-4.8405803E-03	1.0297688E-01	-9.6876576E-01	6.1629812E+02
N	O	-7.8147689E-03	1.6792705E-01	-1.4308628E+00	1.6628859E+03
O	O	-6.4040535E-03	1.4629949E-01	-1.3892121E+00	2.0903441E+03
N2	NO	-1.9295666E-03	2.7995735E-02	-3.1588514E-01	1.2880734E+02
O2	NO	-6.4433840E-04	8.5378580E-03	-2.3225102E-01	1.1371608E+02
NO	N	-1.5770918E-03	1.9578381E-02	-2.7873624E-01	9.9547944E+01
NO	O	-1.0885815E-03	1.1883688E-02	-2.1844909E-01	7.5512560E+01
NO	NO	0.0000000E+00	-1.1056066E-02	-5.9216250E-02	7.2542367E+01
N2	NOp	0.0000000E+00	9.1205839E-02	-1.8728231E+00	2.4432020E+05
O2	NOp	-3.7822765E-03	1.7967016E-01	-2.5409098E+00	1.1840435E+06
N	NOp	-1.9605234E-02	5.5570872E-01	-5.4285702E+00	1.3574446E+09
O	NOp	-1.6409054E-02	4.6352852E-01	-4.5479735E+00	7.4250671E+07
NO	NOp	-8.1158474E-03	2.1474280E-01	-2.0148450E+00	6.2986385E+04
e	N2	-1.0525124E-02	1.3498950E-01	1.2524805E-01	1.5066506E-01
e	O2	2.3527001E-02	-6.9632323E-01	6.8035475E+00	1.8335509E-09
e	N	0.0000000E+00	1.6554247E-01	-3.4986344E+00	5.9268038E+08
e	O	9.9865506E-03	-2.7407431E-01	2.6561032E+00	4.3080676E-04
e	NO	1.0414818E-01	-2.8369126E+00	2.5323135E+01	7.7138358E-32
N2	Np	-1.0687805E-02	2.4479697E-01	-2.3192863E+00	1.0689229E+05
O2	Np	0.0000000E+00	8.7745537E-02	-1.8347158E+00	1.9830120E+05
N	Np	-4.0078980E-03	1.0327487E-01	-9.9473323E-01	2.8178290E+03
O	Np	-1.5767256E-02	3.5405830E-01	-3.0686783E+00	4.6336779E+05
NO	Np	0.0000000E+00	8.6531037E-02	-1.8117931E+00	1.8621272E+05
N2	Op	1.0352091E-02	-1.5733723E-01	2.9326150E-02	2.1003616E+03
O2	Op	0.0000000E+00	9.3559978E-02	-1.9842999E+00	4.3097490E+05
N	Op	-2.4288224E-02	5.6305072E-01	-4.6849679E+00	2.7303024E+07
O	Op	-3.8347988E-03	9.9930498E-02	-9.6288891E-01	1.9669897E+03
NO	Op	8.3856973E-03	-1.0972656E-01	-3.3896281E-01	5.2004690E+03
N2	N2p	-2.9123716E-03	9.6850678E-02	-1.1416540E+00	7.9252169E+03
O2	N2p	-4.0893007E-03	1.7795266E-01	-2.3800543E+00	5.1949298E+05
N	N2p	-1.4501284E-02	4.1085338E-01	-4.0115094E+00	1.5735451E+07
O	N2p	-1.6923472E-02	4.6067692E-01	-4.3294966E+00	2.5538927E+07
NO	N2p	-9.2292933E-03	2.9813226E-01	-3.2899475E+00	4.9147046E+06
N2	O2p	1.2405624E-02	-2.0452111E-01	3.5478475E-01	1.0778357E+03
O2	O2p	-8.9520932E-03	2.2749642E-01	-2.0758341E+00	6.7674419E+04
N	O2p	0.0000000E+00	8.3065769E-02	-1.7501512E+00	1.0846799E+05
O	O2p	-2.9417970E-03	1.5129273E-01	-2.2497964E+00	2.9325215E+05
NO	O2p	1.3731123E-02	-2.3920299E-01	6.7093226E-01	4.0068731E+02

TABLE A.2: Variable values used in calculating Gupta model collision (2,2) integrals $\pi\Omega_{(2,2)}$.

Species 1	Species 2	A	B	C	D
N2	N2	-7.6303990E-03	1.6878089E-01	-1.4004234E+00	2.1427708E+03
N2	O2	-8.0457321E-03	1.9228905E-01	-1.7102854E+00	5.2213857E+03
O2	O2	-6.2931612E-03	1.4624645E-01	-1.3006927E+00	1.8066892E+03
N2	N	-8.3493693E-03	1.7808911E-01	-1.4466155E+00	1.9324210E+03
O2	N	-1.0608832E-03	1.1782595E-02	-2.1246301E-01	8.4561598E+01
N	N	-7.7439615E-03	1.7129007E-01	-1.4809088E+00	2.1284951E+03
N2	O	-8.3110691E-03	1.9617877E-01	-1.7205427E+00	4.0812829E+03
O2	O	-3.7969686E-03	7.6789981E-02	-7.3056809E-01	3.3958171E+02
N	O	-5.0478143E-03	1.0236186E-01	-9.0058935E-01	4.4472565E+02
O	O	-4.2451096E-03	9.6820337E-02	-9.9770795E-01	8.3320644E+02
N2	NO	-6.8237776E-03	1.4360616E-01	-1.1922240E+00	1.2433086E+03
O2	NO	-6.8508672E-03	1.5524564E-01	-1.3479583E+00	2.0037890E+03
NO	N	-1.4719259E-03	1.8446968E-02	-2.6460411E-01	1.0911124E+02
NO	O	-1.0066279E-03	1.1029264E-02	-2.0671266E-01	8.2644384E+01
NO	NO	-7.4942466E-03	1.6626193E-01	-1.4107027E+00	2.3097604E+03
N2	NOp	0.0000000E+00	8.5112236E-02	-1.7460044E+00	1.4498969E+05
O2	NOp	0.0000000E+00	8.4737359E-02	-1.7290488E+00	1.2485194E+05
N	NOp	-2.1009546E-02	5.8910426E-01	-5.6681361E+00	2.4486594E+09
O	NOp	-1.5315132E-02	4.3541627E-01	-4.2864279E+00	3.5125207E+07
NO	NOp	1.1055777E-02	-1.6621846E-01	1.4372166E-01	1.3182061E+03
e	N2	-4.2254948E-03	-5.2965163E-02	1.9157708E+00	6.3263309E-04
e	O2	9.6744867E-03	-3.3759583E-01	3.7952121E+00	6.8468036E-06
e	N	-1.0903638E-01	2.8678381E+00	-2.5297550E+01	3.4838798E+33
e	O	-1.7924100E-02	4.0402656E-01	-2.6712374E+00	4.1447669E+02
e	NO	0.0000000E+00	5.4444485E-02	-1.2854128E+00	1.3857556E+04
N2	Np	-7.0776069E-03	1.7917938E-01	-1.9102410E+00	4.6736263E+04
O2	Np	9.8019578E-03	-1.4699425E-01	3.9382460E-02	1.5112165E+03
N	Np	-1.4271306E-02	3.0401993E-01	-2.4573879E+00	5.3694705E+04
O	Np	-1.7907392E-02	4.1207892E-01	-3.5343610E+00	1.4987678E+06
NO	Np	1.1716366E-02	-1.9289789E-01	4.0269474E-01	6.0891590E+02
N2	Op	1.8733000E-02	-3.6163781E-01	1.6947101E+00	2.5244859E+01
O2	Op	1.4207970E-02	-2.4736726E-01	7.4561859E-01	3.2519188E+02
N	Op	-2.1681211E-02	5.2300453E-01	-4.5118623E+00	2.3467766E+07
O	Op	-1.6032919E-02	3.7114396E-01	-3.2050078E+00	5.8099314E+05
NO	Op	1.8015337E-02	-3.4415293E-01	1.5658151E+00	3.3303758E+01
N2	N2p	-1.6447237E-02	4.7759522E-01	-4.7641986E+00	2.9127542E+08
O2	N2p	-4.9176811E-03	1.9694738E-01	-2.5025540E+00	6.8213629E+05
N	N2p	-1.2882395E-02	3.7306469E-01	-3.7106760E+00	7.5444981E+06
O	N2p	-1.7420606E-02	4.7126950E-01	-4.3841087E+00	2.8275095E+07
NO	N2p	-4.0133981E-03	1.7290664E-01	-2.2855449E+00	3.6429320E+05
N2	O2p	2.2455421E-02	-4.5106797E-01	2.3763420E+00	4.7754696E+00
O2	O2p	2.8664463E-02	-5.8087240E-01	3.2564558E+00	6.6890428E-01
N	O2p	1.1205000E-02	-1.8182149E-01	3.2624972E-01	5.5186183E+02
O	O2p	0.0000000E+00	8.3446262E-02	-1.7191179E+00	8.0539928E+04
NO	O2p	2.2679271E-02	-4.5710920E-01	2.4427275E+00	3.6733514E+00

TABLE A.3: Variable values used in calculating Gupta model charged particle collision parameters. Subscript att and rep denote attractive and repulsive coefficients respectively.

Collision Integral	$\mathbf{C_{att}}$	$\mathbf{c_{att}}$	$\mathbf{D_{att}}$	$\mathbf{C_{rep}}$	$\mathbf{c_{rep}}$	$\mathbf{D_{rep}}$
(1,1)	-0.476	0.0313	0.784	0.138	0.0106	0.765
(2,2)	-0.146	0.0377	1.262	0.157	0.0274	1.235

Appendix B

Tables of Chemical Data Coefficients

These tables list parameter value data used in the calculation of chemical reaction rates as described in chapter 2.

TABLE B.1: Variable values used in the calculation of forward chemical reaction rates within the 5 species air mixture.

Reaction	**Reaction Type**	**C**	η	θ
N2+N=N+N+N	Dissociation	3.000E+22	-1.600E+0	1.132E+05
N2+O=N+N+O	Dissociation	3.000E+22	-1.600E+0	1.132E+05
N2+N2=N+N+N2	Dissociation	7.000E+21	-1.600E+0	1.132E+05
N2+O2=N+N+O2	Dissociation	7.000E+21	-1.600E+0	1.132E+05
N2+NO=N+N+NO	Dissociation	7.000E+21	-1.600E+0	1.132E+05
O2+N=O+O+N	Dissociation	1.000E+22	-1.500E+0	5.936E+04
O2+O=O+O+O	Dissociation	1.000E+22	-1.500E+0	5.936E+04
O2+N2=O+O+N2	Dissociation	2.000E+21	-1.500E+0	5.940E+04
O2+O2=O+O+O2	Dissociation	2.000E+21	-1.500E+0	5.940E+04
O2+NO=O+O+NO	Dissociation	2.000E+21	-1.500E+0	5.940E+04
NO+N=N+O+N	Dissociation	1.100E+17	0.000E+0	7.550E+04
NO+O=N+O+O	Dissociation	1.100E+17	0.000E+0	7.550E+04
NO+N2=N+O+N2	Dissociation	5.000E+15	0.000E+0	7.550E+04
NO+O2=N+O+O2	Dissociation	5.000E+15	0.000E+0	7.550E+04
NO+NO=N+O+NO	Dissociation	5.000E+15	0.000E+0	7.550E+04
N2+O=NO+N	Exchange	6.438E+17	-1.000E+0	3.750E+04
NO+O=O2+N	Exchange	8.360E+12	0.000E+0	1.970E+04

TABLE B.2: Variable values used in the calculation of backward chemical reaction rates within the 5 species air mixture.

Reaction	**n**	**A1**	**A2**	**A3**	**A4**	**A5**
N2+N=N+N+N	1.000E+14	3.491E+0	8.313E-1	4.098E+0	-1.273E+1	7.487E-2
	1.000E+15	2.072E+0	1.390E+0	2.062E+0	-1.183E+1	1.511E-2
	1.000E+16	1.606E+0	1.573E+0	1.392E+0	-1.153E+1	-4.543E-3

	1.000E+17	1.535E+0	1.606E+0	1.299E+0	-1.149E+1	-6.980E-3
	1.000E+18	1.477E+0	1.629E+0	1.215E+0	-1.146E+1	-9.444E-3
	1.000E+19	1.477E+0	1.629E+0	1.215E+0	-1.146E+1	-9.444E-3
N2+O2=N+N+O2	1.000E+14	3.491E+0	8.313E-1	4.098E+0	-1.273E+1	7.487E-2
	1.000E+15	2.072E+0	1.390E+0	2.062E+0	-1.183E+1	1.511E-2
	1.000E+16	1.606E+0	1.573E+0	1.392E+0	-1.153E+1	-4.543E-3
	1.000E+17	1.535E+0	1.606E+0	1.299E+0	-1.149E+1	-6.980E-3
	1.000E+18	1.477E+0	1.629E+0	1.215E+0	-1.146E+1	-9.444E-3
	1.000E+19	1.477E+0	1.629E+0	1.215E+0	-1.146E+1	-9.444E-3
N2+NO=N+N+NO	1.000E+14	3.491E+0	8.313E-1	4.098E+0	-1.273E+1	7.487E-2
	1.000E+15	2.072E+0	1.390E+0	2.062E+0	-1.183E+1	1.511E-2
	1.000E+16	1.606E+0	1.573E+0	1.392E+0	-1.153E+1	-4.543E-3
	1.000E+17	1.535E+0	1.606E+0	1.299E+0	-1.149E+1	-6.980E-3
	1.000E+18	1.477E+0	1.629E+0	1.215E+0	-1.146E+1	-9.444E-3
	1.000E+19	1.477E+0	1.629E+0	1.215E+0	-1.146E+1	-9.444E-3
O2+N=O+O+N	1.000E+14	1.810E+0	1.961E+0	3.572E+0	-7.362E+0	8.386E-2
	1.000E+15	9.135E-1	2.316E+0	2.289E+0	-6.797E+0	4.634E-2
	1.000E+16	6.418E-1	2.425E+0	1.903E+0	-6.628E+0	3.515E-2
	1.000E+17	5.539E-1	2.460E+0	1.776E+0	-6.572E+0	3.145E-2
	1.000E+18	5.246E-1	2.472E+0	1.734E+0	-6.553E+0	3.021E-2
	1.000E+19	5.099E-1	2.477E+0	1.713E+0	-6.544E+0	2.959E-2
O2+O=O+O+O	1.000E+14	1.810E+0	1.961E+0	3.572E+0	-7.362E+0	8.386E-2
	1.000E+15	9.135E-1	2.316E+0	2.289E+0	-6.797E+0	4.634E-2
	1.000E+16	6.418E-1	2.425E+0	1.903E+0	-6.628E+0	3.515E-2
	1.000E+17	5.539E-1	2.460E+0	1.776E+0	-6.572E+0	3.145E-2
	1.000E+18	5.246E-1	2.472E+0	1.734E+0	-6.553E+0	3.021E-2
	1.000E+19	5.099E-1	2.477E+0	1.713E+0	-6.544E+0	2.959E-2
O2+N2=O+O+N2	1.000E+14	1.810E+0	1.961E+0	3.572E+0	-7.362E+0	8.386E-2
	1.000E+15	9.135E-1	2.316E+0	2.289E+0	-6.797E+0	4.634E-2
	1.000E+16	6.418E-1	2.425E+0	1.903E+0	-6.628E+0	3.515E-2
	1.000E+17	5.539E-1	2.460E+0	1.776E+0	-6.572E+0	3.145E-2
	1.000E+18	5.246E-1	2.472E+0	1.734E+0	-6.553E+0	3.021E-2
	1.000E+19	5.099E-1	2.477E+0	1.713E+0	-6.544E+0	2.959E-2
O2+O2=O+O+O2	1.000E+14	1.810E+0	1.961E+0	3.572E+0	-7.362E+0	8.386E-2
	1.000E+15	9.135E-1	2.316E+0	2.289E+0	-6.797E+0	4.634E-2
	1.000E+16	6.418E-1	2.425E+0	1.903E+0	-6.628E+0	3.515E-2
	1.000E+17	5.539E-1	2.460E+0	1.776E+0	-6.572E+0	3.145E-2
	1.000E+18	5.246E-1	2.472E+0	1.734E+0	-6.553E+0	3.021E-2
	1.000E+19	5.099E-1	2.477E+0	1.713E+0	-6.544E+0	2.959E-2

O2+NO=O+O+NO	1.000E+14	1.810E+0	1.961E+0	3.572E+0	-7.362E+0	8.386E-2
	1.000E+15	9.135E-1	2.316E+0	2.289E+0	-6.797E+0	4.634E-2
	1.000E+16	6.418E-1	2.425E+0	1.903E+0	-6.628E+0	3.515E-2
	1.000E+17	5.539E-1	2.460E+0	1.776E+0	-6.572E+0	3.145E-2
	1.000E+18	5.246E-1	2.472E+0	1.734E+0	-6.553E+0	3.021E-2
	1.000E+19	5.099E-1	2.477E+0	1.713E+0	-6.544E+0	2.959E-2
NO+N=N+O+N	1.000E+14	2.165E+0	7.858E-2	2.851E+0	-8.542E+0	5.304E-2
	1.000E+15	1.007E+0	5.355E-1	1.191E+0	-7.810E+0	4.394E-3
	1.000E+16	6.382E-1	6.819E-1	6.634E-1	-7.577E+0	-1.103E-2
	1.000E+17	5.589E-1	7.156E-1	5.540E-1	-7.530E+0	-1.409E-2
	1.000E+18	5.150E-1	7.329E-1	4.910E-1	-7.503E+0	-1.594E-2
	1.000E+19	5.077E-1	7.358E-1	4.804E-1	-7.498E+0	-1.625E-2
NO+O=N+O+O	1.000E+14	2.165E+0	7.858E-2	2.851E+0	-8.542E+0	5.304E-2
	1.000E+15	1.007E+0	5.355E-1	1.191E+0	-7.810E+0	4.394E-3
	1.000E+16	6.382E-1	6.819E-1	6.634E-1	-7.577E+0	-1.103E-2
	1.000E+17	5.589E-1	7.156E-1	5.540E-1	-7.530E+0	-1.409E-2
	1.000E+18	5.150E-1	7.329E-1	4.910E-1	-7.503E+0	-1.594E-2
	1.000E+19	5.077E-1	7.358E-1	4.804E-1	-7.498E+0	-1.625E-2
NO+N2=N+O+N2	1.000E+14	2.165E+0	7.858E-2	2.851E+0	-8.542E+0	5.304E-2
	1.000E+15	1.007E+0	5.355E-1	1.191E+0	-7.810E+0	4.394E-3
	1.000E+16	6.382E-1	6.819E-1	6.634E-1	-7.577E+0	-1.103E-2
	1.000E+17	5.589E-1	7.156E-1	5.540E-1	-7.530E+0	-1.409E-2
	1.000E+18	5.150E-1	7.329E-1	4.910E-1	-7.503E+0	-1.594E-2
	1.000E+19	5.077E-1	7.358E-1	4.804E-1	-7.498E+0	-1.625E-2
NO+O2=N+O+O2	1.000E+14	2.165E+0	7.858E-2	2.851E+0	-8.542E+0	5.304E-2
	1.000E+15	1.007E+0	5.355E-1	1.191E+0	-7.810E+0	4.394E-3
	1.000E+16	6.382E-1	6.819E-1	6.634E-1	-7.577E+0	-1.103E-2
	1.000E+17	5.589E-1	7.156E-1	5.540E-1	-7.530E+0	-1.409E-2
	1.000E+18	5.150E-1	7.329E-1	4.910E-1	-7.503E+0	-1.594E-2
	1.000E+19	5.077E-1	7.358E-1	4.804E-1	-7.498E+0	-1.625E-2
NO+NO=N+O+NO	1.000E+14	2.165E+0	7.858E-2	2.851E+0	-8.542E+0	5.304E-2
	1.000E+15	1.007E+0	5.355E-1	1.191E+0	-7.810E+0	4.394E-3
	1.000E+16	6.382E-1	6.819E-1	6.634E-1	-7.577E+0	-1.103E-2
	1.000E+17	5.589E-1	7.156E-1	5.540E-1	-7.530E+0	-1.409E-2
	1.000E+18	5.150E-1	7.329E-1	4.910E-1	-7.503E+0	-1.594E-2
	1.000E+19	5.077E-1	7.358E-1	4.804E-1	-7.498E+0	-1.625E-2
N2+O=NO+N	1.000E+14	1.326E+0	7.527E-1	1.247E+0	-4.186E+0	2.184E-2
	1.000E+15	1.065E+0	8.542E-1	8.709E-1	-4.019E+0	1.072E-2
	1.000E+16	9.679E-1	8.913E-1	7.291E-1	-3.956E+0	6.488E-3

	1.000E+17	9.765E-1	8.904E-1	7.457E-1	-3.964E+0	7.123E-3
	1.000E+18	9.619E-1	8.962E-1	7.248E-1	-3.955E+0	6.509E-3
	1.000E+19	9.692E-1	8.933E-1	7.353E-1	-3.960E+0	6.818E-3
NO+O=O2+N	1.000E+14	3.544E-1	-1.882E+0	-7.211E-1	-1.180E+0	-3.083E-2
	1.000E+15	9.361E-2	-1.781E+0	-1.098E+0	-1.013E+0	-4.195E-2
	1.000E+16	-3.732E-3	-1.743E+0	-1.239E+0	-9.495E-1	-4.618E-2
	1.000E+17	4.815E-3	-1.744E+0	-1.223E+0	-9.582E-1	-4.555E-2
	1.000E+18	-9.758E-3	-1.739E+0	-1.244E+0	-9.490E-1	-4.616E-2
	1.000E+19	-2.428E-3	-1.742E+0	-1.233E+0	-9.537E-1	-4.585E-2

TABLE B.4: Variable values used in the calculation of backward chemical reaction rates for reactions unique to the 11 species air mixture.

Reaction	**n**	**A1**	**A2**	**A3**	**A4**	**A5**
$N2+N^+=N+N+N^+$	1.00E+14	3.491E+0	8.313E-1	4.098E+0	-1.273E+1	7.487E-2
	1.00E+15	2.072E+0	1.390E+0	2.062E+0	-1.183E+1	1.511E-2
	1.00E+16	1.606E+0	1.573E+0	1.392E+0	-1.153E+1	-4.543E-3
	1.00E+17	1.535E+0	1.606E+0	1.299E+0	-1.149E+1	-6.980E-3
	1.00E+18	1.477E+0	1.629E+0	1.215E+0	-1.146E+1	-9.444E-3
	1.00E+19	1.477E+0	1.629E+0	1.215E+0	-1.146E+1	-9.444E-3
$N2+O^+=N+N+O^+$	1.00E+14	3.491E+0	8.313E-1	4.098E+0	-1.273E+1	7.487E-2
	1.00E+15	2.072E+0	1.390E+0	2.062E+0	-1.183E+1	1.511E-2
	1.00E+16	1.606E+0	1.573E+0	1.392E+0	-1.153E+1	-4.543E-3
	1.00E+17	1.535E+0	1.606E+0	1.299E+0	-1.149E+1	-6.980E-3
	1.00E+18	1.477E+0	1.629E+0	1.215E+0	-1.146E+1	-9.444E-3
	1.00E+19	1.477E+0	1.629E+0	1.215E+0	-1.146E+1	-9.444E-3
$N2+N2^+=N+N+N2^+$	1.00E+14	3.491E+0	8.313E-1	4.098E+0	-1.273E+1	7.487E-2
	1.00E+15	2.072E+0	1.390E+0	2.062E+0	-1.183E+1	1.511E-2
	1.00E+16	1.606E+0	1.573E+0	1.392E+0	-1.153E+1	-4.543E-3
	1.00E+17	1.535E+0	1.606E+0	1.299E+0	-1.149E+1	-6.980E-3
	1.00E+18	1.477E+0	1.629E+0	1.215E+0	-1.146E+1	-9.444E-3
	1.00E+19	1.477E+0	1.629E+0	1.215E+0	-1.146E+1	-9.444E-3
$N2+O2^+=N+N+O2^+$	1.00E+14	3.491E+0	8.313E-1	4.098E+0	-1.273E+1	7.487E-2
	1.00E+15	2.072E+0	1.390E+0	2.062E+0	-1.183E+1	1.511E-2
	1.00E+16	1.606E+0	1.573E+0	1.392E+0	-1.153E+1	-4.543E-3
	1.00E+17	1.535E+0	1.606E+0	1.299E+0	-1.149E+1	-6.980E-3
	1.00E+18	1.477E+0	1.629E+0	1.215E+0	-1.146E+1	-9.444E-3
	1.00E+19	1.477E+0	1.629E+0	1.215E+0	-1.146E+1	-9.444E-3
$N2+NO^+=N+N+NO^+$	1.00E+14	3.491E+0	8.313E-1	4.098E+0	-1.273E+1	7.487E-2
	1.00E+15	2.072E+0	1.390E+0	2.062E+0	-1.183E+1	1.511E-2

	1.00E+16	1.606E+0	1.573E+0	1.392E+0	-1.153E+1	-4.543E-3
	1.00E+17	1.535E+0	1.606E+0	1.299E+0	-1.149E+1	-6.980E-3
	1.00E+18	1.477E+0	1.629E+0	1.215E+0	-1.146E+1	-9.444E-3
	1.00E+19	1.477E+0	1.629E+0	1.215E+0	-1.146E+1	-9.444E-3
$O2+N^+=O+O+N^+$	1.00E+14	1.810E+0	1.961E+0	3.572E+0	-7.362E+0	8.386E-2
	1.00E+15	9.135E-1	2.316E+0	2.289E+0	-6.797E+0	4.634E-2
	1.00E+16	6.418E-1	2.425E+0	1.903E+0	-6.628E+0	3.515E-2
	1.00E+17	5.539E-1	2.460E+0	1.776E+0	-6.572E+0	3.145E-2
	1.00E+18	5.246E-1	2.472E+0	1.734E+0	-6.553E+0	3.021E-2
	1.00E+19	5.099E-1	2.477E+0	1.713E+0	-6.544E+0	2.959E-2
$O2+O^+=O+O+O^+$	1.00E+14	1.810E+0	1.961E+0	3.572E+0	-7.362E+0	8.386E-2
	1.00E+15	9.135E-1	2.316E+0	2.289E+0	-6.797E+0	4.634E-2
	1.00E+16	6.418E-1	2.425E+0	1.903E+0	-6.628E+0	3.515E-2
	1.00E+17	5.539E-1	2.460E+0	1.776E+0	-6.572E+0	3.145E-2
	1.00E+18	5.246E-1	2.472E+0	1.734E+0	-6.553E+0	3.021E-2
	1.00E+19	5.099E-1	2.477E+0	1.713E+0	-6.544E+0	2.959E-2
$O2+N2^+=O+O+N2^+$	1.00E+14	1.810E+0	1.961E+0	3.572E+0	-7.362E+0	8.386E-2
	1.00E+15	9.135E-1	2.316E+0	2.289E+0	-6.797E+0	4.634E-2
	1.00E+16	6.418E-1	2.425E+0	1.903E+0	-6.628E+0	3.515E-2
	1.00E+17	5.539E-1	2.460E+0	1.776E+0	-6.572E+0	3.145E-2
	1.00E+18	5.246E-1	2.472E+0	1.734E+0	-6.553E+0	3.021E-2
	1.00E+19	5.099E-1	2.477E+0	1.713E+0	-6.544E+0	2.959E-2
$O2+O2^+=O+O+O2^+$	1.00E+14	1.810E+0	1.961E+0	3.572E+0	-7.362E+0	8.386E-2
	1.00E+15	9.135E-1	2.316E+0	2.289E+0	-6.797E+0	4.634E-2
	1.00E+16	6.418E-1	2.425E+0	1.903E+0	-6.628E+0	3.515E-2
	1.00E+17	5.539E-1	2.460E+0	1.776E+0	-6.572E+0	3.145E-2
	1.00E+18	5.246E-1	2.472E+0	1.734E+0	-6.553E+0	3.021E-2
	1.00E+19	5.099E-1	2.477E+0	1.713E+0	-6.544E+0	2.959E-2
$O2+NO^+=O+O+NO^+$	1.00E+14	1.810E+0	1.961E+0	3.572E+0	-7.362E+0	8.386E-2
	1.00E+15	9.135E-1	2.316E+0	2.289E+0	-6.797E+0	4.634E-2
	1.00E+16	6.418E-1	2.425E+0	1.903E+0	-6.628E+0	3.515E-2
	1.00E+17	5.539E-1	2.460E+0	1.776E+0	-6.572E+0	3.145E-2
	1.00E+18	5.246E-1	2.472E+0	1.734E+0	-6.553E+0	3.021E-2
	1.00E+19	5.099E-1	2.477E+0	1.713E+0	-6.544E+0	2.959E-2
$NO+N^+=N+O+N^+$	1.00E+14	2.165E+0	7.858E-2	2.851E+0	-8.542E+0	5.304E-2
	1.00E+15	1.007E+0	5.355E-1	1.191E+0	-7.810E+0	4.394E-3
	1.00E+16	6.382E-1	6.819E-1	6.634E-1	-7.577E+0	-1.103E-2
	1.00E+17	5.589E-1	7.156E-1	5.540E-1	-7.530E+0	-1.409E-2
	1.00E+18	5.150E-1	7.329E-1	4.910E-1	-7.503E+0	-1.594E-2

	1.00E+19	5.077E-1	7.358E-1	4.804E-1	-7.498E+0	-1.625E-2
$NO+O^+=N+O+O^+$	1.00E+14	2.165E+0	7.858E-2	2.851E+0	-8.542E+0	5.304E-2
	1.00E+15	1.007E+0	5.355E-1	1.191E+0	-7.810E+0	4.394E-3
	1.00E+16	6.382E-1	6.819E-1	6.634E-1	-7.577E+0	-1.103E-2
	1.00E+17	5.589E-1	7.156E-1	5.540E-1	-7.530E+0	-1.409E-2
	1.00E+18	5.150E-1	7.329E-1	4.910E-1	-7.503E+0	-1.594E-2
	1.00E+19	5.077E-1	7.358E-1	4.804E-1	-7.498E+0	-1.625E-2
$NO+N2^+=N+O+N2^+$	1.00E+14	2.165E+0	7.858E-2	2.851E+0	-8.542E+0	5.304E-2
	1.00E+15	1.007E+0	5.355E-1	1.191E+0	-7.810E+0	4.394E-3
	1.00E+16	6.382E-1	6.819E-1	6.634E-1	-7.577E+0	-1.103E-2
	1.00E+17	5.589E-1	7.156E-1	5.540E-1	-7.530E+0	-1.409E-2
	1.00E+18	5.150E-1	7.329E-1	4.910E-1	-7.503E+0	-1.594E-2
	1.00E+19	5.077E-1	7.358E-1	4.804E-1	-7.498E+0	-1.625E-2
$NO+O2^+=N+O+O2^+$	1.00E+14	2.165E+0	7.858E-2	2.851E+0	-8.542E+0	5.304E-2
	1.00E+15	1.007E+0	5.355E-1	1.191E+0	-7.810E+0	4.394E-3
	1.00E+16	6.382E-1	6.819E-1	6.634E-1	-7.577E+0	-1.103E-2
	1.00E+17	5.589E-1	7.156E-1	5.540E-1	-7.530E+0	-1.409E-2
	1.00E+18	5.150E-1	7.329E-1	4.910E-1	-7.503E+0	-1.594E-2
	1.00E+19	5.077E-1	7.358E-1	4.804E-1	-7.498E+0	-1.625E-2
$NO+NO^+=N+O+NO^+$	1.00E+14	2.165E+0	7.858E-2	2.851E+0	-8.542E+0	5.304E-2
	1.00E+15	1.007E+0	5.355E-1	1.191E+0	-7.810E+0	4.394E-3
	1.00E+16	6.382E-1	6.819E-1	6.634E-1	-7.577E+0	-1.103E-2
	1.00E+17	5.589E-1	7.156E-1	5.540E-1	-7.530E+0	-1.409E-2
	1.00E+18	5.150E-1	7.329E-1	4.910E-1	-7.503E+0	-1.594E-2
	1.00E+19	5.077E-1	7.358E-1	4.804E-1	-7.498E+0	-1.625E-2
$N+O=NO^++e$	1.00E+14	-2.185E+0	-6.671E+0	-4.297E+0	-2.218E+0	-5.075E-2
	1.00E+15	-1.028E+0	-7.128E+0	-2.637E+0	-2.950E+0	-2.100E-3
	1.00E+16	-6.587E-1	-7.274E+0	-2.110E+0	-3.182E+0	1.331E-2
	1.00E+17	-5.792E-1	-7.308E+0	-2.000E+0	-3.229E+0	1.638E-2
	1.00E+18	-5.354E-1	-7.325E+0	-1.937E+0	-3.257E+0	1.823E-2
	1.00E+19	-5.280E-1	-7.328E+0	-1.926E+0	-3.262E+0	1.854E-2
$N+N=N2^++e$	1.00E+14	-4.379E+0	-4.273E+0	-7.871E+0	-4.463E+0	-1.240E-1
	1.00E+15	-2.960E+0	-4.831E+0	-5.835E+0	-5.362E+0	-6.425E-2
	1.00E+16	-2.494E+0	-5.015E+0	-5.165E+0	-5.658E+0	-4.460E-2
	1.00E+17	-2.423E+0	-5.047E+0	-5.072E+0	-5.696E+0	-4.217E-2
	1.00E+18	-2.364E+0	-5.070E+0	-4.989E+0	-5.733E+0	-3.970E-2
	1.00E+19	-2.364E+0	-5.070E+0	-4.989E+0	-5.733E+0	-3.970E-2
$O+O=O2^++e$	1.00E+14	-1.168E-1	-7.688E+0	-2.250E+0	-7.791E+0	-1.108E-2
	1.00E+15	7.799E-1	-8.044E+0	-9.668E-1	-8.356E+0	2.644E-2

	1.00E+16	1.052E+0	-8.153E+0	-5.808E-1	-8.525E+0	3.763E-2
	1.00E+17	1.140E+0	-8.188E+0	-4.546E-1	-8.581E+0	4.133E-2
	1.00E+18	1.169E+0	-8.199E+0	-4.125E-1	-8.600E+0	4.257E-2
	1.00E+19	1.184E+0	-8.205E+0	-3.915E-1	-8.609E+0	4.319E-2
$N2+O2^{+}=N2^{+}+O2$	1.00E+14	-2.581E+0	2.286E+0	-5.095E+0	-2.038E+0	-1.219E-1
	1.00E+15	-2.581E+0	2.286E+0	-5.095E+0	-2.038E+0	-1.219E-1
	1.00E+16	-2.581E+0	2.286E+0	-5.095E+0	-2.038E+0	-1.219E-1
	1.00E+17	-2.581E+0	2.286E+0	-5.095E+0	-2.038E+0	-1.219E-1
	1.00E+18	-2.581E+0	2.286E+0	-5.095E+0	-2.038E+0	-1.219E-1
	1.00E+19	-2.581E+0	2.286E+0	-5.095E+0	-2.038E+0	-1.219E-1
$NO^{+}+N=O^{+}+N2$	1.00E+14	-1.226E+0	1.004E-1	-1.221E+0	-8.988E-1	-2.523E-2
	1.00E+15	-5.163E-1	-1.788E-1	-2.032E-1	-1.349E+0	4.649E-3
	1.00E+16	-2.831E-1	-2.706E-1	1.315E-1	-1.496E+0	1.447E-2
	1.00E+17	-2.477E-1	-2.870E-1	1.780E-1	-1.516E+0	1.569E-2
	1.00E+18	-2.184E-1	-2.985E-1	2.200E-1	-1.534E+0	1.692E-2
	1.00E+19	-2.184E-1	-2.985E-1	2.200E-1	-1.534E+0	1.692E-2
$NO^{+}+O=N^{+}+O2$	1.00E+14	-1.535E+0	1.684E+0	-2.969E+0	-6.464E+0	-8.332E-2
	1.00E+15	-1.086E+0	1.506E+0	-2.327E+0	-6.747E+0	-6.455E-2
	1.00E+16	-9.507E-1	1.451E+0	-2.135E+0	-6.831E+0	-5.896E-2
	1.00E+17	-9.067E-1	1.434E+0	-2.071E+0	-6.859E+0	-5.711E-2
	1.00E+18	-8.921E-1	1.428E+0	-2.050E+0	-6.869E+0	-5.649E-2
	1.00E+19	-8.847E-1	1.425E+0	-2.040E+0	-6.873E+0	-5.618E-2
$NO^{+}+O2=O2^{+}+NO$	1.00E+14	1.714E+0	8.647E-1	2.768E+0	-4.393E+0	7.049E-2
	1.00E+15	1.714E+0	8.647E-1	2.768E+0	-4.393E+0	7.049E-2
	1.00E+16	1.714E+0	8.647E-1	2.768E+0	-4.393E+0	7.049E-2
	1.00E+17	1.714E+0	8.647E-1	2.768E+0	-4.393E+0	7.049E-2
	1.00E+18	1.714E+0	8.647E-1	2.768E+0	-4.393E+0	7.049E-2
	1.00E+19	1.714E+0	8.647E-1	2.768E+0	-4.393E+0	7.049E-2
$NO^{+}+N=N2^{+}+O$	1.00E+14	-2.193E+0	2.398E+0	-3.574E+0	-2.245E+0	-7.327E-2
	1.00E+15	-1.933E+0	2.297E+0	-3.198E+0	-2,412100	-6.215E-2
	1.00E+16	-1.835E+0	2.260E+0	-3.056E+0	-2.475E+0	-5.792E-2
	1.00E+17	-1.844E+0	2.261E+0	-3.073E+0	-2.467E+0	-5.855E-2
	1.00E+18	-1.829E+0	2.255E+0	-3.052E+0	-2.476E+0	-5.794E-2
	1.00E+19	-1.837E+0	2.258E+0	-3.062E+0	-2.471E+0	-5.825E-2
$O2^{+}+N=N^{+}+O2$	1.00E+14	-3.603E+0	2.701E+0	-5.016E+0	-8.913E-1	-1.230E-1
	1.00E+15	-2.894E+0	2.422E+0	-3.998E+0	-1.341E+0	-9.309E-2
	1.00E+16	-2.661E+0	2.330E+0	-3.663E+0	-1.489E+0	-8.326E-2
	1.00E+17	-2.625E+0	2.314E+0	-3.616E+0	-1.508E+0	-8.205E-2
	1.00E+18	-2.596E+0	2.302E+0	-3.574E+0	-1.526E+0	-8.082E-2

	1.00E+19	-2.596E+0	2.302E+0	-3.574E+0	-1.526E+0	-8.082E-2
O^++NO=N^++O2	1.00E+14	-1.636E+0	8.306E-1	-2.995E+0	-1.379E+0	-7.993E-2
	1.00E+15	-1.636E+0	8.306E-1	-2.995E+0	-1.379E+0	-7.993E-2
	1.00E+16	-1.636E+0	8.306E-1	-2.995E+0	-1.379E+0	-7.993E-2
	1.00E+17	-1.636E+0	8.306E-1	-2.995E+0	-1.379E+0	-7.993E-2
	1.00E+18	-1.636E+0	8.306E-1	-2.995E+0	-1.379E+0	-7.993E-2
	1.00E+19	-1.636E+0	8.306E-1	-2.995E+0	-1.379E+0	-7.993E-2
NO^++O=$O2^+$+N	1.00E+14	2.068E+0	-1.017E+0	2.047E+0	-5.573E+0	3.966E-2
	1.00E+15	1.807E+0	-9.158E-1	1.670E+0	-5.406E+0	2.853E-2
	1.00E+16	1.710E+0	-8.787E-1	1.528E+0	-5.343E+0	2.430E-2
	1.00E+17	1.719E+0	-8.796E-1	1.545E+0	-5.351E+0	2.494E-2
	1.00E+18	1.704E+0	-8.738E-1	1.524E+0	-5.342E+0	2.432E-2
	1.00E+19	1.711E+0	-8.767E-1	1.535E+0	-5.347E+0	2.463E-2
O^++N2=$N2^+$+O	1.00E+14	-9.680E-1	2.298E+0	-2.353E+0	-1.346E+0	-4.804E-2
	1.00E+15	-1.416E+0	2.476E+0	-2.995E+0	-1.064E+0	-6.681E-2
	1.00E+16	-1.552E+0	2.530E+0	-3.188E+0	-9.790E-1	-7.240E-2
	1.00E+17	-1.596E+0	2.548E+0	-3.251E+0	-9.512E-1	-7.425E-2
	1.00E+18	-1.611E+0	2.553E+0	-3.272E+0	-9.419E-1	-7.487E-2
	1.00E+19	-1.618E+0	2.556E+0	-3.282E+0	-9.372E-1	-7.518E-2
N2+e=N+N+e	1.00E+14	3.491E+0	8.313E-1	4.098E+0	-1.273E+1	7.487E-2
	1.00E+15	2.072E+0	1.390E+0	2.062E+0	-1.183E+1	1.511E-2
	1.00E+16	1.606E+0	1.573E+0	1.392E+0	-1.153E+1	-4.543E-3
	1.00E+17	1.535E+0	1.606E+0	1.299E+0	-1.149E+1	-6.980E-3
	1.00E+18	1.477E+0	1.629E+0	1.215E+0	-1.146E+1	-9.444E-3
	1.00E+19	1.477E+0	1.629E+0	1.215E+0	-1.146E+1	-9.444E-3
N+e=N^++e+e	1.00E+14	-1.909E+0	-3.027E+0	-3.694E+0	-1.604E+1	-5.018E-2
	1.00E+15	-1.200E+0	-3.306E+0	-2.676E+0	-1.649E+1	-2.030E-2
	1.00E+16	-9.671E-1	-3.398E+0	-2.341E+0	-1.664E+1	-1.048E-2
	1.00E+17	-9.318E-1	-3.414E+0	-2.295E+0	-1.666E+1	-9.269E-3
	1.00E+18	-9.026E-1	-3.426E+0	-2.253E+0	-1.668E+1	-8.037E-3
	1.00E+19	-9.026E-1	-3.426E+0	-2.253E+0	-1.668E+1	-8.037E-3
O+e=O^++e+e	1.00E+14	8.045E-2	-5.739E+0	-1.420E+0	-1.584E+1	-1.087E-3
	1.00E+15	5.288E-1	-5.917E+0	-7.780E-1	-1.613E+1	1.768E-2
	1.00E+16	6.648E-1	-5.972E+0	-5.849E-1	-1.621E+1	2.327E-2
	1.00E+17	7.088E-1	-5.989E+0	-5.217E-1	-1.624E+1	2.513E-2
	1.00E+18	7.234E-1	-5.995E+0	-5.007E-1	-1.625E+1	2.574E-2
	1.00E+19	7.308E-1	-5.998E+0	-4.901E-1	-1.625E+1	2.605E-2

TABLE B.3: Variable values used in the calculation of forward chemical reaction rates for reactions unique to the 11 species air mixture.

Reaction	**Reaction Type**	**C**	η	θ
$N2+N^+=N+N+N^+$	Dissociation	3.000E+22	-1.600E+0	1.132E+5
$N2+O^+=N+N+O^+$	Dissociation	3.000E+22	-1.600E+0	1.132E+5
$N2+N2^+=N+N+N2^+$	Dissociation	7.000E+21	-1.600E+0	1.132E+5
$N2+O2^+=N+N+O2^+$	Dissociation	7.000E+21	-1.600E+0	1.132E+5
$N2+NO^+=N+N+NO^+$	Dissociation	7.000E+21	-1.600E+0	1.132E+5
$O2+N^+=O+O+N^+$	Dissociation	1.000E+22	-1.500E+0	5.950E+4
$O2+O^+=O+O+O^+$	Dissociation	1.000E+22	-1.500E+0	5.950E+4
$O2+N2^+=O+O+N2^+$	Dissociation	2.000E+21	-1.500E+0	5.950E+4
$O2+O2^+=O+O+O2^+$	Dissociation	2.000E+21	-1.500E+0	5.950E+4
$O2+NO^+=O+O+NO^+$	Dissociation	2.000E+21	-1.500E+0	5.950E+4
$NO+N^+=N+O+N^+$	Dissociation	1.100E+17	0.000E+0	7.550E+4
$NO+O^+=N+O+O^+$	Dissociation	1.100E+17	0.000E+0	7.550E+4
$NO+N2^+=N+O+N2^+$	Dissociation	5.000E+15	0.000E+0	7.550E+4
$NO+O2^+=N+O+O2^+$	Dissociation	5.000E+15	0.000E+0	7.550E+4
$NO+NO^+=N+O+NO^+$	Dissociation	000E+15	0.000E+0	7.550E+4
$N+O=NO^++e$	Dissociative Recombination	5.300E+12	0.000E+0	3.190E+4
$N+N=N2^++e$	Dissociative Recombination	2.000E+13	0.000E+0	6.750E+4
$O+O=O2^++e$	Dissociative Recombination	1.100E+13	0.000E+0	8.060E+4
$N2+O2^+=N2^++O2$	Charge Exchange	9.900E+12	0.000E+0	4.070E+4
$NO^++N=O^++N2$	Charge Exchange	3.400E+13	-1.080E+0	1.280E+4
$NO^++O=N^++O2$	Charge Exchange	1.000E+12	5.000E-1	7.720E+4
$NO^++O2=O2^++NO$	Charge Exchange	2.400E+13	4.100E-1	3.260E+4
$NO^++N=N2^++O$	Charge Exchange	7.200E+13	0.000E+0	3.550E+4
$O2^++N=N^++O2$	Charge Exchange	8.700E+13	1.400E-1	2.860E+4
$O^++NO=N^++O2$	Charge Exchange	1.400E+5	1.900E+0	1.530E+4
$NO^++O=O2^++N$	Charge Exchange	7.200E+12	2.900E-1	4.860E+4
$O^++N2=N2^++O$	Charge Exchange	9.100E+11	3.600E-1	2.280E+4
$N2+e=N+N+e$	Dissociation	3.000E+24	-1.600E+0	1.132E+5
$N+e=N^++e+e$	Electron Impact Ionisation	2.500E+34	-3.820E+0	1.686E+5
$O+e=O^++e+e$	Electron Impact Ionisation	3.900E+33	-3.780E+0	1.585E+5

Appendix C

Acknowledgement of Resources

All of the routines, algorithms and models described in this thesis were written and implemented by the author unless otherwise stated. This work was undertaken with the support of the Centre for Doctoral Training in Next-Gen Computational Modelling, including financial and computational resources. These computational resources included access to specific resource of the Iridis 5 supercomputer cluster at the University of Southampton. Third party software utilised in the construction of OP2A and the simulations undertaken includes the PLATO chemical modelling library (integrated, but not used in the work presented) and the METIS library for mesh partitioning. Their usage is described in the appropriate sections of this document.

References

M. Aguilar, G. Alberti, B. Alpat, A. Alvino, G. Ambrosi, K. Andeen, H. Anderhub, L. Arruda, P. Azzarello, A. Bachlechner, F. Barao, B. Baret, A. Barrau, L. Barrin, A. Bartoloni, L. Basara, A. Basili, L. Batalha, J. Bates, R. Battiston, J. Bazo, R. Becker, U. Becker, M. Behlmann, B. Beischer, J. Berdugo, P. Berges, B. Bertucci, G. Bigongiari, A. Biland, V. Bindi, S. Bizzaglia, G. Boella, W. de Boer, K. Bollweg, J. Bolmont, B. Borgia, S. Borsini, M. J. Boschini, G. Boudoul, M. Bourquin, P. Brun, M. Buénerd, J. Burger, W. Burger, F. Cadoux, X. D. Cai, M. Capell, D. Casadei, J. Casaus, V. Cascioli, G. Castellini, I. Cernuda, F. Cervelli, M. J. Chae, Y. H. Chang, A. I. Chen, C. R. Chen, H. Chen, G. M. Cheng, H. S. Chen, L. Cheng, N. Chernoplyiokov, A. Chikanian, E. Choumilov, V. Choutko, C. H. Chung, C. Clark, R. Clavero, G. Coignet, V. Commichau, C. Consolandi, A. Contin, C. Corti, M. T. Costado Dios, B. Coste, D. Crespo, Z. Cui, M. Dai, C. Delgado, S. Della Torre, B. Demirkoz, P. Dennett, L. Derome, S. Di Falco, X. H. Diao, A. Diago, L. Djambazov, C. Díaz, P. von Doetinchem, W. J. Du, J. M. Dubois, R. Duperay, M. Duranti, D. D'Urso, A. Egorov, A. Eline, F. J. Eppling, T. Eronen, J. van Es, H. Esser, A. Falvard, E. Fiandrini, A. Fiasson, E. Finch, P. Fisher, K. Flood, R. Foglio, M. Fohey, S. Fopp, N. Fouque, Y. Galaktionov, M. Gallilee, L. Gallin-Martel, G. Gallucci, B. García, J. García, R. García-López, L. García-Tabares, C. Gargiulo, H. Gast, I. Gebauer, S. Gentile, M. Gervasi, W. Gillard, F. Giovacchini, L. Girard, P. Goglov, J. Gong, C. Goy-Henningsen, D. Grandi, M. Graziani, A. Grechko, A. Gross, I. Guerri, C. de la Guía, K. H. Guo, M. Habiby, S. Haino, F. Hauler, Z. H. He, M. Heil, J. Heilig, R. Hermel, H. Hofer, Z. C. Huang, W. Hungerford, M. Incagli, M. Ionica, A. Jacholkowska, W. Y. Jang, H. Jinchi, M. Jongmanns, L. Journet, L. Jungermann, W. Karpinski, G. N. Kim, K. S. Kim, Th. Kirn, R. Kossakowski, A. Koulemzine, O. Kounina, A. Kounine, V. Koutsenko, M. S. Krafczyk, E. Laudi, G. Laurenti, C. Lauritzen, A. Lebedev, M. W. Lee, S. C. Lee, C. Leluc, H. León Vargas, V. Lepareur, J. Q. Li, Q. Li, T. X. Li, W. Li, Z. H. Li, P. Lipari, C. H. Lin, D. Liu, H. Liu, T. Lomtadze, Y. S. Lu, S. Lucidi, K. Lübelsmeyer, J. Z. Luo, W. Lustermann, S. Lv, J. Madsen, R. Majka, A. Malinin, C. Mañá, J. Marín, T. Martin, G. Martínez, F. Masciocchi, N. Masi, D. Maurin, A. McInturff, P. McIntyre, A. Menchaca-Rocha, Q. Meng, M. Menichelli, I. Mereu, M. Millinger, D. C. Mo, M. Molina, P. Mott, A. Mujunen, S. Natale, P. Nemeth, J. Q. Ni, N. Nikonov, F. Nozzoli, P. Nunes, A. Obermeier, S. Oh, A. Oliva, F. Palmonari, C. Palomares,

M. Paniccia, A. Papi, W. H. Park, M. Pauluzzi, F. Pauss, A. Pauw, E. Pedreschi, S. Pensotti, R. Pereira, E. Perrin, G. Pessina, G. Pierschel, F. Pilo, A. Piluso, C. Pizzolotto, V. Plyaskin, J. Pochon, M. Pohl, V. Poireau, S. Porter, J. Pouxe, A. Putze, L. Quadrani, X. N. Qi, P. G. Rancoita, D. Rapin, Z. L. Ren, J. S. Ricol, E. Riihonen, I. Rodríguez, U. Roeser, S. Rosier-Lees, L. Rossi, A. Rozhkov, D. Rozza, A. Sabellek, R. Sagdeev, J. Sandweiss, B. Santos, P. Saouter, M. Sarchioni, S. Schael, D. Schinzel, M. Schmanau, G. Schwering, A. Schulz von Dratzig, G. Scolieri, E. S. Seo, B. S. Shan, J. Y. Shi, Y. M. Shi, T. Siedenburg, R. Siedling, D. Son, F. Spada, F. Spinella, M. Steuer, K. Stiff, W. Sun, W. H. Sun, X. H. Sun, M. Tacconi, C. P. Tang, X. W. Tang, Z. C. Tang, L. Tao, J. Tassan-Viol, Samuel C. C. Ting, S. M. Ting, C. Titus, N. Tomassetti, F. Toral, J. Torsti, J. R. Tsai, J. C. Tutt, J. Ulbricht, T. Urban, V. Vagelli, E. Valente, C. Vannini, E. Valtonen, M. Vargas Trevino, S. Vaurynovich, M. Vecchi, M. Vergain, B. Verlaat, C. Vescovi, J. P. Vialle, G. Viertel, G. Volpini, D. Wang, N. H. Wang, Q. L. Wang, R. S. Wang, X. Wang, Z. X. Wang, W. Wallraff, Z. L. Weng, M. Willenbrock, M. Wlochal, H. Wu, K. Y. Wu, Z. S. Wu, W. J. Xiao, S. Xie, R. Q. Xiong, G. M. Xin, N. S. Xu, W. Xu, Q. Yan, J. Yang, M. Yang, Q. H. Ye, H. Yi, Y. J. Yu, Z. Q. Yu, S. Zeissler, J. G. Zhang, Z. Zhang, M. M. Zhang, Z. M. Zheng, H. L. Zhuang, V. Zhukov, A. Zichichi, P. Zuccon, and C. Zurbach. First result from the alpha magnetic spectrometer on the international space station: Precision measurement of the positron fraction in primary cosmic rays of 0.5–350 GeV. *Phys. Rev. Lett.*, 110:141102, Apr 2013. URL https://link.aps.org/doi/10.1103/PhysRevLett.110.141102.

R. A. Allen, J. C. Camm, M. H. Rose, and P. H Rose. Non-equilibrium and equilibrium radiation at supersatellite re-entry velocities. Technical report, NASA, 1962.

R. Allouche, R. Haoui, and R. Renane. Numerical simulation of reactive flow in non-equilibrium behind a strong shock wave during re-entry into earth's atmosphere. *Mechanics & Industry*, 15(1):81–87, Feb 2014. URL https://doi.org/10.1051/meca/2014002.

Julien Annaloro, Stéphane Galera, Cédric Thiebaut, Martin Spel, Pierre Van Hauwaert, Guillaume Grossir, Sébastien Paris, Olivier Chazot, and Pierre Omaly. Aerothermodynamics modelling of complex shapes in the debrisk atmospheric reentry tool: Methodology and validation. *Acta Astronautica*, 171:388–402, June 2020. ISSN 0094-5765. URL https://www.sciencedirect.com/science/article/pii/S009457652030134X.

Chay Atkins and Ralf Deiterding. *Towards a Strand-Cartesian Solver for Modelling Hypersonic Flows in Thermochemical Non-Equilibrium*. AIAA, 2020. URL https://arc.aiaa.org/doi/abs/10.2514/6.2020-2404.

Dikran Babikian, Chul Park, and George Raiche. *Spectroscopic determination of enthalpy in an arc-jet wind tunnel*. AIAA, 1995. URL https://arc.aiaa.org/doi/abs/10.2514/6.1995-712.

Ata O. Baskaya, Michele Capriati, Davide Ninni, Francesco Bonelli, Giuseppe Pascazio, Alessandro Turchi, Thierry Magin, and Stefan Hickel. *Verification and Validation of Immersed Boundary Solvers for Hypersonic Flows with Gas-Surface Interactions*. AIAA, 2022. URL https://arc.aiaa.org/doi/abs/10.2514/6.2022-3276.

V. Bityurin, A. Bocharov, and John Lineberry. *Results of Experiments on MHD Hypersonic Flow Control*. AIAA, 2004. URL https://arc.aiaa.org/doi/abs/10.2514/6.2004-2263.

F G Blottner, M Johnson, and M Ellis. Chemically reacting viscous flow program for multi-component gas mixtures. Technical report, Sandia National Lab, 1 1971. URL https://www.osti.gov/biblio/4658539.

Francisco Borges, Albert Gutierrez-Milla, Remo Suppi, and Emilio Luque. A hybrid mpi+openmp solution of the distributed cluster-based fish schooling simulator. *Procedia Computer Science*, 29:2111–2120, 2014. ISSN 1877-0509. URL https://www.sciencedirect.com/science/article/pii/S187705091400372X. 2014 International Conference on Computational Science.

M. Born and R. Oppenheimer. Zur quantentheorie der molekeln. *Annalen der Physik*, 389(20):457–484, 1927. URL https://onlinelibrary.wiley.com/doi/abs/10.1002/andp.19273892002.

Stuart W. Bowen and Chul Park. Computer study of nonequilibrium excitation in recombining nitrogen plasma nozzle flows. *AIAA Journal*, 9(3):493–499, 1971. URL https://doi.org/10.2514/3.6208.

Iain D. Boyd and Eswar Josyula. State resolved vibrational relaxation modeling for strongly nonequilibrium flows. *Physics of Fluids*, 23(5):057101, 2011. URL https://doi.org/10.1063/1.3584128.

J.C. Buckey. *Space Physiology*. OUP E-Books. Oxford University Press, 2006. ISBN 9780195137255. URL https://books.google.co.uk/books?id=RYnxmAEACAAJ.

Thomas R. A. Bussing and Earll M. Murman. Finite-volume method for the calculation of compressible chemically reacting flows. *AIAA Journal*, 26(9):1070–1078, 1988. URL https://doi.org/10.2514/3.10013.

Elias Bögel, Manuel A. La Rosa Betancourt, and Marcus R. Collier-Wright. *Magnetohydrodynamic Enhanced Entry System for Space Transportation (MEESST) as a Key Building Block for Future Exploration Missions*. AIAA, 2021. URL https://arc.aiaa.org/doi/abs/10.2514/6.2021-3272.

G. Candler, I. Nompelis, M.-C. Druguet, M. Holden, T. Wadhams, I. Boyd, and W.-L. Wang. *CFD validation for hypersonic flight - Hypersonic double-cone flow simulations*. AIAA, 2002. URL https://arc.aiaa.org/doi/abs/10.2514/6.2002-581.

Graham V. Candler, Heath B. Johnson, Ioannis Nompelis, Vladimyr M. Gidzak, Pramod K. Subbareddy, and Michael Barnhardt. *Development of the US3D Code for Advanced Compressible and Reacting Flow Simulations*. AIAA, 2015a. URL https://arc.aiaa.org/doi/abs/10.2514/6.2015-1893.

Graham V. Candler, Pramod K. Subbareddy, and Joseph M. Brock. Advances in computational fluid dynamics methods for hypersonic flows. *Journal of Spacecraft and Rockets*, 52(1):17–28, 2015b. URL https://doi.org/10.2514/1.A33023.

Vincent Casseau, Thomas J Scanlon, and Richard E. Brown. *Development of a Two-Temperature Open-Source CFD Model for Hypersonic Reacting Flows*. AIAA, 2015. URL https://arc.aiaa.org/doi/abs/10.2514/6.2015-3637.

Vincent Casseau, Daniel E. R. Espinoza, Thomas J. Scanlon, and Richard E. Brown. A two-temperature open-source cfd model for hypersonic reacting flows, part two: Multi-dimensional analysis. *Aerospace*, 3(4), 2016a. ISSN 2226-4310. URL https://www.mdpi.com/2226-4310/3/4/45.

Vincent Casseau, Rodrigo C. Palharini, Thomas J. Scanlon, and Richard E. Brown. A two-temperature open-source cfd model for hypersonic reacting flows, part one: Zero-dimensional analysis. *Aerospace*, 3(4), 2016b. ISSN 2226-4310. URL https://www.mdpi.com/2226-4310/3/4/34.

Vincent Casseau, Wenbo Zhang, Shrutakeerti Mallikarjun, Wagdi G. Habashi, Song Gao, and Abolfazl Karchani. Halo3d: An all-mach approach to hypersonic flows simulation. *International Journal of Computational Fluid Dynamics*, 36(3):187–206, 2022. URL https://doi.org/10.1080/10618562.2022.2094917.

J.H. Chae, T.K. Mankodi, and S.M. et al. Choi. Combined effects of thermal non-equilibrium and chemical reactions on hypersonic air flows around an orbital reentry vehicle. *Int. J. Aeronaut. Space Sci.*, (21):612–626, 2020. URL https://doi.org/10.1007/s42405-019-00243-9.

Ting-Lung Chiang and Klaus Hoffmann. *Determination of computational time step for chemically reacting flows*. AIAA, 1989. URL https://arc.aiaa.org/doi/abs/10.2514/6.1989-1855.

Matthew Clarey and Robert Greendyke. *Parametric Study of the Wake of Slender Hypersonic Vehicles using a Three-Temperature Model*. AIAA, 2018. URL https://arc.aiaa.org/doi/abs/10.2514/6.2018-3436.

Matthew P Clarey. Thermochemical non-equilibrium models for weakly ionized hypersonic flows with application to slender-body wakes. Technical report, Air Force Institute Of Technology Wright-Patterson AFB OH, 2018.

S. J. Colgan and B. P. Levitt. Vibrational relaxation of nitrogen by various collision partners at 2500°K. *Trans. Faraday Soc.*, 63:2898–2905, 1967. URL http://dx.doi.org/10.1039/TF9676302898.

C. F. Curtiss and J. O. Hirschfelder. Integration of stiff equations. *Proceedings of the National Academy of Sciences*, 38(3):235–243, 1952. URL https://www.pnas.org/doi/abs/10.1073/pnas.38.3.235.

A. Chiroux de Gavelle de Roany, C. Flament, J. W. Rich, V. V. Subramaniam, and Walter R. Warren. Strong vibrational nonequilibrium in supersonic nozzle flows. *AIAA Journal*, 31(1):119–128, 1993. URL https://doi.org/10.2514/3.49006.

G Degrez, A Lani, M Panesi, O Chazot, and H Deconinck. Modelling of high-enthalpy, high-mach number flows. *Journal of Physics D: Applied Physics*, 42(19):194004, sep 2009. URL https://doi.org/10.1088/0022-3727/42/19/194004.

Sinan Demir, Prithwish Kundu, Austin C. Nunno, Sibendu Som, Robert A. Baurle, and Tomasz G. Drozda. *Deep neural network based unsteady flamelet progress variable approach in a supersonic combustor*. AIAA, 2022. URL https://arc.aiaa.org/doi/abs/10.2514/6.2022-2073.

Prasun N. Desai, Dan T. Lyons, Jeff Tooley, and Julie Kangas. Entry, descent, and landing operations analysis for the Stardust entry capsule. *Journal of Spacecraft and Rockets*, 45(6):1262–1268, 2008. URL https://doi.org/10.2514/1.37090.

Timothy R. Deschenes and Iain D. Boyd. Extension of a modular particle-continuum method to vibrationally excited, hypersonic flows. *AIAA Journal*, 49(9):1951–1959, 2011. URL https://doi.org/10.2514/1.J050908.

Timothy R. Deschenes, Timothy D. Holman, and Iain D. Boyd. Effects of rotational energy relaxation in a modular particle-continuum method. *Journal of Thermophysics and Heat Transfer*, 25(2):218–227, 2011. URL https://doi.org/10.2514/1.50720.

D. E. R. Espinoza, V. Casseau, T. J. Scanlon, and R. E. Brown. An open-source hybrid cfd-dsmc solver for high speed flows. *AIP Conference Proceedings*, 1786(1):050007, 2016. URL https://aip.scitation.org/doi/abs/10.1063/1.4967557.

Diego Expósito and Zeeshan A. Rana. Computational investigations into heat transfer over a double wedge in hypersonic flows. *Aerospace Science and Technology*, 92: 839–846, 2019. ISSN 1270-9638. URL https://www.sciencedirect.com/science/article/pii/S1270963818325537.

Elise J. Fahy, David R. Buttsworth, Rowan J. Gollan, Peter A. Jacobs, Richard G. Morgan, and Christopher M. James. Experimental and computational fluid dynamics study of Hayabusa reentry peak heating. *Journal of Spacecraft and Rockets*, 58(6):1833–1846, 2021. URL https://doi.org/10.2514/1.A34863.

P. G. T. Fogg, P. A. Hanks, and J. D. Lambert. Ultrasonic dispersion in halo-methane vapours. *Proceedings of the Royal Society of London. Series A, Mathematical and Physical Sciences*, 219(1139):490–499, 1953. ISSN 00804630. URL http://www.jstor.org/stable/99249.

Felipe Martín Rodríguez Fuentes and Bernard Parent. *Use of Fuel Injection to Attenuate Scramjet Inlet Recirculations*. AIAA, 2022. URL https://arc.aiaa.org/doi/abs/10.2514/6.2022-3442.

Michiko Furudate, Toshiyuki Suzuki, and Keisuke Sawada. *Calculation of intermediate hypersonic flow using multi-temperature model*. AIAA, 2000. URL https://arc.aiaa.org/doi/abs/10.2514/6.2000-343.

U. Gerlinger, H.-H. Fruehauf, T. Boenisch, T. Boenisch, U. Gerlinger, and H.-H. Fruehauf. *Implicit upwind Navier-Stokes solver for re-entry nonequilibrium flows*. AIAA, 1997. URL https://arc.aiaa.org/doi/abs/10.2514/6.1997-2547.

Vincent F. Giangaspero, Andrea Lani, Stefaan Poedts, Jan Thoemel, and Alessandro Munafò. *Radio communication blackout analysis of ExoMars re-entry mission using ray-tracing method*. AIAA, 2021. URL https://arc.aiaa.org/doi/abs/10.2514/6.2021-0154.

Jay H Grinstead, Michael C Wilder, Daniel C Reda, Charles J Cornelison, Brett A Cruden, and David W Bogdanoff. Shock tube and ballistic range facilities at nasa ames research center. Technical report, NASA, 2010.

Roop Gupta, Jerrold Yos, Richard Thompson, and Kam-Pui Lee. A review of reaction rates and thermodynamic and transport properties for an 11-species air model for chemical and thermal nonequilibrium calculations to 30000 K. Technical report, NASA, 09 1990.

Roop N. Gupta, James N. Moss, and Joseph M. Price. Assessment of thermochemical nonequilibrium and slip effects for orbital re-entry experiment. *Journal of Thermophysics and Heat Transfer*, 11(4):562–569, 1997. URL https://doi.org/10.2514/2.6280.

Brian L. Haas and Jeffrey D. McDonald. Validation of chemistry models employed in a particle simulation method. *Journal of Thermophysics and Heat Transfer*, 7(1):42–48, 1993. URL https://doi.org/10.2514/3.11567.

M. Hajman, O. Bublik, and J. Vimmr. On the modelling of compressible inviscid flow problems using AUSM schemes. *Applied and Computational Mechanics*, 1(2):469–478, 2007. ISSN 1802-680X. URL https://www.ingentaconnect.com/content/doaj/1802680x/2007/00000001/00000002/art00011.

Logan D. Halstrom, Thomas H. Pulliam, Robert Childs, and Paul Stremel. *OVERFLOW Analysis of Supersonic Retropropulsion Testing on a Blunt Mars Entry Vehicle Concept*. AIAA, 2022. URL https://arc.aiaa.org/doi/abs/10.2514/6.2022-0914.

Klaus Hannemann, Christian Hepp, Violetta Winkler, Volker Hannemann, Thomas Schlegat, and Martin Grabe. Numerical and experimental analysis of rarefaction effects on aerodynamic coefficients of a slender re-entry vehicle. In *International Conference on High-Speed Vehicle Science and Technology (HiSST)*, November 2018. URL https://elib.dlr.de/123370/.

David Hash, Joseph Olejniczak, Michael Wright, Dinesh Prabhu, Maria Pulsonetti, Brian Hollis, Peter Gnoffo, Michael Barnhardt, Ioannis Nompelis, and Graham Candler. *FIRE II Calculations for Hypersonic Nonequilibrium Aerothermodynamics Code Verification: DPLR, LAURA, and US3D*. AIAA, 2007a. URL https://arc.aiaa.org/doi/abs/10.2514/6.2007-605.

David Hash, Joseph Olejniczak, Michael Wright, Dinesh Prabhu, Maria Pulsonetti, Brian Hollis, Peter Gnoffo, Michael Barnhardt, Ioannis Nompelis, and Graham Candler. *FIRE II Calculations for Hypersonic Nonequilibrium Aerothermodynamics Code Verification: DPLR, LAURA, and US3D*. AIAA, 2007b. URL https://arc.aiaa.org/doi/abs/10.2514/6.2007-605.

Bernd Helber, Olivier Chazot, Thierry Magin, and Annick Hubin. *Ablation of Carbon Preform In the VKI Plasmatron*. AIAA, 2012. URL https://arc.aiaa.org/doi/abs/10.2514/6.2012-2876.

Michael E. Holloway, Ross S. Chaudhry, and Iain D. Boyd. Assessment of hypersonic double-cone experiments for validation of thermochemistry models. *Journal of Spacecraft and Rockets*, 59(2):389–400, 2022. URL https://doi.org/10.2514/1.A35052.

Timothy D. Holman and Iain D. Boyd. Effects of continuum breakdown on the surface properties of a hypersonic sphere. *Journal of Thermophysics and Heat Transfer*, 23(4): 660–673, 2009. URL https://doi.org/10.2514/1.43509.

Kyu Hong Kim, Joon Ho Lee, and Oh Hyun Rho. An improvement of AUSM schemes by introducing the pressure-based weight functions. *Computers & Fluids*, 27(3): 311–346, 1998. ISSN 0045-7930. URL https://www.sciencedirect.com/science/article/pii/S0045793097000698.

Nobuaki ISHII, Tetsuya YAMADA, Koju HIRAKI, and Yoshifumi INATANI. Reentry motion and aerodynamics of the MUSES-C sample return capsule. *Transactions Of The Japan Society For Aeronautical And Space Sciences*, 51(172):65–70, 2008.

George Karypis and Vipin Kumar. A fast and high quality multilevel scheme for partitioning irregular graphs. *SIAM Journal on Scientific Computing*, 20(1):359–392, 1998. URL https://doi.org/10.1137/S1064827595287997.

Yuko Kawaguchi, Mio Shibuya, Iori Kinoshita, Jun Yatabe, Issay Narumi, Hiromi Shibata, Risako Hayashi, Daisuke Fujiwara, Yuka Murano, Hirofumi Hashimoto, Eiichi Imai, Satoshi Kodaira, Yukio Uchihori, Kazumichi Nakagawa, Hajime Mita, Shinichi Yokobori, and Akihiko Yamagishi. Dna damage and survival time course of deinococcal cell pellets during 3 years of exposure to outer space. *Frontiers in Microbiology*, 11, 2020. ISSN 1664-302X. URL https://www.frontiersin.org/articles/10.3389/fmicb.2020.02050.

James Keck and George Carrier. Diffusion theory of nonequilibrium dissociation and recombination. *The Journal of Chemical Physics*, 43(7):2284–2298, 1965. URL https://doi.org/10.1063/1.1697125.

D J Kewley. Numerical study of anharmonic diatomic relaxation rates in shock waves and nozzles. *Journal of Physics B: Atomic and Molecular Physics*, 8(15):2565, oct 1975. URL https://dx.doi.org/10.1088/0022-3700/8/15/018.

Hisashi Kihara, Naoya Hirata, Ken-ichi Abe, et al. A study of thermal response and flow field coupling simulation around Hayabusa capsule loaded with light-weight ablator. *Open Journal of Fluid Dynamics*, 3(02):100, 2013.

Jae Gang Kim and Sung Min Jo. Modification of chemical-kinetic parameters for 11-air species in re-entry flows. *International Journal of Heat and Mass Transfer*, 169:120950, 2021. ISSN 0017-9310. URL https://www.sciencedirect.com/science/article/pii/S0017931021000533.

Kyu Hong Kim, Chongam Kim, and Oh-Hyun Rho. Methods for the accurate computations of hypersonic flows: I. AUSMPW+scheme. *Journal of Computational Physics*, 174 (1):38–80, 2001. ISSN 0021-9991. URL https://www.sciencedirect.com/science/article/pii/S0021999101968731.

Min Kwan Kim, Burkard Esser, Uwe Koch, and Ali Guelhan. *Numerical and Experimental Study of High Enthalpy Flows in a Hypersonic Plasma Wind Tunnel: L3K*. AIAA, 2011. URL https://arc.aiaa.org/doi/abs/10.2514/6.2011-3777.

Minkwan Kim, Michael Keidar, and Iain D. Boyd. Analysis of an electromagnetic mitigation scheme for reentry telemetry through plasma. *Journal of Spacecraft and Rockets*, 45(6):1223–1229, 2008. URL https://doi.org/10.2514/1.37395.

Minkwan Kim, Ali Gülhan, and Iain D. Boyd. Modeling of electron energy phenomena in hypersonic flows. *Journal of Thermophysics and Heat Transfer*, 26(2):244–257, 2012. URL https://doi.org/10.2514/1.T3716.

O. Knab, H.-H. Fruehauf, and E. W. Messerschmid. Theory and validation of the physically consistent coupled vibration-chemistry-vibration model. *Journal of Thermophysics and Heat Transfer*, 9(2):219–226, 1995. URL https://doi.org/10.2514/3.649.

Doyle Knight, José Longo, Dimitris Drikakis, Datta Gaitonde, Andrea Lani, Ioannis Nompelis, Bodo Reimann, and Louis Walpot. Assessment of cfd capability for prediction of hypersonic shock interactions. *Progress in Aerospace Sciences*, 48-49:8–26, 2012. ISSN 0376-0421. URL https://www.sciencedirect.com/science/article/pii/S0376042111001023. Assessment of Aerothermodynamic Flight Prediction Tools.

L. Landau and E. Teller. Theory of monomolecular reactions. *Zur Theore der Schalldispersion*, page 34, 1936. URL https://www.scopus.com/inward/record.uri?eid=2-s2.0-84883607868&partnerID=40&md5=137956dde726529b5e271f8b9ddedc13. Cited by: 2.

Stefan Langer. Investigation and application of point implicit runge–kutta methods to inviscid flow problems. *International Journal for Numerical Methods in Fluids*, 69(2): 332–352, 2012. URL https://onlinelibrary.wiley.com/doi/abs/10.1002/fld.2561.

J. H. Lee. *Basic governing equations for the flight regimes of aeroassisted orbital transfer vehicles*. AIAA, 1984. URL https://arc.aiaa.org/doi/abs/10.2514/6.1984-1729.

Sanghoon Lee, Ikhyun Kim, Gisu Park, Jong Kook Lee, and Jae Gang Kim. Thermochemical nonequilibrium flow analysis in low enthalpy shock-tunnel facility. *PLOS ONE*, 15(10):1–24, 10 2020. URL https://doi.org/10.1371/journal.pone.0240300.

D. Lequang, Y. Babou, and P. Andre. Experimental assessment of local thermodynamic equilibrium in vki plasmatron air plasma jet. *Journal of Technical Physics*, Vol. 50, no 3:151–162, 2009.

Meng-Sing Liou. A sequel to AUSM: AUSM+. *Journal of Computational Physics*, 129(2): 364–382, 1996. ISSN 0021-9991. URL https://www.sciencedirect.com/science/article/pii/S0021999196902569.

Meng-Sing Liou. The evolution of AUSM schemes. *Defence Science Journal*, 60(6):606–613, Sep. 2010. URL https://publications.drdo.gov.in/ojs/index.php/dsj/article/view/580.

Meng-Sing Liou and Christopher J. Steffen. A new flux splitting scheme. *Journal of Computational Physics*, 107(1):23–39, 1993. ISSN 0021-9991. URL https://www.sciencedirect.com/science/article/pii/S0021999183711228.

Yen Liu, Dinesh Prabhu, Kerry A. Trumble, David Saunders, and Peter Jenniskens. Radiation modeling for the reentry of the Stardust sample return capsule. *Journal of Spacecraft and Rockets*, 47(5):741–752, 2010. URL https://doi.org/10.2514/1.37813.

Stefan Loehle, Arne Meindl, Erik Poloni, Joseph Steer, Tamara Sopek, Matthew McGilvray, and Louis Walpot. *Experimental Simulation of Gas Giant Entry in the PWK1 Arcjet Facility including CH4*. AIAA, 2022. URL https://arc.aiaa.org/doi/abs/10.2514/6.2022-0264.

Han Luo, Alina A. Alexeenko, and Sergey O. Macheret. Assessment of classical impulsive models of dissociation in thermochemical nonequilibrium. *Journal of Thermophysics and Heat Transfer*, 32(4):861–868, 2018. URL https://doi.org/10.2514/1.T5375.

Robyn Lindsay Macdonald. *Reduced-order model framework for thermochemical nonequilibrium hypersonic flows*. PhD thesis, University of Illinois at Urbana-Champaign, 2019.

S. O. Macheret, A. A. Fridman, I. V. Adamovich, J. W. Rich, and Treanor C. E. *Mechanisms of nonequilibrium dissociation of diatomic molecules*. AIAA, 1994. URL https://arc.aiaa.org/doi/abs/10.2514/6.1994-1984.

Walter T. Maier, Jacob T. Needels, Catarina Garbacz, Fábio Morgado, Juan J. Alonso, and Marco Fossati. Su2-nemo: An open-source framework for high-mach nonequilibrium multi-species flows. *Aerospace*, 8(7), 2021. ISSN 2226-4310. URL https://www.mdpi.com/2226-4310/8/7/193.

Tapan K. Mankodi, Upendra V. Bhandarkar, and Bhalchandra P. Puranik. Hypersonic flow over Stardust re-entry capsule using ab-initio based chemical reaction model. *Acta Astronautica*, 162:243–255, 2019. ISSN 0094-5765. URL https://www.sciencedirect.com/science/article/pii/S0094576519301146.

Paul V. Marrone and Charles E. Treanor. Chemical relaxation with preferential dissociation from excited vibrational levels. *The Physics of Fluids*, 6(9):1215–1221, 1963. URL https://aip.scitation.org/doi/abs/10.1063/1.1706888.

Alexandre Martin, Iain Boyd, and Erin Farbar. *Numerical modeling of the CN spectral emission of the Stardust re-entry vehicle*. AIAA, 2012. URL https://arc.aiaa.org/doi/abs/10.2514/6.2011-3125.

Atsushi Matsuda, Hirotaka Otsu, Masaaki Kawamura, Detlev Konigorski, Yuji Takizawa, and Takashi Abe. Model surface conductivity effect for the electromagnetic heat shield in re-entry flight. *Physics of Fluids*, 20(12):127103, 2008. URL https://doi.org/10.1063/1.3054149.

P. W. McDonald. The Computation of Transonic Flow Through Two-Dimensional Gas Turbine Cascades. In *ASME 1971 International Gas Turbine Conference and Products Show*, volume ASME 1971 International Gas Turbine Conference and Products Show of *Turbo Expo: Power for Land, Sea, and Air*, 03 1971. URL https://doi.org/10.1115/71-GT-89. V001T01A089.

Roger C. Millikan and Donald R. White. Systematics of vibrational relaxation. *The Journal of Chemical Physics*, 39(12):3209–3213, 1963. URL https://doi.org/10.1063/1.1734182.

R. P. Mueller. A Review of Extra-Terrestrial Mining and Construction Concepts. In LPI Editorial Board, editor, *Lunar ISRU 2019 - Developing a New Space Economy Through Lunar Resources and Their Utilization*, volume 2152 of *LPI Contributions*, page 5066, July 2019.

Robin A. Müller, Adam S. Pagan, Partho P. Upadhyay, and Georg Herdrich. Numerical assessment of magnetohydrodynamic heat flux mitigation for pico-sized entry capsule mockup. *Journal of Thermophysics and Heat Transfer*, 33(4):1018–1025, 2019. URL https://doi.org/10.2514/1.T5679.

S. Mungiguerra, L. Silvestroni, R. Savino, L. Zoli, B. Esser, M. Lagos, and D. Sciti. Qualification and reusability of long and short fibre-reinforced ultra-refractory composites for aerospace thermal protection systems. *Corrosion Science*, 195:109955, 2022. ISSN 0010-938X. URL https://www.sciencedirect.com/science/article/pii/S0010938X2100723X.

Jacob T. Needels, Umran Duzel, Kyle M. Hanquist, and Juan J. Alonso. *Sensitivity Analysis of Gas-Surface Modeling in Nonequilibrium Flows*. AIAA, 2022. URL https://arc.aiaa.org/doi/abs/10.2514/6.2022-1636.

Kevin Neitzel, Daniil Andrienko, and Iain D. Boyd. Aerothermochemical nonequilibrium modeling for oxygen flows. *Journal of Thermophysics and Heat Transfer*, 31(3):634–645, 2017. URL https://doi.org/10.2514/1.T4962.

Ioannis Nompelis. *Computational Study of Hypersonic Double-Cone Experiments for Code Validation.* PhD thesis, University of Minnesota, 2004.

Michael Olsen, Dinesh Prabhu, and T. Olsen. *Implementation of Finite Rate Chemistry Capability in OVERFLOW*. AIAA, 2004. URL https://arc.aiaa.org/doi/abs/10.2514/6.2004-2372.

David R. Olynick, Jeff C. Taylor, and H. A. Hassan. Comparisons between monte carlo methods and navier-stokes equations for re-entry flows. *Journal of Thermophysics and Heat Transfer*, 8(2):251–258, 1994. URL https://doi.org/10.2514/3.531.

G. R. Otey and H. A. Dwyer. Numerical study of the interaction of fast chemistry and diffusion. *AIAA Journal*, 17(6):606–613, 1979. URL https://doi.org/10.2514/3.61184.

Takashi Ozawa, Toshiyuki Suzuki, Hiroki Takayanagi, and Kazuhisa Fujita. *Analysis of Non-Continuum Hypersonic Flows for the Hayabusa Reentry*. AIAA, 2011. URL https://arc.aiaa.org/doi/abs/10.2514/6.2011-3311.

Grant Palmer. *An improved flux-split algorithm applied to hypersonic flows in chemical equilibrium*. AIAA, 1988. URL https://arc.aiaa.org/doi/abs/10.2514/6.1988-2693.

Grant Palmer. Explicit thermochemical nonequilibrium algorithm applied to compute three-dimensional aeroassist flight experiment flowfields. *Journal of Spacecraft and Rockets*, 27(5):545–553, 1990. URL https://doi.org/10.2514/3.26178.

Grant E. Palmer and Michael J. Wright. Comparison of methods to compute high-temperature gas viscosity. *Journal of Thermophysics and Heat Transfer*, 17(2):232–239, 2003. URL https://doi.org/10.2514/2.6756.

Marco Panesi, Richard L. Jaffe, David W. Schwenke, and Thierry E. Magin. Rovibrational internal energy transfer and dissociation of n2(1σg+)-n(4su) system in hypersonic flows. *The Journal of Chemical Physics*, 138(4):044312, 2013. URL https://doi.org/10.1063/1.4774412.

Bernard Parent, Prasanna T. Rajendran, Robert W. Moses, Christopher O. Johnston, F. M. Cheatwood, Sergey O. Macheret, and Justin Little. *Effect of Plasma Sheaths on Earth Re-entry MHD Processes*. AIAA, 2022. URL https://arc.aiaa.org/doi/abs/10.2514/6.2022-0980.

C. Park. *On convergence of computation of chemically reacting flows*. AIAA, 1985a. URL https://arc.aiaa.org/doi/abs/10.2514/6.1985-247.

C. Park. *Nonequilibrium Hypersonic Aerothermodynamics*. Wiley, 1990. ISBN 9780471510932. URL https://books.google.pt/books?id=jSN0QgAACAAJ.

Chul Park. Radiation enhancement by nonequilibrium in earth's atmosphere. *Journal of Spacecraft and Rockets*, 22(1):27–36, 1985b. URL https://doi.org/10.2514/3.25706.

Chul Park. Assessment of a two-temperature kinetic model for dissociating and weakly ionizing nitrogen. *Journal of Thermophysics and Heat Transfer*, 2(1):8–16, 1988. URL https://doi.org/10.2514/3.55.

Chul Park. Review of chemical-kinetic problems of future nasa missions. i - earth entries. *Journal of Thermophysics and Heat Transfer*, 7(3):385–398, 1993. URL https://doi.org/10.2514/3.431.

Chul Park. Hypersonic aerothermodynamics: Past, present and future. *International Journal of Aeronautical and Space Sciences*, 1(1), Mar 2013. URL http://dx.doi.org/10.5139/IJASS.2013.14.1.1.

Chul Park, John T. Howe, Richard L. Jaffe, and Graham V. Candler. Review of chemical-kinetic problems of future nasa missions. ii - mars entries. *Journal of Thermophysics and Heat Transfer*, 8(1):9–23, 1994. URL https://doi.org/10.2514/3.496.

Chul Park, Richard L. Jaffe, and Harry Partridge. Chemical-kinetic parameters of hyperbolic earth entry. *Journal of Thermophysics and Heat Transfer*, 15(1):76–90, 2001. URL https://doi.org/10.2514/2.6582.

Raffaele Pepe, Aldo Bonfiglioli, Antonio D'Angola, Gianpiero Colonna, and Renato Paciorri. *An unstructured solver for argon plasma flows with reduced state-to-state kinetics*. AIAA, 2013. URL https://arc.aiaa.org/doi/abs/10.2514/6.2013-3004.

G Pezzella. Ablative heat shield design for a sample return vehicle. *Journal of Space Exploration*, 2(1):52–64, 2013.

Tracie Prater, Jennifer Edmunsson, Michael R. Fiske, Frank E. Ledbetter, Curtis E. Hill, Meyya Meyyappan, Christopher Roberts, Lawrence D. Huebner, Phillip B. Hall, and Niki J. Werkheiser. Nasa's in-space manufacturing project: Update on manufacturing technologies and materials to enable more sustainable and safer exploration. In *Proceedings of the 70th International Astronautical Congress (IAC)*, 2019.

Donald Rapp and P. Englander-Golden. Resonant and near-resonant vibrational—vibrational energy transfer between molecules in collisions. *The Journal of Chemical Physics*, 40(2):573–575, 1964. URL https://doi.org/10.1063/1.1725158.

R C Reid, J M Prausnitz, and B E Poling. *The properties of gases and liquids*. McGraw-Hill, 1 1987. URL https://www.osti.gov/biblio/6504847.

Felipe Martín Rodríguez Fuentes and Bernard Parent. Control of scramjet inlet recirculations using fuel injection. *AIAA Journal*, pages 1–11, 2023. URL https://doi.org/10.2514/1.J062166.

P.L Roe. Approximate riemann solvers, parameter vectors, and difference schemes. *Journal of Computational Physics*, 43(2):357–372, 1981. ISSN 0021-9991. URL https://www.sciencedirect.com/science/article/pii/0021999181901285.

Leonardo Scalabrin and Iain Boyd. *Numerical Simulations of the FIRE-II Convective and Radiative Heating Rates*. AIAA, 2007. URL https://arc.aiaa.org/doi/abs/10.2514/6.2007-4044.

Leonardo C. Scalabrin. *Numerical simulation of weakly ionized hypersonic flow over reentry capsules*. PhD thesis, University of Michigan, Jan 2007.

Thomas J. Scanlon, Craig White, Matthew K. Borg, Rodrigo C. Palharini, Erin Farbar, Iain D. Boyd, Jason M. Reese, and Richard E. Brown. Open-source direct simulation monte carlo chemistry modeling for hypersonic flows. *AIAA Journal*, 53(6):1670–1680, 2015. URL https://doi.org/10.2514/1.J053370.

Thomas E. Schwartzentruber and Iain D. Boyd. Progress and future prospects for particle-based simulation of hypersonic flow. *Progress in Aerospace Sciences*, 72:66–79, 2015. ISSN 0376-0421. URL https://www.sciencedirect.com/science/article/

pii/S0376042114000827. Celebrating 60 Years of the Air Force Office of Scientific Research (AFOSR): A Review of Hypersonic Aerothermodynamics.

Carey F. Scott and Jennifer A. Inman. *SCIFLI Airborne Observation of the Hayabusa2 Sample Return Capsule Re-Entry*. AIAA, 2022. URL https://arc.aiaa.org/doi/abs/10.2514/6.2022-3798.

Thomas Scott, Walter Dieudonne, and Martin Spel. *MISTRAL: CONUS Debut Flow Field and Heat Transfer Calculations*. AIAA, 2004. URL https://arc.aiaa.org/doi/abs/10.2514/6.2004-2423.

J. S. Shang and S. T. Surzhikov. Simulating Stardust earth reentry with radiation heat transfer. *Journal of Spacecraft and Rockets*, 48(3):385–396, 2011. URL https://doi.org/10.2514/1.52029.

Shu sheng Chen, Fang jie Cai, Hai chao Xue, Ning Wang, and Chao Yan. An improved AUSM-family scheme with robustness and accuracy for all mach number flows. *Applied Mathematical Modelling*, 77:1065–1081, 2020. ISSN 0307-904X. URL https://www.sciencedirect.com/science/article/pii/S0307904X19305359.

Eiji Shima and Keiichi Kitamura. Parameter-free simple low-dissipation AUSM-family scheme for all speeds. *AIAA Journal*, 49(8):1693–1709, 2011. URL https://doi.org/10.2514/1.J050905.

Chen Shu-sheng, Hua Yang, Cai Fang-jie, and Gao Zheng-hong. Multi-dimensional dissipation strategy within advection upstream splitting methods in hypersonic flows. *Journal of Physics: Conference Series*, 1786(1):012050, Feb 2021. URL https://doi.org/10.1088/1742-6596/1786/1/012050.

Narendra Singh and Thomas Schwartzentruber. Nonequilibrium internal energy distributions during dissociation. *Proceedings of the National Academy of Sciences*, 115(1):47–52, 2018. URL https://www.pnas.org/doi/abs/10.1073/pnas.1713840115.

L.Douglas Smoot, William C. Hecker, and Gerald A. Williams. Prediction of propagating methane-air flames. *Combustion and Flame*, 26:323–342, 1976. ISSN 0010-2180. URL https://www.sciencedirect.com/science/article/pii/0010218076900869.

Gary A Sod. A survey of several finite difference methods for systems of nonlinear hyperbolic conservation laws. *Journal of Computational Physics*, 27(1):1–31, 1978. ISSN 0021-9991. URL https://www.sciencedirect.com/science/article/pii/0021999178900232.

Dmitry Starodubov, Shelly Mechery, David Miller, Chris Ulmer, Phil Willems, Jeff Ganley, and Dennis Tucker. Zblan fibers: From zero gravity tests to orbital manufacturing. In *Imaging and Applied Optics 2014*, page AM4A.2. Optica Publishing Group, 2014. URL http://opg.optica.org/abstract.cfm?URI=AIO-2014-AM4A.2.

J.L. Stollery, J.E. Smith, and C. Park. Chapter 3 - The effects of vibrational relaxation on hypersonic nozzle flows. In WILBUR C. NELSON, editor, *The High Temperature Aspects of Hypersonic Flow*, volume 68 of *AGARDograph*, pages 49–66. Elsevier, 1964. URL https://www.sciencedirect.com/science/article/pii/B9781483198286500084.

Jesse W. Streicher, Ajay Krish, and Ronald K. Hanson. Vibrational relaxation time measurements in shock-heated oxygen and air from 2000 K to 9000 K using ultraviolet laser absorption. *Physics of Fluids*, 32(8):086101, 2020. URL https://doi.org/10.1063/5.0015890.

Kenneth Sutton and Peter Gnoffo. *Multi-component diffusion with application to computational aerothermodynamics*. AIAA, 1998. URL https://arc.aiaa.org/doi/abs/10.2514/6.1998-2575.

Toshiyuki Suzuki, Kazuhisa Fujita, Tetsuya Yamada, Yoshifumi Inatani, and Nobuaki Ishii. Postflight thermal protection system analysis of Hayabusa reentry capsule. *Journal of Spacecraft and Rockets*, 51(1):96–105, 2014. URL https://doi.org/10.2514/1.A32549.

Sachiko Takahashi, Kazunori Ohta, Naoki Furubayashi, Bin Yan, Misako Koga, Yoshio Wada, Mitsugu Yamada, Koji Inaka, Hiroaki Tanaka, Hiroshi Miyoshi, et al. Jaxa protein crystallization in space: ongoing improvements for growing high-quality crystals. *Journal of Synchrotron Radiation*, 20(6):968–973, 2013.

Yusuke Takahashi and Kazuhiko Yamada. Aerodynamic-heating analysis of sample-return capsule in future trojan-asteroid exploration. *Journal of Thermophysics and Heat Transfer*, 32(3):547–559, 2018. URL https://doi.org/10.2514/1.T4837.

L. Tam and C. Li. *Three-dimensional thermochemical nonequilibrium flow modeling for hypersonic flows*. AIAA, 1989. URL https://arc.aiaa.org/doi/abs/10.2514/6.1989-1860.

E Torres, T Gross, E Geistfeld, and TE Schwartzentruber. Verification of nonequilibrium thermochemistry models for hypersonic cfd by first-principles simulation. In *Eleventh International Conference on Computational Fluid Dynamics (ICCFD11)*. ICCFD, 2022.

Kerry A. Trumble, Ioana Cozmuta, Steve Sepka, Peter Jenniskens, and Michael Winter. Postflight aerothermal analysis of the Stardust sample return capsule. *Journal of Spacecraft and Rockets*, 47(5):765–774, 2010a. URL https://doi.org/10.2514/1.41514.

Kerry A. Trumble, Ioana Cozmuta, Steve Sepka, Peter Jenniskens, and Michael Winter. Postflight aerothermal analysis of the Stardust sample return capsule. *Journal*

of Spacecraft and Rockets, 47(5):765–774, 2010b. URL https://doi.org/10.2514/1.41514.

Michele Tuttafesta, Gianpiero Colonna, and Giuseppe Pascazio. Computing unsteady compressible flows using roe's flux-difference splitting scheme on gpus. *Computer Physics Communications*, 184(6):1497–1510, 2013. ISSN 0010-4655. URL https://www.sciencedirect.com/science/article/pii/S0010465513000350.

Yasuhiro Wada and Meng-Sing Liou. An accurate and robust flux splitting scheme for shock and contact discontinuities. *SIAM Journal on Scientific Computing*, 18(3):633–657, 1997. URL https://doi.org/10.1137/S1064827595287626.

Tian Wan, Graham Candler, Sergey Macheret, Mikhail Shneider, and Richard Miles. *CFD Modeling and Simulations of MHD Power Generation During Re-Entry*. AIAA, 2004. URL https://arc.aiaa.org/doi/abs/10.2514/6.2004-2562.

C. R. Wilke. A viscosity equation for gas mixtures. *The Journal of Chemical Physics*, 18 (4):517–519, 1950. URL https://doi.org/10.1063/1.1747673.

Michael W. Winter, Ryan D. McDaniel, Yih-Kanq Chen, David Saunders, and Peter Jenniskens. Radiation modeling for reentry of Hayabusa sample return capsule. *Journal of Spacecraft and Rockets*, 56(4):1152–1164, 2019. URL https://doi.org/10.2514/1.A34381.

Gouji Yamada. Electron density measurements of shocked argon using stark profile of the Hβ line. *AIAA Journal*, pages 1–7, 2022. URL https://doi.org/10.2514/1.J061470.

Ivan Zanardi, Simone Venturi, and Marco Panesi. *Towards Efficient Simulations of Non-Equilibrium Chemistry in Hypersonic Flows: A Physics-Informed Neural Network Framework*. AIAA, 2022. URL https://arc.aiaa.org/doi/abs/10.2514/6.2022-1639.

Surzhikov S.T. Zheleznyakova A.L. Calculation of a hypersonic flow over bodies of complex configuration on unstructured tetrahedral meshes using the AUSM scheme. *High Temperature*, (52):271–281, 2014. URL https://doi.org/10.1134/S0018151X14020217.